



SAPIENZA
UNIVERSITÀ DI ROMA

Remote Sensing and Electromagnetic Modeling Applied to Weather and Forward Scatter Radar

MARTA TECLA FALCONI

A thesis submitted
in partial fulfillment of the requirements for the degree of

Doctor of Philosophy in
Information and Communications Technologies

Curriculum in Radar and Remote Sensing

at

Sapienza University of Rome
Rome, Italy

February 2018

Cycle XXX

Author:

MARTA TECLA FALCONI

DIET, Sapienza

Thesis Supervisor:

PROF. FRANK S. MARZANO

DIET, Sapienza

Marta Tecla Falconi: *Remote Sensing and Electromagnetic Modeling Applied to Weather and Forward Scatter Radar*

© February 2018

THESIS SUPERVISOR:

Prof. Frank S. Marzano

LOCATION:

Rome, Italy

TIME FRAME:

February 2018

This thesis was evaluated by the two following external referees:

Dr. Marina Gashinova

School of Electronic, Electrical and Systems Engineering (ESEE), University of Birmingham, Edgbaston, Birmingham, United Kingdom

Roberto Cremonini

Agenzia Regionale per la Protezione Ambientale (ARPA) Piemonte, Torino, Italy

Dr. Domenico Cimini

Consiglio Nazionale delle Ricerche - Istituto di Metodologie per l'Analisi Ambientale (CNR-IMAA), Tito Scalo (PZ), Italy

Dr. Prof. Alexis Berne

École polytechnique fédérale de Lausanne (EPFL), Lausanne, Switzerland

The time and effort of the external referees in evaluating this thesis, as well as their valuable and constructive suggestions, are very much appreciated and greatly acknowledged.

Je suis dans la nuit, et j'essaie d'y voir clair.

— Albert Camus, *La Peste*, 1947

Voyagez, écrivez, traduisez, apprenez à vivre partout.

Commencez tout de suite. L'avenir est aux curieux de profession.

Les Français sont restés trop longtemps enfermés derrière leurs frontières.

— François Truffaut, *Jules et Jim*, Screenplay, 1962

ABSTRACT

This dissertation deals with electromagnetic modelling and data analysis, related to radar remote sensing and applied to forward scatter and meteorological polarimetric systems. After an overview of radar fundamentals to introduce the general terminology and concepts, results are presented at the end of each chapter.

In this respect, a generalized electromagnetic model is first presented in order to predict the response of forward scatter radars (FSRs) for air-target surveillance applications in both near-field and far-field regions. The model is discussed for increasing levels of complexity: a simplified near-field model, a near-field receiver model and a near-field receiver and transmitter model. FSR results have been evaluated in terms of the effects of different target electrical sizes and detection distances on the received signal, as well as the impact of the trajectory of the moving objects and compared with a customized implementation of a full-wave numerical tool.

Secondly, a new data processing methodology, based on the statistical analysis of ground-clutter echoes and aimed at investigating the monitoring of the weather radar relative calibration, is presented. A preliminary study for an improvement of the ground-clutter calibration technique is formulated using as a permanent scatter analysis (PSA) and applied to real radar scenarios. The weather radar relative calibration has been applied to a dataset collected by a C-band weather radar in southern Italy and an evaluation with statistical score indexes has drawn through the comparison with a deterministic clutter map. The PSA technique has been proposed using a big metallic roof with a periodic mesh grid structure and having a hemispherical shape in the near-field of a polarimetric C-band radar and evaluated also with an ad-hoc numerical implementation of a full-wave solution.

Finally, a radar-based snowfall intensity retrieval is investigated at centimeter and millimeter wavelengths (i.e., at X, Ka and W band) using a high-quality database of collocated ground-based precipitation measurements and radar multi-frequency observations. Coefficients for the multi-frequency radar snowfall intensity retrieval are empirically derived using

multivariate regression techniques and their interpretation is carried out by particle scattering simulations with soft-ice spheroids.

For each topic, conclusions are proposed to highlight the goals of the whole work and pave the way for future studies.

SOMMARIO

Questa tesi riguarda la modellizzazione elettromagnetica e l'analisi dei dati legate al telerilevamento e applicate ai sistemi radar a diffusione in avanti e radar meteorologici. Dopo una panoramica dei fondamenti radar per introdurre la terminologia e i concetti generali, i capitoli successivi mostrano i risultati finali.

Un modello elettromagnetico generalizzato è presentato per predire la risposta di un radar a diffusione in avanti (FSR) per essere applicato nella sorveglianza di bersagli aerei in campo vicino e lontano. Il modello è discusso aumentando progressivamente il livello di complessità: un modello semplificato in campo vicino, un modello con ricevitore in campo vicino e un modello con sia ricevitore che trasmettitore in campo vicino. I risultati del FSR sono stati valutati in termini dell'effetto di differenti bersagli con variabili dimensioni e cambiando la distanza dal ricevitore, tanto quanto l'impatto della traiettoria sull'oggetto in movimento. Tali risultati sono confrontati con una implementazione sviluppata appositamente con uno strumento numerico ad onda continua.

Successivamente, viene presentata una nuova metodologia di elaborazione del dato, basata sull'analisi statistica degli echi di clutter di terra, avente lo scopo di investigare il monitoraggio della calibrazione relativa di radar meteorologici. Uno studio preliminare è formulato per ottenere un miglioramento della tecnica di calibrazione con il clutter di terra usando un'analisi di scatteratori permanenti (PSA) applicata in scenari radar reali. La calibrazione relativa di radar meteorologici è stata provata su un insieme di dati collezionato da un radar meteorologico C-band presente in Sud Italia. Una valutazione con indici di qualità statistica è stata delineata attraverso il confronto con una mappa di clutter deterministica. La tecnica PSA è stata proposta usando come scatteratore di riferimento un grande tetto metallico con una struttura periodica a griglia, avente una forma emisferica, situato nel campo vicino di un radar polarimetrico in banda C. La valutazione prevede in questo caso una implementazione numerica ad-hoc di una soluzione ad onda continua.

Alla fine, un'inversione dell'intensità di precipitazione nevosa su base radar è investigata con lunghezze d'onda centimetriche e millimetriche (i.e., in banda X, Ka e W) usando un database ad alta-qualità di collocate

osservazioni di strumenti a terra e radar multifrequenza. Coefficienti per l'inversione dell'intensità di precipitazione nevosa a multifrequenza sono empiricamente derivati usando tecniche di regressione multivariate e la loro interpretazione è argomentata con simulazioni di particelle diffuse con sferoidi di ghiaccio-soffice.

Le conclusioni sono proposte per ogni argomento allo scopo di evidenziare i traguardi dell'intero lavoro e gettare le basi per gli sviluppi futuri.

PUBLICATIONS OF THE PH.D. CANDIDATE

ARTICLES

- **Marta Tecla Falconi**, Mario MONTOPOLI, and Frank S. MARZANO, "Bayesian statistical analysis of ground-clutter for the relative calibration of dual polarization weather radars," *European Journal of Remote Sensing*, 49, pp. 933-953, 2016, doi: 10.5721/EuJRS20164949.
- **Marta Tecla Falconi**, Davide COMITE, Alessandro GALLI, Debora PASTINA, Pierfrancesco LOMBARDO, and Frank S. MARZANO, "Forward Scatter Radar for Air Surveillance: Characterizing the Target-Receiver Transition from Far-Field to Near-Field Regions," *Remote Sensing*, 2017, 9(1), 50, doi: 10.3390/rs9010050.
- **Marta Tecla Falconi**, Annakaisa VON LERBER, Davide ORI, Frank Silvio MARZANO, and Dmitri MOISSEEV, "Snowfall retrieval at X, Ka and W band: consistency of backscattering and microphysical properties using BA ECC ground-based measurements," *Atmos. Meas. Tech. Discuss.*, in review, 2018, doi:<https://doi.org/10.5194/amt-2017-485>.

CONFERENCE PAPERS

- **Marta Tecla Falconi**, Davide COMITE, Alessandro GALLI, Pierfrancesco LOMBARDO, and Frank S. MARZANO, "Forward Scatter Radar Modeling: Effects of Near Field for Canonical Targets," *Proc. 2015 IEEE International Symposium on Antennas and Propagation & USNC/URSI National Radio Science Meeting*, doi:10.1109/APS.2015.7304632.
- **Marta Tecla Falconi**, Gianfranco VULPIANI, Mario MONTOPOLI, and Frank S. MARZANO, "C-band polarimetric weather radar calibration using a fuzzy logic fusion of three techniques," *Proc. 2015 IEEE IGARSS*, doi:10.1109/IGARSS.2015.7327047.
- **Marta Tecla Falconi**, Davide COMITE, Frank S. MARZANO, Alessandro GALLI, and Pierfrancesco LOMBARDO, "Analysis of canonical targets in near field for Forward Scatter Radar applications," *Proc. 2015 Radar Conference (EuRAD)*, doi:10.1109/EuRAD.2015.7346241.
- **Marta Tecla Falconi** and Davide COMITE, "Electromagnetic Modeling of Forward Scatter Radar," *Proc. 2016 Rinem*.
- **Marta Tecla Falconi**, Davide COMITE, Debora PASTINA, Alessandro GALLI, F. S. MARZANO, and Pierfrancesco LOMBARDO, "Analytical Modeling and

Numerical Validation of Forward Scattering for Radar Applications," *Proc. 2016 Radar Conference (EuRAD)*.

- **Marta Tecla Falconi**, Frank S. MARZANO, Mario MONTOPOLI, and Luca BALDINI, "Optimal Combination Of External Calibration Techniques For C-Band Polarimetric Weather Radar Performance Monitoring," *Proc. ERAD 2016*. **Best Young Scientist Award at ERAD 2016**.
- **Marta Tecla Falconi**, Davide COMITE, Alessandro GALLI, Frank S. MARZANO, Debora PASTINA, and Pierfrancesco LOMBARDO, "Monitoring by forward scatter radar techniques: an improved second-order analytical model," *Proc. SPIE Remote Sensing 2017*. **Best Student Paper at SPIE Remote Sensing 2017**.
- **Marta Tecla Falconi**, Frank S. MARZANO, Mario MONTOPOLI, and Luca BALDINI, "Weather Radar Performance Monitoring using a Metallic-Grid Ground-Scatterer," *Proc. SPIE Remote Sensing 2017*.
- Davide COMITE, **Marta Tecla Falconi**, Pierfrancesco LOMBARDO, Frank S. MARZANO, and Alessandro GALLI, "Investigating Shadow Radiation of 3-Dimensional Radar Targets in the Near Field," *Proc. 2017 Radar Conference (EuRAD)*.

Freud definisce la salute mentale in un modo che mi è sempre piaciuto, anche se mi pareva inaccessibile: la capacità di amare e lavorare. Ero capace di amare, meglio ancora di accettare che qualcuno mi amasse, il lavoro sarebbe seguito.

— Emmanuel Carrère, *D'autres vies que la mienne*

ACKNOWLEDGMENTS

I wish to thank Professor Frank Silvio Marzano, my advisor, for his fundamental support before and during the preparation of this thesis. I sincerely thank Professor Debora Pastina, Professor Pierfrancesco Lombardo and Professor Alessandro Galli for their guidance during this three-years-long journey. I express my deep gratitude to Professor Dmitri Moisseev of the University of Helsinki for having accepted me in the Radar Laboratory at Department of Physics, University of Helsinki. I thank Dr. Davide Comite, Dr. Mario Montopoli and Dr. Luca Baldini who really pushed me toward the PhD.

I thank all the PostDoc and PhD colleagues of the DIET Department for the period spent together, in particular Laura Farina, Nertjana Ustalli and Roberta Anniballe. I also thank all the Radar Laboratory in Helsinki in particular Annakaisa Von Lerber, Jussi Tiira, Haoran Li and Lorenzo Cima.

I want to thank my parents and my aunt Alberta for their unconditional support and for staying always close to me during the last three years. Thanks to Davide, Mery and Stefano: you are my people. Thanks to Elena for those happy carefree and humorous times. Last but not least thanks to Simone for all the moments spent together.

CONTENTS

1	Introduction	1
2	Radar Remote Sensing	5
2.1	Radar systems and fundamental equations	6
2.1.1	Single-scattering equation	7
2.1.2	Distributed-scatterer equation	9
2.1.3	Radar measurements and applications	10
2.2	Electromagnetic scattering theory	15
2.2.1	An overview of the scattering theories	16
2.2.2	Radiation from Apertures	18
2.2.3	Scattering by complex object	25
2.3	Introduction to forward scatter radar (FSR)	27
2.3.1	Bistatic radar	27
2.3.2	FSR effect	29
2.3.3	FSR: advantages and limitations	30
2.3.4	FSR: system and coverage	31
2.3.5	FSR signal and electromagnetic modeling	33
2.4	Introduction to weather radar	36
2.4.1	Hydrometeor microphysics	36
2.4.2	Weather radar observables	47
2.5	Conclusion	50
3	Forward scatter radar	51
3.1	Theoretical backgrounds	51
3.1.1	Physical Theory of Diffraction (PTD)	52
3.1.2	Arago spot and "black spot" effects	55
3.1.3	Shadow Contour Theorem	56
3.2	Electromagnetic model	60
3.2.1	Near-field simplified model	60
3.2.2	Near-field Rx and Tx-Rx models	61
3.2.3	Model sensitivity	65
3.3	Results for simplified model	67
3.3.1	Transition to near-field for a rectangular target	68
3.3.2	Transition to near-field for a circular target	68
3.4	Results for near-field receiver model	70
3.4.1	Transition from far field to near field	70
3.4.2	Effect of the target size	75

3.4.3	Effect of the trajectory	79
3.4.4	Effect of the 1-O and 2-O approximations	84
3.5	Conclusion	84
4	Monitoring of Weather Radars Calibration	85
4.1	Weather radar calibration	85
4.1.1	Self-consistency and Solar calibration	86
4.1.2	Ground clutter techniques	86
4.2	Weather-radar relative calibration technique	87
4.2.1	Overall approach	88
4.2.2	System and data	89
4.2.3	Ground-clutter Bayesian classification	91
4.2.4	Ground-clutter spatial analysis and calibration	96
4.3	Permanent Scatter Analysis (PSA)	105
4.3.1	Radar scenario	106
4.3.2	Calibration: a case study	108
4.3.3	Results of Electromagnetic Simulation	109
4.4	Conclusion	113
5	Snow retrieval from multifrequency radar	115
5.1	Radar remote sensing in snowfall	116
5.1.1	The multifrequency approach	116
5.1.2	Multifrequency in snowfall detection	120
5.1.3	Ze-S relations and its importance	127
5.1.4	Connection to satellite and ground validation	132
5.1.5	Challenges and proposed solution	133
5.2	Field campaign BAecc	134
5.2.1	Surface precipitation measurements	134
5.2.2	C-band Polarimetric Doppler weather radar	136
5.2.3	ARM cloud radar system (X/Ka/W): Sky-noise, cross- calibration and attenuation analysis	137
5.3	Methods	145
5.3.1	Ze-S relations at X/Ka/W-band	145
5.3.2	Direct computations using the T-matrix method	146
5.3.3	Computations using particle scattering database	148
5.4	Results	149
5.4.1	Analysis of X, Ka and W band Ze – S empirical relations	150
5.4.2	Explaining Ze-S relations with computations	152
5.5	Conclusion	163
6	Conclusions	165
A	Computing scattering: T-matrix	169

B Analytical Formulas for FSR EM Models	175
B.1 Near-field receiver 1-O	175
B.2 Near-field receiver2-O	176
 Bibliography	 179

LIST OF FIGURES

1	Electromagnetic remote sensing scheme.	6
2	Single and distributed scatterers inside the radar beam.	7
3	Backscattering efficiency as a function of a dimensionless size parameter χ , useful to highlight the three domains of scattering [21].	17
4	Volume V_0 surrounded by S_f , S_0 , S and S_∞ . The observation point \mathbf{r} is outside S	19
5	Aperture A on screen S . Top-right Green's function which satisfies Dirichlet's condition.	22
6	Babinet's principle applied to a screen (a) and a slot (b).	27
7	Bistatic geometry.	28
8	Forward scatter radar one-dimensional geometry.	30
9	Block diagram of a CW FSR.	32
10	Simulated scenario and frame for the FSR model.	34
11	Amplitude of the total signal following the model of equation (69) in [9].	35
12	As in Figure 11 for the phase signature of a point-like target (equation (67)).	36
13	As in Figure 11 for the extended FS-CS of a target (equation (68)).	37
14	Complex relative permittivity of water: (a) permittivity; (b) loss factor. In yellow is highlighted the C band between 5 and 6 GHz. Figure from [21].	39
15	Spheroids described in terms of aspect ratio.	40
16	Computed shape of selected drops of various radii from [33]: (a) 0.11 cm; (b) 0.14 cm; (c) 0.18 cm; (d) 0.20 cm; (e) 0.25 cm; (f) 0.29 cm; (g) 0.30 cm; (h) 0.35 cm; (i) 0.40 cm.	41
17	Complex relative permittivity of ice from [31]. In orange is highlighted the C band between 5 and 6 GHz. The yellow area indicates a much larger range between 0.3 and 300 GHz.	45
18	Reference scenario for the analysis of FSR problems.	52
19	Geometry of FSR that takes into account the near-field condition with respect to both the transmitter and the receiver.	53
20	Arago spot and "black spot" effects.	56

21 Scattered (subscripts 'S') and total (subscripts 'T') signals collected by the receiving antenna as the target moves along the x direction (see Figure 29), for three different near-field/far-field distances using the numerical solutions of equations (111)-(112). 57

22 Scattered (subscripts 'S') and total (subscripts 'T') signals collected by the receiving antenna as the target moves along the x direction (see Figure 29), for three different three different target sizes using the numerical solutions of equations (111)-(112). 58

23 Different regions of EM propagation. 59

24 Map of the phase error from equation (130) for a horizontal angle $\alpha_h = 30^\circ$ and tilt angle $\psi = 0^\circ$ 65

25 Map of the phase error from equation (131) for a horizontal angle $\alpha_h = 30^\circ$ and tilt angle $\psi = 0^\circ$ 66

26 Map of the area where the phase error does not exceed $\pi/8$ to compare the 1-O and 2-O formulations. 67

27 The rectangular shape signature is presented in terms of FS-CSS and signal model as the target/Rx distance z_{Rx} is varied, evaluated by equation (114) using the simplified near-field model. 69

28 The circular shape signature is presented in terms of FS-CSSs and signal model as the target/Rx distance z_{Rx} is varied, evaluated by equation (114) using the simplified near-field model. 71

29 Simulated FSR scenario for different Rx-target distances. 72

30 Scattered (subscripts 'S') and total (subscripts 'T') signals collected by the receiving antenna as the target moves along the x direction (see Figure 29), for three different near-field/far-field distances using the near-field receiver model. 73

31 Simulated FSR scenario to investigate the effects of the target dimension and shape. Three different square and a rectangular metallic plates are considered. 76

32 Scattered ('S') and total ('T') signals vs. target horizontal position, collected by the receiving antenna for three different square PEC objects using the near-field receiver model. 77

33 Scattered ('S') and total ('T') signals vs. target horizontal position, collected by the receiving antenna for various rectangular shape PEC objects using the near-field receiver model. 78

34 Amplitude and phase of the scattered field collected by the receiving antenna for different tilt angles ψ of the target trajectory (see Figure 19) using the near-field receiver model. 81

35	Amplitude and phase of the total field collected by the receiving antenna for different tilt angles ψ of the target trajectory (see Figure 19) using the near-field receiver model.	82
36	FSR scattered (subscripts 'S') and total (subscripts 'T') fields collected by the receiving antenna for a square metallic object fields collected by the receiving antenna for a square metallic object showing the comparison between the AM, 1-O and AM, 2O models. 83	83
37	The overall algorithm to analyze the calibration status of a radar system following the new data processing methodology, based on the statistical analysis of ground-clutter echoes for a C-band radar presented to me in [13].	88
38	The clutter mask shows the clutter scenario surround the radar-site of Mt. Pettinascura and the closest available radiosounding near Brindisi is also shown. Background image from: Google Earth. 90	90
39	Normalized spatial and temporal PDFs for precipitation and clutter for the 0.5° elevation, 1 μ s pulse-length, 750 Hz PRF, 360° scans and 5 rpm obtained on data from 1 to 2 August.	94
40	Precipitation and clutter normalized PDFs at the 0.5° elevation for the Bayes classifier, standard deviation of, respectively, differential reflectivity, differential phase shift and co-polar correlation coefficient obtained on data from 1 to 2 August.	95
41	Case of study of the 5 August 2014 at the 17:10 UTC shown for the co-polar reflectivity Z_{hh} time frame: a) before and c, d) after the application of the Bayesian classification. Also the conditional posterior probability that is the argument of equation (134) is shown.	97
42	Case study of the 5 August 2014 at the 17:10 UTC after the application of the Bayesian classification and region merging in which I obtain three clutter maps (in co-polar reflectivity) for three clutter sub-regions selected on spatial base.	99
43	The normalized PDFs of the three clutter sub-regions selected on spatial base.	100
44	Temporal trend of acquisition of the mean value of the probability distribution for the co-polar reflectivity (a) and differential reflectivity (b).	101
45	Temporal trend in time of acquisition of the 95th percentile of the cumulative distribution for the co-polar reflectivity (a) and differential reflectivity (b).	102

46 Radar clutter scenario considered: C-band Doppler dual-polarization Polar 55C located South-East of Rome (Italy) and the permanent scatterer used for the study, that is named Vela di Calatrava. . . . 106

47 The considered PSS, Vela di Calatrava (Rome, Italy), is shown. Background image from Google Earth. 108

48 Monitoring of the reflectivity factor (Z_{hh}) looking at the PSS (Vela di Calatrava) on the 14th October 2015. 109

49 Monitoring of the differential reflectivity Z_{dr} on the 14th October 2015: (a) looking at the PSS (Vela di Calatrava); (b) looking at the vertical profile in ice above the radar (as in [57]) where V is the falling velocity in m/s. 110

50 Geometry of the EM scenario represented by the PSS "Vela di Calatrava" element in the full-wave tool. 111

51 (a) Horizontal component of the EM field (E_{hh}) and (b) differential component of the EM field ($E_{dr} = E_{hh}/E_{vv}$) for the simulated scenario in Figure 50. 112

52 Exponential spectrum of particles within a storm. Figure in [78]. 118

53 Back-scatter cross-section σ of spheres of ice with dry surfaces (a) and of liquid water (b), at the indicated wavelengths. Figures in [78]. 119

54 Z_e , the equivalent Z , of the four exponential hail spectra, as a function of wavelength. Figure in [78]. 120

55 Values of $10\log(Z_e)\text{mm}^6\text{m}^3$ corresponding to 1gm^{-3} of hailstones of uniform diameter D at three wave-length. Figure in [87].121

56 Backscattering efficiency of a snowflake: Rayleigh-Gans approximation vs Rayleigh approximation. 125

57 Reflectivities at different frequencies of a snowflakes ensemble following the Rayleigh-Gans approximation. 126

58 DWR following the Rayleigh-Gans approximation. 127

59 Triple-Frequency space: DWR_{K_u, K_a} against $DWR_{K_a, W}$ in dB.128

60 Theoretical relation for falling velocity of snowflakes. 130

61 Theoretical relations Z_e - S in snowfall at multifrequency. 131

62 Measurement site shown with in situ and remote sensing instruments during the BAecc campaign 2014 at Hyytiälä, Finland. . . 135

63 Radar profiles at C, X, Ka and W band for the 15 February 2014 at 17:13 UTC in which I performed the calibration in the most stable interval in height between 4 and 6 km. 138

64 Calibration error histograms relates to the differences (Δ) between: X and C band radars, Ka and X band radars, and W and Ka radars.139

65	Sky noise for the Ka band for 12 February 2014: (a) A-scope at Ka-band; (b) Sky Noise histogram in dBm; (c) Sky Noise time-series in dBm; (d) Sky brightness temperature on the left, surface temperature on the right.	140
66	Relative frequency histograms of the sky noise for the Ka and W Band radars for all the ten days of BAECC IOP.	141
67	Case study: 15 February 2014 - Input of the MPM.	144
68	Case study: 15 February 2014 - Specific power attenuation in K_a band.	144
69	Case study: 15 February 2014 - Cumulative double-power attenuation in K_a band.	144
70	Case study: 15 February 2014 - Specific power attenuation in W band.	144
71	Case study: 15 February 2014 - Cumulative double-power attenuation in W band.	145
72	Case study: 12 February 2014 - Scatter plot of the equivalent reflectivities measured by the radar (points) with respect to the snow-rates S measured by PIP are shown.	150
73	Case study: 15-16 February 2014 - Scatter plot of the equivalent reflectivities measured by the radar (black points) with respect to the snow-rates S measured by PIP are shown.	151
74	Case study: 21-22 February 2014 - Scatter plot of the equivalent reflectivities measured by the radar (black points) with respect to the snow-rates S measured by PIP are shown.	152
75	Case study: 20 March 2014 - Scatter plot of the equivalent reflectivities measured by the radar (black points) with respect to the snow-rates S measured by PIP are shown.	153
76	Case study: 12 February 2014 - Equivalent reflectivity measured by the radar compared with the TMM results for aspect ratios from 0.2-1.	158
77	Case study: 15-16 February 2014 - Equivalent reflectivity measured by the radar compared with the TMM results for aspect ratios from 0.2-1.	159
78	Case study: 21-22 February 2014 - Equivalent reflectivity measured by the radar compared with the TMM results for aspect ratios from 0.2-1.	160
79	Case study: 20 March 2014 - Equivalent reflectivity measured by the radar compared with the TMM results for aspect ratios from 0.2-1.	161

80 The horizontal cross section in the W band by comparing DDA computations and TMM computations. The product between the horizontal cross section and snowflake size distribution shows the main contribute of the particles with respect to the diameter disk-equivalent. 162

81 T-matrix method geometry. 169

LIST OF TABLES

1	Radio-frequency bands according to IEEE standards.	13
2	Operational parameters for the first (1-O) and second-order (2-O) models (horizontal angle set to 30°).	67
3	Parameters of the trajectories for the FSR using the near-field receiver model.	80
4	List of the data-set for the my study in [13] acquired by the radar-site of Mt. Pettinascura on seven days every 10 minutes, divided in clear air and meteorological data.	91
5	The CSI, POD, FAR results shown in the table for three different windows size are given by using as a reference a dynamical clutter map.	96
6	Standard deviations for the co-polar reflectivity and differential reflectivity of the ground-clutter sub-regions \mathbf{D}_m^*1 , \mathbf{D}_m^*2 , \mathbf{D}_m^*3 and the whole clutter scenario \mathbf{D} using the mean value statistical parameter.	104
7	Standard deviations for the co-polar reflectivity and differential reflectivity of the ground-clutter regions \mathbf{D}_m^*1 , \mathbf{D}_m^*2 , \mathbf{D}_m^*3 and the whole clutter scenario \mathbf{D} using the 95th percentile statistical parameter.	104
8	Absolute and relative calibrations for the co-polar reflectivity and for the differential reflectivity.	104
9	EM numerical results for the scenario in Figure 50.	112
10	Parameters of selected exponential hail size spectra in [78].	117
11	Complex refractive indices of dry snow m_s at multifrequency in [7].	123
12	Theoretical evaluation of the Z_e -S coefficients in [7].	129
13	Theoretical evaluation of the Z_e -S coefficients in [115].	132
14	Technical properties of the radars: second column for the C-band polarimetric Doppler weather radar monitored by the FMI; the last two columns for the ARM cloud radar systems at X, Ka and W bands.	136
15	Attenuation for Ka and W band at 6 km for the 15 February 2014 at 17:24 UTC.	139
16	Line parameters defined in [130].	142

17 Z_e - S at X, Ka and W band measured by the radars and PIP instrument evaluated using the least-square in the log-log space. . . 154

18 Variability of the Z_e - S (Z_e in mm^6m^{-3} , S in mmh^{-1}) relations due to main assumption about the aspect ratio that influenced the refractive index and the scattering properties. 155

LIST OF SYMBOLS

- [T] Transition-matrix of the TMM.
- $\alpha_{h,Rx}$ Horizontal angle with respect to the Rx in FSR configuration.
- $\alpha_{h,Tx}$ Horizontal angle with respect to the Tx in FSR configuration.
- β Bistatic angle in FSR configuration.
- χ Dimensionless size parameter.
- $\Delta\Phi$ Phase error of the FSR models in radians.
- Δr Theoretical range resolution cell of a radar system in units of meters.
- $\Delta Z_{dr}^{D^*}$ Relative calibration index for the differential reflectivity Z_{dr} in the most stable domain D^* .
- $\Delta Z_{hh}^{D^*}$ Relative calibration index for the copolar reflectivity Z_{hh} in the most stable domain D^* .
- ϵ Permittivity or absolute permittivity measured in Farad per meter.
- ϵ_r Complex relative permittivity or dielectric constant.
- ϵ_r^∞ Value of ϵ_r for $\omega \gg 1/\tau_r$.
- ϵ_{sphere} Radius of a small sphere.
- $\eta(\mathbf{r})$ Radar reflectivity in unit over meters.
- Λ Slope parameter of the DSD.
- λ Wavelength in units of meters.
- λ_c Carrier radar wavelength in units of meters.
- c** Classes for the ground-clutter Bayesian classification.
- D** Set of grid points within the radar domain affected by ground clutter.

- \mathbf{D}^* Different sub-domains of ground-clutter after selection made by the region merging approach.
- $\mathbf{E}, \mathbf{E}(\mathbf{r}), \mathbf{E}(\mathbf{r}')$ Electric vector field in units of Volts over meters.
- $\mathbf{E}_i, \mathbf{E}_i(\mathbf{r}), \mathbf{E}_i(\mathbf{r}')$ Incident electric vector field in units of Volts over meters.
- $\mathbf{E}_s, \mathbf{E}_s(\mathbf{r})$ Scattered electric vector field in units of Volts over meters.
- $\mathbf{H}, \mathbf{H}(\mathbf{r}), \mathbf{H}(\mathbf{r}')$ Magnetic vector field in units of amperes over meters.
- $\mathbf{H}_i, \mathbf{H}_i(\mathbf{r}), \mathbf{H}_i(\mathbf{r}')$ Incident magnetic vector field in units of amperes over meters.
- $\mathbf{H}_s, \mathbf{H}_s(\mathbf{r})$ Scattered magnetic vector field in units of amperes over meters.
- \mathbf{J}_m Magnetic current density vector measured in Volts per square metre.
- \mathbf{J}_s Surface current density vector measured in amperes per square metre.
- \mathbf{J} Electric current density vector measured in amperes per square metre.
- $\mathbf{P}(\mathbf{r}), \mathbf{Q}(\mathbf{r})$ Vector fields in the volume V .
- \mathbf{r}'' Image point distance vector in units of meters.
- \mathbf{r}' Point distance vector inside the source in units of meters.
- \mathbf{r}_o Vector range to the resolution volume center in units of meters.
- \mathbf{r} Distance/range vector at the receiving point (or observation point) in units of meters.
- \mathbf{t} Distance/range vector at the transmitting point in units of meters.
- \mathbf{x} Radar measurements vector.
- μ Adimensional parameter of the gamma DSD.
- μ Permeability measured in Henries per meter in Section 2.2-2.3 and Chapter 3.
- μ, σ, k In Chapter 4 are parameter of the GEV distribution, location parameter, scale parameter and shape parameter respectively.
- μ_{ρ_s} Dimensionless parameter depends on the snowflake density.

∇	Del, or nabla operator.
∇'	Del, or nabla operator respect to \mathbf{r}' .
v_i	Percentage of inclusions in the host material.
ω	Angular frequency measured in radians per seconds.
ω_c	Angular carrier frequency measured in radians per second.
ω_d	Angular frequency measured in radians per second.
\bar{P}_r	Mean value of the received signal power in watts..
Φ	Total phase change expressed in radians.
ϕ	Elevation angle in degrees.
ϕ_0	Elevation angle respect to the beam direction in degrees.
ϕ_{3dB}	3-dB width in radians of the elevation angle pattern.
Φ_{dp}	Integrated phase shift measured in degrees.
Π	Power density in units of watts per square meters.
Π_i	Power density related to isotropic element in units of watt per square meters.
Π_r	Power density returned to the radar in units of watt per square meters.
Ψ	Tilt angle in FSR configuration measured in units of degrees.
ρ_{air}	Density of the air.
ρ_a	Antenna aperture efficiency in adimensional unit.
ρ_{hv}	Co-polar correlation coefficient in adimensional units.
ρ_{ice}	Density of the pure ice.
ρ_s	Density of the snowflake.
ρ_w	Water density measured in 1 gm^{-3} .
$\sigma, \sigma(D)$	Radar cross section (RCS) in meters squared.
σ_c	Extra frequency-independent conductivity term.

- σ_{FS} Forward Scattering Radar cross section (FS-RCS) in meters squared.
- σ_m Standard deviation of the mass-weighted mean diameter D_m .
- τ Pulse width or signal duration in units of seconds.
- τ_d Delay
- τ_r Relaxation time of water.
- θ Azimuth angle in degrees.
- θ_0 Azimuth angle respect to the beam direction in degrees.
- θ_{3dB} 3-dB width in radians of the azimuth angle pattern.
- ξ_b Backscattering efficiency a dimensionless parameter.
- $a \times b$ Sizes of the rectangular-shaped target on x and y axis in Section 2.2-2.3 and Chapter 3.
- A Real area or aperture in square meters.
- a Radius of a sphere in centimeters.
- A, b Coefficients of the retrieval between Z_e -S in Chapter 5.
- A_{dp} Specific differential attenuation measured in dB/km
- A_e Effective antenna area in square meters.
- A_g Target cross section area in square meters.
- B Signal bandwidth.
- BL Baseline in FSR configuration.
- c Speed of light in vacuum, its exact value is 299,792,458 meters per seconds.
- C_F, S_F Cosine and sine of Fresnel.
- C_{RADAR} Radar constant.
- D Diameter of a hydrometeor in units of centimeters.
- d Distance from the target to the center of the baseline.
- $d\phi$ Elemental elevation angle in units of degrees.

- $d\theta$ Elemental azimuth angle in units of degrees.
- D_0 Median volume diameter in millimeter.
- D_a Diameter of the radar antenna in units of meters.
- D_{deq} Diameter of disk-equivalent spheres.
- d_d Doppler frequency shift in Herz.
- D_{max} Maximum diameter.
- D_{mm} Maximum melted diameter of snowflakes.
- D_m Mass-weighted mean diameter in millimeter.
- D_s Diameter of a snowflake.
- D_{Veq} Diameter of equal-volume spheres.
- dc Duty cycle.
- dr Elemental distance in units of meters.
- dV Elemental volume in units of cubic meters.
- DWR Dual-Wavelength Ratio measured in dBZ between two equivalent reflectivity factor Z_e at two different wavelengths.
- $E, E(\mathbf{r}), E(\mathbf{r}')$ Electric scalar field in units of Volts over meters.
- $E(dP_r)$ Expected received signal power in watts.
- E_0 Amplitude of a uniform plane wave (UPW) in the initial point 0.
- E_{dr} Differential electric scalar field.
- E_{hh} Electric scalar field in units of Volts over meters observed with transmitted and received fields of horizontal polarization.
- $E_i, E_i(\mathbf{r}), E_i(\mathbf{r}')$ Incident electric scalar field in units of Volts over meters.
- $E_s, E_s(\mathbf{r})$ Scattered electric scalar field in units of Volts over meters.
- E_T Total electric scalar field in units of Volts over meters.
- E_{vv} Electric scalar field in units of Volts over meters observed with transmitted and received fields of vertical polarization.

- F Radiation function.
- f Frequency in Hertz.
- $f(\mathbf{r})$ Source of radiation.
- f_c Carrier radar frequency in units of Hertz.
- $f_{d,max}$ Maximum Doppler frequency.
- FAR False Allarm Rate.
- G Antenna gain expressed in decibels.
- g Gravitational acceleration.
- $G, G(\mathbf{r}, \mathbf{r}')$ Green's function.
- $G_0, G_0(\mathbf{r}, \mathbf{r}')$ Free-space Green's function.
- $G_O, G_O(\mathbf{r}')$ Green's function without singularity at $\mathbf{r} = \mathbf{r}'$.
- G_{RX} Receiving antenna gain expressed in decibels.
- G_{TX} Transmitting antenna gain expressed in decibels.
- h Horizontal polarization.
- H, F and M In Chapter 4, inside the definition of the performance indexes:
H, F and M stands for the number of Hit (event observed and predicted), False (event not observed but predicted), Miss (event observed but not predicted).
- $H, H(\mathbf{r}), H(\mathbf{r}')$ Magnetic scalar field in units of amperes over meters.
- $H_i, H_i(\mathbf{r}), H_i(\mathbf{r}')$ Incident magnetic scalar field in units of amperes over meters.
- H_n Hankel functions.
- $H_s, H_s(\mathbf{r})$ Scattered magnetic scalar field in units of amperes over meters.
- J_n Bessel functions.
- K Dielectric factor.
- k Wave number in units over meters.
- k_0 Wave number in vacuum in units over meters.

- K_{dp} Specific differential phase measured in $^{\circ}km^{-1}$.
- l l -th variables of the radar measurements vector \mathbf{x} .
- LDR Linear depolarization ratio in adimensional units.
- m Complex index of refraction, a dimensionless number.
- $M_{\bar{c}}$ Dynamical map as an output of the ground-clutter Bayesian classification.
- m_D Mass in g dependent to the diameter.
- m_i Complex index of refraction for ice.
- M_n Statistical moments of the DSD.
- m_s Complex index of refraction for snowflake.
- m_w Complex index of refraction for water.
- $m_{Z_x}^D(t)$ Statistical moment of Z_x in the domain \mathbf{D} where the subscript " x " stands for "hh" or "dr", indicating the co-polar or the differential reflectivity.
- N Complex refractive index in ppm.
- n Normal at the arbitrary surface S .
- n' Normal at the surface of the source S' .
- $N''(f)$ Refractive absorption spectra.
- $N'(f)$ Refractive dispersion spectra.
- $N(D, \mathbf{r}), N(D)$ Particle Size Distribution(PSD) or Diameter Size Distribution (DSD) of a hydrometeor in units of $m^{-3}cm^{-1}$.
- N_0 Complex refractive index f -independent component., $N'(f)$ is the refractive dispersion spectra and $N''(f)$ is the refractive absorption spectra.
- N_0 Intercept parameter of the DSD.
- N_{RC} Number of resolution cells.
- n_R Size of the radar measurements vector ($n_R = \dim(\mathbf{x})$).

- n_T, n_α, n_f Numbers of resolution cells in the domains of time, azimuth and Doppler frequency.
- N_w Intercept parameter of the normalized Gamma DSD.
- P Barometric pressure in KPa.
- P_a Relative volume ratio of air.
- P_i Relative volume ratio of ice.
- P_r Received signal power in watts.
- P_t Transmitter power in units of watts.
- P_w Relative volume ratio of water.
- PRF Pulse repetition frequency measured in pulses per Herz.
- PRT Pulse repetition time measured in pulses per second.
- Q Coverage.
- R Distance/range between the receiving point (observation point) and the target point in Section 2.2-2.3 and Chapter 3.
- R Rain rate measured in mmhr^{-1} .
- r Distance/range at the receiving point (or observation point) in units of meters in Section 2.2-2.3 and Chapter 3.
- $r = b/a$ Aspect ratio for a major axis a and the minor axis b of a spheroid.
- r_{\max} Maximum range of a radar in units of meters.
- r_{Rx} Distance between target and receiving antenna in units of meters.
- r_{Tx} Distance between target and transmitting antenna in units of meters.
- r_{un} Maximum unambiguous range in units of meters.
- RH Relative Humidity
- S Arbitrary surface or plane screen.
- S In Chapter 5 is defined as liquid-water equivalent snowfall rate measured in mmhr^{-1} .
- S' Surface of the source.

- $s = (i, j)$, \mathbf{s} Positions inside the clutter map in range (i) and azimuth (j).
- S_{∞} Surface at infinity.
- S_C Circumscribed cylinder.
- S_{dp} Power of the direct path signal.
- S_{FSA} Scattering matrix in forward scatter alignment (FSA) geometry
- S_f Surface around the volume in which the source of radiation is located.
- S_{min} Minimum detectable radar signal in watts.
- S_O Surface of a small sphere.
- S_{pt} Phase signature of a point-like target (pt).
- S_{tgt} Power of the signal generated by the target.
- S_T Total FSR signal.
- S_t Total surface.
- T Distance/range between the transmitting point and the target point.
- t Distance/range at the transmitting point in units of meters.
- t In Chapter 4 is the time frame.
- T_{Arr} Time of arrivals in units of seconds, the time for the radar signal to arrive to the target and return back at the antenna.
- T_{dry} Temperature or dry-bulb temperature in K.
- t_{sp} Moving time of the point-like target.
- u_0, u_n Illumination functions.
- V Volume in units of cubic centimeters.
- v Vertical polarization.
- $v(D)$ Raindrops fallspeed in meter per seconds.
- V_D Doppler velocity measured in meters over seconds.
- V_f Volume in which the source of radiation is located.

- V_O Volume surrounded by the arbitrary surface S .
- v_r Radial velocity measured as meters per second.
- W Rainwater content measured in gm^{-3} .
- w Suspended droplet concentration.
- W_D Doppler spectrum width.
- x,y,z Cartesian coordinate system of the observation point.
- x',y',z' Cartesian coordinate system of the source point.
- x_t,y_t Coordinates of the target center on the $z = 0$ plane at each instant of the movement.
- Z Radar reflectivity factor measured in mm^6m^{-3} or in dBZ.
- Z_{dr} Differential reflectivity measured in dB.
- Z_e Radar equivalent reflectivity factor measured in mm^6m^{-3} or in dBZ.
- Z_{hh} Radar reflectivity factor measured in mm^6m^{-3} or in dBZ observed with transmitted and received signals of horizontal polarization or copolar reflectivity.
- z_{Rx} Distance/range between the target and the receiving antenna (Rx) in FSR configuration.
- z_{Tx} Distance/range between the target and the transmitting antenna (Tx) in FSR configuration.
- Z_{vv} Radar reflectivity factor measured in mm^6m^{-3} or in dBZ observed with transmitted and received signals of vertical polarization or copolar reflectivity.
- CSI Performance index, Critical Success Index (CSI)
- FAR Performance index, False Alarm Rate (FAR)
- POD Performance index, Probability Of Detection (POD)

ACRONYMS

2D Two-Dimensional

3D Three-Dimensional

AMF2 Second ARM mobile facility

AOA Angles Of Arrival

ARM Atmospheric Radiation Measurement

BAECC Biogenic Aerosols Effects on Clouds and Climate

BL Baseline

CAD Computer-Aided Design

CDD Clutter Daily Differences

CDF Cumulative Distribution Function

CPR Cloud Profiling Radar

CSI Critical Success Index

CW Continuous wave

DDA Discrete Dipole Approximation

DSD Diameter Size Distribution

DWR Dual-Wavelength Ratio

EEW Elementary Edge Waves

EFIE Electric Field Integral Equation

EMA Effective Medium Approximation

EM Electromagnetic

ESA European Space Agency

FAR False Alarm Rate

- FLH Freezing-Level Height
- FM-CW Frequency Modulation - Continuous Wave
- FMI Finnish Meteorological Institute
- FSA Forward Scatter Alignment
- FS Forward Scattering
- FS-CS Forward Scatter- Cross Section
- FSR Forward Scatter Radar
- GEV Generalized Extreme Value
- GPM Global Precipitation Measurement
- GV Ground Validation
- HF High Frequency
- IEEE Institute of Electrical and Electronic Engineers
- IKA C-band dual-polarization Doppler weather radar in Ikaalinen.
- IOP Intensive Observation Period
- ITU International Telecommunication Union
- JAXA Japan Aerospace Exploration Agency
- KAZR Ka-band ARM Zenith Radar
- LDR Linear Depolarization Ratio
- LIBR Station identifier of the radiosonde site in Brindisi (IT)
- LOS Line-Of-Sight
- LUT Look Up Table
- MFIE Magnetic Field Integral Equation
- MPM Millimeter-wave Propagation Model
- MRT Mountain Reference Technique
- MTI Moving Target Indication

MWACR	Marine W band ARM Cloud Radar
NASA	National Aeronautics and Space Administration
NICT	National Institute of Information and Comm. Technology
PDF	Probability Distribution Function
PEC	Perfect Electric Conductor
PIA	Path-Integrated Attenuations
PIP	Particle Imaging Package
POD	Probability Of Detection
PO	Physical optics
PPI	Plan Position Indicator
PRF	Pulse Repetition Frequency
PRT	Pulse Repetition Time
PSA	Permanent Scatter Analysis
PSD	Particle Size DIstribution
PSS	Permanent Single Scatterer
PT	Point-like Target
PTD	Physical Theory of Diffraction
RADAR	RAdio Detection And Ranging
RCA	Relative Calibration Adjustment
RCS	Radar Cross Section
SAC	Sun Absolute Calibration
SAR	Synthetic Aperture Radar
SDD	Sun Daily Differences
SVI	Snow Video Imager
TEM	Transverse Electromagnetic

TMM Transition-matrix method

UAV Unmanned Aerial Vehicle

UHF Ultra High Frequency

UPW Uniforme Plane Wave

VHF Very High Frequency

WDS Weather Distributed Scatterer

WR Weather Radar

XSACR X-band Scanning ARM Cloud Radar

INTRODUCTION

*"Lei dirà che la realtà non ha il minimo obbligo d'essere interessante.
Io replicherò che se la realtà può sottrarsi a quest'obbligo,
non possono sottrarsi le ipotesi."*

— Jorge Luis Borges, *La morte e la bussola*, 1942

Radar remote sensing is a well established technique to detect targets and estimate their features by exploiting the interaction between the electromagnetic wave and the target itself [1, 2]. Radar targets can be either artificial (e.g., boats, cars, airplanes) or natural (e.g., vegetation, raindrops, snowflakes) such as in the surveillance [3] and meteorological applications [4]. Within this wide range of topics, this dissertation has been focused on three major open issues that have obtained recently an increasing attention in the worldwide radar community: i) models for forward scatter radar systems [5]; ii) relative and absolute calibration of polarimetric weather radars [6]; iii) signature and retrieval of snowfall rate from multi-frequency meteorological radars [7].

The Forward Scatter Radar (FSR) is becoming a more and more important technique within the surveillance radar community [5]. FSR is a viable alternative with respect to backscatter radar systems due to the increase of the forward-scattering radar cross-section (FS-CS) for the same operational conditions. The FS-CS enhancement is several dBs higher if compared with the backscattering radar cross-section (RCS), opening the peculiar capabilities to detect low-observable targets. One of the main FSR applications is the traffic control of airspaces where ground-based controllers are being hindered by an ever increasing diffusion of unmanned aerial vehicles (UAVs), such as drones. Drones are a good example of low-observable targets with reduced RCS due to the shape, materials and dimensions. These targets, characterized by a reduced RCS, may result invisible to the most common monostatic and bistatic radars but they can be visible for FSR.

The forward scattering (FS) phenomenon has been investigated by analyzing black bodies illuminated by arbitrary sources to define the so-called shadow radiation in [8]. A simplified, but effective, electromagnetic modeling was proposed in [9] on the basis of Babinet's principle [10] and assuming the far-field condition. By removing the latter limiting hypothesis, this dissertation has the purpose to show a generalized electromagnetic model in order to predict the response of FSR systems for air-target surveillance applications in both far-field and near-field conditions [11]. This can be a fundamental step for setting up a framework to detect and classify low-observable targets.

System errors affect weather radar (WR) products in a sensible way, both for quantitative estimation of the precipitation intensity and hydrometeor classification [4]. System calibration is an activity devoted to correct these errors and their impact on WR measurements. The aim of conventional calibration techniques is to estimate the copolar and differential reflectivity miscalibration by obtaining an uncertainty not exceeding 1 dBZ and 0.1 dB, respectively [6]. Recently, the renewed attention on the calibration topic is aimed at obtaining a consolidated approach to monitor all system parameters in a continuous manner and at underlining the limits to use a single method which is neither sufficient nor accurate for this purpose [12]. As a matter of fact, there is not a single technique that can be considered an optimal choice to obtain a real-time WR performance monitoring. This dissertation will present a new data processing methodology, based on the statistical analysis of ground-clutter echoes and aimed at investigating the stability of the WR relative calibration [13]. The new methodology is able to estimate the miscalibration for copolar and differential reflectivity in all the weather conditions and without modifying the system operational capability. Finally, a preliminary investigation on the feasibility of using the permanent scatterers to monitor the polarimetric weather radar calibration is proposed as in [14].

One of the most important measurement campaigns to bridge the gap between physical and scattering properties of ice particles was the Biogenic Aerosols Effects on Clouds and Climate (BAECC) campaign. BAECC hosted by the University of Helsinki Hyytiälä Forestry Field Station was an 8-month measurement campaign from February to September 2014 [15]. During my period abroad at the University of Helsinki I worked with the Radar Laboratory at the measurements from the snowfall intensive observation period (BAECC SNEX IOP) that took place between 1 February and 30 April 2014. My work has been devoted to investigate the radar-based snowfall intensity retrieval at centimeter and millimeter wavelengths us-

ing a high-quality database of collocated ground-based precipitation and multi-frequency radar observations [16]. The measurements of liquid-water equivalent snowfall rate S were compared to radar equivalent reflectivity factors Z_e measured by the Atmospheric Radiation Measurement (ARM) cloud radars operating at X , K_a and W frequency bands. I performed scattering simulations in order to understand the connection between snowflake microphysical and backscattering properties and how they translate to multi-frequency $Z_e - S$ relations. Accurate snowfall retrieval algorithms using millimeter wavelength are of greater importance considering the increasing amount of ongoing and planned satellite radar missions for cloud and precipitation measurements, e.g. CloudSat [17], NASA/JAXA Global Precipitation Measurement (GPM) [18] and (ESA/JAXA/NICT) *Earth-CARE* [19]. In this sense my work proposed $Z_e - S$ coefficients at X , K_a and W frequency bands by showing also scattering simulations with soft-spheroid approximation to explain the results.

My dissertation is organized as follows. Chapter 2 is devoted to introduce the RADAR systems focusing on forward scattering and weather radars. Being the radar an electromagnetic (EM) device, fundamental EM equations and scattering theory are presented. Chapter 3 introduces a general model to characterize the electromagnetic field, scattered and total, developed for FSR systems. Chapter 4 presents the results of two data processing methodology to check the calibration on the WR observables. Chapter 5 shows the multi-frequency $Z_e - S$ relations using the BAecc IOP data measurements and scattering simulations. Conclusions are presented in Chapter 6.

RADAR REMOTE SENSING

"I think you should keep it," Ted said, staring at the screen.

"Just in case it's a message."

"A message from where?"

"From the sphere."

— Michael Crichton, *Sphere*, 1987

One of the most influence science capable to obtain information about an object, area or phenomenon through the analysis of data acquired by a device that is not in contact with the object, area or phenomenon under investigation, is the remote sensing [2]. A more physically-based definition of remote sensing is the science of acquiring, processing, and interpreting data that record the interaction between electromagnetic energy and matter [1]. When the energy is naturally emitted, radiated or reflected from an object, I refer to passive remote sensing. Opposite, the returned energy from an active source that produces an impinging wave on the object is related to active remote sensing.

Figure 1 schematically illustrates the generalized processes and elements involved in electromagnetic remote sensing. The two basic processes involved are data acquisition and data analysis. The elements of the data acquisition process are transmitter and receiver systems (a), resulting in the generation of sensor data in pictorial and/or digital form (b). The data analysis process (c) involves examining the data using various viewing and interpretation devices to analyze pictorial data and/or a computer to digital sensor data. With the aid of the reference data, the analyst extracts information of the various resources over which the sensor data were collected. This information is then an output in graphical or tabular form (d). Finally, the information is presented to users (e) who apply it to their decision-making process.

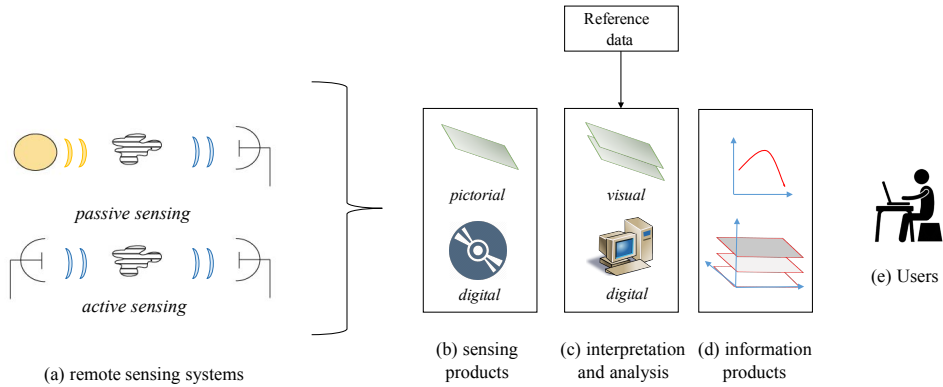


Figure 1: Electromagnetic remote sensing scheme.

I focus on the active remote sensing (see Figure 1(a)) using an active radiating device, the RADAR, contracted form of the words radio detection and ranging. Then the main aims are to detect the presence of an object and to measure its range [3]. In the following Sections I will define the RADAR systems with their fundamental equations and the electromagnetic scattering theory behind these equations. I will present also the radar systems used in my thesis work: forward scatter radar (FSR) and weather radar (WR).

2.1 RADAR SYSTEMS AND FUNDAMENTAL EQUATIONS

RADAR is an electromagnetic device that radiates energy into space by a transmitting antenna. The radiation carries an electromagnetic signal generated by the transmitter part. When the radiation into the space bumps into an object, a portion of the transmitted energy is intercepted and reradiated in many directions. The reradiation is collected by the receiving antenna and the collected signal contains the information on the object [3].

The radar equations are an important tool for the radar system design able to define the relation between the system parameters to the object under test. I will define the equations by dividing them for the different kinds of objects, where the object is considered as matter that scatters

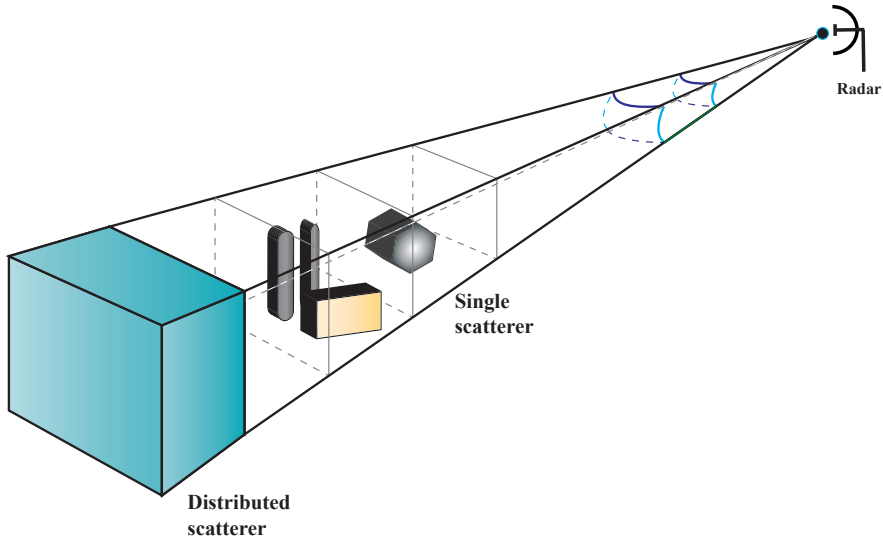


Figure 2: Single and distributed scatterers inside the radar beam.

the radiation or scatterer. In particular I will divide the formulation for a single scatterer, a non-penetrating point or object, that can be considered as a 2D-shape or area, and a distributed scatterer, a volumetric 3D-object penetrable by the radiation as in Figure 2. After I will concentrate the attention on the characteristics of the systems: detection, range, Doppler and polarimetric radars.

2.1.1.1 *Single-scattering equation*

The single-scattering equation is the most simple form of the radar range equation or radar equation [3].

I consider the transmitting antenna as an isotropic element that radiates uniformly in all the directions the transmitter power P_t in units of watts. Then the power density Π_i (where 'i' is for isotropic element) at a distance r from the radar is equal to the power distributed on an imaginary sphere of radius r , or

$$\Pi_i = \frac{P_t}{4\pi r^2} \quad (1)$$

measured in units of watts per square meters. Usually radar systems need to concentrate the radiated power in particular directions employing directive antennas with narrow beamwidth and a gain G that is the maximum power density radiated by a directive antenna $\max(\Pi)$ divided by the power density by a lossless isotropic antenna Π_i with the same power input. Then to measure the power density Π I should take into account the transmitting gain G and I obtain

$$\Pi = \frac{P_t G}{4\pi r^2}. \quad (2)$$

Now, the single scatterer intercepts a portion of the incident energy and reradiates in all the directions. I have defined the single scatterer as a non penetrable target and then as an area that interacts with the radiation (see Figure 2). The radar cross section (RCS) σ of a single scatterer measured in units of area determines the power density returned to the radar Π_r is

$$\Pi_r = \frac{P_t G}{4\pi r^2} \frac{\sigma}{4\pi r^2}. \quad (3)$$

The real radar antenna captures a portion of the power density returned back using the effective antenna area related to the real area A through the relation $A_e = \rho_a A$ where ρ_a is the antenna aperture efficiency. At the end the received signal power in watts is

$$P_r = \frac{P_t G}{4\pi r^2} \frac{\sigma}{4\pi r^2} A_e = \frac{P_t G \sigma A_e}{(4\pi)^2 r^4}. \quad (4)$$

The single scatterer is not detectable beyond the maximum range of a radar r_{\max} , it occurs when the received signal power is equal to the minimum detectable signal S_{\min} . And then the fundamental form of the radar range equation is

$$r_{\max} = \left[\frac{P_t G A_e \sigma}{(4\pi)^2 S_{\min}} \right]^{1/4}. \quad (5)$$

Remembering the relation between the effective antenna area and the antenna gain $G = (4\pi A_e)/\lambda^2$ I can rewrite for a system in which the same antenna is used for both transmitting and receiving as

$$r_{\max} = \left[\frac{P_t G^2 \lambda_c^2 \sigma}{(4\pi)^3 S_{\min}} \right]^{1/4} \quad (6)$$

where the carrier wavelength λ_c is $\lambda_c = c/f_c$ with c the velocity of propagation and f_c the carrier frequency of the radar system.

Equation (6) is the radar range equation for monostatic or backscattering radar configuration, when the transmitting and the receiving antennas are collocated in the same point [20].

In the bistatic radar configuration the transmitter and receiver are separated by a considerable distance such that scattering phenomenology differs from the monostatic case. In that case the radar range equation can be written from equation (3) as

$$P_r = \frac{P_t G_{Tx} G_{Rx} \lambda_c^2 \sigma}{(4\pi)^3 r_{Tx}^2 r_{Rx}^2} \quad (7)$$

where r_{Tx} and r_{Rx} are respectively the distance between the transmitter and the receiver and the single scatterer [20].

2.1.2 Distributed-scatterer equation

The weather radar equation from an elemental volume dV containing hydrometeors is clearly a distributed scatterer (see Figure 2). Inside the volume, hydrometeors change continuously in shape or orientation as it falls through the air and their backscattering cross section fluctuates around a mean value. The expected signal power $E(dP_r)$ from an elemental volume dV is determined from the expected value of the radar cross section σ , i.e. the mean over the ensemble of the scatterer's cross section [4].

Now, using equation (4), $E(dP_r)$ can be expressed as

$$E(dP_r) = \frac{P_t G^2 F^4 (\theta - \theta_0, \phi - \phi_0) \lambda_c^2}{(4\pi)^3 r^4} dV \int_0^\infty \sigma(D) N(D, \mathbf{r}) dD \quad (8)$$

where the radiation function F defines, inside the antenna pattern, the dependency of the gain G from the azimuth θ and the elevation ϕ in degrees respect to the beam direction θ_0 and ϕ_0 . The expected radar cross section σ is defined in terms of the diameter D , the diameter of a water sphere having the same mass as the actual hydrometeor. The particle size distribution $N(D, \mathbf{r})$ determines the expected number density of hydrometeors having diameters between D and $D + dD$ and it is dependent also from the range, azimuth and elevation with r . Then $\sigma(D)N(D, \mathbf{r})dD$ is the radar cross section per unit volume associated with all the hydrometeors within dV having diameters between D and $D + dD$.

The integral in equation (8) defines the radar reflectivity $\eta(\mathbf{r})$ in unit over meters

$$\eta(\mathbf{r}) = \int_0^\infty \sigma(D) N(D, \mathbf{r}) dD \quad (9)$$

or the expected radar cross section per unit volume. Finally the weather signal power can be written substituting equation (9) inside equation (8) and integrating over all the space

$$\bar{P}_r(\mathbf{r}_0) = \int_0^{c\tau/2} \int_0^\pi \int_0^{2\pi} \frac{P_t G^2 F^4(\theta, \phi) \lambda_c^2}{(4\pi)^3 r^4} \eta(\mathbf{r}) dV \quad (10)$$

where $dV = r^2 dr \sin\theta d\theta d\phi$, \mathbf{r}_0 is the vector range to the resolution volume center and τ is the pulse width or signal duration.

It is needed to note that equation (8) is valid only in the far field of the radar antenna (when $r > 2D_a^2/\lambda$, where D_a is the diameter of the antenna) because of r^4 and F^4 in equation (8) are not valid near to the radar antenna. Assuming that the range r_0 to this volume is large compared to the range r , I can approximate

$$\bar{P}_r(\mathbf{r}_0) = \frac{P_t G^2 \lambda_c^2}{(4\pi)^3 r_0^2} \eta(\mathbf{r}_0) \int_0^{c\tau/2} dr \int_0^\pi \int_0^{2\pi} F^4(\theta, \phi) \sin\theta d\theta d\phi. \quad (11)$$

Considering the presence of a Gaussian antenna pattern circularly symmetric I can rewrite

$$\bar{P}_r(\mathbf{r}_0) = \frac{P_t G^2 \lambda_c^2}{(4\pi)^3 r_0^2} \eta(\mathbf{r}_0) \frac{c\tau}{2} \frac{\pi\theta_{3dB}\phi_{3dB}}{8\ln 2} = \frac{P_t G^2 \eta c \tau \pi \theta_{3dB} \phi_{3dB} \lambda_c^2}{(4\pi)^3 r_0^2 16\ln 2} \quad (12)$$

and the last expression is the usual form of the weather radar equation where θ_{3dB} and ϕ_{3dB} are the 3-dB widths in radians of the pattern respectively of the azimuth angle and elevation angle. Usually I will call radar constant the term $C_{RADAR} = P_t G^2 \lambda_c^2 / (4\pi)^3$.

2.1.3 Radar measurements and applications

Inside the term RADAR, detection and ranging represent the main measurements extracted from a radar system. In the modern radar community, new measurements, such as Doppler frequency shift, multifrequency and polarimetric features have obtained relevance to characterized the object under study. I will present now the radar measurements currently used for different applications.

Detection

Detection of an echo signal is limited basically from the presence in the frequency spectrum of the radar of both signal and noise. The minimum

detectable signal or the weakest echo signal at the receiver is defined using in equation (4) S_{\min} as in the fundamental form of the radar range equation (5). The most common way to define the detection is a threshold system, based on establish a threshold at the output of the receiver, if the echo signal is large enough to exceed this level, the signal is detected and the target is present. Opposite if the echo signal is under threshold, only the noise is considered in the radar frequency spectrum. The so-called threshold detection [3] has been employed to detect targets especially in military application such as surveillance and weapon control.

Range

The measurement of range from the radar to a target is one of the most important functions also for a modern radar and it can be derived from $T_{A_{rr}}$, the time for the radar signal to arrive to the target and return back at the antenna. The radar signal or waveform travels as an electromagnetic wave and it is well-known that in free space the velocity is the speed of light, which is $c = 3 \times 10^8$ m/s. For a target at the range r respect to the radar the time for the signal to travel and return back is $2r/c$ and then the range is

$$r = \frac{cT_{A_{rr}}}{2}. \quad (13)$$

To easily obtain the range for a target is needed match correctly the returned signal to the correct transmitted pulse. Echo signals that return after the transmission of the next pulse are called second-time-around echoes (or multiple) and appear in a closest range. Using the time between pulses or pulse repetition time (PRT or the reciprocal PRF, pulse repetition frequency) is possible to calculate the maximum unambiguous range r_{un}

$$r_{un} = \frac{cPRT}{2} = \frac{c}{2PRF}. \quad (14)$$

It is also important define the radar signal or waveform, the most simple version is the pulse train, a series of short rectangular-shaped pulses modulating a sine wave carrier (with carrier frequency f_c) of pulse width τ . The theoretical range resolution cell of a radar system is defined as $\Delta r = (c\tau)/2$ that expresses the ability of the radar to distinguish between targets major or equal in range to Δr . On the other hand for small target at long range is needed to have sufficient energy to detect the target and then a very long pulse. It follows that a long pulse has a lacking range resolution, but pulse compression of frequency or phase modulation are suitable

to increase the spectral width and obtain better range resolution [3]. Another important definition is the concept of duty cycle, the fraction of time in which the radar is in an active state, product of pulse width and pulse repetition frequency

$$dc = \tau \text{PRF} = \frac{\tau}{\text{PRT}}. \quad (15)$$

Continuous wave (CW) radars use CW waveform, they depend on the Doppler frequency shift of the echo signal from a moving target. A simple CW radar is not able to measure the range but combined with the modulation (e.g. frequency modulation FM-CW) also the range can be obtained.

Doppler frequency shift

The detection has been presented until now only as a problem of threshold over the receiver noise. The real world is noisy and the noise is due to the returned signals from all the scatterers that are not the object of study, it is called "clutter" [3].

Detect moving target in large clutter scenario can be easy using the Doppler effect, the Doppler frequency shift of the returned echo signal due to the relative velocity between the radar and the targets. Generally speaking, the Doppler effect is a shift in the frequency of a wave radiated, reflected, or received by an object in motion. Along a two-way path from the radar to the target at distance in range r , the phase changes, for each wavelength, of 2π inside this path and then the total phase change is

$$\Phi = 2\pi \frac{2r}{\lambda} = 4\pi r / \lambda. \quad (16)$$

If I look at a moving target the range distance r changes during the moving time and then it changes also the phase. Differentiating equation (16) I obtain this changing and then the angular frequency ω_d is

$$\omega_d = \frac{d\Phi}{dt} = \frac{4\pi}{\lambda} v_r = 2\pi f_d \quad (17)$$

where v_r is the radial velocity of the target and then I rewrite

$$f_d = \frac{2v_r}{\lambda} = \frac{2v_r}{c} f_c. \quad (18)$$

At the end the Doppler frequency shift f_d is the shift respect to the carrier frequency f_c of the radar due to the moving target.

Pulse radars that apply the Doppler frequency shift for detection of moving targets are:

- Moving target indication (MTI) radars having low PRF with the aim of avoid range ambiguities but with many ambiguities in Doppler domain;
- Pulse Doppler radars having high PRF producing an opposite behaviour respect to the MTI radar.

Other uses of the Doppler frequency shift are:

- CW radars to detect moving targets and to measure radial velocity;
- Synthetic aperture radar (SAR) and inverse SAR for producing images of targets;
- Weather radars (WR) to measure wind shear.

Radar frequency band

Radars operate in the frequency band of microwave radiation. During the World War II, a notation designated by letters was used for the radar frequency band; these letters are still in common use, as I can see in Table 1, from L to G band. For the frequency below 1 GHz the regulation imposed by the International Telecommunication Union (ITU) is considered the reference.

Band designation	Frequency range GHz	Wavelength range cm	
HF	0.003 to 0.03	10000 to 1000	High Frequency
VHF	0.03 to 0.3	1000 to 100	Very High Frequency
P	0.3	100	Very High Frequency
UHF	0.3 to 1	100 to 30	Ultra High Frequency
L	1 to 2	30 to 15	Long wave
S	2 to 4	15 to 7.5	Short wave
C	4 to 8	7.5 to 3.75	Compromise between X and S bands
X	8 to 12	3.75 to 2.5	Secret band during World War II
K _u	12 to 18	2.5 to 1.67	Kurz-under
K	18 to 27	1.67 to 1.11	Kurz (German word for short)
K _a	27 to 40	1.11 to 0.75	Kurz-above
V	40 to 75	0.75 to 0.40	Very strongly absorbed by oxygen (60 GHz)
W	75 to 110	0.40 to 0.27	W follows V in the alphabet
mm or G	110 to 300	0.27 to 0.10	Millimeter

Table 1: Radio-frequency bands according to Institute of Electrical and Electronic Engineers (IEEE) standards.

For the frequency bands below 1 GHz the main applications are coastal radar systems, over-the-horizon radars (HF band), ground penetrating and

wind profilers (VHF, P and UHF bands) and ballistic missile early warning and foliage penetrating (UHF band).

Long waves, L band, are used for long range traffic control and surveillance. For moderate range surveillance, marine and airport radar the main useful bands used are S, C, X, Ku, K and Ka bands.

Radars operating in the S, C, and X bands are the ones mainly used for weather applications. Nevertheless for cloud observations and snowfall measurements radars operating in the K, Ka and W band are used. In particular W band is applied as a visual sensor for experimental autonomous vehicles, high-resolution meteorological observation and imaging.

Only to introduce the multi-frequency concept, analyzed in Section 5, the advantage is be able to have for a target, different signatures in different scattering domains.

Polarimetric radar measurements

A polarimetric radar is a system capable of control the polarization of the transmitted wave and select the desired polarization state of the received wave for each pulse. The polarization switching enables additional parameters, called weather radar (WR) observables, for recognising and classifying different hydrometeors and also for improving the quality of quantitative rain estimates [4]. Hydrometeors, rain or ice particles, have different shapes, different orientations during falling and different dielectric constants and then differently polarized waves, impinging on the weather target, will return different scattered signals.

Polarimetric radars usually use only two selected orthogonal polarizations, horizontal, h , and vertical, v , to transmit and receive. Common technical configuration for polarimetric radars are:

- The switched dual-polarization radar that switches the polarization state from pulse to pulse.
- The dual-channel dual-polarization radar that transmits a selected polarization and receives two polarizations simultaneously.
- The switched dual-channel, polarization-agile radar that is one of the most versatile system and it is a combination of the last two.

In the modern WR community usually the most applied systems combine polarimetric features with Doppler capability and then the WR observables are

- The radar reflectivity factor Z , measured in mm^6m^{-3} or in logarithmic scale in units of dBZ, may be computed by summing the sixth-powers of the diameters of all the drops contained in a unit volume

of space. As I will show in the next sections the radar reflectivity factor is proportional to the radar reflectivity in equation (9) when the precipitation particles are spheres small compared with the radar wavelength.

- The differential reflectivity Z_{dr} is the ratio of the reflectivity observed with transmitted and received signals of horizontal polarization (Z_{hh}) to that observed with signals of vertical polarization (Z_{vv}).
- The co-polar correlation coefficient ρ_{hv} that measures the correlation of the time series of Z_{hh} and Z_{vv} .
- The linear depolarization ratio (LDR) is the ratio of the power received in the cross-polarized channel (Z_{vh}) to that received in the copolarized channel (Z_{hh}) of a dual-channel radar when a linearly polarized signal is transmitted.
- The specific differential phase K_{dp} is the difference of phase shifts for horizontally and vertically polarized radiation on propagation over distance and measured in $^{\circ}\text{km}^{-1}$.
- The integrated phase shift Φ_{dp} is the sum of phases due to the Doppler shift in the two polarized channels and the two-way differential propagation phase shift. Measured in degree this parameter is obtained by the integral of the K_{dp} .
- The Doppler velocity V_D , measured in ms^{-1} , is estimated from the phase shift between the return signals of consecutive transmitted pulses.

More details about the WR observables are given in Section 2.4.2.

2.2 ELECTROMAGNETIC SCATTERING THEORY

The mathematical techniques used in electromagnetic theory are applicable to investigate problems related to radar scattering, polarimetric radars and microwave remote sensing. I present now the fundamental concepts and formulations of the electromagnetic theory used for modeling and analytical studies [10] of RADAR applications.

I present the scattering and the diffraction concepts using the problem of the radiation field from apertures. I discuss the extinction theorem and Huygens formula formulated by the Green's theorem applied to the field produced by the sources and on a surface. After I consider the problem with Kirchoff approximation to obtain Fresnel and Fraunhofer diffraction formulas. I consider the vector Green's theorem to extend the mathemat-

ical expression of the field in presence of a volume at the vectorial case with the Stratton-Chu formula. The Kirchoff approximation for the scalar field is also extended to the vectorial formulation.

The electromagnetic scattering by complex objects is presented with scalar and vector formulation of integral equations. For completeness Babinet's principle for scalar and electromagnetic fields, electric field integral equation (EFIE), and magnetic field integral equation (MFIE) are discussed. The extended boundary condition method, well-known as T-matrix method (TMM), is discussed in Appendix A.

2.2.1 An overview of the scattering theories

The physical process of scattering [10] is verified when forms of radiation are forced to deviate from a trajectory by one or more paths due to localized non-uniformities in the medium. Models of light scattering can be divided into three domains based on a dimensionless size parameter, χ which is defined as:

$$\chi = k_0 a = \frac{2\pi}{\lambda} a \quad (19)$$

where k_0 is the wave number, λ is the carrier wavelength of the radiation and a is the radius of a sphere. Based on the value χ , a dimensionless size parameter, these domains are:

- $\chi \ll 1$: Rayleigh scattering region (small particle compared to wavelength of light);
- $\chi \approx 1$: Mie scattering or resonance region (particle about the same size as wavelength of light);
- $\chi \gg 1$: geometric scattering or optical region (particle much larger than wavelength of light).

A typical representation of the three domains in Figure 3 is given in term of the backscattering efficiency ξ_b which is defined as:

$$\xi_b = \frac{\sigma}{\pi a^2} \quad (20)$$

where σ is the radar cross section (RCS). For Rayleigh backscattering by a dielectric sphere, the RCS can be expressed as

$$\sigma = \frac{k_0^4}{4\pi} \left| \frac{3(\epsilon_r - 1)}{\epsilon_r + 2} \right|^2 V^2 = \frac{\pi^5}{\lambda^4} |K|^2 D^6 \quad (21)$$

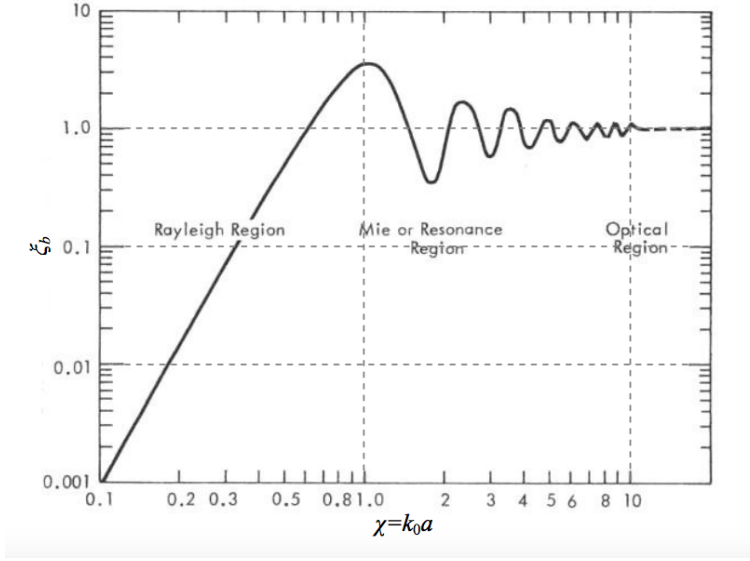


Figure 3: Backscattering efficiency as a function of a dimensionless size parameter χ , useful to highlight the three domains of scattering [21].

where D is the sphere diameter, and $|K|^2 = |(\epsilon_r - 1)/(\epsilon_r + 2)|^2$ is the dielectric factor and $V = \pi/6D^3$ is the volume of a sphere. The backscattering efficiency for a dielectric sphere in Rayleigh domain is given replaced equation (21) inside equation (20) and then I have

$$\xi_b = \frac{\pi^5}{\lambda^4} |K|^2 (2a)^6 \frac{1}{\pi a^2} = 4(k_0 a)^4 |K|^2 \quad (22)$$

Figure 3 shows the backscattering efficiency of a dielectric sphere as a function of χ . In the Rayleigh scattering region, when a particle is very small, the efficiency factor monotonically increases as the size increase. When a particle is about the size of the wavelength, the efficiency oscillates, which is called resonance or Mie region. When the particle size is very large compared with the wavelength the efficiency approaches to a constant value, where geometric optics theory is applied.

2.2.2 Radiation from Apertures

Extinction theorem and Huygens principle

I consider the scalar field $E(\mathbf{r})$ function of the distance vector at the observation point \mathbf{r} generated by the source $f(\mathbf{r})$ located in the volume V_f surrounded by S_f (with point distance vector \mathbf{r}' inside the source)

$$(\nabla^2 + k^2)E(\mathbf{r}) = -f(\mathbf{r}). \quad (23)$$

The scalar field function E is a solution of an inhomogeneous wave equation with f as an exciting source. I apply Green's theorem to the volume V_O surrounded by the arbitrary surface S , the surface at infinity S_∞ and a surface of a small sphere S_O centered at \mathbf{r} with radius $\epsilon_{\text{sphere}} = |\mathbf{r} - \mathbf{r}'|$, the observation point (see Figure 4). I have

$$\int_{V_O} (u \nabla^2 v - v \nabla^2 u) dV = \int_{S_t} \left(u \frac{\partial v}{\partial n} - v \frac{\partial u}{\partial n} \right) dS \quad (24)$$

where $u = E(\mathbf{r}')$, $v = G(\mathbf{r}, \mathbf{r}')$ is the Green's function, $S_t = S + S_\infty + S_O$, and $\partial/\partial n$ is the derivative out to the volume V_O (nothing that $\partial/\partial n = -\partial/\partial n'$ into the volume V_O). Developing the Laplacian with respect to \mathbf{r}' I obtain

$$E \nabla^2 G - G \nabla^2 E = G f \quad \text{in } V_O. \quad (25)$$

Therefore equation (23) becomes

$$E_i(\mathbf{r}) = - \int_{S_t} \left[E(\mathbf{r}') \frac{\partial G(\mathbf{r}, \mathbf{r}')}{\partial n'} - G(\mathbf{r}, \mathbf{r}') \frac{\partial E(\mathbf{r}')}{\partial n'} \right] dS' \quad (26)$$

where $E_i(\mathbf{r}) = \int_{V_f} G(\mathbf{r}, \mathbf{r}') f(\mathbf{r}') dV'$ is the incident field in absence of the surface S . If I consider the field at infinity on S_∞ , it is an outgoing spherical wave and vanishes following the radiation condition

$$\lim_{r \rightarrow +\infty} r \left(\frac{\partial}{\partial r} + jk \right) E(\mathbf{r}) = 0. \quad (27)$$

To consider the integral on S_O I should remember that $G(\mathbf{r}, \mathbf{r}')$ has a singularity at $\mathbf{r} = \mathbf{r}'$ and then I can write

$$G(\mathbf{r}, \mathbf{r}') = \frac{e^{-jk\epsilon_{\text{sphere}}}}{4\pi\epsilon_{\text{sphere}}} + G_O(\mathbf{r}'), \quad (28)$$

where $\epsilon_{\text{sphere}} = |\mathbf{r} - \mathbf{r}'|$ and G_O has no singularity at $\mathbf{r} = \mathbf{r}'$. I then get

$$\lim_{\epsilon \rightarrow 0} \int_{S_O} E(\mathbf{r}') \frac{\partial G(\mathbf{r}, \mathbf{r}')}{\partial n'} dS' = -E(\mathbf{r}) \quad (29)$$

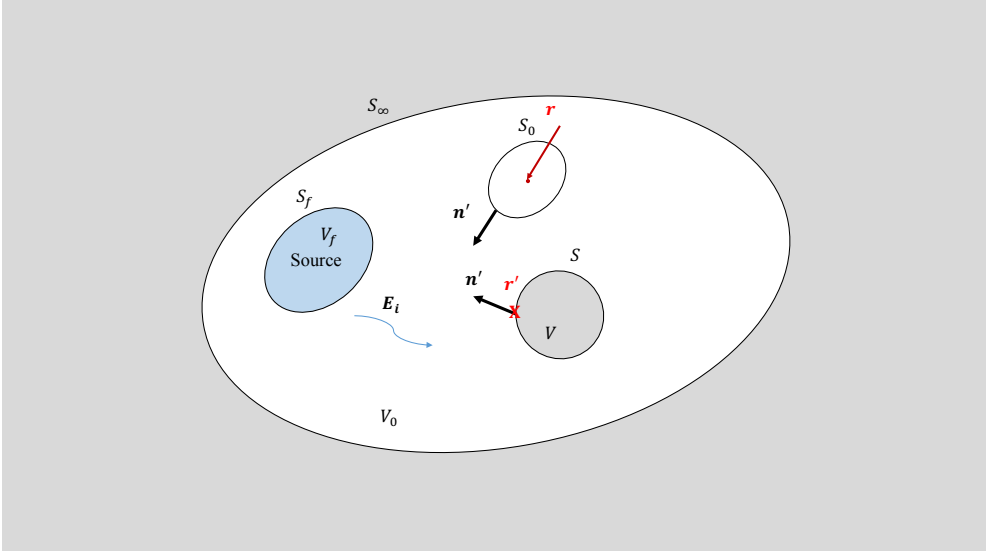


Figure 4: Volume V_0 surrounded by S_f , S_0 , S and S_∞ . The observation point \mathbf{r} is outside S .

and also I have

$$\lim_{\epsilon \rightarrow 0} \int_{S_0} G(\mathbf{r}, \mathbf{r}') \frac{\partial E(\mathbf{r}')}{\partial n'} dS' = 0. \quad (30)$$

At the end I obtain from equation (26)

$$E_i(\mathbf{r}) + \int_S \left[E(\mathbf{r}') \frac{\partial G(\mathbf{r}, \mathbf{r}')}{\partial n'} - G(\mathbf{r}, \mathbf{r}') \frac{\partial E(\mathbf{r}')}{\partial n'} \right] dS' = E(\mathbf{r})$$

if \mathbf{r} is outside S

(31)

where inside the integral the field and the partial derivate are evaluated as \mathbf{r}' approaches the surface from outside.

Equation (31) is the mathematical expression of the field $E(\mathbf{r})$ outside the object composed by the incident field $E_i(\mathbf{r})$ and the scattered field which is the contribution from the field on the surface S .

If I consider the equation (26) when the observation point \mathbf{r} is inside the surface S I have

$$E_i(\mathbf{r}) + \int_S \left[E(\mathbf{r}') \frac{\partial G(\mathbf{r}, \mathbf{r}')}{\partial n'} - G(\mathbf{r}, \mathbf{r}') \frac{\partial E(\mathbf{r}')}{\partial n'} \right] dS' = 0$$

if \mathbf{r} is inside S .

(32)

Equation (32), called extinction theorem, means that the incident field $E_i(\mathbf{r})$ inside the surface is extinguished by the surface contribution and gives us the null field. The extinction theorem becomes a boundary condition to obtain an extended integral equation called the extended boundary condition method or T-matrix method (TMM, see Appendix A).

If I rewrite the extinction theorem thinking that there is not object inside S I have

$$E_i(\mathbf{r}) = \int_S \left[E_i(\mathbf{r}') \frac{\partial G_0(\mathbf{r}, \mathbf{r}')}{\partial \mathbf{n}} - G_0(\mathbf{r}, \mathbf{r}') \frac{\partial E_i(\mathbf{r}')}{\partial \mathbf{n}} \right] dS' \quad (33)$$

where $G_0(\mathbf{r}, \mathbf{r}') = \exp(-jk|\mathbf{r} - \mathbf{r}'|)/(4\pi|\mathbf{r}' - \mathbf{r}|)$ is a free-space Green's function and the partial derivate is now pointed inside S. Equation (33) is the mathematical statement of Huygens principle meaning that the field at \mathbf{r} can be calculated by knowing the field E and $\partial E/\partial \mathbf{n}$ on a surface S which acts as the secondary source for spherical waves.

Aperture field and Kirchoff approximation

The total scalar field in equation (31) is the field due to an incident field $E_i(\mathbf{r})$ when it impinges on a surface S producing a scattered field $E_s(\mathbf{r})$ where \mathbf{r} is outside the surface

$$E(\mathbf{r}) = E_i(\mathbf{r}) + E_s(\mathbf{r}) \quad (34)$$

where

$$E_s(\mathbf{r}) = \int_S \left[E(\mathbf{r}') \frac{\partial G_0(\mathbf{r}, \mathbf{r}')}{\partial \mathbf{n}} - G_0(\mathbf{r}, \mathbf{r}') \frac{\partial E(\mathbf{r}')}{\partial \mathbf{n}} \right] dS' \quad (35)$$

where the free-space Green's function is used

$$G_0(\mathbf{r}, \mathbf{r}') = \frac{\exp(-jk|\mathbf{r} - \mathbf{r}'|)}{4\pi|\mathbf{r}' - \mathbf{r}|} \quad (36)$$

Equation (35) is well-known as Helmholtz-Kirchoff formula. I should remember that for the uniqueness theorem [10] if the field E or $(\partial E/\partial \mathbf{n})$ is known on the surface, the field should be uniquely determined everywhere outside the surface. Then two other exact expressions of equation (35) are

$$E_s(\mathbf{r}) = \int_S E(\mathbf{r}') \frac{\partial G_1(\mathbf{r}, \mathbf{r}')}{\partial \mathbf{n}} dS' \quad (37)$$

$$G_1(\mathbf{r}, \mathbf{r}') = 0 \quad \text{when } \mathbf{r}' \text{ is on } S$$

and

$$E_s(\mathbf{r}) = - \int_S G_2(\mathbf{r}, \mathbf{r}') \frac{\partial E(\mathbf{r}')}{\partial n} dS' \quad (38)$$

$$\frac{\partial}{\partial n'} G_2(\mathbf{r}, \mathbf{r}') = 0 \quad \text{when } \mathbf{r}' \text{ is on } S$$

Now I introduce the aperture field problem considering a scattering field $E_s(\mathbf{r})$ behind a plane screen S with an aperture A (see Figure 5) and assuming that the aperture field $E(\mathbf{r})$ is known on the aperture. Using to solve equation (37), it follows that the Green's function is the difference between free-space due to \mathbf{r}' and his image position \mathbf{r}'' as can be seen in Figure 5

$$G_1(\mathbf{r}, \mathbf{r}') = \frac{\exp(-jk r_1)}{4\pi r_1} - \frac{\exp(-jk r_2)}{4\pi r_2} \quad (39)$$

where $r_1 = |\mathbf{r} - \mathbf{r}'|$ and $r_2 = |\mathbf{r} - \mathbf{r}''|$. Solving the partial derivative out to the aperture A I have

$$\frac{\partial}{\partial n'} G_1(\mathbf{r}, \mathbf{r}') = \frac{\exp(-jkR)}{2\pi R} \left(jk + \frac{1}{R} \right) \frac{z}{R}, \quad (40)$$

where $R = \sqrt{(x - x')^2 + (y - y')^2 + z^2}$.

At the end the scattered field from an aperture is then given by

$$E_s(\mathbf{r}) = \int_S \frac{\exp(-jkR)}{2\pi R} \left(jk + \frac{1}{R} \right) \frac{z}{R} E(\mathbf{r}') dS'. \quad (41)$$

Looking at equation (41) the open issue to obtain the scattered field from an aperture is the exact evaluation of the aperture field $E(\mathbf{r})$ on a screen. The exact solution can be given solve complete boundary value problem. An approximate solution exists if the aperture size is large in terms of wavelength, in this case the aperture field is considered equals to the incident field. I obtain

$$E_s(\mathbf{r}) = \int_S \frac{\exp(-jkR)}{2\pi R} \left(jk + \frac{1}{R} \right) \frac{z}{R} E_i(\mathbf{r}') dS' \quad (42)$$

that is an optics approximation in which the field at any point on the surface is equal to the field for a plane tangent to the surface, and it is called tangent approximation or Kirchoff approximation. This optic approximation equivalent for electromagnetic field is named physical optics (PO) approximation [10].

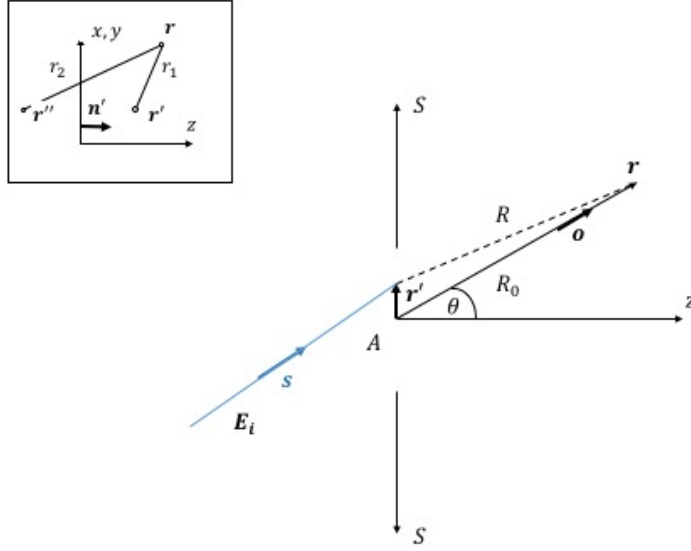


Figure 5: Aperture A on screen S. Top-right Green's function which satisfies Dirichlet's condition.

Fresnell and Fraunhofer diffraction

I consider the scattered field in equation (42) after the Kirchoff approximation and I assume also that the observation point, and then the vector \mathbf{r} , is close to the z axis and then $z/R \approx 1$, $kR \gg 1$ and $1/R = 1/z$ and then

$$E_s(\mathbf{r}) = \frac{jk}{2\pi z} \int_S \exp(-jkR) E_i(\mathbf{r}') dS'. \tag{43}$$

Then the phase kR should be approximated following two different kinds of approximations (assuming a as aperture size) [10]:

1. Fresnel diffraction, applied to the propagation of waves in near field from the diffracting object, where the near field is defined maintaining the quadratic terms of \mathbf{r}' in the phase and for $z < a^2/2$. And then

$$R \approx z + \frac{(x - x')^2 + (y - y')^2}{2z}$$

and

$$E_s(\mathbf{r}) = \frac{jk}{2\pi z} e^{-jkz} \iint \exp\left[-jk \frac{(x-x')^2 + (y-y')^2}{2z}\right] E_i(\mathbf{r}') dx' dy' \quad (44)$$

2. Fraunhofer diffraction, applied to the propagation of waves in far field from the diffracting object, where the far field is defined considering $kx'^2/z < 1$, $ky'^2/z < 1$ at large distance such as $z \gg a^2/2$. And then

$$R \approx z + \frac{x^2 + y^2}{2z} - \frac{xx' + yy'}{z}$$

$$E_s(\mathbf{r}) = \frac{jk}{2\pi z} e^{-jk\left(z + \frac{x^2 + y^2}{2z}\right)} \iint \exp\left[+jk \frac{xx' + yy'}{z}\right] E_i(\mathbf{r}') dx' dy'. \quad (45)$$

Stratton-Chu formula and Kirchoff approximation for vector fields

I want to extend the problem of a scalar field in presence of an incident field on a surface at a vectorial problem in presence of a body of volume V . In order to do that I introduce the vector fields $\mathbf{P}(\mathbf{r})$ and $\mathbf{Q}(\mathbf{r})$ in the volume V surrounded by the surface S and I assume that the first and second derivatives are continuous in V and on S . I can express the vector Green's first identity:

$$\int_V (\nabla \times \mathbf{Q} \cdot \nabla \times \mathbf{P} - \mathbf{P} \cdot \nabla \times \nabla \times \mathbf{Q}) dV = \int_S \mathbf{P} \times \nabla \times \mathbf{Q} \cdot d\mathbf{S} \quad (46)$$

and the vector Green's second identity:

$$\int_V (\mathbf{Q} \cdot \nabla \times \nabla \times \mathbf{P} - \mathbf{P} \cdot \nabla \times \nabla \times \mathbf{Q}) dV = \int_S (\mathbf{P} \times \nabla \times \mathbf{Q} - \mathbf{Q} \times \nabla \times \mathbf{P}) \cdot d\mathbf{S} \quad (47)$$

I now apply the vector Green's theorem at the problem of an electromagnetic field E_i and H_i impinge on a volume V surrounded by the surface S to obtain the three cases of the Stratton-Chu formula [10]:

1. when the observation point \mathbf{r} is outside the surface S (analog to the scalar formulation (31))

$$\mathbf{E}_i(\mathbf{r}) + \int_S \mathbf{E}_S dS' = \mathbf{E}(\mathbf{r})$$

$$\mathbf{H}_i(\mathbf{r}) + \int_S \mathbf{H}_S dS' = \mathbf{H}(\mathbf{r}) \quad (48)$$

2. when the observation point \mathbf{r} is on the surface S

$$\mathbf{E}_i(\mathbf{r}) + \int_S \mathbf{E}_S dS' = \frac{1}{2} \mathbf{E}(\mathbf{r})$$

$$\mathbf{H}_i(\mathbf{r}) + \int_S \mathbf{H}_S dS' = \frac{1}{2} \mathbf{H}(\mathbf{r}) \quad (49)$$

3. when the observation point \mathbf{r} is inside the surface S (analog to the scalar formulation (32))

$$\mathbf{E}_i(\mathbf{r}) + \int_S \mathbf{E}_S dS' = 0$$

$$\mathbf{H}_i(\mathbf{r}) + \int_S \mathbf{H}_S dS' = 0 \quad (50)$$

where

$$\mathbf{E}_S = -[j\omega\mu\mathbf{G}\mathbf{n}' \times \mathbf{H} - (\mathbf{n}' \times \mathbf{E}) \times \nabla' \mathbf{G} - (\mathbf{n}' \cdot \mathbf{E}) \nabla' \mathbf{G}],$$

$$\mathbf{H}_S = j\omega\mu\mathbf{G}\mathbf{n}' \times \mathbf{E} + (\mathbf{n}' \times \mathbf{H}) \times \nabla' \mathbf{G} + (\mathbf{n}' \cdot \mathbf{H}) \nabla' \mathbf{G} \quad (51)$$

being

$$\mathbf{E} = \mathbf{E}(\mathbf{r}') \quad \mathbf{H} = \mathbf{H}(\mathbf{r}')$$

where $G(\mathbf{r} - \mathbf{r}') = \exp(-jk|\mathbf{r} - \mathbf{r}'|)/(4\pi|\mathbf{r} - \mathbf{r}'|)$ is the scalar free-space Green's function, and ∇' is the gradient with respect to \mathbf{r}' . Tai has shown [10] that the Stratton-Chu formula for the case in equation (48) of observation point \mathbf{r} outside S is equivalent to the Franz formula

$$\mathbf{E}(\mathbf{r}) = \mathbf{E}_i(\mathbf{r}) + \nabla \times \nabla \times \pi - j\omega\mu \nabla \times \pi_m,$$

$$\mathbf{H}(\mathbf{r}) = \mathbf{H}_i(\mathbf{r}) + \nabla \times \nabla \times \pi_m + j\omega\epsilon \nabla \times \pi \quad (52)$$

where

$$\pi(\mathbf{r}) = \frac{1}{j\omega\epsilon} \left(\int_V \mathbf{J} \mathbf{G} dV' + \int_S \mathbf{n}' \times \mathbf{H} \mathbf{G} dS' \right),$$

$$\pi_m(\mathbf{r}) = \frac{1}{j\omega\mu} \left(\int_V \mathbf{J}_m \mathbf{G} dV' - \int_S \mathbf{n}' \times \mathbf{E} \mathbf{G} dS' \right). \quad (53)$$

I can also extend the scalar Kirchoff approximation, valids for a large aperture on a screen, at the vector fields assuming that the electric and

magnetic fields tangential to the aperture are equal to those of the incident field [10]:

$$\begin{aligned}\mathbf{n}' \times \mathbf{H} &= \mathbf{n}' \times \mathbf{H}_i \\ \mathbf{E} \times \mathbf{n}' &= \mathbf{E}_i \times \mathbf{n}'.\end{aligned}\quad (54)$$

Then I rewrite the Franz formula in equation (52) using the Kirchoff approximation

$$\mathbf{E}(\mathbf{r}) = \mathbf{E}_i(\mathbf{r}) + \frac{\nabla \times \nabla}{j\omega\epsilon} \times \int_S \mathbf{n}' \times \mathbf{H}_i G dS' - j\omega\mu \nabla \times \int_S \mathbf{E}_i \times \mathbf{n}' G dS' \quad (55)$$

where $G(\mathbf{r} - \mathbf{r}') = \exp(-jk|\mathbf{r} - \mathbf{r}'|)/(4\pi|\mathbf{r} - \mathbf{r}'|)$.

2.2.3 Scattering by complex object

EFIE and MFIE

Another formulation of the scattering problem in terms of the surface integral equations is considered. I have an electromagnetic wave $(\mathbf{E}_i, \mathbf{H}_i)$ incident on a perfectly conducting body with surface S and I obtain two surface integral equations [10]:

1. Electric field integral equation (EFIE) in terms of electric field is obtained using equation (49)

$$\mathbf{E}_i(\mathbf{r}) + \int_S \mathbf{E}_S dS' = \frac{1}{2} \mathbf{E}(\mathbf{r})$$

with the boundary condition on S of electrical field equals to zero for the tangential component

$$\mathbf{n}' \times \mathbf{E}(\mathbf{r}) = 0$$

I obtain the EFIE [10] more useful for a thin object:

$$\mathbf{n}' \times \mathbf{E}_i(\mathbf{r}) = \frac{1}{j\omega\epsilon} \mathbf{n}' \times \int_S [-k^2 G(\mathbf{r}, \mathbf{r}') \mathbf{J}_S(\mathbf{r}') + (\nabla'_S \cdot \mathbf{J}_S(\mathbf{r}')) \nabla' G(\mathbf{r}, \mathbf{r}')] dS' \quad (56)$$

where $\nabla'_S \cdot$ is the surface divergence, \mathbf{J}_S is the surface current and G is the free-space Green function.

2. Magnetic field integral equation (MFIE) in terms of magnetic field is given starting with equation (49)

$$\mathbf{H}_i(\mathbf{r}) + \int_S \mathbf{H}_S dS' = \frac{1}{2} \mathbf{H}(\mathbf{r})$$

with the boundary condition on S of electrical field equals to zero for the tangential component and magnetic field equals to zero for the normal component

$$\begin{aligned} \mathbf{n}' \times \mathbf{E}(\mathbf{r}) &= 0 \\ \mathbf{n}' \cdot \mathbf{H}(\mathbf{r}) &= 0 \end{aligned}$$

I obtain the MFIE [10]

$$\mathbf{n}' \times \mathbf{H}_i(\mathbf{r}) + \int_S [\mathbf{n}' \times \mathbf{J}_S(\mathbf{r}') \times \nabla' G(\mathbf{r}, \mathbf{r}')] dS' = \frac{1}{2} \mathbf{J}_S(\mathbf{r}) \quad (57)$$

Finally, I note that for MFIE, the first term gives the physical optics approximation ($\mathbf{J}_S = 2\mathbf{n}' \times \mathbf{H}_i$) and then the equation (57) is useful for large object with a smooth surface whose radius of curvature is large compared with a wavelength. Then the second term in the MFIE is a small correction term respect to the physical optics approximation [10].

Babinet's principle

I recall here Babinet's principle which in optics states that when the field behind a screen with an opening is added to the field of a complementary structure, the sum is equal to the field when there is no screen [10, 22].

Babinet's principle in other words is an equivalent relationship between two complementary problems:

1. A slot on a screen of perfect electric conductor (PEC) material, illuminated by an electric current \mathbf{J} , produces a field diffracted ($\mathbf{E}_I, \mathbf{H}_I$), see Figure 6(a).
2. A PEC piece with the same sizes of the slot excited by the source current $(\epsilon/\mu)^{1/2} \mathbf{J}_{mc}$ produces instead a field scattered ($\mathbf{E}_{cs}, \mathbf{H}_{cs}$), see Figure 6(b).

Then Babinet's principle states that

$$\begin{aligned} \mathbf{E}_I &= \sqrt{\frac{\mu}{\epsilon}} \mathbf{H}_{cs}, \\ \mathbf{H}_I &= -\sqrt{\frac{\epsilon}{\mu}} \mathbf{E}_{cs}. \end{aligned} \quad (58)$$

An extension of Babinet's principle which includes polarization and conducting screens was introduced by Booker in [23].

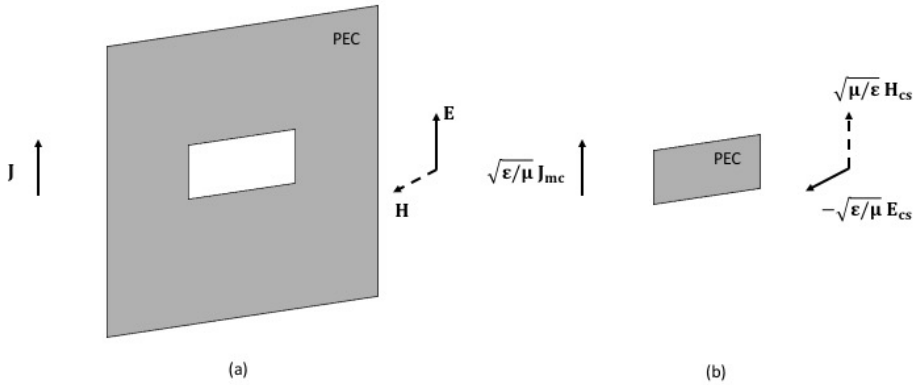


Figure 6: Babinet's principle applied to a screen (a) and a slot (b).

2.3 INTRODUCTION TO FORWARD SCATTER RADAR (FSR)

The basic definition for bistatic radar and forward scatter radar (FSR) is outlined in this section.

2.3.1 Bistatic radar

The definition of a bistatic radar is straightforward a radar that uses antennas at different locations for transmission and reception [24, 25]. In Figure 7 a transmitting antenna (Tx) is on the opposite side respect to the receiving antenna (Rx) describing a baseline (BL, $BL = z_{Tx} + z_{Rx}$ on the z -axis). The target is located at the third corner of the bistatic triangle in Figure 7. The three elements (Tx, Rx and target) can be on the earth, airborne, or in space, and may be stationary or moving with respect to the baseline. The bistatic angle β is between the transmitter and receiver with the vertex at the target. This angle is used to characterize the difference between monostatic, bistatic and forward radar performance. Inside the bistatic triangle two horizontal angles illustrate respectively the target position respect to the Tx ($\alpha_{h,Tx}$) and to the Rx ($\alpha_{h,Rx}$). The variable T and

R are defined as the distance between the arbitrary source point on the target shape and respectively the transmitting radiation source t and the observation source point r .

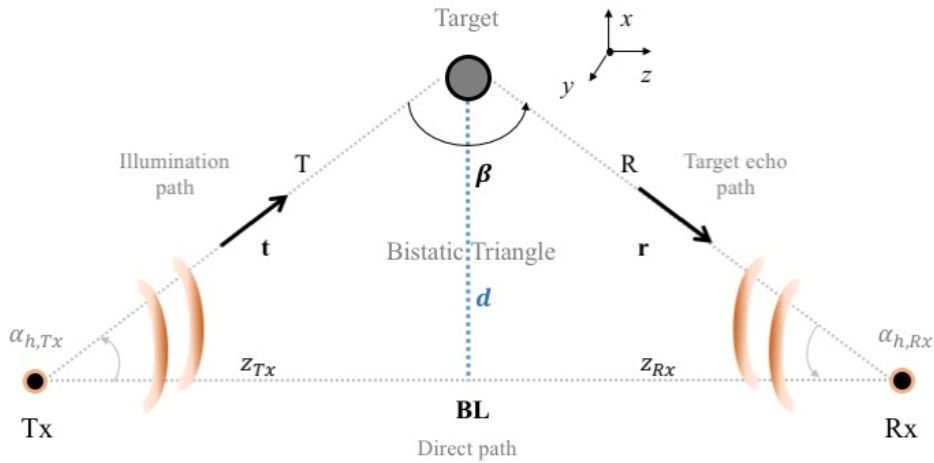


Figure 7: Bistatic geometry.

Bistatic target detection and location are similar to those of a monostatic radar but more complicated because the measures are related to the total signal propagation from transmitter to target to receiver [24, 25]. The bistatic range estimates are derived from the $T + R$ distance. In a monostatic radar $T = R$; in a bistatic radar $T \neq R$ in nearly all cases (as in Figure 7) and then the measure of the angles of arrival (AOA) becomes very important to solve the transmitter-target receiver triangle, called bistatic triangle.

The transmission time and phase data can be known at the receiver in two ways: (1) directly on the direct path if a reasonable line-of-sight (LOS) is available; (2) indirectly, if a stable clock has been synchronized at the start of operations. Using a data link or an intercept receiver, transmitting waveform and position data can be obtained.

The main applications for the bistatic radar systems are:

1. semiactive homing missiles, a particular configuration in which the transmitter is located on the launch platform and the receiver on the missile.
2. forward-scatter radar (FSR), a configuration in which the illumination path and the target echo path are the same and correspond to the BL. Then the transmitter looks at the receiver, and the bistatic angle approaches to 180° , to obtain an enhancement of the RCS.
3. multistatic radars, used mostly to enhance detection and location of aircraft, missiles, and satellites.
4. hitchhikers use a transmitter of opportunity (cooperative or not), usually another radar, to detect and locate targets near the transmitting or receiving site.

2.3.2 FSR effect

The forward scatter radar (FSR) can be considered as a class of bistatic systems showing a bistatic angle of $\beta = 180^\circ$ with targets crossing the BL as in Figure 8. In the narrow region defined along the baseline the RCS increases due to the so-called forward-scattering (FS) effect [26].

The RCS of a target in forward-scattering condition or the forward-scatter cross-section FS-CS is significantly different to the monostatic case due to the field formation in the shadow region, i.e. the region behind the body with respect to the illumination source. Usually the RCS of a target can be defined as the ratio between the electric field intensity of the incident wave (E_i) and the electric field intensity at the receiver (E_T) weighted by the surface of the sphere designed by the target range from the receiver R that is

$$\sigma = 4\pi R^2 \left(\frac{E_T^2}{E_i^2} \right). \quad (59)$$

In Figure 8, ρ is the radius vector of an arbitrary point of the aperture, A , \mathbf{r}_0 is a unit vector oriented towards the receive side, x, y, z are Cartesian coordinates with an origin in the centre of the aperture. The FS-CS close to $\beta = 180^\circ$ is determined by the expression:

$$\sigma_{FS}(\mathbf{r}_0) = \frac{4\pi}{\lambda^2} \left| \int_A \exp \left[j \left(\frac{2\pi}{\lambda} \right) \rho \mathbf{r}_0 \right] dS \right|^2, \quad (60)$$

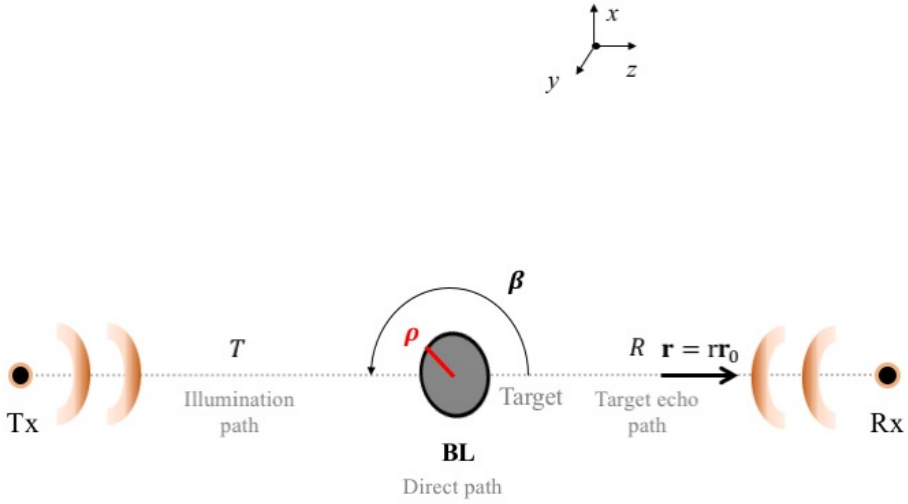


Figure 8: Forward scatter radar one-dimensional geometry.

where λ is the wavelength of the transmitter and dS is the surface element of the aperture. The FS-CS reaches the maximum when $\mathbf{r}_0 \perp \rho$ and then is proportional to the square of the electrical aperture of the target

$$\sigma_{FS}(\mathbf{0}) = 4\pi \left(\frac{A}{\lambda} \right)^2 \tag{61}$$

Equation (61) explains the FS effect that makes it possible to improve the power budget of the radar respect to the common monostatic and bistatic radar. It can be useful to mention that it is impossible to reduce the target's FS-CS by applying ideally absorbent coating on the target usually used to reduce the monostatic RCS [26].

2.3.3 FSR: advantages and limitations

The main advantage of a FSR is, as said in the previous section, the essential increase in the power budget close to a BL and the possibility to detect also targets with radio absorbent coating or with particular shapes [26].

Another advantage is related to the reduction of the fluctuations in the forward-scattered signal [26]. It is proof that the influence of a target's natural swinging upon the phase difference between signals returned from considered reflection points is insignificant for a FSR.

Instead the inherent drawbacks of a FSR system are [5, 26]:

1. The advantages related to the FS effect are visible only within a relatively small solid angle along the baseline.
2. When the target crosses the BL the observed Doppler frequency shift of the received signal is zero and then the radar loses its ability to measure the range distance.
3. A background of passive interference due to all the ground returns toward the BL are expected on the received signal.
4. The presence of a very strong direct signal may exceed the receiver dynamic range and put it in saturation.
5. The synchronization needed between transmitter and receiver may cause technical problems.

These problems are the main reasons why the FSR is not widely applied at present but possible ways to solve those are now available [5, 24–26].

2.3.4 FSR: system and coverage

For what concerns the FSR system two possibilities are now used: pulse radar or continuous wave (CW) radar. Looking at Figure 7, thinking to a two-dimensional FSR on the xz plane, the radar allows to measure the horizontal target coordinates x , z and their derivatives V_x , V_z and it does not allow measurement of the target altitude h on y -axis. I assume a pulse radar system and I want obtain unambiguously measurement of the range sum ($T + R$), the way to do that is take into account the delay of the target return with respect to the direct transmitted signal. The delay is small due to the FS effect stretched along the BL and then the signal bandwidth should be sufficiently wide.

To evaluate the needed bandwidth I have to measure the delay τ of the scattered signal with respect to the direct signal assuming the geometry in Figure 7 and I get

$$\tau_d = \frac{z_{Tx} + z_{Rx}}{c} \left[\left(1 + \frac{4d^2}{(z_{Tx} + z_{Rx})^2} \right)^{1/2} - 1 \right] \quad (62)$$

where d is the distance from the target to the center of the BL and c is the speed of light. When the distance from the center of the BL is less

big than the BL $d/(z_{Tx} + z_{Rx}) \ll 1$ and then the delay becomes $\tau_d \cong 2d^2/[(z_{Tx} + z_{Rx})c]$. A measure of this delay, with sufficient accuracy, can be obtained if the needed time to optimize process of the echo signal is less long than the delay themselves and then the frequency band of the power spectrum B is

$$B \geq \frac{(z_{Tx} + z_{Rx})c}{2d^2}. \tag{63}$$

For example by taking in consideration $z_{Tx} + z_{Rx} = 4 \times 10^4$ m and $d = 10^3$ m, the signal bandwidth should be $B > 6\text{MHz}$; and for $d = 1 \times 10^2$ m it should be $B > 600\text{MHz}$. Then if I consider a pulse radar, a wide band signal (more of 100 MHz for hundred meters from a baseline) is needed and the technical realization is much more complicated respect to a CW FSR. Also the transmitter power needs for a pulse radar is much bigger respect to the CW FSR. The last considerations are because from now I will consider a CW FSR.

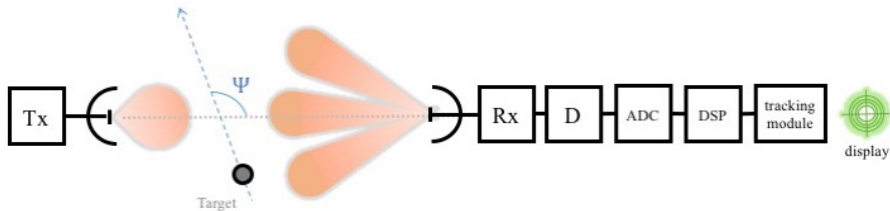


Figure 9: Block diagram of a CW FSR.

A simplified block diagram of the FSR is shown in Figure 9 considering a quasi-harmonic CW signal utilization where:

1. At the transmitting side (Tx) a quasi-harmonic CW signal is used and it is propagated using a low-gain antenna simultaneously illuminating all the FS region.
2. A monopulse antenna is used at the receiving side (Rx), where an analogue receivers in receiving channels of each directional pattern partial beam.
3. The receiving channels pass into the amplitude detectors (D), after into the analogue-to-digital converters (ADC) and at the end into

the module of digital signal processing (DSP). The output of these modules are the Doppler frequency shift and the angle of arrival (AOA) that are the primary parameters for the radar.

4. At the end the tracking module uses the primary parameters to track the target in spatial Cartesian coordinates.

The coverage of a FSR system [26] is defined as a region of space where the detection probability D is more than a threshold value and the false alarm rate F does not exceed those value. The coverage is based on the ratio between the radar equation for a bistatic system in equation (7) and the threshold signal P_0

$$P_r = \frac{P_t G_t G_R \lambda^2 \sigma}{(4\pi)^3 r_T^2 r_R^2} \quad (64)$$

in other words the coverage Q is the excess of the received signal over a threshold signal. The false alarm rate FAR is determined by the total number of resolution cells N_{RC} in the observation space

$$FAR \cong \frac{1}{N_{RC}} = \frac{1}{n_T n_\alpha n_f} \quad (65)$$

where n_T , n_α and n_f are respectively the numbers of resolution cells in time, azimuth and Doppler frequency domains. Having in mind the equation (18) it follows that the maximum possible Doppler shift of the signal returned by a target is defined as

$$f_{d,max} = \frac{2v_{r,max}}{\lambda} \cos\left(\frac{\beta_{min}}{2}\right) \quad (66)$$

where $v_{r,max}$ is the maximum possible target velocity, β_{min} is the minimum value of the bistatic angle within the coverage. From this expression I can be seen that f_d is at a maximum value when the target crosses in the middle the BL.

2.3.5 FSR signal and electromagnetic modeling

There is a simple and effective model in literature able to show the advantages of the FS effect to enhance the RCS. The model approach suggested by Gashinova et al. [9] defines the target signature representing the movement, trajectory and speed, with the Doppler signature of a point-like target and the shape with the FS-CS of an extended target. The modulation of the Doppler signature and the FS-CS produces the target signature that

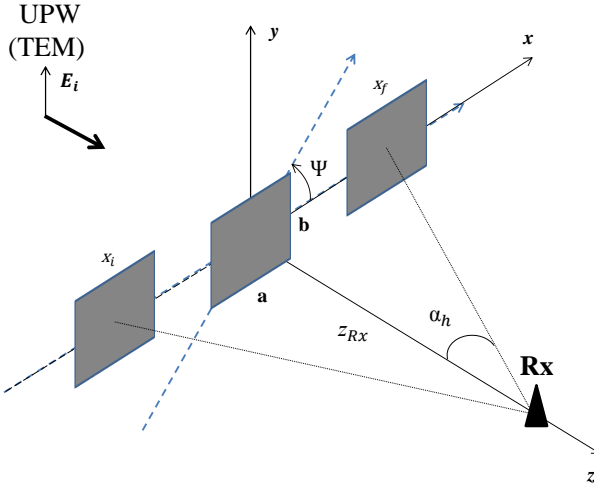


Figure 10: Simulated scenario and frame for the FSR model. The illuminated field is due to a uniform plane wave (UPW), transverse electromagnetic (TEM), that impinges on a rectangular shape target. It crosses the baseline moving from x_i to x_f with a uniform linear motion (constant velocity or zero acceleration).

can be used to provide matched filtering in coherent processing [27]. The model is verified experimentally [9] and applied for example in [28, 29].

As said the model considers first the phase signature of a point-like target (pt) that is

$$S_{pt} = S_{dp} - S_{sp} \sin(\omega_0 t_{sp}) \tag{67}$$

where

- S_{dp} is the power of the direct path signal
- $S_{sp} = S_{dp} S_{tgt}$ is the power of the scattered path signal equals to the product between the power of the direct path signal and the power of the signal generated by the target
- ω_c is the angular carrier frequency
- $t_{sp} = (T + R - BL)/c$ is the moving time of the point-like target.

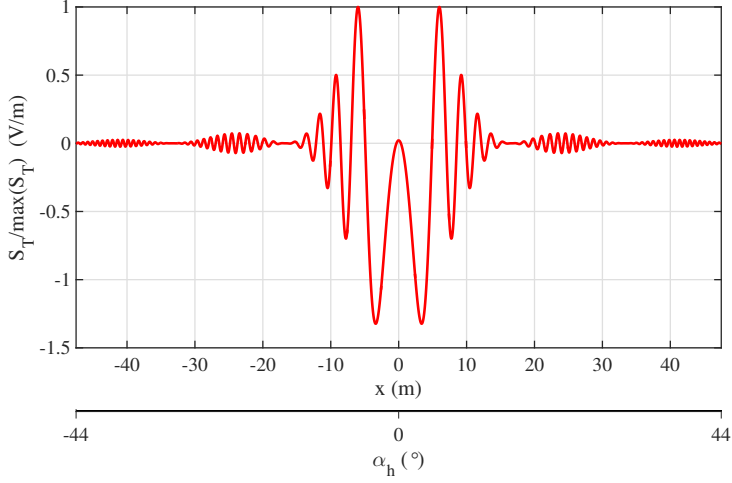


Figure 11: Amplitude of the total signal (equation (69)) collected by the receiver for a square metallic object horizontally moving in the far-field with respect to the receiver having size $a = b = 3\lambda$. The distance object-Rx $z_{Rx} = 50\lambda$ for a $\lambda = 0.5$ m.

Separately the model takes into account the FS-CS looking at a rectangular target that crosses the baseline as in Figure 10. Then the FS-CS is

$$\sigma_{FS} = \frac{4\pi}{\lambda} a^2 \text{sinc}\left(\frac{x_t/z_{Rx}}{a\lambda}\right)^2 b^2 \text{sinc}\left(\frac{y_t/z_{Rx}}{b\lambda}\right)^2 \quad (68)$$

where x_t and y_t are the coordinates of the target center on the $z = 0$ plane at each instant of the movement; z_{Rx} is the distance from the Rx antenna to the center of the target shape when the BL is crossed and a and b are the sizes of the rectangular-shaped target, with respect to the x and y axis. At the end having the FS-CS of an extended target in equation (68) and the Doppler phase signature in Equation (67) of a point-like target the final target signature can be presented as

$$S_T = S_{pt} \sigma_{FS} \quad (69)$$

The model is shown for a square object having dimensions $a = b = 3\lambda$ where the receiver is placed at distance $z_{Rx} = 50\lambda$ for a carrier wavelength of $\lambda = 0.5$ m. In Figure 11 the target signature produced by the modulation between the phase signature of a point-like target (Figure 12) and the extended FS-CS (Figure 13) is shown.

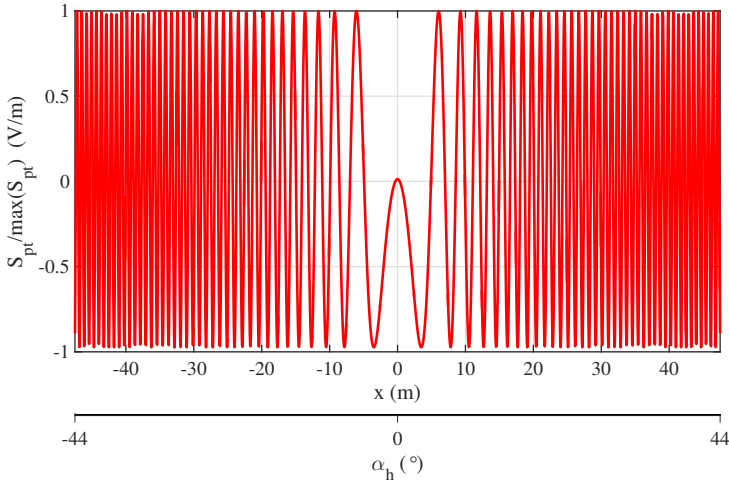


Figure 12: As in Figure 11 for the phase signature of a point-like target (equation (67)).

2.4 INTRODUCTION TO WEATHER RADAR

This section is divided in two parts concerning the physical and the technical aspects. The first is devoted to introduce the hydrometeor microphysics [30]. The distinction between liquid, solid and mixed hydrometeors is extensively explained. The second concerns the way to obtain the weather radar observables suitable for my thesis work [6].

2.4.1 *Hydrometeor microphysics*

A good physical model of the hydrometeors allows to develop efficient retrieval algorithms for estimate of the precipitation intensity, to classify and simulate the weather radar (WR) observables. Results and relations for the most common hydrometeors are presented in this section. Each class of hydrometeors is analyzed distinguishing one to another with respect to the basic element: water, ice or mixture of water, ice and air respectively [21].

Liquid phase: raindrops

Raindrops are generally assumed to be homogeneous in composition, and most commonly composed only to liquid water. This is often not valid for middle and high latitudes in winter. Instead the larger raindrops in

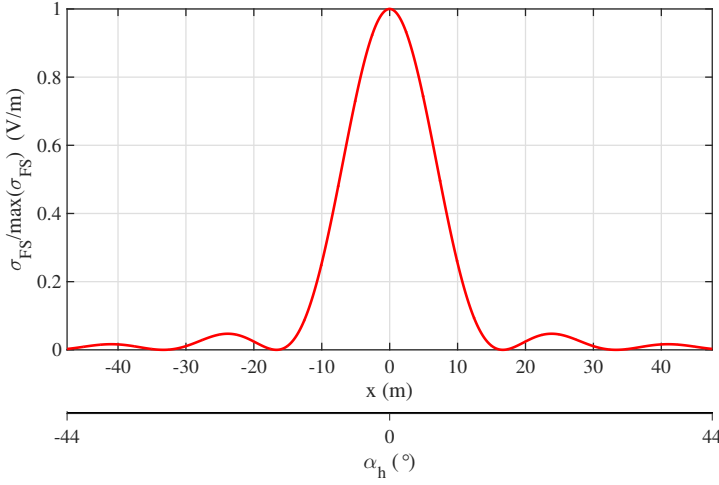


Figure 13: As in Figure 11 for the extended FS-CS of a target (equation (68)).

showery rain, that occur up to 1 km or more below the 0°C isotherm, have an ice core nucleus [30]. The effects of the ice core are at millimeter wavelengths mostly related to give a lower mean drop temperature and at microwave frequencies to the overestimation of the drops size due to the depolarization.

For frequency range from 1 GHz to 1000 GHz and in temperature range from -20°C to 50°C , raindrops may be modelled as homogeneous using semi-empirical formulas for the dielectric properties as in Ray [31]. The complex relative permittivity ϵ_r is related to the complex index of refraction m by

$$m^2 = m'^2 - m''^2 + j2m'm'' = \epsilon_r = \epsilon'_r + j\epsilon''_r \quad (70)$$

and follows that the real part is $\epsilon'_r = m'^2 - m''^2$ and the imaginary part is $\epsilon''_r = 2m'm''$. The complex relative permittivity of pure water, as a function of frequency, has been given by Debye:

$$\epsilon_r = \epsilon_r^\infty + \frac{\epsilon_r^0 - \epsilon_r^\infty}{1 - j\omega\tau_r} = \begin{cases} \epsilon'_r = \epsilon_r^\infty + \frac{\epsilon_r^0 - \epsilon_r^\infty}{1 + \omega^2\tau_r^2} \\ \epsilon''_r = \frac{(\epsilon_r^0 - \epsilon_r^\infty)\omega\tau_r}{1 + \omega^2\tau_r^2} \end{cases} \quad (71)$$

where τ_r is the relaxation time of water, ω is the angular frequency, ϵ_r^0 is the value of ϵ_r for $\omega \ll 1/\tau_r$ and ϵ_r^∞ is the value of ϵ_r for $\omega \gg 1/\tau_r$. The relaxation time can be physically explained as related to the statistical correlation time between consecutive quantum jumps of a single water

molecule. The values of the parameters of the Debye model for pure water at $T = 25^\circ\text{C}$ are $\epsilon_r^0 = 78.36$, $\epsilon_r^\infty = 5.16$ and $\tau_r = 8.27 \times 10^{-12}$ s. Ray [31] in his model adopts an extension of the Debye theory that contains a spread in the relaxation time s and an extra frequency-independent conductivity term σ_c :

$$\epsilon_r = \begin{cases} \epsilon_r' = \epsilon_r^\infty + \frac{(\epsilon_r^0 - \epsilon_r^\infty)[1 + (\omega\tau_r)^{1-s}\sin(0.5s\pi)]}{1 + 2(\omega\tau_r)^{1-s}\sin(0.5s\pi) + (\omega\tau_r)^{2(1-s)}} \\ \epsilon_r'' = \frac{(\epsilon_r^0 - \epsilon_r^\infty)(\omega\tau_r)^{1-s}\cos(0.5s\pi)}{1 + 2(\omega\tau_r)^{1-s}\sin(0.5s\pi) + (\omega\tau_r)^{2(1-s)}} + \frac{\sigma_c}{\epsilon_0\omega} \end{cases} \quad (72)$$

which returns the Debye model when σ_c and s are equal to zero. Here $\sigma_c/\epsilon_0 = 12.5664 \times 10^8$ (or $\sigma_c = 0.0111265 \Omega^{-1}\text{m}^{-1}$).

All these parameters are dependent on temperature, I can find in Ulaby, Moore and Fung [21] the expressions for ϵ_0 and τ_r and in Ray [31] the expression for s :

$$\begin{cases} \epsilon_0 = 88.045 - 0.4147(T - 273) + 6.295 \times 10^{-4}(T - 273)^2 \\ \quad + 1.075 \times 10^{-5}(T - 273)^3 \\ \epsilon_\infty = 5.27137 + 0.0216474T - 0.00131198T^2 \\ \tau_r(\text{ps}) = \frac{1}{2\pi}[111.09 - 3824(T - 273) + 0.06938(T - 273)^2] \\ s = 16.8123/T + 0.0609265. \end{cases} \quad (73)$$

For microwave frequencies the complex relative permittivity of water is shown in Figure 14 in terms of permittivity and loss factor.

In [30] the difference in dielectric behaviour of saline water with respect to pure water is investigated, highlighting that the main effect is conductance loss. For $f > 1$ GHz in acid rain the loss is too low to be measured and then in those cases it does not have to be taken into account in the modeling. Photographs in still air and wind tunnels show that the shape of water drops falling at terminal velocity is assumed to be well-approximated by oblate spheroids [32]. Inside the wind tunnel has been observed that raindrops vibrate around a mean spheroidal shape characterized by an axis ratio that is the ratio defined between the major axis a and the minor axis b of a spheroid as in Figure 15. The Pruppacher and Pitter [33] drop shape is used in most papers on microwave propagation and in Figure 16 I show these shapes for various drop sizes. The relation between the axis ratio and the diameter volume-equivalent D is defined as an equivalent diameter of a sphere for volume and is given by: $(\pi/6)D^3 \equiv (4\pi/3)a^2b$, then if D increases, also increases the oblate factor of the raindrop. Then small

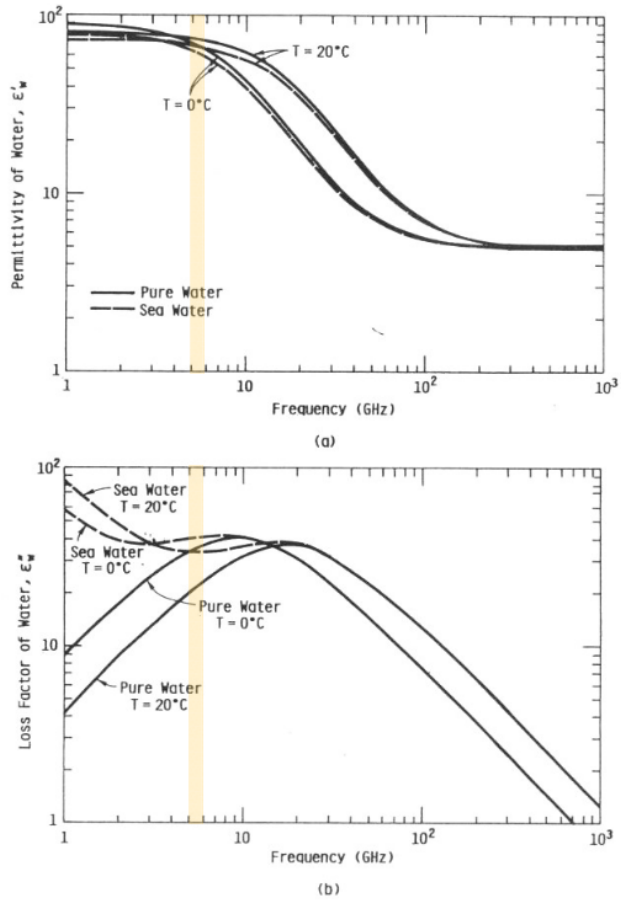


Figure 14: Complex relative permittivity of water: (a) permittivity; (b) loss factor. In yellow is highlighted the C band between 5 and 6 GHz. Figure from [21].

raindrops are almost spherical and the big ones are heavily oblate with axis ratio less than 1. A commonly used approximation relating the axis ratio of a raindrop to the diameter is given by Pruppacher and Beard [34]

$$b/a = 1.03 - 0.062D. \quad (74)$$

A model for the raindrop orientations is given in [35] in terms of the mean value for the canting angle. A general fallspeed law, valid for all the size range of the raindrops, is given in [36] as

$$v(D) = 3.78D^{0.67} \quad (75)$$

measured in meter per second with D in mm and valid for D within 0.5 mm and 5 mm.

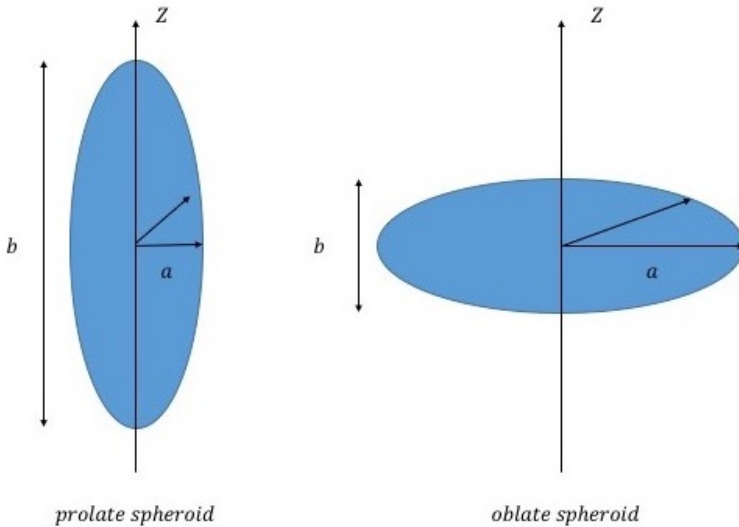


Figure 15: Spheroids described in terms of aspect ratio ($r = a/b$): prolate ($r < 1$), oblate ($r > 1$). The spherical shape not shown is for $r = 1$.

The raindrop size distribution or diameter size distribution (or DSD) $N(D)$ is simply the number of drops measured as a function of diameter in some samples [37]. The important role of the DSD is in determining the radar parameters [6]. From a microphysical perspective, the small drop concentrations are important to study the drop growth via coalescence, drop breakup and evaporation. These processes are determined for the shape of the DSD over the entire range of drop diameters (from

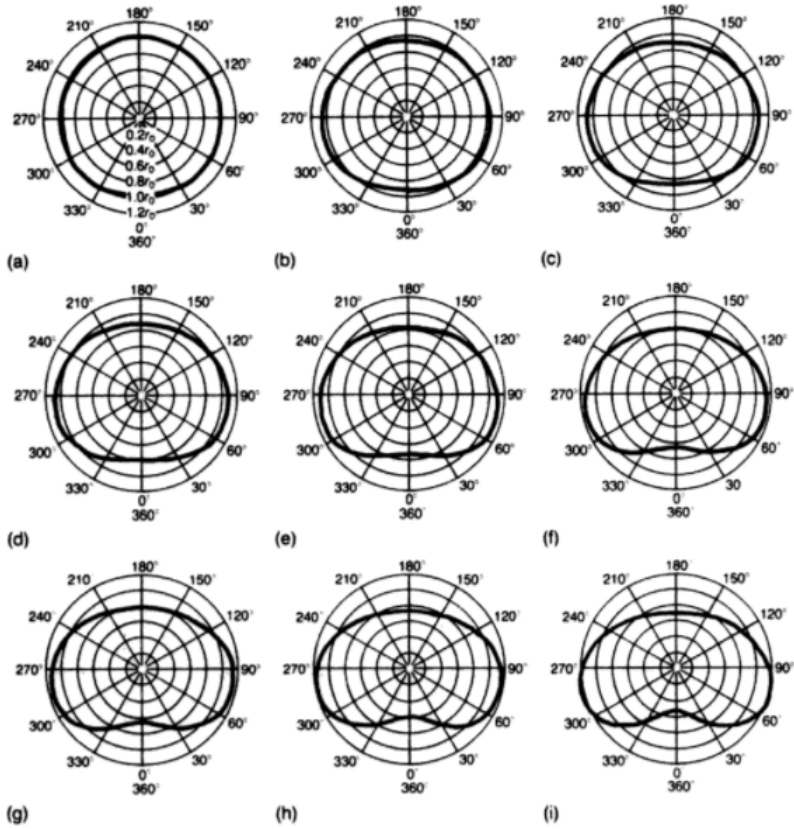


Figure 16: Computed shape of selected drops of various radii from [33]: (a) 0.11 cm; (b) 0.14 cm; (c) 0.18 cm; (d) 0.20 cm; (e) 0.25 cm; (f) 0.29 cm; (g) 0.30 cm; (h) 0.35 cm; (i) 0.40 cm.

0.1 to 6–8 mm) and to obtain simple analytical forms such as the exponential [38] or the gamma DSDs [39]. I first show the exponential DSD expressed as,

$$N(D) = N_0 \exp(-\Lambda D) = N_0 \exp\left(-3.67 \frac{D}{D_0}\right) \quad (76)$$

measured in $\text{mm}^{-1} \text{m}^{-3}$, where N_0 is the intercept parameter also measured in the same unit, Λ is the slope parameter in mm^{-1} and D_0 is the median volume diameter in mm. Similarly for a gamma DSD (in $\text{mm}^{-1} \text{m}^{-3}$) I have

$$N(D) = N_0 D^\mu \exp(-\Lambda D) = N_0 D^\mu \exp\left[-(3.67 + \mu) \frac{D}{D_0}\right] \quad (77)$$

where μ is an adimensional parameter of the gamma distribution. The moments of the DSD M_n in $\text{mm}^n \text{m}^{-3}$ are also fundamental to define the radar parameters, and are expressed as

$$M_n = \int D^n N(D) dD. \quad (78)$$

I also remember that the low order moments are more sensitive to the small particles, the high order moments to the large particles [6]. The zero-moment M_0 in m^{-3} defines the number of spheres per unit-volume with sizes in the interval D to $D + dD$. I first define the mass-weighted mean diameter D_m in mm as

$$D_m = M_4/M_3 \quad (79)$$

that is closely related to the median volume diameter D_0 defined for a gamma DSD as:

$$\begin{cases} \Lambda D_0 = 3.67 + \mu \\ \Lambda D_m = 4 + \mu \end{cases} \quad (80)$$

where it is assumed that the size integration goes from 0 to ∞ [6]. Related to the D_m is the standard deviation of the mass-weighted mean diameter σ_m in millimeter

$$\sigma_m = \sqrt{\frac{\int (D - D_m)^2 D^3 N(D) dD}{M_3}}. \quad (81)$$

The amount of precipitation is characterized by the rainwater content W in gm^{-3} and the rain rate R in mmhr^{-1} that are

$$W = \frac{\pi}{6} \rho_w 10^{-3} M_3 \quad (82)$$

and

$$R = 0.6\pi \times 10^{-3} \int v(D) D^3 N(D) dD \quad (83)$$

where the water density ρ_w is equal to 1 gm^{-3} . The scaled distribution $N(D)$ by varying the rainwater contents W is due to Sekhon and Srivastava [40] and for a gamma DSD in equation (77) the water content is expressed as

$$W = 10^{-3} \frac{\pi \rho_w N_0 \Gamma(\mu + 4)}{6 \Lambda^{\mu+4}} = 10^{-3} \frac{\pi \rho_w N_0 \Gamma(\mu + 4)}{6 (3.67 + \mu)^{\mu+4}} D_0^{\mu+4} \quad (84)$$

and the normalized $N(D)$ is given as

$$N_{\text{norm}}(D) = \left(\frac{\rho_w D_0^4}{10^3 W} \right) N(D). \quad (85)$$

From equation (85), $N(D)$ in compact form can be re-expressed as

$$N(D) = \frac{6W10^3}{\pi\rho_w D_0^4} \frac{(3.67+\mu)^{\mu+4}}{\Gamma(\mu+4)} \left(\frac{D}{D_0} \right)^\mu \exp \left[- (3.67 + \mu) \frac{D}{D_0} \right] \quad (86)$$

$$= N_w f(\mu) \left(\frac{D}{D_0} \right)^\mu \exp \left[- (3.67 + \mu) \frac{D}{D_0} \right] \quad (87)$$

where N_w in $\text{mm}^{-1} \text{m}^{-3}$ is an intercept parameter defined as

$$N_w = \frac{(3.67)^4}{\pi\rho_w} \left(\frac{10^3 W}{D_0^4} \right), \quad (88)$$

and

$$f(\mu) = \frac{6}{(3.67)^4} \frac{(3.67 + \mu)^{\mu+4}}{\Gamma(\mu + 4)}. \quad (89)$$

Only to clarify the characteristics presented for the raindrops go to consider rain as falling drop that must have a diameter equal to, or greater than 0.5 mm [41]. Instead the so-called drizzle represents fine uniform drops of water whose diameters are smaller than 0.5 mm [41].

Solid phase: ice

To understand the evolution of precipitation in different climatic regimes is needed to know the distinction between liquid and solid hydrometeors [30]. One of the main characteristics of ice particle in microwave regime is the depolarization due to the alignment of the ice crystals. The permittivity of ice is lower than water and therefore lower is the attenuation of ice. Empirical models of the refractive index of the ice are given in [31, 42]. At the microwave frequencies, ice is similar to a perfect dielectric, without losses. The results show that the real part of the complex relative permittivity is independent from the frequency and the temperature and then is reasonable to give it a constant value:

$$\epsilon'_r = 3.15. \quad (90)$$

For the imaginary part different models exist, one of this is a semiempirical model of Hufford in [43] which can be expressed as

$$\epsilon''_r = \frac{A_\epsilon}{f_\epsilon} + B_\epsilon f_\epsilon \quad (91)$$

$$\begin{cases} A_\epsilon = [50.4 + 62(\theta_\epsilon - 1)]10^{-4}e^{-22.1(\theta_\epsilon - 1)} \\ B_\epsilon = \left(\frac{0.633}{\theta_\epsilon - 0.131}\right)10^{-4} + \left[\frac{7.36 \times 10^{-4}\theta_\epsilon}{\theta_\epsilon - 0.9927}\right] \\ \theta_\epsilon = \frac{300}{T}. \end{cases}$$

The uncertainty on the imaginary part of the complex relative permittivity of ice due to the different applied models is not relevant because for the ice the diffusion is prevalent on the absorption.

There are different types of precipitation in ice phase [41]:

- Snow, white (or translucent) aggregates of ice crystals in complex hexagonal (six-sided) shapes that often join together to form snowflakes.
- Sleet, or so called ice pellets, frozen raindrops that form as cold raindrops (or partially melted snowflakes) refreeze while falling through a relatively deep subfreezing layer.
- Freezing rain, supercooled raindrops that fall through a relatively shallow subfreezing layer and freeze upon contact with cold objects at the surface.
- Snow grains, or so called granular snow, white or opaque particles of ice less than 1 mm in diameter that usually fall from stratus clouds and are the solid equivalent of drizzle.

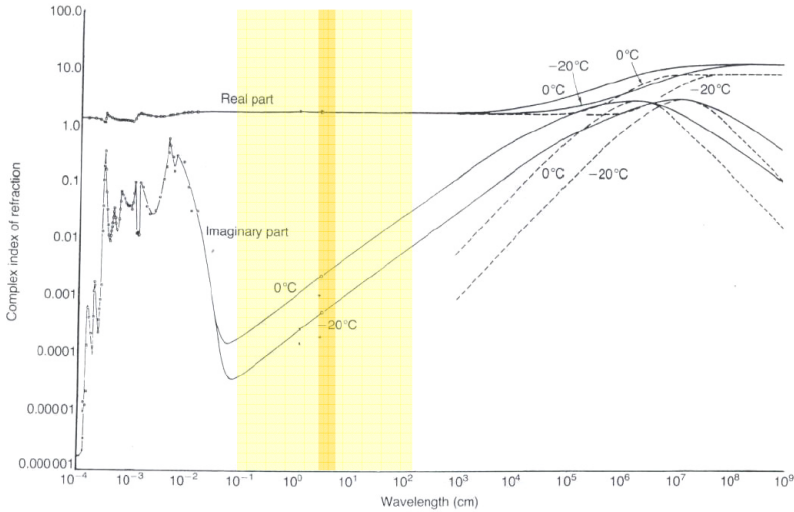


Figure 17: Complex relative permittivity of ice from [31]. In orange is highlighted the C band between 5 and 6 GHz. The yellow area indicates a much larger range between 0.3 and 300 GHz.

- Snow pellets, or so called graupel, brittle, soft white or opaque, usually round particles of ice with diameters less than 5 mm that generally fall as showers from cumuliform clouds; they are softer and larger than snow grains.
- Hail, transparent or partially opaque ice particles in the shape of balls or irregular lumps, has a diameter of 5 millimetres or more. Hailstones can grow to 15 centimetres and weigh more than 0.5 kilograms [44]; the larger form of precipitation. Almost all hail is produced in thunderstorms.

Hail is dry or wet, it can alternate layers of opaque and clear ice because hailstone that passes through a thunderstorm changes the liquid-water content. A cross-section through a large hailstone shows an onion-like structure. Usually superficial layer is composed by water and because of that the complex relative permittivity increases until the same value of the pure water; in [45] is reported the value of the complex relative permittivity at 0 °C in S band around 3 GHz: $\epsilon_r = 80.9 - j23.865$. Instead it exists a simple linear model for the hail composed to a variable percentage of ice and water [21]:

$$\epsilon_m = \nu_i \epsilon_i + (1 - \nu_i) \epsilon_h \quad (92)$$

where v_i is the percentage of inclusions in the host material, indicated as the subscript 'h'. The falling velocity is proportional to the hail diameter D and his density (density of the pure ice is $\rho_{ice} = 900 \text{ kgm}^{-3}$) using a semi-empirical relation presented in [45]:

$$v(D) = \sqrt{\frac{4\rho_{ice}Dg}{3\rho_{air}C_d}} \quad (93)$$

where the density of the air is $\rho_{air} \cong 1.2 \text{ kgm}^{-3}$, the gravitational acceleration is $g = 9.81 \text{ ms}^{-1}$ and $0.45 < C_d < 0.6$. An overview of all the size distributions for the ice crystals is presented in [45]. Values of N_0 (usually from 2 and $300 \text{ mm}^{-1} \text{ m}^{-3}$) and Λ (usually from 0.3 and 0.4 mm^{-1}) are included in [46].

Mixed phase: Snow

In nature, most hydrometeors are assembled in a mixture of air, water and ice. The dry snow is a mixture of ice particles, and air; instead the wet snow is a mixture of ice particles, air and liquid water.

The fundamental problem to have particles in mixed phase is to model the complex relative permittivity. A simple model for a two-phase material consists to assume a mean electromagnetic field resulting from a linear combination of electromagnetic fields weighted for the volumetric fraction q and the dielectric constants [30]

$$\epsilon_{eff}E = \epsilon_1 qE_1 + \epsilon_2(1 - q)E_2 \quad (94)$$

from this expression I are able to obtain a two-phase complex relative permittivity.

In Brongi and Chandrasekar [6] is presented the Maxwell-Garnett mixing formula from an electrostatic perspective. In the Rayleigh region is possible to obtain an expression of the complex relative permittivity for a material composed by a mixture of different components. The inclusions inside the material are considered as N per unit volume dielectric spheres (having volume V) and are treated as elemental dipoles. The single dielectric spheres have complex relative permittivity ϵ_i and are immersed in a matrix material of complex relative permittivities ϵ_m . And then I express the Maxwell-Garnett formula [47]

$$\frac{\epsilon_{eff}}{\epsilon_m} = \frac{1 + 2c_{MG}F_{MG}}{1 - c_{MG}F_{MG}} \quad (95)$$

where $c_{MG} = NV$ is the volume concentration of dielectric spheres (or inclusions) and $F_{MG} = (\epsilon_i - \epsilon_m)/(\epsilon_i + 2\epsilon_m)$.

The density of the snowflakes [30] changes inside the range between 0.15 and 0.45 gcm⁻³ but it could be lower for the rarefied snow ($\rho = 0.05$ gcm⁻³) or higher for melted snow ($\rho = 0.7$ gcm⁻³). The maximum equivalent diameter of the snowflakes is around 15 mm but usually is inside the range 2 and 5 mm [30]. The shape of the snowflakes varies a lot but it is reasonable to assume that an approximated shape changes from the sphere to the spheroid [45].

For what concerns the DSD of the snowflakes, a reference model is in exponential form proposed by Sekhon and Srivastava [48] with the parameters that depend on the liquid-water equivalent snowfall rate S in mmhr⁻¹ as

$$N(D) = N_0 \exp -\Lambda D \quad (96)$$

$$\begin{cases} N_0 = 2.5 \times 10^3 S^{-0.94} \\ \Lambda = 2.29 S^{-0.45} \end{cases}$$

where D is the diameter of a melted snowflake and S is obtained using equation (83) with the snowflake density.

The falling velocity of the aggregates is inside the range of 1 and 1.5 ms⁻¹ and it increases with the sizes. Only to have a benchmark a falling velocity relation depending to the equivalent diameter (mm) is expressed as in [45]:

$$v(D) = 4.836 \left(\frac{D}{10^3} \right)^{0.25} \quad (97)$$

2.4.2 Weather radar observables

In section 2.1.3 I made a list of the WR observables. Now I will show a mathematical meaning of all the WR observables.

Connecting equation (9) of the radar reflectivity to the RCS in equation (21), I obtain the radar reflectivity in Rayleigh domain for a dielectric sphere [6]

$$\eta = \frac{\pi^5}{\lambda^4} |K|^2 \int_0^\infty D^6 N(D, \mathbf{r}) dD = \frac{\pi^5}{\lambda^4} |K|^2 Z. \quad (98)$$

The last equation (98) allows to introduce the radar reflectivity factor that may be computed by summing the sixth-powers of the diameters of all

the drops contained in a unit volume of space. Then the radar reflectivity factor, measured in mm^6m^{-3} or in units of dBZ is defined by

$$Z = \int_0^\infty D^6 N(D, \mathbf{r}) dD \quad (99)$$

It is also possible to express the radar reflectivity factor for Mie scattering or for an unknown scattering domain (if the composition and sizes of the particles are unknown) from the equivalent reflectivity factor Z_e expressed by

$$\eta = \frac{\pi^5}{\lambda^4} |K|^2 Z_e$$

$$Z_e = \frac{\lambda^4}{\pi^5 |K|^2} \int_0^\infty \sigma(D) N(D, \mathbf{r}) dD \quad (100)$$

From the equivalent reflectivity factor I am able to obtain directly the definition of copolar reflectivity for the two polarizations, horizontal ('h') and vertical ('v') as

$$Z_{hh} = \frac{\lambda^4}{\pi^5 |K|^2} \eta_{hh} = \frac{\lambda^4}{\pi^5 |K|^2} \langle \sigma_{hh} \rangle$$

$$Z_{vv} = \frac{\lambda^4}{\pi^5 |K|^2} \eta_{vv} = \frac{\lambda^4}{\pi^5 |K|^2} \langle \sigma_{vv} \rangle \quad (101)$$

where the brackets $\langle \rangle$ indicate the operation of expected value on the distribution of diameters, shapes, angles, compositions and dielectric constant [6]. The differential reflectivity Z_{dr} is the ratio in logarithmic scale of the reflectivity observed with transmitted and received signals of horizontal polarization Z_{hh} to that observed with signals of vertical polarization Z_{vv} :

$$Z_{dr} = 10 \log_{10} \frac{Z_{hh}}{Z_{vv}}. \quad (102)$$

Now I consider a dielectric particle with a total internal field \mathbf{E}_T^{in} placed in a known incident field \mathbf{E}_i that produces a scattered field \mathbf{E}_s . Without more explanation (well-presented in [6]) I present the scattered field at the observation point \mathbf{r} in the far field (see Figure 5)

$$\mathbf{E}_s(\mathbf{r}) = \frac{k_0^2}{4\pi} (\epsilon_r - 1) \frac{e^{-jk_0 r}}{r} \int_\tau [\mathbf{E}_T^{\text{in}}(\mathbf{r}') - \mathbf{n}'(\mathbf{n}' \cdot \mathbf{E}_T^{\text{in}}(\mathbf{r}'))] e^{jk_0 \mathbf{r}' \cdot \mathbf{n}'} d\tau' = \mathbf{f} \frac{e^{-jk_0 r}}{r}. \quad (103)$$

Considering now the decomposition in the horizontal and vertical polarized fields [6], I have

$$\begin{bmatrix} E_h^s \\ E_v^s \end{bmatrix} = \frac{e^{-jk_0 r}}{r} \begin{bmatrix} S_{hh} & S_{hv} \\ S_{vh} & S_{vv} \end{bmatrix}_{FSA} \begin{bmatrix} E_h^i \\ E_v^i \end{bmatrix} \quad (104)$$

where I now have expressed the scattering matrix S_{FSA} in forward scatter alignment (FSA) geometry. From the Maxwell-Garnett formula in equation (95), the slab of discrete dielectric spheres in the Rayleigh scattering regime is equivalent to a uniform permittivity ϵ_{eff} . This concept can be extended at the non-Rayleigh scattering that now I express in terms of effective propagation constant of the slab

$$\frac{k_{eff}}{k_0} = 1 + \frac{2\pi n}{k_0^2} \mathbf{e}_i \cdot \mathbf{f}(\mathbf{i}, \mathbf{i}) \quad (105)$$

where $\mathbf{f}(\mathbf{i}, \mathbf{i})$ is the vectorial function of forward scattering and \mathbf{e}_i is the vector of the polarized field.

Then the specific differential attenuation A_{dp} in dB/km is defined as:

$$\begin{aligned} A_{dp} &= 8.686 \times 10^3 (\text{Im}(k_{eff,h}) - \text{Im}(k_{eff,v})) \\ &= 8.686 \times 10^3 \frac{2\pi n}{k_0} \text{Im}(\mathbf{h} \cdot \mathbf{f}(\mathbf{i}, \mathbf{i}) - \mathbf{v} \cdot \mathbf{f}(\mathbf{i}, \mathbf{i})). \end{aligned} \quad (106)$$

The differential specific phase K_{dp} in rad/km is expressed as:

$$K_{dp} = 10^3 (\text{Re}(k_{eff,h}) - \text{Re}(k_{eff,v})) = 10^3 \frac{2\pi n}{k_0} \text{Re}(\mathbf{h} \cdot \mathbf{f}(\mathbf{i}, \mathbf{i}) - \mathbf{v} \cdot \mathbf{f}(\mathbf{i}, \mathbf{i})). \quad (107)$$

Integrating the differential specific phase on the double path I obtain the total differential phase Φ_{dp} :

$$\Phi_{dp} = \Phi_{hh} - \Phi_{vv} = 2 \int_{r_1}^{r_2} K_{dp}(s) ds. \quad (108)$$

The copolar reflectivity ρ_{hv} is defined as

$$\rho_{hv} = \frac{\langle S_{hh} S_{vv}^* \rangle}{\sqrt{\langle |S_{hh}|^2 \rangle \langle |S_{vv}|^2 \rangle}}. \quad (109)$$

And at the end I define the linear depolarization ratio in dB:

$$\text{LDR} = 10 \log_{10} \frac{\langle |S_{vh}|^2 \rangle}{\langle |S_{hv}|^2 \rangle}. \quad (110)$$

2.5 CONCLUSION

In this Chapter I have reviewed the fundamental aspects of radar remote sensing. The radar equations have been presented for a single scatterer (2D-shape or area) and a distributed scatterer (3D-object). The characteristics of the radar system have also discussed focusing on detection, range, Doppler and polarimetric radars. I have introduced the fundamental concepts and formulations of the electromagnetic theory used for modeling and analytical studies of RADAR applications. The rest of the Chapter presents the two radar systems used in my thesis work: forward scatter radar (FSR) and weather radar (WR).

FORWARD SCATTER RADAR

"Remember, the shadow are just as important as the light."

— Franco Zeffirelli, *Jane Eyre*, Screenplay, 1996

I propose a general model to characterize the electromagnetic field, scattered and total, in FSR systems, when canonical metallic targets cross the BL along arbitrary trajectories. A theoretical background is provided in Section 3.1, including the electromagnetic theory behind the proposed modeling. After Section 3.2 is devoted to show the proposed numerical and analytical models, a near-field simplified model, a near-field Rx and Tx-Rx models. Numerical results and discussions are presented in Section 3.3 for the near-field simplified model. Numerical results are also presented in Section 3.4 for the near-field Rx model with full-wave validations through an ad hoc implementation of an EM CAD tool.

3.1 THEORETICAL BACKGROUNDS

An obstacle hit by an EM wave produces a scattered (diffracted) field in all directions from his self. The FS problem can be considered a standard diffraction problem in which the direction of interest is the forward direction respect to the hit obstacle (see Figure 18). The exact solutions for the scattered field could be obtained using classical modal analysis such as Mie solutions for a sphere. The application limit at realistic problems is that only simple cases are available in exact form. The purpose of this section is to present my approximated solution at the FS problem in terms of an asymptotic high-frequency technique, known as Kirchoff approximation [10]. The formulation achieved by the physical theory of diffraction (PTD) belongs to the source-based theory in which the scattered field is considered as radiation by surface sources which are induced (due to the diffraction) on the scattering objects by incident waves [8]. The PTD is used

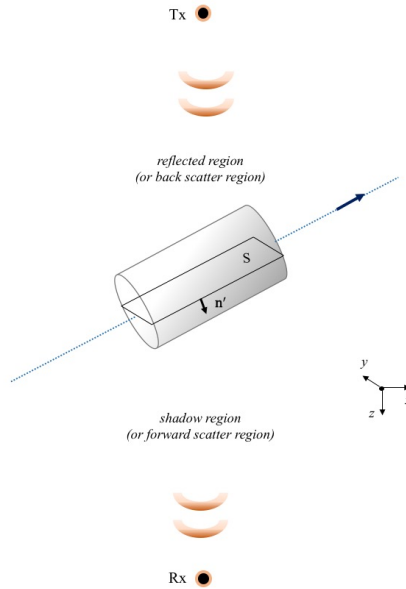


Figure 18: Reference scenario for the analysis of FSR problems.

here in terms of Physical Optics (PO), starting from the mathematical formulation of the Huygen's principle in the special case that explains the extinction theorem. The scattered and total field of the FS problem are presented by applying the extinction theorem already presented in equation (32). The effects of the FS on the total field are investigated in terms of extinction (or shadow) out and on the axis-center of the shadow region (or forward region). The phenomenology of the center-axis effect called Arago spot and the progressive extinction of this in a "black spot" are thoroughly explained. The Shadow Contour Theorem is also expressed in terms of extinction highlighting the application limit for marked near-field contexts.

3.1.1 Physical Theory of Diffraction (PTD)

The modern PTD [8], based on the concept of elementary edge waves (EEWs) was developed for electromagnetic waves scattered by perfectly reflecting objects. The scattering objects were considered as perfectly conducting bodies located into the vacuum and the assumption of infinite

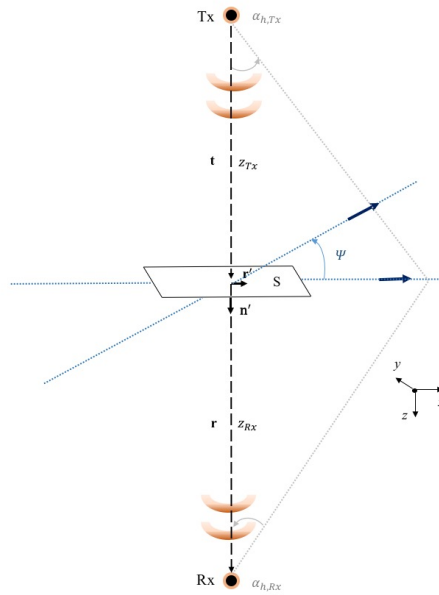


Figure 19: Geometry of FSR that takes into account the near-field condition with respect to both the transmitter and the receiver.

conductivity was considered acceptable for metallic objects detected by radar. I remember that the boundary condition for perfectly conducting bodies states that the tangential component of the electric vector is equal to zero [22]. For our purposes I consider the scalar version of the vectorial PTD theory but the results can be generalized as in [8]. When an electromagnetic wave impinges on an object that induces (due to the diffraction) surface sources, these sources for metallic objects are electric charges and currents, from these the scattered radiation is produced. It is useful to note that the scattered field not have continually a ray structure because of that the ray-based techniques are neglected. The PTD allows the calculation of the scattered field everywhere, also in diffraction regions, such as foci and caustics. The theory separates the surface sources into uniform and non-uniform components. In the following I will consider only the uniform component defined as the scattering sources induced on the infinite plane tangent to the object at a source point. The field found by the integration of the uniform component is known as PO approach. The scattered field in PO is separated into the reflected field and the field of extinction, the last one produces the shadow radiation. Follows that the geometrical optic re-

gion is dominated by the reflected field that has a ray and beam structure. The shadow radiation is equivalent to the field scattered from a black body (of the same shape and size as the actual scattering object) and dominates inside the shadow region (or forward scatter region, see Figure 18). The FS is so a phenomenon of shadow radiation. Also the PTD can be considered as a ray theory but on the level of elementary rays, and this meant that the PO field can be understood as the linear superposition of elementary rays. Follows that the formulation of the PTD in terms of elementary sources or rays can be understood referring to the intuitive Huygen's principle, which was rigorously formulated by Helmholtz in terms of elementary spherical waves/rays [10], [8]. As said the mathematical statement of the Huygen's principle for scalar waves can be expressed as a special case of the extinction theorem [10] in equation (32). If I consider a case in which there is no object inside S then the field everywhere is the incident field expressed as follows by the Huygen's principle in equation (33). The contribution that extinguishes the incident field in equation (32) is the scattered field $E_S(\mathbf{r})$ responsible of the shadow radiation in shadow region (or forward region)

$$E_S(\mathbf{r}) = - \int_S \left(E(\mathbf{r}') \frac{\partial G_0(\mathbf{r}, \mathbf{r}')}{\partial n'} - G_0(\mathbf{r}, \mathbf{r}') \frac{\partial E(\mathbf{r}')}{\partial n'} \right) dS' \quad (111)$$

in which I have considered the simplest Green's function in free-space. I note that with positive sign, this equation is called the Helmholtz-Kirchhoff formula [10]. The exact evaluation of the field integral in equation (111) on a surface is difficult to obtain and requires the solution of the complete boundary value problem. Because of that I should apply an approximated solution called Kirchoff approximation [10]. This asymptotic high-frequency solution is valid if the surface of the object is large in terms of wavelength (λ) and it allows to consider the field on the surface equal to the incident field. And then the scattered field in equation (111) can be resolved with $E = E_i$ inside the integral.

However, until now I have described the scattered field from a surface in shadow region; to obtain the total field I have to take into account the effect of extinction produced by the scattered field on the incident field at the observation point

$$E_T(\mathbf{r}) = E_i(\mathbf{r}) - \int_S \left(E_i(\mathbf{r}') \frac{\partial G_0(\mathbf{r}, \mathbf{r}')}{\partial n'} - G_0(\mathbf{r}, \mathbf{r}') \frac{\partial E_i(\mathbf{r}')}{\partial n'} \right) dS' \quad (112)$$

The equation (112) can be seen as a result of the Babinet's Principle presented in Section 2.2.2. In our case I obtain the field of the comple-

mentary structure as the subtraction of the field when there is no structure and the field produced by an aperture. To better explain the shadow region, it identifies a zone opposite from the direction in which the incident field impinges the object and it can be called forward region. In this zone, the total field is the incident field extinguished by the presence of the obstacle. Follows that the scattered field in equation (111) represents the contribute of extinction and brings progressively to reduce the total field. This reduction has been called "shadow", to recall an intuitive phenomena typical of the visible light and for that reason, so often, the total field in equation (112) is called shadow radiation.

3.1.2 *Arago spot and "black spot" effects*

The Huygen's principle in equation (33) explains also the presence of the Arago spot. This phenomenon is usually visible for aperture on a screen but can be also seen for complementary structure following the Babinet's principle [49]. The secondary wave that is responsible of the extinction of the total field or shadow radiation leads also to a bright spot in the shadow region or forward region called Arago spot. The extinction and the bright spot could appear two opposite effects but both can be explained by using the PO concept of the surface sources. Every point on the surface of the object illuminated by the incident field provides as said to a secondary source of radiation. Each one of these secondary point sources provides to a contribute of radiation that always accumulated along the same optical path upon propagation from the edge toward the center of the illuminated object. Therefore, all the radiation arrives in phase on the center of the shadow region opposite to the object and may constructively interfere to create the bright spot. The width of the Arago spot is strictly dependent on the electrical size of the object and the distance of the observation point with respect to the wavelength. It obvious that this explanation is peculiar of the optical theory but it can be easily converted to the electromagnetic theory by using the Fresnel zone concept [22]. I show you in Figure 21(b) and 22(b) that progressively, by going from the radiative to the reactive near-field, the Arago spot disappears, and the condition is verified when the electrical dimension of the object increases or the distance of the observation point decreases (as in Figure 23). From a physical point of view, this occurs because the extra distance that the secondary waves must do to propagate, compared to the main pulse front, from the edge to the object to reach the z-axis increases (see Figure 20). So increases also the relative delay of the secondary waves and the bright spot for the

reduced constructive interference decreases [49]. I show you that for very large objects the bright spot collapses in a effect of "black spot" on the total field because the extinction prevails on the constructive interference (as in Figure 22(b)).

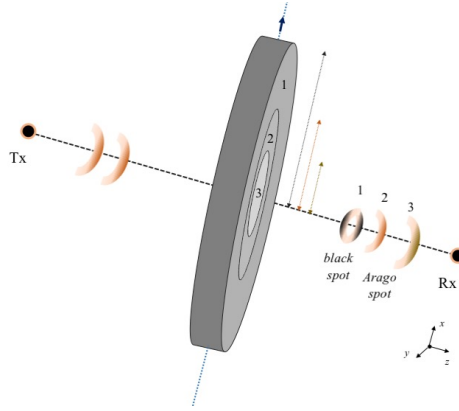


Figure 20: Arago spot and "black spot" effects.

3.1.3 *Shadow Contour Theorem*

The total field in equation (112) has been obtained starting from the mathematical statement of the Huygen's principle in equation (33) and the extinction theorem in equation (32). All the remark has been originally formulated in terms of surface as a two-dimensional problem. From this consideration I can also express the Shadow Contour Theorem states that two different objects with the same shadow contour produce the same shadow radiation [8]. The shadow contour is defined as the surface that cuts the object volume on respect to the external normal to the object. In other words the contribution in forward scatter region that extinguishes the incident field is the same for objects that have the same shadow contour (as in Figure 18). Also the theorem says that the shadow radiation does not depend on the whole shape of a scattering object but it is completely determined only by the size and geometry of the shadow contour. I want point out that this consideration is not always valid but is strictly dependent from the electrical dimensions of the object volume and from the distance of the observation point with respect to the wavelength. That is due to the fact that the Shadow Contour Theorem has been developed starting from the extinction theorem in equation (32) that considers only a 2D-problem. If I insert also the third dimension of the object, the thickness,

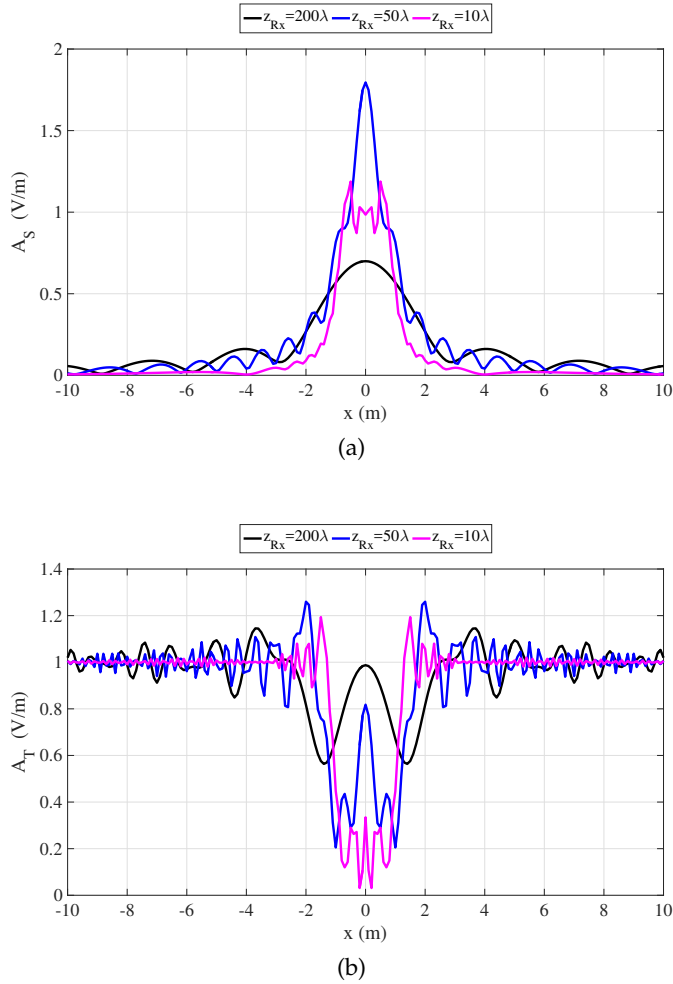


Figure 21: Scattered (subscripts 'S') and total (subscripts 'T') signals collected by the receiving antenna ($f_c = 1.75$ GHz) as the target ($12\lambda \times 12\lambda$) moves along the x direction (see Figure 29), for three different near-field/far-field distances, equal to 200λ (black curves), 50λ (blue curves), 10λ (magenta curves) looking at the numerical solutions of equations (111)-(112). (a): Scattered amplitude; (b) Amplitude of the total received signal.

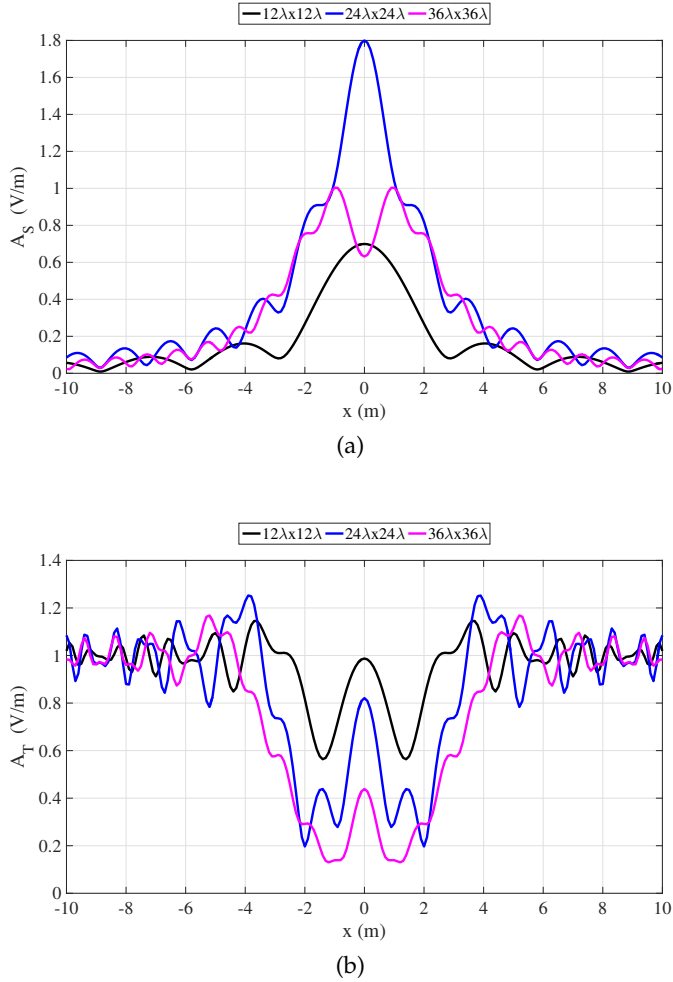


Figure 22: Scattered (subscripts 'S') and total (subscripts 'T') signals collected by the receiving antenna ($f_c = 1.75$ GHz) as the target moves along the x direction (see Figure 29) at the distance along z of 200λ , for three different sizes, equal to $12\lambda \times 12\lambda$ (black curves), $24\lambda \times 24\lambda$ (blue curves), $36\lambda \times 36\lambda$ (magenta curves) looking at the numerical solutions of equations (111)-(112). (a): Scattered amplitude; (b) Amplitude of the total received signal.

the extinction effect that is produced from the depth will have also a contribute on the total field (or shadow radiation). Referring to the cases for which this theorem has been extensively applied, the stealth technology and the surveillance radar, the validity is due to the far-field condition always verified in these radar contests [9]. The most critical aspect is in fact that in marked near-field cases this extinction effect must be considered to not threaten the validity of the formulation. An analysis of the third dimension, the tickness, is out of the scope of my thesis work but further investigations are presented in [50]. I want concentrate my efforts here investigate fully the two-dimensional problem.

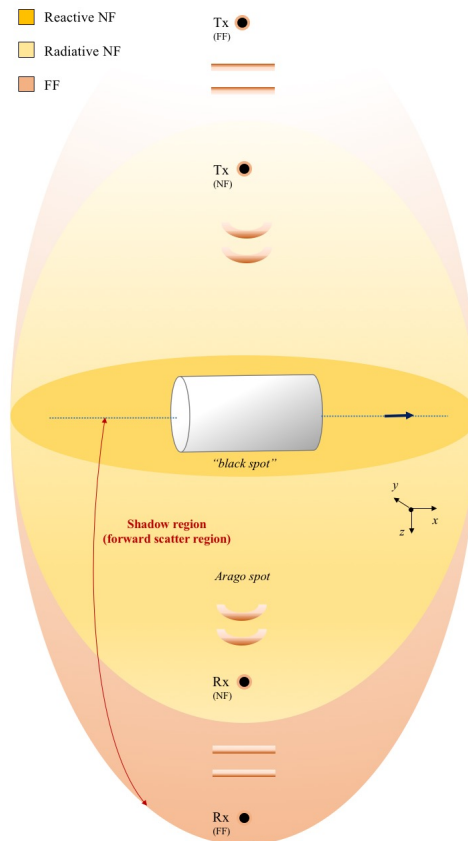


Figure 23: Different regions of EM propagation.

3.2 ELECTROMAGNETIC MODEL

In this section, the general numerical and analytical models are described. The simplified model in [51, 52] is an extension of the model presented in Section 2.3.5 by Gashinova et al. [9]. After I have presented an analytical model in [11, 53–55] to take into account the near-field condition with respect to receiver. I further generalized the analytical model presented to take into account the near-field condition with respect to both the transmitter and the receiver. The sensitivity of the models proposed with respect to the approximations are also analyzed.

3.2.1 Near-field simplified model

The model approach suggested by Gashinova et al. [9] and introduced in Section 2.3.5 shows that the Doppler signature of the target can be decomposed into a chirp-like waveform, related to the motion, and an envelope pattern, related to target shape and dimensions. The fundamental assumption of far-field condition was employed for the evaluation of the envelope pattern. In particular, both the Tx/Rx and the target/Rx distances were assumed to be sufficiently high to let the use of Fraunhofer approximation in the evaluation of the target's scattering problem. Such a strongly limiting hypothesis has been removed in [51, 52] presenting a near-field simplified model.

The attention has been focused on the evaluation of the FS-CS in near-field conditions by computing the Fresnel 2D diffraction integrals on the aperture [10]. To better understand the Gashinova et al. [9] took as a reference the integral for the Fraunhofer Diffraction in equation (45), instead here the reference has been equation (44). Then I can express the Fresnel 2D diffraction integral as

$$\mathbf{u}_n(\mathbf{r}) = \iint \exp\left[-jk \frac{(x-x')^2 + (y-y')^2}{2z}\right] \mathbf{u}_0(\mathbf{r}') dx' dy' \quad (113)$$

where \mathbf{u}_0 is the target illumination function. This allowed us to evaluate the FS-CS at a distance $z = z_{Rx}$ (see Figure 10) from Rx in more general terms also for the near-field region, according to:

$$\sigma_{FS} = \frac{4\pi}{\lambda^2} (A_g |\mathbf{u}_n(\mathbf{r})|)^2 \quad (114)$$

where λ is the carrier wavelength and A_g is the target cross section area. In Section 3.3 I will consider the numerical solutions of the integral-diffraction

formula and interpret the received signal features for a rectangular and circular target.

3.2.2 Near-field Rx and Tx-Rx models

Equations (42) and (112) represent the basic step toward the derivation of a simple analytical expression for the electric field re-irradiated by a target and collected by the Rx antenna in general FSR scenarios.

The basic FSR geometry is sketched in Figure 10 and I consider specifically a rectangular target having dimensions a and b with respect to the x and y axes, respectively. The fundamental geometrical parameter z_{Rx} is the distance from the Rx antenna to the center of the target shape when the BL is crossed (that is the origin of the coordinate system of Figure 10). By transmitting a continuous wave (CW) at angular frequency ω , the received total field due to the target plate can be expressed from equation (112)

$$E_T(\mathbf{r}) = E_0 \left(e^{-jkz_{Rx}} - \frac{1}{2\pi} \int_A \left(j\mathbf{k} + \frac{1}{R} \right) \frac{z_{Rx}}{R^2} e^{-jkR} dA' \right) \quad (115)$$

where

$$R = |\mathbf{r} - \mathbf{r}'| = \sqrt{(x_t - x')^2 + (y_t - y')^2 + (z_{Rx})^2} = \lambda \tilde{R} \quad (116)$$

and

$$\tilde{R} = \sqrt{(\tilde{x}_t - \tilde{x}')^2 + (\tilde{y}_t - \tilde{y}')^2 + (\tilde{z}_{Rx})^2} \quad (117)$$

being R the distance between the observation point \mathbf{r} (where the Rx antenna is located) and the arbitrary source point \mathbf{r}' of the target shape; x_t and y_t are the coordinates of the target center on the $z = 0$ plane at each instant, and x' and y' are the target local coordinates referred to its center. The incident field that impinges on the target is in this case an uniform plane wave defined as: $E_i(\mathbf{r}) = E_0 e^{-jkz_{Rx}}$.

In order to generalize the previous expressions, I define \tilde{R} in equation (117) as the distance R normalized with respect to the wavelength λ . The rectangular coordinates are normalized as follows: $\tilde{x}_t = x_t/\lambda$, $\tilde{y}_t = y_t/\lambda$, $\tilde{x}' = x'/\lambda$, $\tilde{y}' = y'/\lambda$ and $\tilde{z}_{Rx} = z_{Rx}/\lambda$ (i.e., all the quantities with the 'tilde' are normalized with respect to the wavelength). By introducing the normalized coordinates and the normalized wavenumber $\tilde{k} = k\lambda = 2\pi$ equation (115) becomes independent by the angular frequency ω ; I can therefore write the expression of the received total field as follows

$$E_T(\tilde{\mathbf{r}}) = E_0 \left(e^{-j\tilde{k}\tilde{z}_{Rx}} - \frac{1}{2\pi} \int_{\tilde{A}} \left(j\tilde{\mathbf{k}} + \frac{1}{\tilde{R}} \right) \frac{\tilde{z}_{Rx}}{\tilde{R}^2} e^{-j\tilde{k}\tilde{R}} d\tilde{A}' \right) \quad (118)$$

being the integral evaluated on the surface of normalized area $\tilde{A} = A/\lambda^2$. These are reference expressions for our model and allow to numerically evaluate the FSR effects for arbitrary angular frequencies and arbitrary metallic targets, both in far-field and near-field conditions. My first aim with this model presented in [11] has been achieved a simple but accurate closed-form solution of the considered integral in equation (118) also accounting for near-field conditions that may occur between illuminated rectangular-shaped target and receiver.

I exploit two canonical approximations: *i) paraxial approximation*, valid in general when the longitudinal distance of a point-like target from the Rx can be considered greater than the transverse distance; *ii) first-order Taylor's approximation on the phase expansion* of the re-irradiated signal given by equation (118). Hence, equation (117) for the first-order approximation ('1-O') can be written as follows

$$\tilde{R} \approx \tilde{z}_{Rx} + \frac{(\tilde{x}_t - \tilde{x}')^2 + (\tilde{y}_t - \tilde{y}')^2}{2\tilde{z}_{Rx}}. \quad (119)$$

On this basis, a closed-form solution of the integral in equation (118) can be obtained for rectangular-shaped target with normalized sizes $\tilde{a} = a/\lambda$ and $\tilde{b} = b/\lambda$, with respect to x and y axis. After some algebra (the relevant details are reported in Appendix B.1), equation (118) reduces to

$$\begin{aligned} E_T(\tilde{\mathbf{r}}) = E_0 e^{-j\tilde{k}\tilde{z}_{Rx}} & \left(1 - \frac{1}{2\tilde{k}} \frac{\tilde{z}_{Rx}^2}{\tilde{R}_0^2} \left(j\tilde{k} + \frac{1}{\tilde{R}_0} \right) \right) \\ & [-C_F(\mathbf{p}^-) + jS_F(\mathbf{p}^-) + C_F(\mathbf{p}^+) - jS_F(\mathbf{p}^+)] \\ & [-C_F(\mathbf{q}^-) + jS_F(\mathbf{q}^-) + C_F(\mathbf{q}^+) - jS_F(\mathbf{q}^+)] \end{aligned} \quad (120)$$

being $\tilde{R}_0 = \sqrt{\tilde{x}_t^2 + \tilde{y}_t^2 + \tilde{z}_{Rx}^2}$, C_F and S_F the cosine and sine Fresnel integrals [10], and

$$\mathbf{p}^\pm = \left(\tilde{x}_t \pm \frac{\tilde{a}}{2} \right) \sqrt{\frac{2}{\tilde{z}_{Rx}}} \quad (121)$$

$$\mathbf{q}^\pm = \left(\tilde{y}_t \pm \frac{\tilde{b}}{2} \right) \sqrt{\frac{2}{\tilde{z}_{Rx}}}. \quad (122)$$

In contrast to the mentioned 1-O paraxial approximated formulation, a more accurate closed form solution for the reference expression (118) can be obtained by using a polynomial expansion of the phase, and keeping all terms up to the 2-O approximation. The paraxial modeling is maintained only along the axis orthogonal to the target motion direction (i.e.,

along y). Following this assumption, I can write (as better explained in Appendix B.2):

$$\begin{aligned} E_T(\mathbf{r}) = E_0 & \left[e^{-j\tilde{k}\tilde{z}_{Rx}} - \frac{1}{2\tilde{k}} \frac{\tilde{z}_{Rx}}{\tilde{R}_0} \right. \\ & \frac{1}{\sqrt{1 - \tilde{x}_t^2/\tilde{R}_0^2}} e^{-j\tilde{k} \left[\tilde{R}_0 - \frac{1}{2\tilde{R}_0} \left(\frac{\tilde{x}_t^2}{1 - \tilde{x}_t^2/\tilde{R}_0^2} + \tilde{y}_t^2 \right) \right]} \left(j\tilde{k} + \frac{1}{\tilde{R}_0} \right) \\ & (-C_F(p^-) + jS_F(p^-) + C_F(p^+) - jS_F(p^+)) \\ & \left. (-C_F(q^-) + jS_F(q^-) + C_F(q^+) - jS_F(q^+)) \right] \end{aligned} \quad (123)$$

being the distance expressed under the 2-O approximation as follows

$$\tilde{R} = \tilde{R}_0 \left[1 + \frac{\tilde{x}'^2 - 2\tilde{x}_t\tilde{x}' + \tilde{y}'^2 - 2\tilde{y}_t\tilde{y}'}{2\tilde{R}_0^2} - \frac{4\tilde{x}_t^2\tilde{x}'^2}{8\tilde{R}_0^4} \right] \quad (124)$$

being $p^\pm = \left(-\frac{\tilde{x}_t}{1 - \tilde{x}_t^2/\tilde{R}_0^2} \pm \tilde{a}/2 \right) \sqrt{2(1 - \tilde{x}_t^2/\tilde{R}_0^2)/(\tilde{R}_0)}$ and $q^\pm = \left(-\tilde{y}_t \pm \tilde{b}/2 \right) \sqrt{2/(\tilde{R}_0)}$.

For completeness I also assuming a distance z_{Rx} much larger than the target size and the wavelength ($\tilde{z}_{Rx} > 1$), and then the well-known Fraunhofer formula is obtained

$$\begin{aligned} E_T(\tilde{\mathbf{r}}) = E_0 & \left(e^{-j\tilde{k}\tilde{z}_{Rx}} - \frac{1}{2\pi} \frac{\tilde{z}_{Rx}}{\tilde{R}_0^2} \left(j\tilde{k} + \frac{1}{\tilde{R}_0} \right) e^{-j\tilde{k} \left(\tilde{z}_{Rx} + \frac{\tilde{x}_t^2 + \tilde{y}_t^2}{2\tilde{z}_{Rx}} \right)} \right. \\ & \left. \tilde{a}\tilde{b}\text{sinc}\left(\frac{\tilde{x}_t\tilde{a}}{\tilde{z}_R}\right)\text{sinc}\left(\frac{\tilde{y}_t\tilde{b}}{\tilde{z}_R}\right) \right). \end{aligned} \quad (125)$$

It is interesting to note that equation (125) correctly models the FS phenomenon in the far-field (Fraunhofer) region by means of the Babinet's principle, showing the diffraction pattern, but in general it fails in predicting well a neat shadow effect, which is instead present in the near-field case. Indeed, by neglecting the quadratic phase term I prevent the creation of the shadow effect that is responsible of the persistent destructive interference between the direct and the scattered field. In other words, the Fraunhofer approximation gives a field radiated by a target that can be derived from elementary surfaces radiating in a parallel fashion; as a result the interference phenomenon does not generate a shadow region. Such observations are in full agreement with results in [9], where it is shown that a model for the FSR in the far-field region can be obtained by modulating the signal re-irradiated by the target in the far zone with the Doppler signature produced by a moving point-like scatterer. Both the 1-O paraxial

and 2-O approximated formulations are able to take into account what happens for a target that crosses the baseline in the near-field respect to the Rx antenna. Instead a correction factor is needed to consider what happens for a target that crosses the baseline with a tilt angle Ψ where also the shape moves in accord to that angle. I can write equation (118) as

$$E_T(\tilde{\mathbf{r}}) = E_0 \left(e^{-j\tilde{k}\tilde{z}_{Rx}} - \frac{1}{2\pi} \int_{\tilde{\Lambda}} \left(j\tilde{k} + \frac{1}{\tilde{R}} \right) \frac{\tilde{z}_{Rx}}{\tilde{R}^2} e^{-j\tilde{k}(\tilde{R} + \tilde{y}' \tan(\Psi))} d\tilde{\Lambda}' \right) \quad (126)$$

where is visible the correction factor inside the exponential phase due to the movement on the y-axis and the tilt-angle Ψ . Equation (118) and (126) was the expressions of the received total field due to the target plate when an UPW impinges on a target plate with the receiver everywhere in the space. I want extend this expression at the case in which the impinging wave can be also spherical and then also the transmitter can be considered in near-field. Simply from equation (112) I have

$$E_T(\mathbf{t}, \mathbf{r}, \omega) = E_0 \frac{e^{-jk(z_{Tx} + z_{Rx})}}{z_{Tx} + z_{Rx}} + \frac{1}{4\pi} \int_S E_0 \frac{e^{-jk(T+R)}}{TR} \left[\left(jk + \frac{1}{R} \right) \frac{z_{Rx}}{R} + \left(jk + \frac{1}{T} \right) \frac{z_{Tx}}{T} \right] dS' \quad (127)$$

where the Green's function in free-space has been defined as $G_0(\mathbf{r}, \mathbf{r}') = e^{-jkR}/4\pi R$, k is the wavenumber ($k = \omega/c$, c the speed of light in vacuum). The variable T and R are defined as the distance between the arbitrary source point \mathbf{r}' (or \mathbf{t}') on the target shape and respectively the transmitter radiation source \mathbf{t} and the observation source point \mathbf{r}

$$T = |\mathbf{r} - \mathbf{r}'| = \sqrt{(x_t - x')^2 + (y_t - y')^2 + z_{Tx}^2}$$

$$R = |\mathbf{t} - \mathbf{t}'| = \sqrt{(x_t - x')^2 + (y_t - y')^2 + z_{Rx}^2} \quad (128)$$

where x_t and y_t are the coordinates of the target center on the $z = 0$ plane at each instant, and x' and y' are the target local coordinates referred to its center (as in Figure 19). I define also the same T and R distances when the target is considered as a point-target as

$$T_0 = |\mathbf{r} - \mathbf{r}'| = \sqrt{x_t^2 + y_t^2 + z_{Tx}^2}$$

$$R_0 = |\mathbf{t} - \mathbf{t}'| = \sqrt{x_t^2 + y_t^2 + z_{Rx}^2}. \quad (129)$$

Equation (127) represents the numerical expression that is the basis for the derivation of the analytical model with transmitter and receiver both in near-field respect to the target.

3.2.3 Model sensitivity

The impact of the different modeling (i.e., 1-O vs 2-O approximation) is then analyzed comparing the phase error formulations. The phase error $\Delta\Phi$ obtained from the 1-O paraxial formulation in equation (120) can be expressed as follows:

$$\Delta\Phi = k \frac{1}{8} \left[\frac{(x_t - x')^2 + (y_t - y')^2}{z_{Rx}^2} \right]^2 z_{Rx}. \quad (130)$$

Instead, the phase error $\Delta\Phi$ obtained from the 2-O paraxial formulation and by applying the paraxial approximation on y in equation (123), is reported in the following

$$\Delta\Phi = k \frac{1}{8} \left[\frac{(x'^2 - 2x_t x' + y'^2 - 2y_t y')^2}{R_0^4} - \frac{4x_t^2 x'^2}{R_0^4} \right] R_0. \quad (131)$$

The sensitivity of the EM model presented in [11], summarized in equation (120), is here analyzed with respect to the improved version of this formulation, reported in equation (123) from [55].

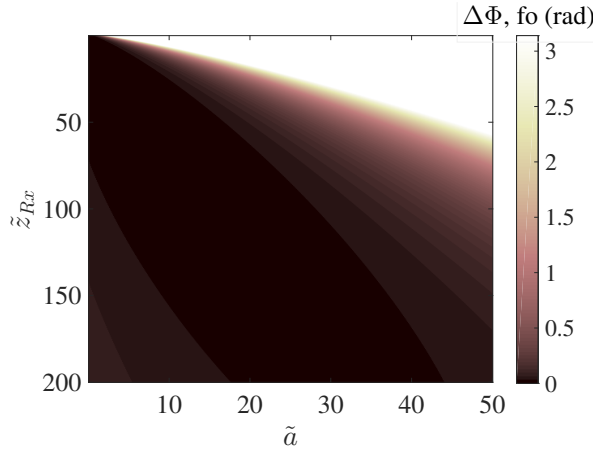


Figure 24: Map of the phase error from equation (130) for a horizontal angle $\alpha_h = 30^\circ$ and tilt angle $\psi = 0^\circ$.

In Figure 24, a 2D representation of the phase error in equation (130) is shown for a square target with variable size (setting $\tilde{a} = \tilde{b}$), and for variable target-to-Rx distances z_{Rx} . The result is obtained replacing the coordinates \tilde{x}_t and \tilde{y}_t with the maximum position assumed by the target, that is given a value of the horizontal angle equal to 30° . The same representation is shown in Figure 25 according to the phase error in equation (131). In Figure 26, the sensitivity of the model based on the 1-O and the 2-O approximation is illustrated with respect to the FSR system parameters. Specifically, the figure shows the areas where the phase error is below $\pi/8$. These results are obtained by setting the relevant threshold equal to $\pi/8$ on the phase error maps presented in Figures 24 and 25. The black and pink areas correspond, respectively, to the values of the target-to-Rx distance and of the target size for which the phase error of the 1-O model exceeds the threshold of $\pi/8$. For the 2-O model this area corresponds only to the black one. In other words, for this case study, the pink area is the 2D representation of the extension of the range of validity of the model moving from first to second-order approximation.

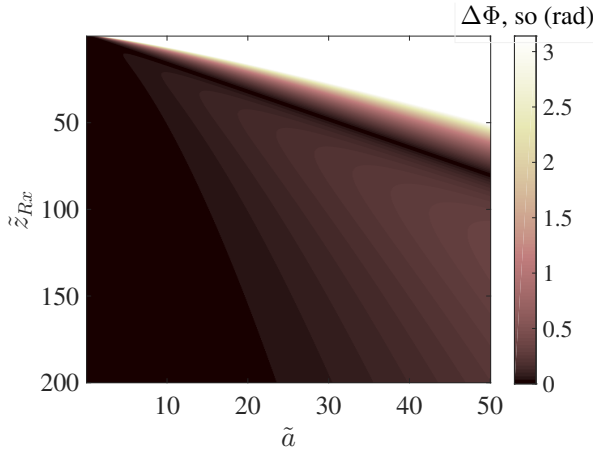


Figure 25: Map of the phase error from equation (131) for a horizontal angle $\alpha_h = 30^\circ$ and tilt angle $\psi = 0^\circ$.

As an example, Table 2 shows a possible setup of the FSR configuration obtained by fixing the wavelength, the horizontal angle, and the target size, and by evaluating the minimum target-to-Rx distance allowing a phase error below $\pi/8$ when 1-O and 2-O approximations are used.

As expected, the 2-O model advantageously extends the minimum target-to-Rx distance for given wavelength and target size. The same result can

λ [m]	f [GHz]	$a = b$ [m]	$\min(z_{Rx}), 1\text{-O}$	$\min(z_{Rx}), 2\text{-O}$
0.1	3	3	10.7	7.12
0.33	0.9	20	25.08	18.38

Table 2: Operational parameters for the first (1-O) and second-order (2-O) models (horizontal angle set to 30°).

be obtained by fixing the wavelength and the target-to-Rx distance and by observing the increase of the maximum target size allowed by this novel 2-O model.

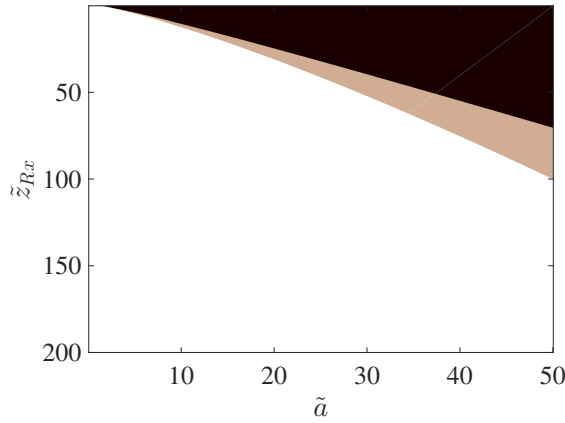


Figure 26: Map of the area where the phase error does not exceed $\pi/8$ (i.e., threshold $\pi/8$ applied to the maps of Figs. 24 and 25). The black and pink areas refer to the values in which the first-order model exceeds the threshold and only black in which the second-order model exceeds the threshold.

3.3 RESULTS FOR SIMPLIFIED MODEL

The near-field effects of the variable distance target/Rx both on the FS-CS and on the modulated received signal are shown in this section in terms of numerical solutions of the FS-CS in equation (114) putting inside equation (69).

3.3.1 *Transition to near-field for a rectangular target*

The results in Figures 27 are referred to three conductive 2D targets moving perpendicularly to the baseline with a constant velocity, i.e., three cases of rectangular shapes with different areas: $A_g = 2.4 \text{ m}^2$, $A_g = 6.6667 \text{ m}^2$, $A_g = 26.6667 \text{ m}^2$, respectively; further details on the physical parameters are found in figure captions and labels. Each figure shows the FS-CS for rectangular shape (Top) and the FSR overall signature (Bottom).

The first apparent feature that I can analyze is related to the configuration with a size-fixed target getting closer to the receiver. Looking at Figure 27, when the overall distance $T + R$ (See Figure 7) increases, the signal parabolic phase and frequency increase more quickly assuming larger values. The chirp-like signal is then narrower because the time-axis is contracted.

Results in Figures 27 are based on the FS-CS model using the Babinet's principle (Section 2.2.3) so that the target basically acts as re-irradiating antenna, illuminated by the transmitter field. The well-known far field concepts of directivity and RCS can be generalized in the near field, where these definitions become dependent on the target/Rx distance (z_{Rx}). Therefore, when the target is getting closer to the receiver, the ratio between the target size and target/Rx distance increases so that the exponential term in equation (113) decreases and the width of the FS-CS is narrower. Furthermore, the transition from far field (red-curves) to near field (blue and black curves) also changes the theoretical FS-CS form (which is, for a far-field condition, a sinc function). The amplitude of the complex envelope, evaluated through equation (113), decreases from far field to the near field and this effect is shown on the received signal due to the absence of the field factor in equation (44).

With respect to the classical results for the far-field FSR, I note that the chirp-like nature of the signal is gradually lost in the near-field case. This would prevent a potential target classification based on the signal phase analysis. Nevertheless to this aim in near field I may also extract useful features from the Rx waveform amplitude characterized by a diffraction hole previously mentioned as black spot (see Figure 20).

3.3.2 *Transition to near-field for a circular target*

The results in Figures 28 are referred to three conductive 2D targets moving perpendicularly to the baseline with a constant velocity, i.e., a circle

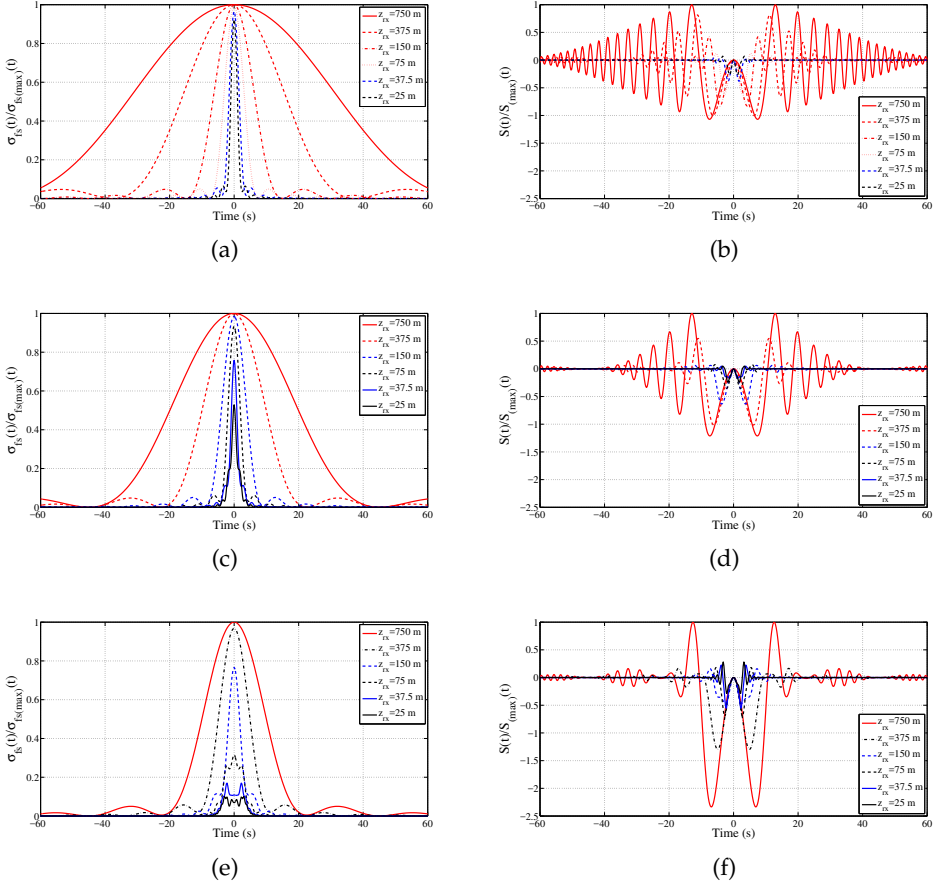


Figure 27: The rectangular shape signature is presented in terms of FS-CSS (a, b, c) and signal model (d, e, f), as the target/Rx distance z_{Rx} is varied, evaluated by equation (114). The area of the shape is: (a, d) 2.4 m^2 , (b, e) 6.6667 m^2 , (c, f) 26.6667 m^2 . Size of the rectangles along x-y: $3 \times 0.8 \text{ m}$, $5 \times 1.33 \text{ m}$ and $10 \times 2.67 \text{ m}$. The Fraunhofer distances at $f= 1 \text{ GHz}$ are:(a, d) 60 m , (b, e) 166.6667 m , (c, f) 666.6667 m .

shape with same geometrical cross section respect to the previous shown rectangular shape.

These results highlight that the target's shape also influences the FS-CS whereas the signal model is unvaried because it is obtained considering a point target. The complex envelope due to the rectangular target shows typical ripples, generated by the presence of sharp diffracting edges. These ripples are less visible for the circular shape due to its smooth profile. As said the theoretical FS-CS form is, for a far-field condition, a sinc function for rectangular shapes and instead for circular shapes I have a Besinc function.

Choosing a configuration, I compare Figure 27 and 28, there are some significant differences in the signature between rectangular and circular targets with the same area: i) for the rectangular shape, the amplitude of the FS-CS is reduced; ii) the amplitude of the hole is higher. I may infer the features previously expressed from the received signal, for example through the peak-to-peak value and the null-to-null width.

3.4 RESULTS FOR NEAR-FIELD RECEIVER MODEL

In this section, I illustrate and discuss in more details the original scattering features of a FSR system when the transition from far-field to near-field regions occurs; the effects of the target electrical dimensions on the received signal are evaluated; also trajectories describing a certain angle with respect to the baseline are considered.

3.4.1 *Transition from far field to near field*

In Figure 29 the plane wave propagating along the BL direction z , having the electric field linearly polarized, e.g., along y , impinges on a square target when it traces a certain number of rectilinear trajectories sweeping from the far-field to near-field regions (i.e., by considering different values for $z_{R\chi}$). The choice of a simple square shape, characterized by just one geometrical parameter ($a = b$), allows us to clearly emphasize the distinctive features of the scattering problem both in far-field and near-field conditions.

In Figure 30 the total and scattered field vs. χ for a square object having side $\tilde{a} = \tilde{b} = 3$ crossing the BL at different distances with respect to the receiver, from 10 to 100, is presented. The signal at the receiver is evaluated through the analytical closed-form model proposed in section 3.2.2 in

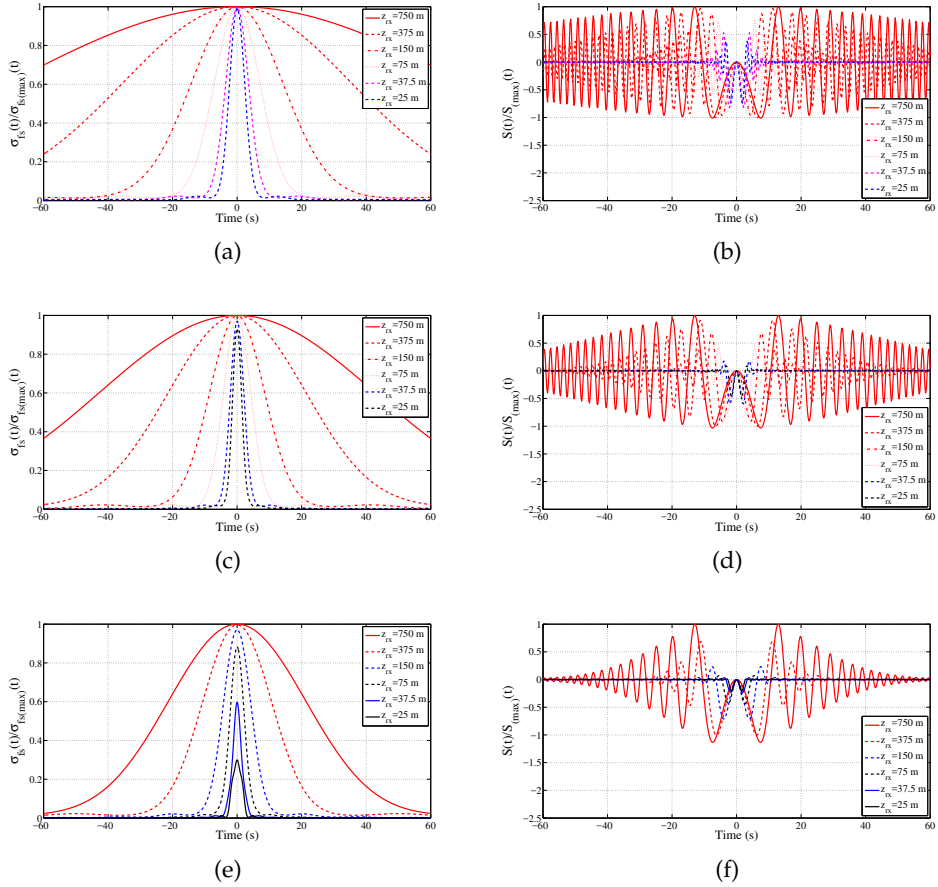


Figure 28: The circular shape signature is presented in terms of FS-CSS (a, b, c) and signal model (d, e, f), as the target/Rx distance z_{Rx} is varied, evaluated by equation (114). The area of the shape is the same for the rectangular target: (a, d) 2.4 m^2 , (b, e) 6.6667 m^2 , (c, f) 26.6667 m^2 . Diameters of the circle: 1.7481 m, 2.9135 m and 5.84 m. The Fraunhofer distances at $f= 1$ GHz are:(a, d) 20.3718 m, (b, e) 56.5884 m, (c, f) 226.3537 m.

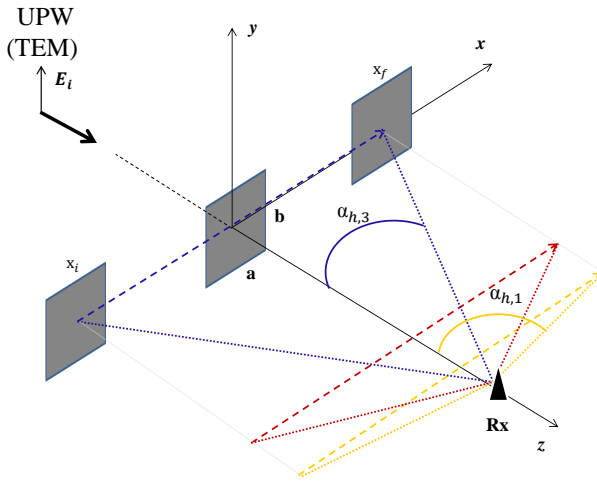


Figure 29: Simulated FSR scenario for different Rx-target distances: $\tilde{z}_{Rx_1} = 10$, $\tilde{z}_{Rx_2} = 30$, $\tilde{z}_{Rx_3} = 100$. The target is here a square metallic object having side $\tilde{a} = \tilde{b} = 3$ illuminated by CW having frequency f . Each distance generates a different angle-of-view from Rx, ranging from near-field to far-field (\tilde{z}_{Rx_1} to \tilde{z}_{Rx_3}), i.e., $\alpha_{h,1} = 74^\circ$, $\alpha_{h,2} = 49.4^\circ$, and $\alpha_{h,3} = 19.3^\circ$ (plot not in scale).

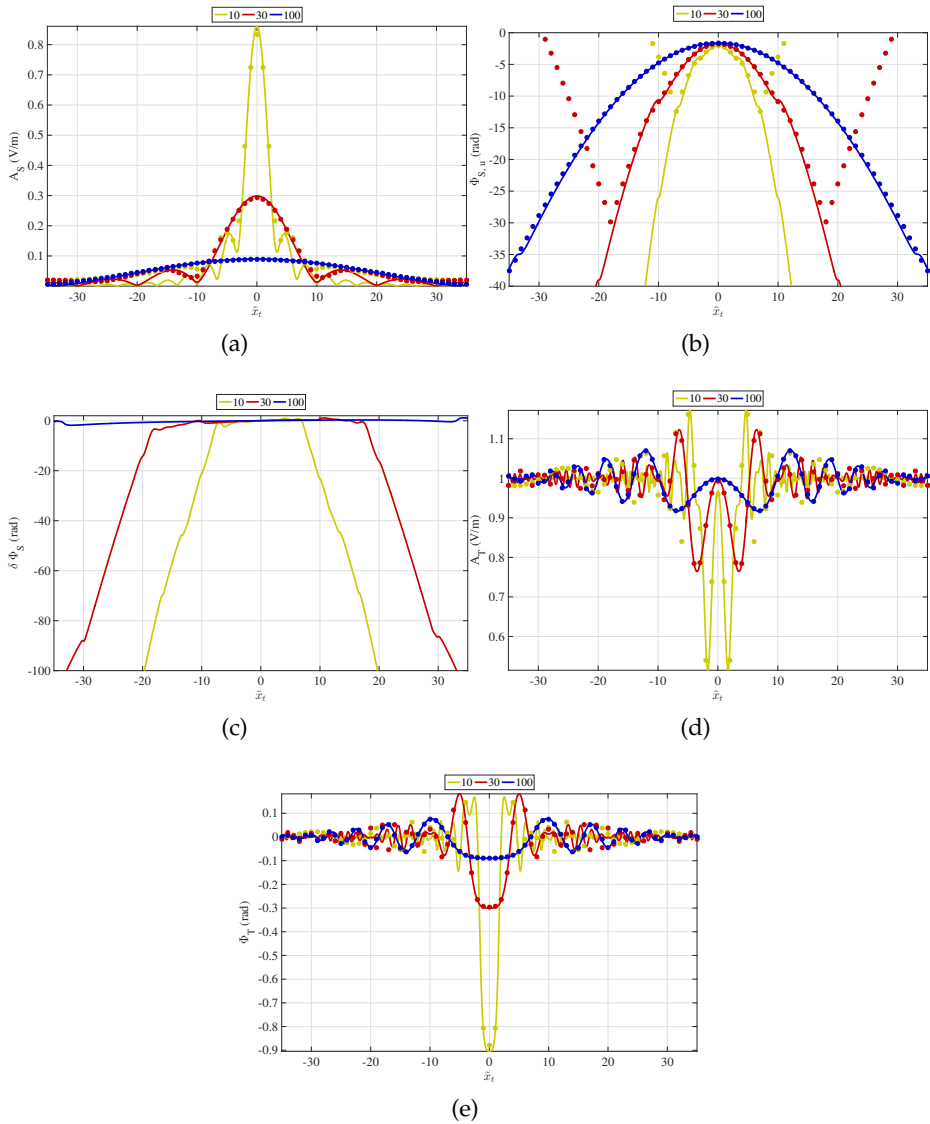


Figure 30: Scattered (subscripts 'S') and total (subscripts 'T') signals collected by the receiving antenna as the target moves along the x direction (see Figure 29), for three different near-field/far-field distances, equal to 10 (yellow curves), 30 (red curves), 100 (blue curves), where the solid lines refer to our analytical approach and dots to numerical CAD results. (a): Scattered amplitude; (b) Unwrapped scattered phase; (c) Phase difference between first-order approximation and numerical evaluation; (d) Amplitude of the total received signal; (e) Phase of the total received signal. Solid lines: AM, dots: FW.

equation (120) (AM, solid lines). I assume that the target follows a linear horizontal trajectory along x between $\tilde{x}_i = -35$ and $\tilde{x}_f = 35$ and is moving with a uniform velocity spanning an angle of view α_h on the xz plane that is a function of the distance from the Rx antenna (see Figure 29). By selecting a fixed value for the length of the trajectory, α_h obviously results wider for shorter distances. In the results of Figure 30, I show 10 (yellow curves), 30 (red curves), 100 (blue curves), thus considering both far-field and near-field operation conditions.

In Figure 30(a)-(c) the scattered field is reported as a function of x : in particular, the amplitude A_S is shown in Figure 30(a); in Figure 30(b) I display the values of the unwrapped phase $\Phi_{S,u}$, and in Figure 30(c) I plot the phase differences of the first-order approximations with respect to the correct numerical value, according to the considerations previously presented (Section 3.4). Comparisons between the analytical formulation (solid lines) and numerical full-wave CAD results (dots) are also provided.

As expected, the amplitude of the field scattered by the object (which acts as a re-irradiating element) is particularly sensitive to the distance \tilde{z}_{Rx} . This is coherent with the fact that, when I am no longer in far-field conditions, the re-irradiated field can be viewed as a spherical wave whose power can decrease in a more complex way than $1/\tilde{z}_{Rx}^2$. The behavior of the beamwidth may result less predictable and should be interpreted by taking into account the relevant angle-of-view and the movement of the target; indeed, by moving farther from the Rx antenna, the angle of view decreases while covering the same distance along the x axis, and the object generates a re-irradiation that appears less variable. At the same time, even though when the far-field is approached, the directivity of the object generally increases and becomes independent of \tilde{z}_{Rx} (and dependent just on θ and ϕ in the relevant spherical coordinate system): in fact, when the object is farther (i.e., \tilde{z}_{Rx} is larger) it re-irradiates almost inside the main lobe of the radiation pattern, and consequently the field at the receiving point results less variable (see, e.g., the blue curve in Figure 30(a)). The well-known far field concepts of directivity can be generalized in the near field, where this definition become dependent on the target/Rx distance [52] as said before. The phase of the scattered field has a typical chirp-like behavior, where the phase oscillations along the distance are related to the well-known Doppler effect. Indeed, the unwrapped phase of the scattered signal, shown in Figure 30(b), results in the expected parabolic trend. In Figure 30(d) and (e), the values of the amplitude and phase of the total received signal, respectively, are presented. The effect of the interference between direct and re-irradiated waves confirms the expect-

ted FS phenomenon. In fact, the magnitude of the total field is oscillating around 1 V/m and a fast variation is observed in the central part for reduced distances, due to strong variations of the field re-irradiated when the object is moving closer to the receiver. This aspect could result counter-intuitive and represents indeed an original feature of the FS phenomenon. As concerns the phase, going from the far-field case up to the near-field, the chirp-like nature of the signal is progressively lost.

As said, all our results have been validated through the full-wave commercial code FEKO (all the dotted data in Figure 30): it results an excellent agreement obtained for the amplitude of both scattered and total fields (Figures 30(a) and (d), respectively). It is interesting to note that the proposed model fails in predicting the phase of the field re-irradiated outside the central region, as clearly shown in Figures 30(b) and (c): this is due to the truncated first-order expansion introduced to obtain the closed-form expression in (125) and it results manifestly worse when the target gets closer to the receiver (i.e. when \tilde{a} is comparable to \tilde{z}_{R_x} and I am no longer in far-field conditions). In this case, to better approximate the phase behavior, more terms of the series expansion are needed, preventing the possibility to obtain a closed-form expression.

3.4.2 *Effect of the target size*

In order to analyze the effects of the target size on the FSR signal I consider here two different shapes, i.e., the square and the rectangle, each one having three different dimensions, as shown in Figure 31. In this case I fix $\tilde{z}_{R_x} = 50$, with a correspondent overall angle-of-view equal to 70° ; all the other parameters describing the trajectory and the FSR system remain unchanged, with the target still illuminated by a linear-polarized plane wave as in Figure 29.

In Figures 32 and 33, the scattered and the total fields are shown for increasing dimensions of the target profile, for a square and a rectangular shape, respectively: for the square side (Figure 32), it is $\tilde{a} = \tilde{b} = 1$ (blue), 3 (red), and 4 (yellow); for the rectangle (Figure 33), the same choices refer to the minor side \tilde{b} along \tilde{y} , being the major side $\tilde{a} = 2\tilde{b}$ along x (see Figure 31). Again, our closed-form in equation (120) results (solid lines) are compared to full-wave CAD (dots).

Both amplitude and phase of the scattered field mainly confirm the characteristics previously discussed. Differences on the re-irradiated field between the square and the rectangular shapes showing a common dimension for one of the two sides are anyway clearly visible. In both cases,

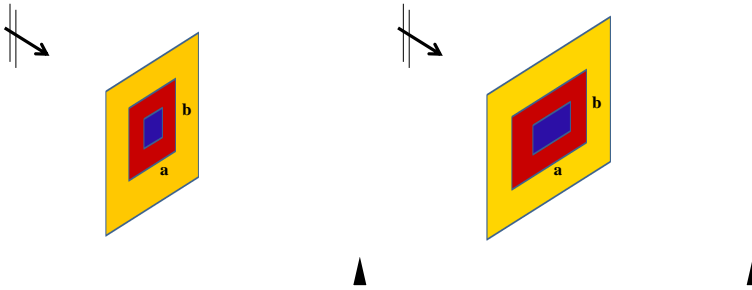


Figure 31: Simulated FSR scenario to investigate the effects of the target dimension and shape. Three different square (left) and a rectangular (right) metallic plates are considered. Squares size along x - y : 1 (blue), 3 (red), 4 (yellow); rectangular size along x - y : 2×1 (blue), 6×3 (red), 8×4 (yellow).

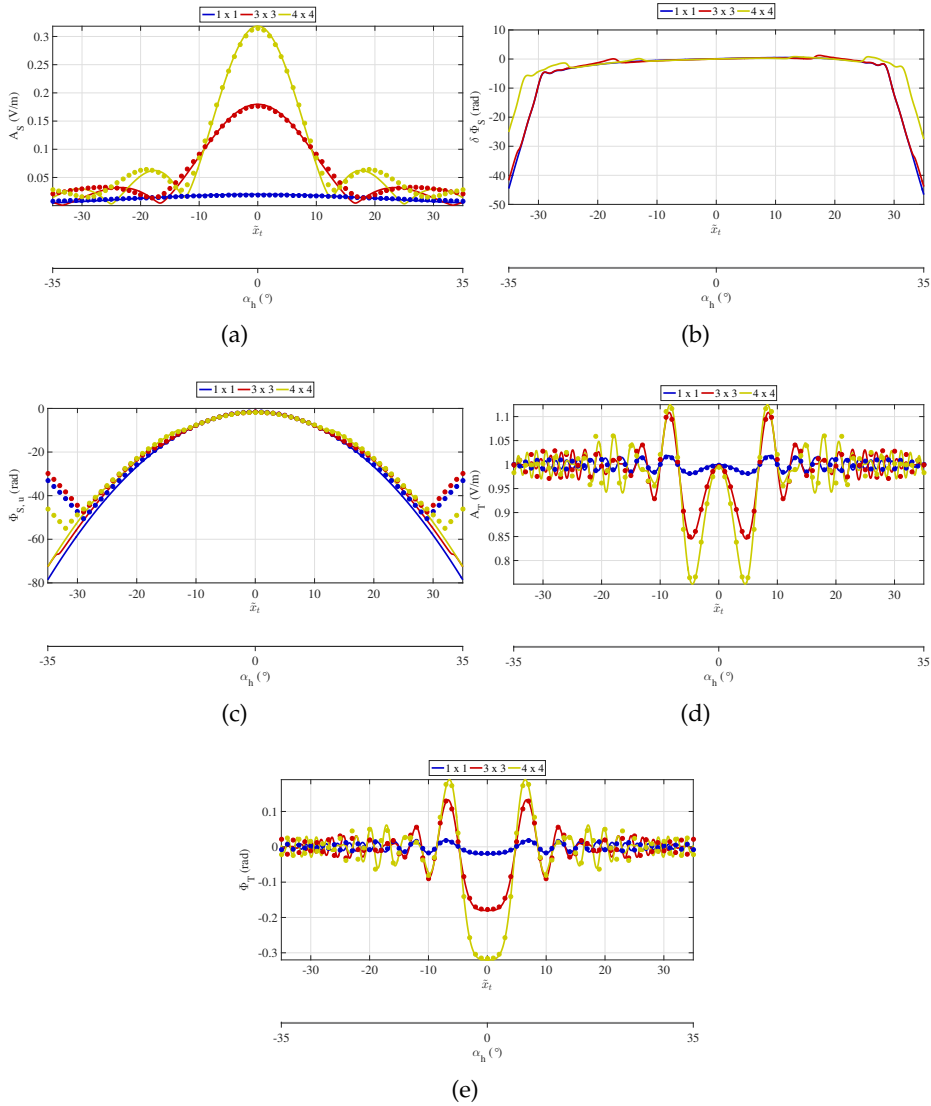


Figure 32: Scattered ('S') and total ('T') signals vs. target horizontal position, collected by the receiving antenna for three different square PEC objects as in Figure 31: side 1 (blue), 3 (red), 4 (yellow). (a) Scattered-field amplitude; (b) Scattered-field phase difference; (c) Scattered-field unwrapped phase; (d) Total-field amplitude; (e) Total-field phase. Closed-form results (solid) and full-wave CAD (dots) are compared.

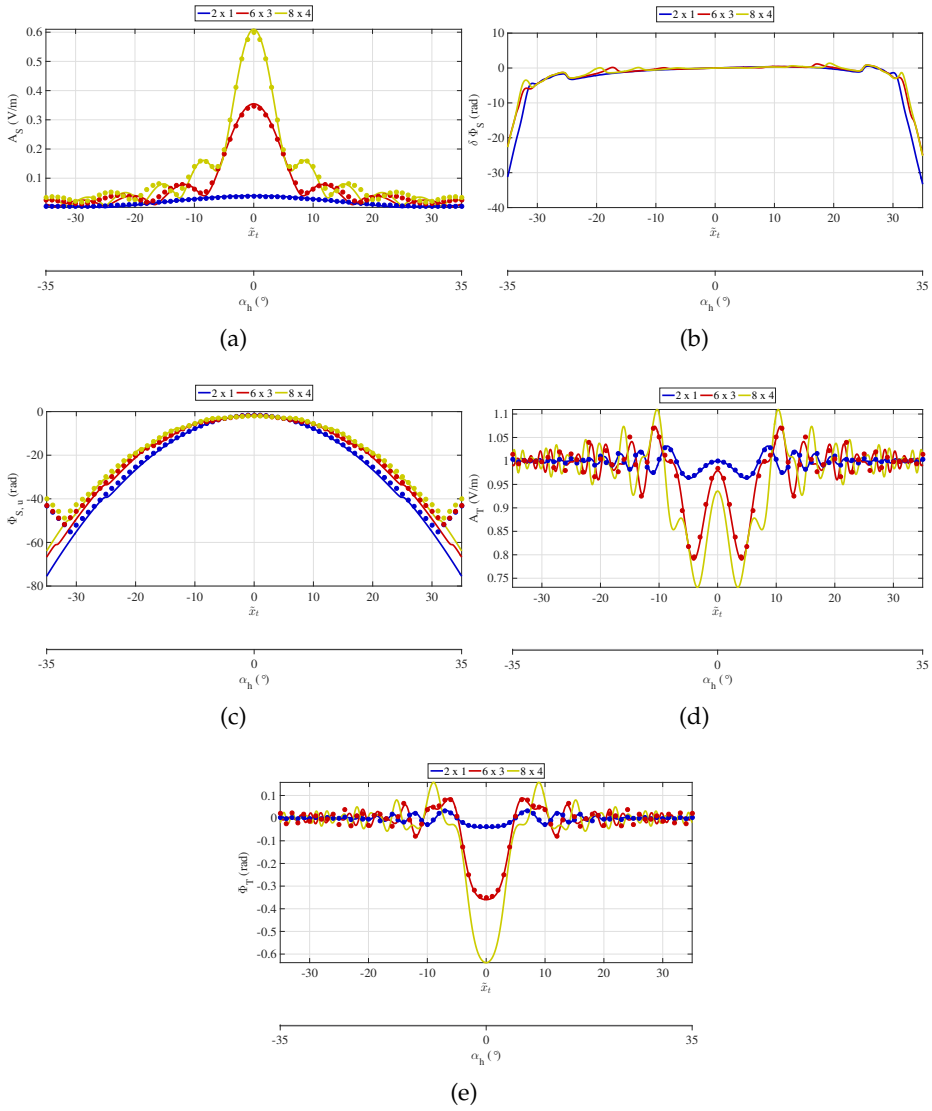


Figure 33: Same as of Figure 32 for various rectangular shapes, with $\tilde{b} = \tilde{a}/2 = 1$ (blue), 3 (red), 4 (yellow); see also Figure 31.

as the object becomes larger, the field in the forward direction tends to be stronger and its distribution along the x axis narrower, whereas the phase distribution results less sensitive to the same variations. It is important to note that these results have been obtained by keeping fixed the Rx-antenna distance, hence, as expected, the effect generated by a larger object on the re-irradiated field is similar to that one produced by a smaller object whose trajectory runs closer to the receiving antenna. In Figs. 32(c) and 33(c) the unwrapped phase, along with the full-wave validation, is reported again for square and rectangle, respectively, confirming the accuracy of the proposed formulation. In Figs. 32(d), (e) and Figure 33(d),(e), the amplitude and phase of the total field are displayed again for square and rectangular targets, respectively. Also in these cases the amplitude of the total field oscillates around 1 V/m and a fast variation is observed in the central part, for smaller objects. This is coherent with the strong variation observed in Figure 30(d) for the field re-irradiated when the same object is moving closer to the receiver. As concerns the phase, by increasing the target size the chirp-like nature of the signal is progressively lost, since the presence of a larger object makes smaller the apparent distance between the re-irradiating target and the Rx antenna. It is still emphasized an excellent agreement between closed-form (solid lines) and full-wave CAD results (dots).

3.4.3 *Effect of the trajectory*

To analyze the effect of the trajectory, i.e., when a target is moving not necessarily perpendicular to the BL, in this subsection different values of the ψ angle (see Figure 10) are considered. The distance from the receiver is set to $\tilde{z}_{R_x} = 100$ with respect to the central point (i.e., for $x = 0$) and the initial and final positions are $\tilde{x}_i = -90$ and $\tilde{x}_f = 90$. The moving object is a metallic square ($\tilde{a} = \tilde{b} = 3$), while all the remaining parameters, included the impinging plane wave, are unchanged. Three different linear trajectories are considered at different tilt angles, i.e., $\psi_1 = 0^\circ$, $\psi_2 = 30^\circ$, $\psi_3 = 45^\circ$; in order to evaluate the effect of each tilted trajectory, I keep fixed \tilde{x}_i and \tilde{x}_f , so that the target could move along its path from far-field to near-field regions. Consequently, three different asymmetric couples of angles of view are generated: the relevant geometrical details are reported in Table 3. Let us stress that, accordingly to Figure 10, for $\psi > 0$, the moving object may result in the far-field region for positive values of x and in the near-field for those negative. For these results I furnish again a comparison among our analytical model of equation (32) ('AM', gray

Table 3: Parameters of the trajectories for the FSR using the near-field receiver model.

$\psi [^\circ]$	$\tilde{z}_{R_x} _{\tilde{x}=0}$	$z_{R_x} _{\tilde{x}=\tilde{x}_i}$	$\tilde{z}_{R_x} _{\tilde{x}=\tilde{x}_f}$	$\alpha_{h,\min}/\alpha_{h,\max} [^\circ]$
0	100	100	100	-42/42
30	100	50	160	-62/31
45	100	10	200	-84/25

curves), the numerical model of Figure 29 ('NM', black curves) based on the computation of the diffraction integral, and the full-wave ('FW', dotted green curves) CAD implementation.

In Figs. 34(a) and (b) the scattered field (amplitude and phase, respectively) for $\psi = 0^\circ$ (straight trajectory, perpendicular to BL) is presented: with respect to the results reported in the previous sections in this case I can test the effect of the paraxial approximation (fully satisfied for relatively small α_h) on the re-irradiated field. An excellent agreement is obtained in the central region for both amplitude and phase of the signal, whereas the agreement is gradually lost as x and consequently α_h increase. In Figs. 34(c)-(f), the amplitude and phase results of the scattered fields for the two tilted trajectories, ψ_2 and ψ_3 , are presented: as expected the amplitude of the scattered field loses its symmetry and the agreement among the analytical model, the numerical solution of the integral, and the full-wave validation is gradually lost along the path, i.e., in particular as the object approaches toward the negative values of x , entering near-field regions.

In Figure 35, the same results of tilted trajectories are for the total field. Again, the symmetry is lost for $\psi \neq 0$ and the amplitude of the total field oscillates around 1 V/m ; even though the typical chirp signature results perturbed, this behavior allows us to recognize a trajectory different from 0° and to potentially provide an estimation of the tilted angle. Once again the results have been validated by means of the full-wave CAD solution, and an excellent agreement has still been obtained as long as the paraxial approximation is satisfied.

Finally, it is important to note that, for modeling purposes, I have considered here an object moving on a tilted trajectory but showing always its flat face to the receiver; indeed, to consider an object whose profile is oriented along the direction of movement one, the shadow-contour theorem is needed, whose validity along the transition between far-field-near-field region deserves further investigation.

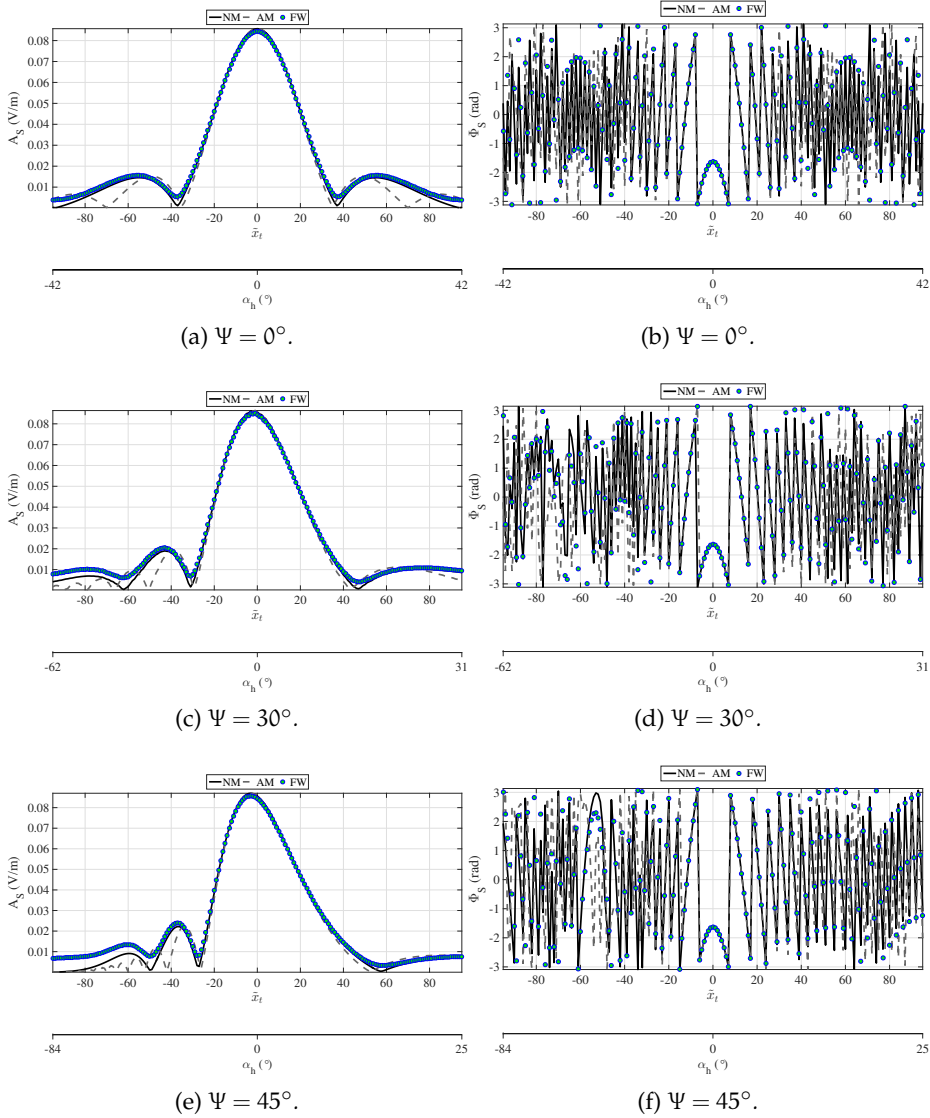


Figure 34: Amplitude (left column) and phase (right column) of the scattered field collected by the receiving antenna for different tilt angles ψ of the target trajectory (see Figure 19). Parameters: $\tilde{a} = \tilde{b} = 3$, frequency f . The EM field radiated by the source is still assumed as a z -directed plane wave polarized along the y direction. Comparisons between analytical model (AM, gray curves), numerical model (NM, black curves), and full-wave (FW, green dots) CAD are displayed. Cases (a) and (b) for $\psi = 0^\circ$, (c) and (d) for $\psi = 30^\circ$, (e) and (f) for $\psi = 45^\circ$.

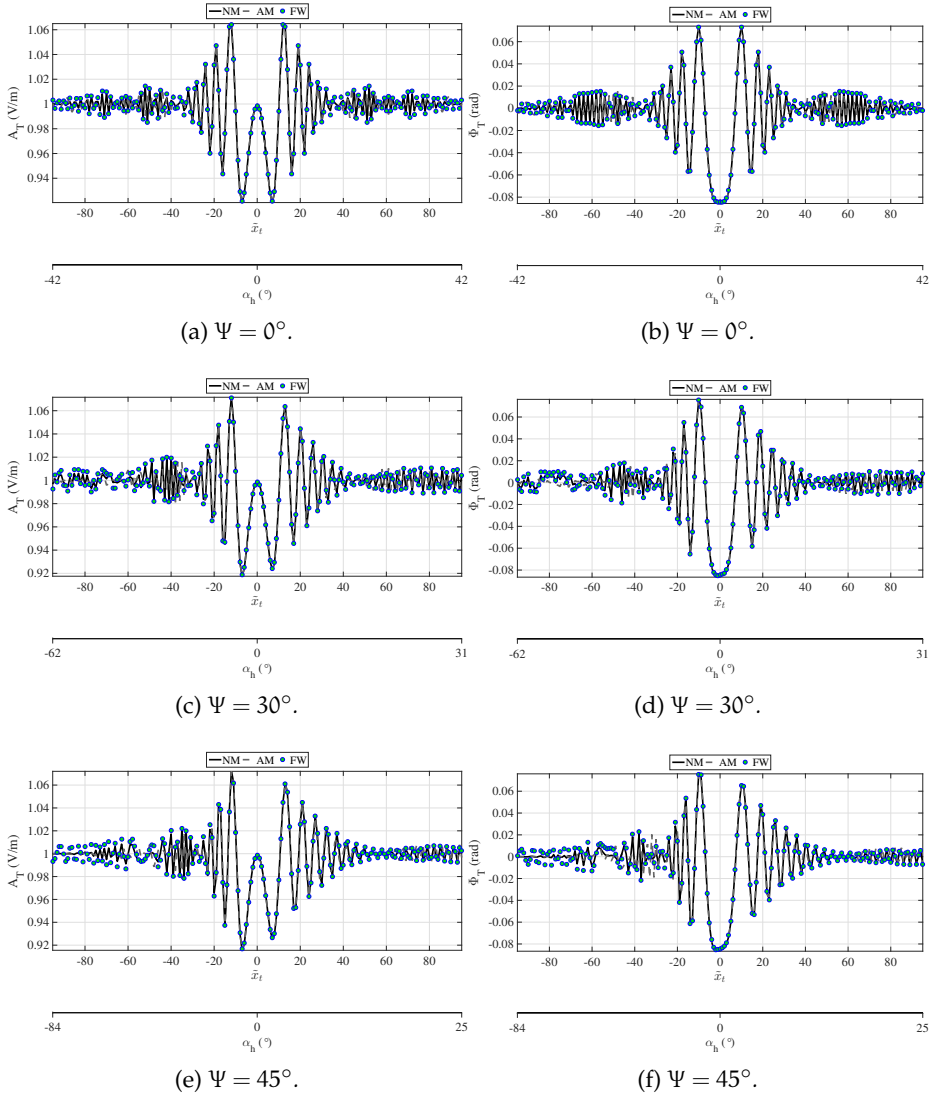


Figure 35: As in Figure 34 for the total field.

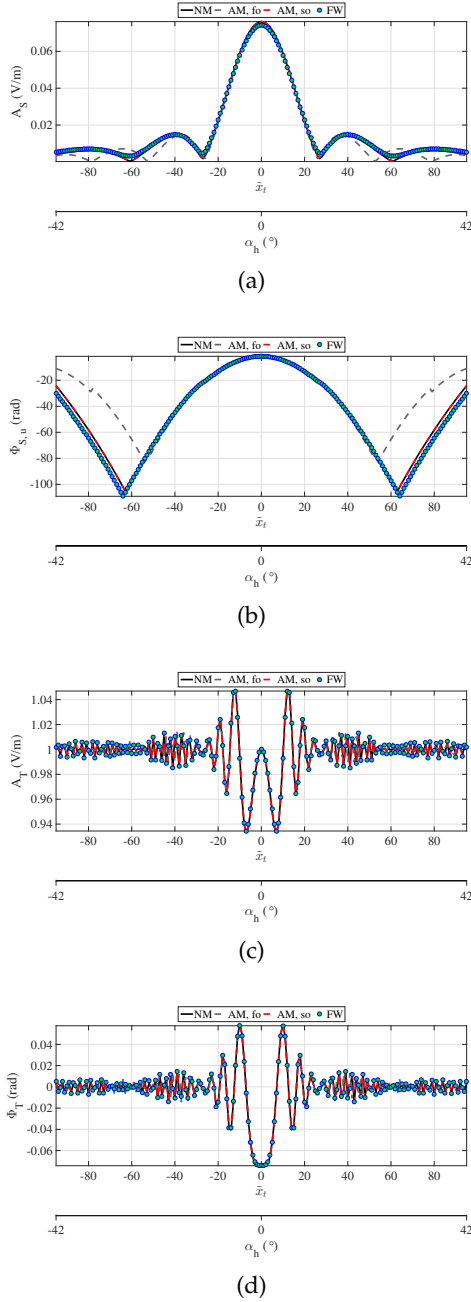


Figure 36: FSR scattered (subscripts 'S') and total (subscripts 'T') fields collected by the receiving antenna for a square metallic object (size $\tilde{a} = 4$, $\tilde{b} = 2$) horizontally moving at a distance from Rx antenna $\tilde{z}_{R\tilde{x}} = 200$ for a frequency f . Legend: NM = Numerical solution of integral (equation (118)), AM, 1-O = Analytical solution with a first-order approximation on the phase (equation (120)), AM, 2-O = second-order analytical solution (equation(123)), FW = full-wave numerical solution.

3.4.4 Effect of the 1-O and 2-O approximations

Figure 36 shows the field collected by the receiving antenna placed at the distance $z_{\tilde{R}_x} = 200$ from a rectangular object having dimension $\tilde{a} = 4$, $\tilde{b} = 2$, and illuminated through a plane wave having a linear x -polarized electric field with amplitude equals to 1 V/m. The double axis, representing the target movement along x and the relevant spanned horizontal angle α_h , is useful to evaluate the improvement of the phase extension. Looking at the amplitude (A) and phase (Φ) of the 'scattered' field (subscripts 'S'), respectively in Figure 36(a) and (b), related to the FS-CS of the $|\alpha_h| \geq 20^\circ$ (or $|\tilde{x}_t| \geq 40$), the first-order analytical model (AM, 1-O) in equation (120) does not well approximate the numerical model (NM) (i.e., the numerical evaluation of the integral in equation (118)), as well as the full-wave solution (FW) derived by means of the CAD tool. Instead, the second-order analytical model (AM, 2-O) in equation (123) provides a better approximation of the numerical models. This is also clearly visible for the amplitude (A) and phase (Φ) of the 'total' field (subscripts 'T') in Figure 36(c) and (d), which are generated through the interference between the impinging and the re-irradiated waves, respectively. As is manifest, the close matching between the improved second-order analytical model and the numerical solutions confirms the enhanced accuracy of the proposed improved modeling for the FSR signal [55].

3.5 CONCLUSION

In this Chapter I have discussed the realisation of an electromagnetic modeling of the target signature characterizing the transition from far-field to near-field regions for FSR. The electromagnetic field has been studied when canonical metallic targets cross the BL along arbitrary trajectories. The electromagnetic theory behind the proposed modeling has been extensively presented. The model approach suggested by Gashinova et al. [9] has been extended to near-field regions, it was named near-field simplified model [51, 52]. Two more complete models have been shown, named near-field receiver model [11, 53–55] and transmitter-receiver model, derived directly from the Huygen's principle expressed in terms of extinction. Full-wave CAD solutions have been used to validate the results.

MONITORING OF WEATHER RADARS CALIBRATION

"C'è una rete nella quale pare sia ormai impossibile non essere catturati, ed è una rete a strascico. In questa rete io insisto a cercare buchi."

— Antonio Tabucchi, *Si sta facendo sempre piu tardi*, 2001

Calibration is a key element to control the impact of the radar system error on the weather radar measurements. A general overview of the most useful calibration techniques is shown in Section 4.1. A new data processing methodology, based on the statistical analysis of ground-clutter echoes for a C-band radar is presented in Section 4.2 [13] with the aim to monitoring the relative calibration of reflectivity and differential reflectivity factor. After that a preliminary investigation on the feasibility of using the permanent scatterers to monitor the polarimetric weather radar calibration is proposed in Section 4.3 [14].

4.1 WEATHER RADAR CALIBRATION

Ground-based weather radars are typically used to locate precipitation over large areas and classify its type (e.g., rain, snow, hail) as well as quantitatively estimate rain accumulations at the ground level. The outcome of the aforementioned applications is strongly dependent by a proper radar system calibration in both single- and dual-polarization modes, that is, by the exact definition of the radar constants involved when trying to convert the received backscattered power into the co-polar reflectivity (Z_{hh}) and the differential reflectivity (Z_{dr}) in the radar equation in (12) with (98) and (99). Both Z_{hh} and Z_{dr} are the radar quantities considered to estimate rain precipitation and perform hydrometeor classifications. They are often used together with the specific differential phase shift (K_{dp}) that is not affected by miscalibration effects being a measure of the rate of range variations of the differential signal phase between the horizontal

(h) and vertical polarization (v). It happens that such radar constants (i.e. transmitted peak power, antenna technical features and in general all the radar transmitter and receiver system parameters) may slightly change over time departing from their nominal values. Several techniques have been developed to check the degree of calibration of a radar system and compensate for it [56]. In the following two subsections (Sec. 4.1.1- 4.1.2) I present to you three important kinds of monitoring.

4.1.1 *Self-consistency and Solar calibration*

In Gorgucci et al. [57], the degree of redundancy shown in the dual polarization radar measurements of Z_{hh} , Z_{dr} and K_{dp} , in light rain regimes, is exploited to find an absolute calibration factor for Z_{hh} . For the Z_{dr} calibration, the same Authors, have proposed a vertical looking strategy of rain drops while they fall on the radar. Later, Bringi and Chandrasekar [6] and Ryzhkov et al. [58] have used a theoretical curve relating the vertical looking observations of Z_{dr} to the slanted ones, thus providing an alternative way to find a calibration factor for Z_{dr} that is not limited to the availability of vertical scan only. Holleman in [59] has proposed to observe the incoherent radiation from the Sun as a stable reference to define the level of miscalibrations in the receiver section of the radar systems in terms of Z_{hh} . Both of them, self-consistency and solar calibration, have some limits. The self-consistency can be applied only in presence of light rain. The solar calibration is a kind of technique valid only for a single radar component: the receiver.

4.1.2 *Ground clutter techniques*

Calibration techniques used routinely or at scheduled maintenance include measures of antenna gain, standard targets and solar radiation [56]. Calibration through standard targets, such as suspended spheres, can be very cumbersome and not always applicable. In this respect, permanent scatterers, such as the ground clutter around the radar, allow to have a constant monitoring in space and time of the whole radar system. A statistical approach using numerous ground targets to check the reflectivity factor was proposed by Rinehart in [60]. He also introduced the idea to monitoring the system using an individual target return. Another approach [61] extends the "Mountain Reference Technique" (MRT), typically used in space-borne radar configurations, to the ground-based radar by

using the path-integrated attenuations (PIA) calculated using the ground clutter, to calibrate the system. An improvement of the statistical approach of Rinehart has been proposed in [62] and applied in [63] and [64], usually known as Relative Calibration Adjustment (RCA) Technique. These methods use the daily average clutter echoes at lowest elevation scan to obtain cumulative distribution function (CDF) of combined precipitation and clutter reflectivity. Then looking at the stability of the CDF, the miscalibration of the system can be inferred for example monitoring the time variations of the 95th percentile of the CDF. An application of this statistical approach coming from a multiplicity of ground targets during clear-sky days to control the radar signal stability has been also proposed in [65] for a prototype of a X-band mini weather radar. More recently in [66] the role of the urban ground clutter has been tested for X-band and S-band radars to calibrate the reflectivity factor and the differential reflectivity on polarimetric radars. A similar methodology, but more accurate (since it introduces a separation of clear air and precipitation echoes using the whole radar clutter domain) has been proposed to me in [13] and presented in Section 4.2 for a C-band radar with the aim to monitoring the relative calibration of reflectivity and differential reflectivity factor. I have also developed a preliminary study presented in [14] and replaced in Section 4.3 that improve the Rinehart [60] approach.

4.2 WEATHER-RADAR RELATIVE CALIBRATION TECHNIQUE

Actually, a detailed spatial analysis of the ground-clutter might suggest that there exists “targeted clutter areas” more suitable for a robust implementation of the relative calibration strategy. On the other hand, a temporal analysis of such targeted clutter areas can be a very useful tool to estimate the relative calibration and evaluate its uncertainty. Indeed, the temporal monitoring of the variation of the calibration parameters aims at two goals: i) provide a synthetic and intuitive visualization of the relative calibration errors and ii) measure the uncertainty on such relative calibration errors using for example a moving window standard deviation on daily basis. Starting from the aforementioned considerations, this work focuses on the following three aspects: (1) apply a Bayesian classifier to identify the ground-clutter areas more suitable for calibration purposes [67]. A statistical analysis based on score indexes is carried out as well to have a degree of accuracy of the clutter identification performed; (2) present a statistical analysis of the targeted ground clutter areas in terms of Z_{hh} and Z_{dr} by applying an automated region merging algorithm [68]; (3) monitor

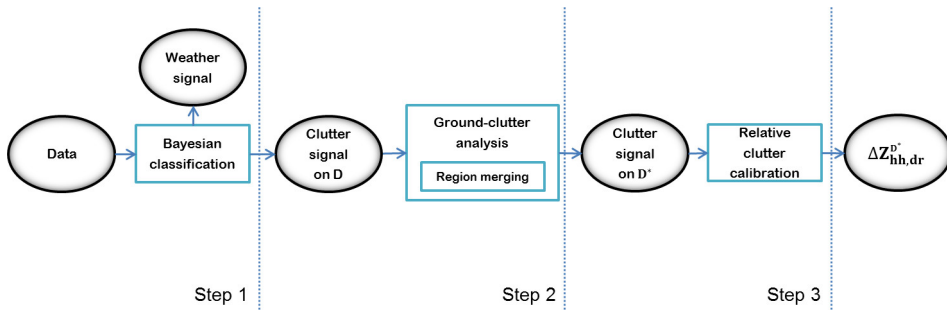


Figure 37: The overall algorithm to analyze the calibration status of a radar system is shown as detailed in Section 4.2.1. The block diagram starts with the weather radar data volume and ends in output with the relative calibration results for the co-polar reflectivity and differential reflectivity in the spatial region \mathbf{D}^* . The sub-domain \mathbf{D}^* is defined as a stable area in terms of standard deviation of the clutter distribution from the previous ground-clutter analysis as in Section 4.2.4.

the ground-clutter probability and cumulative distributions in terms of its statistical moments and specifically the mean and 95th percentile [62]. To accomplish the objectives proposed in this study, the radar-site of Petinascura (Cosenza, Calabria) in Southern Italy, which is part of the Italian weather radar network, is considered. This is one of the first works on the characterization of the ground-clutter applied to peculiar Italian complex orography scenario, whose orographic characteristics are dominated by coastlines and mountains [69, 70]. In Section 4.2.1 I define the overall approach together with the study area and available weather radar data. Section 4.2.3 is devoted to introduce the Bayesian classification and score indexes, whereas section 4.2.4 presents the region merging algorithm for ground-clutter spatial analysis and illustrates the results in terms of relative calibrations and uncertainty, based on the ground-clutter reference technique, and comparing it with respect to the well-established radar receiver calibration based on Sun monitoring.

4.2.1 Overall approach

Figure 37 shows the block diagram of the overall approach followed to use ground-clutter for monitoring a weather radar system in terms of its relative calibration. The relative calibration approach follows various steps:

1. The first step is aimed at separating the ground-clutter from the weather signal. A Bayesian classification is applied for this purpose. The output of this procedure is a real-time selection indicating the areas affected by clutter and those where hydrometeors are likely present in terms of probabilistic membership. The set of grid points within the radar domain affected by ground clutter is indicated by \mathbf{D} . A training data set extracted from measurements of Mt. Pettinascura radar is used to estimate the a priori and the likelihood probability density functions as specified after.
2. The second step is generally devoted to use the clutter signal in the domain \mathbf{D} , for monitoring the radar system performances. Two statistical moments of the ground clutter probability distribution, namely the mean value or the 95th percentile, are used to synthesize the information brought by the ground-clutter signature. The choice of consider these two statistical moments instead of the overall clutter distribution is made to have a more stable evaluation as will be clear later on. At this step I apply a ground-clutter spatial analysis based on a region merging approach to select different sub-domains of \mathbf{D} (hereafter indicated by \mathbf{D}^*). The region merging approach works in statistical terms using the cumulative distributions defined on spatial basis and its aim is to verify if there exist optimal sub domains, \mathbf{D}^* , which are more stable in terms of ground-clutter statistical parameters. The stability of the result is then evaluated using the daily temporal standard deviation, by assuming that the value of Z_{hh} or Z_{dr} at the grid points of stable clutter within \mathbf{D}^* should not vary significantly. The different results are evaluated using both the mean value and the 95th percentile index of the ground clutter probability distribution.
3. The last step is the numerical estimation of the relative calibration value for both radar observables, i.e. co-polar reflectivity $\Delta Z_{hh}^{\mathbf{D}^*}$ and differential reflectivity $\Delta Z_{dr}^{\mathbf{D}^*}$, using the most stable region domain \mathbf{D}^* derived from the previous step. The daily relative calibration index is computed using the mean value of the two radar observable statistics.

4.2.2 *System and data*

Weather radar network in Italy is mainly used to detect severe weather and related hydro-geological risks. The Italian orography, characterized by small catchments along most coastlines and by the Alpine and Ap-

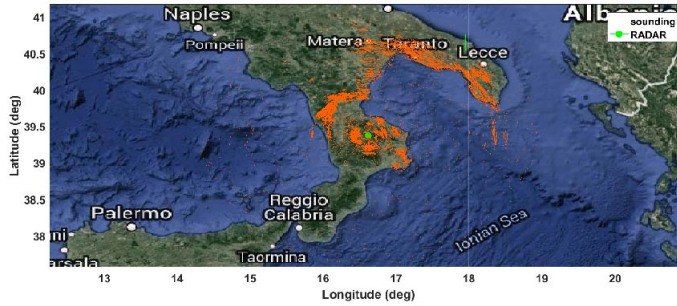


Figure 38: The clutter mask (red) shows the clutter scenario surround the radar-site of Mt. Pettinascura (green-point), the closest available radiosounding near Brindisi is also shown (green-cross). Background image from: Google Earth.

penine chains, increases the flood hazard especially during the fall season [69]. In the last years, many extreme rainfall events have highlighted the need of a real time monitoring system. In this scenario the presence of a complex-orography conditions heavily affects the quality of the retrieved radar products and estimation of the rainfall rate is more difficult [70]. For this study, I have considered the C-band dual polarization radar in Southern Italy along the Ionian sea, sited at Mt. Pettinascura (Cosenza, Calabria, Italy). At the basis of this work there is the idea to use the orography as a stable robust reference (“geographical constraint”) to estimate the relative radar calibration for the weather radar observables. The radar position is located at about 1705 m and is surrounded by the southern Apennines and the Sila mountain (Figure 38). The weather radar exhibits 1° for azimuth resolution as well as 150 and 100 m for the range resolution at slanted and vertical pointing, respectively. The radar system, having Doppler capacity, has different operation modes such as: radar single mode, radar dual h mode, radar dual v mode. The time sampling of the radar scan is 10 minutes and for each sampling time a polar volume, composed by 360° sectors for 11 elevation steps plus a vertical one, is acquired. The radar operates with a nominal wavelength of 5.3 cm and a pulse width, which varies from 1 μ s until the fourth elevation (3.5°) to 0.5 μ s until the eleventh elevation (15.99°), and 0.66 μ s at vertical incidence. This results in a variable range resolution which is sampled at 150; 75; 99 m, respectively.

Table 4: List of the data-set for the study acquired by the radar-site of Mt. Petrinascura on seven days every 10 minutes (first column). The second two columns present the number of hours in which the acquisition are interested respectively by clear air and meteorological data. The determination of clear-air and precipitation conditions are obtained by using the texture of the differential phase-shift along with a visual inspection of the data. The fourth column shows the freezing-level height (FLH) range as retrieved from the closest available radiosounding of Brindisi (Puglia, Italy) (Radiosonde Database - University of Wyoming), useful information for the Sun monitoring. The last column shows the number of daily acquisition at the first elevation interested by the solar interference.

Date	Clear air periods (UTC)	Meteo periods (UTC)	FLH (km)	Sun interf. (#)
1 August	20:00 – 23:50	00:00 – 20:00	3.6890	1
2 August	00:00 – 12:00 15:00 – 22:30	12:00 – 15:00 22:30 – 23:50	4.5045	1
3 August	14:00 – 23:50	00:00 – 14:00	4.5640	1
4 August	00:00 – 13:00 19:30 – 23:50	13:00 – 19:30	4.2495	2
5 August	00:00 – 12:00 22:00 – 23:50	12:00 – 22:00	4.7825	2
6 August	-	00:00 – 23:50	3.7800	1
7 August	-	00:00 – 23:50	3.8800	1

In this study I have selected the radar data acquired on seven days every 10 min in 2014 from the August 1 until August 7. The events are listed in Table 4 together with the number of hours in clear air and those interested by precipitation and, the freezing-level height (FLH) as derived from the closest available radiosounding observations of Brindisi (LIBR, Radiosonde Database - University of Wyoming) and the solar interferences (Solar Database - Commission geologique du Canada). The solar interference availability is included in Table 4 as well.

4.2.3 *Ground-clutter Bayesian classification*

In this section I introduce the Bayesian methodology used to perform the clutter identification. The Bayesian classifier segments the radar polar volume in terms of probabilistic membership for the two classes of meteo and clutter targets. In addition, the score indexes, such as critical

success index, the probability of detection and the false alarm rate, are individually analyzed to evaluate the classification performance as well as to find an optimal window size, needed to calculate the input quantities to run the Bayesian classifier. The results are shown separately at the end of this section.

Methodology

The statistical analysis of the observed radar measurements affected by ground clutter is the basis for our study and starts with the ground-clutter Bayesian classification to separate the clutter from the weather signal. The Bayes classifier has to be trained and for this reason I divide the entire data set, described in Table 4, in two parts consisting of a training and a test group of samples. The training data set consists of two days on August 1 and 2, 2014 and it contains both precipitation and clutter echoes whereas the test dataset includes the remaining days. From the training dataset I extracted the likelihood conditional probability distribution functions (PDFs), indicated as $p(\mathbf{x}|\mathbf{c})$, of a set n_R radar measurement $\mathbf{x} = [x_1 x_2 \dots x_{n_R}]$ for the class \mathbf{c} ($\mathbf{c} = 1$ for clutter echoes or $\mathbf{c} = 0$ for weather echoes). The term $p(\mathbf{x}|\mathbf{c})$ represents the conditional probability of the input radar measurement, \mathbf{x} , given the class \mathbf{c} . Note that in general the vector \mathbf{x} can have several number of components although in our case I will limit n_R to 3 as will be clear later on. The PDFs of the single l -th radar variables, $p(x_l, \mathbf{c})$, are then modelled using the generalized extreme value (GEV) distribution for all the raw radar variables, namely, the co-polar reflectivity, the differential reflectivity, the co-polar correlation coefficient, the differential phase shift, the radial Doppler velocity and the Doppler spectrum width, labelled as Z_{hh} , Z_{dr} , ρ_{hv} , Φ_{dp} , V_D and W_D , respectively previously defined in Sections 2.1.3 and 2.4.2. These distributions are shown in Figure 39 and 40. The PDF for the GEV distribution with location parameter μ , scale parameter σ and shape parameter $k \neq 0$ is defined as in [71]:

$$p(x_l|\mathbf{c}; k; \mu; \sigma) = \frac{1}{\sigma} \exp \left[- \left(1 + k \frac{x_l - \mu}{\sigma} \right)^{-1/k} \right] \left(1 + k \frac{x_l - \mu}{\sigma} \right)^{-1-1/k} \quad (132)$$

Assuming $(1 + k(x_l - \mu)/\sigma) > 0$, the condition $k > 0$ corresponds to the Type II case, while $k < 0$ corresponds to the Type III case whereas $k = 0$ indicates the Type I case. The GEV distributions are introduced in order to implement the naïve Bayes classifier. The term “naïve” is inspired by the fact that the likelihood conditional PDF is not described by a multivariate Gaussian distribution as typically done in Bayesian implementations to

simplify the theoretical formulation, but instead, by a product of single normalized PDFs:

$$p(\mathbf{x}|\mathbf{c}; k, \mu, \sigma) = \prod_{l=1}^n p(x_l|\mathbf{c}; k, \mu, \sigma) \quad (133)$$

under the hypothesis that the input radar measurements x_l are independent. An advantage of naïve Bayes is that it only requires a small number of training data to estimate the parameters necessary for classification. In my study, the naïve Bayesian classifier foresees three input measurements: the standard deviation of differential reflectivity, differential phase-shift and co-polar correlation coefficient [67]. The normalized conditional PDFs, $(x_l|\mathbf{c} = 1)$ and $(x_l|\mathbf{c} = 0)$ with $l = 1, 2, \text{ or } 3$, are shown in Figure 39 for the training dataset of our case of study in black and red curves for ground clutter and meteo-targets, respectively. The normalization is performed with respect to the probability value of the statistical mode of each density distribution. The formulation of the naïve Bayesian classifier assumes that all input measurements are spatially independent and is given by:

$$p(\mathbf{c}|\mathbf{x}) = \frac{p(\mathbf{c})p(\mathbf{x}|\mathbf{c}; k, \mu, \sigma)}{p(\mathbf{x})} = \frac{p(\mathbf{c}) \prod_{l=1}^{n_R} p(x_l|\mathbf{c}; k, \mu, \sigma)}{\prod_{l=1}^{n_R} p(x_l|\mathbf{c}; k, \mu, \sigma)} \quad (134)$$

where $p(\mathbf{c})$ is the a-priori probability of the class \mathbf{c} and it is assumed to be the same for clutter and precipitation ($p(\mathbf{c}) = 0.5$) and $p(\mathbf{x}) = \prod_{l=1}^{n_R} p(x_l|\mathbf{c}; k, \mu, \sigma)$ under the assumption of independent radar variables. The classification result is obtained using an argument-maximum rule (modal value of the PDF) applied on the naïve Bayes metrics for each position $\mathbf{s} = (i, j)$ and each time frame t :

$$\tilde{\mathbf{c}}(\mathbf{s}, t) = \operatorname{argmax}_{\mathbf{c}=0,1} \left[p(\mathbf{c}) \prod_{l=1}^3 p(x_l(\mathbf{s}, t)|\mathbf{c}) \right] \quad (135)$$

where I introduced the space and time dependency and the predicted class $\tilde{\mathbf{c}}(\mathbf{s}, t)$ corresponds to the highest posterior probability. Note that when applying equation (135) on actual radar measurements, the input quantity $x_l(\mathbf{s}, t)$ is dynamically evaluated for each time frame on moving windows covering the whole radar domain and centered, at each visiting step, on positions \mathbf{s} . It is worth mentioning that the Bayes classifier is strictly dependent on the size of the spatial-moving windows applied. To define the optimal size of these windows I have used an optimization step using the score indexes as I will discuss in more detail in the following section. Another aspect to highlight in equation (135) is that while the term $x_l(\mathbf{s}, t)$ is

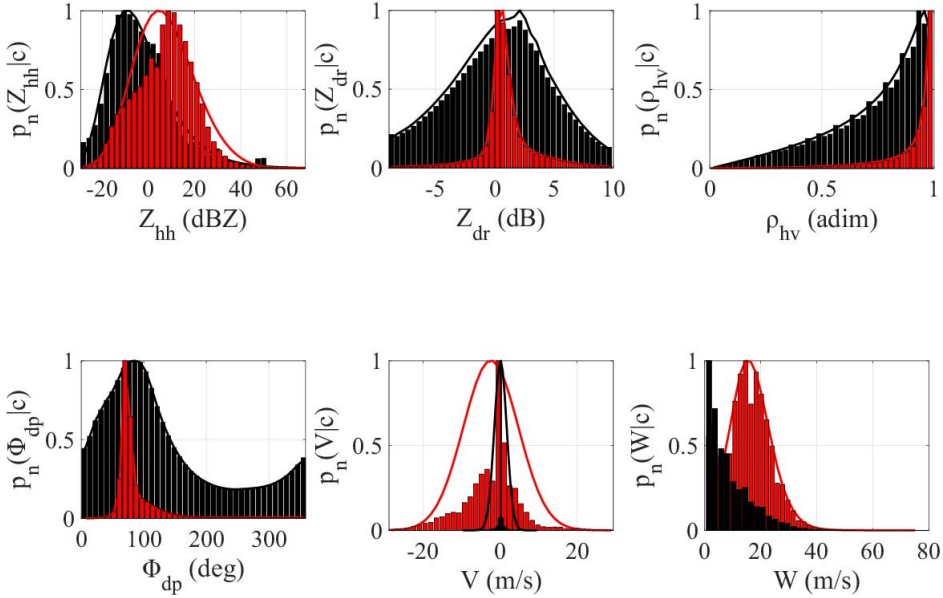


Figure 39: Normalized spatial and temporal PDFs for precipitation (red) and clutter (black) for the 0.5° elevation, 1 μ s pulse-length, 750 Hz PRF, 360° scans and 5 rpm obtained on data from 1 to 2 August. The bars represents the data selected in precipitation (red) and clutter (black), and the line represents the GEV-approximation. The method used to separate precipitation and clutter is a basic filter on the texture of the differential phase improved with the visual inspection of the data.

dynamically updated at each time step, the conditional probability functions, p , are fixed and defined from the analysis of the training dataset. At the end of the Bayesian procedure, once defined the terms $p(\mathbf{c})$ and $p(\mathbf{x}|\mathbf{c})$ on a training dataset, I have two dynamical maps ($M_{\tilde{c}}$) corresponding to the clutter ($\tilde{c} = 1$) and to the weather signal ($\tilde{c} = 0$), respectively:

$$M_{\tilde{c}}(\mathbf{s}, t) = U_{\mathbf{s}}\tilde{c}(\mathbf{s})|_{\tilde{c}}. \quad (136)$$

Score indexes and results

The dynamical clutter map obtained for each time frame applying the described Bayes classifier is validated on the test dataset by using some performance indexes, namely: the critical success index (CSI), the probability of detection (POD) and the false alarm rate (FAR) as a measure of classification results. The reference clutter map used as ground-truth for

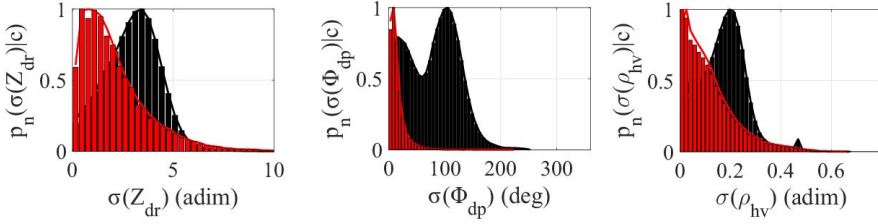


Figure 40: Precipitation (red) and clutter (black) normalized PDFs at the 0.5° elevation for the Bayes classifier, from left the standard deviation of, respectively, differential reflectivity, differential phase shift and co-polar correlation coefficient obtained on data from 1 to 2 August.

the validation of the Bayes classifier is a deterministic clutter mask obtained with the average of Z_{hh} for one-month of data acquired earlier. The definition of the performance indexes used is :

$$\text{CSI} = \frac{H}{H+M+F} \quad (137)$$

$$\text{POD} = \frac{H}{H+M} \quad (138)$$

$$\text{FAR} = \frac{F}{H+M} \quad (139)$$

where H, F and M stands for the number of Hit (event observed and predicted), False (event not observed but predicted), Miss (event observed but not predicted). The CSI score is a valid indicator of the relative worth of different forecast techniques when they are applied to the same environment and is very useful to validate the Bayes classifier [72]. I use, as a validation data set, five days on August 3-7, 2014, from the data in Table 4 to calculate the performance scores of the classification, CSI, POD and FAR, that are summarised in Table 5. The indexes are calculated on the entire validation data set, and the resulting values in Table 5 refer to daily means. One of the most critical aspect of the Bayesian classification is the size of the spatial moving windows in which the standard deviation of the input radar variables are calculated (i.e. the $x_1(\mathbf{s}, t)$ in equation (135)) thus allowing the definition of the probability density functions ($p(x_1(\mathbf{s}, t)|\mathbf{c})$). I have used the performance scores, calculated testing various size of the spatial windows, to set their optimal value. Indeed, the results are shown for three different spatial windows where I can apply the Bayesian classification. The score indexes indicate that the use of a 5×5 spatial window provides the best results for our analysis. Figure 41 shows an example, before and after the Bayesian classification, for a single time step of the analysed event where the proposed Bayesian classifier is able to discriminate between weather signals and ground-clutter even where they appear

Table 5: By using the deterministic clutter mask as a reference for the dynamical clutter map, obtained from the Bayesian classification, I give you the CSI, POD, FAR results shown in the table for three different windows size. The performance indexes are defined in Section “Score indexes and results” through equations (139). The spatial-window is the critical parameter for the Bayesian classification and has been tested for three different sizes (3×3 ; 5×5 ; 7×7) shown in the first left column of the table. The optimal window correspond to the 5×5 size in which the best performance indexes are obtained.

		3 Aug 2014			4 Aug 2014			5 Aug 2014			6 Aug 2014			7 Aug 2014		
		CSI	POD	FAR												
Window Size	3x3	0.79	0.98	0.19	0.87	0.98	0.12	0.84	0.98	0.14	0.79	0.93	0.17	0.85	0.97	0.13
	5x5	0.82	0.98	0.17	0.87	0.99	0.12	0.86	0.97	0.12	0.81	0.92	0.14	0.87	0.97	0.12
	7x7	0.71	0.99	0.28	0.86	0.99	0.13	0.80	0.99	0.19	0.72	0.97	0.27	0.81	0.99	0.19

to be superimposed. This result is significantly better than the common one obtained using a deterministic clutter map [67] where a given grid-point can be classified as ground clutter or as meteo-target without the possibility to quantify the degree of coexistence of the two classes at the same location.

4.2.4 *Ground-clutter spatial analysis and calibration*

In this section I first present the formulas for the characterization of ground-clutter relative calibrations. The second part shows the ground-clutter spatial analysis by using the region-merging algorithm in which clutter areas are divided into statistically stable sub-regions that share consistent statistical distributions. Finally, the results of the relative calibration with conventional approaches (i.e. using the whole unpartitioned domain) and the proposed approach (using the statistically-stable sub-regions) are discussed. Note that, as an indirect validation, I also compare the overall proposed approach with the results obtained from the Sun-interference technique.

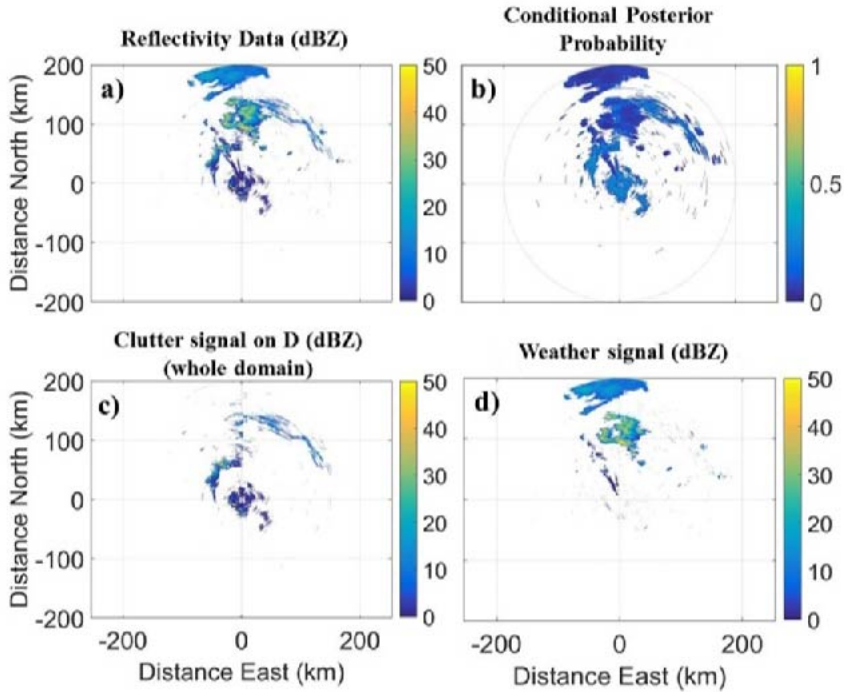


Figure 41: Case of study of the 5 August 2014 at the 17:10 UTC shown for the co-polar reflectivity Z_{hh} time frame: a) before and c, d) after the application of the Bayesian classification (c for the clutter signal on the whole domain \mathbf{D} and d for the weather signal); in (b) the conditional posterior probability that is the argument of equation (134).

Characterization of ground-clutter relative calibration

The radar ground-clutter relative calibration can be defined as the temporal difference between statistical moments of co-polar reflectivity ($m_{Z_{hh}}$) or differential reflectivity ($m_{Z_{dr}}$) selected in the whole spatial domain of clutter echoes (indicated by \mathbf{D}), between two verification periods at time t and $t - 1$:

$$\Delta m_{Z_x}^{\mathbf{D}}(t) = m_{Z_x}^{\mathbf{D}}(t) - m_{Z_x}^{\mathbf{D}}(t - 1) \quad (140)$$

In equation (140) $m_{Z_x}^{\mathbf{D}}(t)$ is a statistical moment of Z_x in the domain \mathbf{D} where the subscript “ x ” stands for “ hh ” or “ dr ”, indicating the co-polar or the differential reflectivity, respectively. The two moments considered for

the ground-clutter characterization are the mean and the 95th percentile: $m_{Z_x}^D = \bar{Z}_{Z_x}^D$, $m_{Z_x}^D = 95Z_x^D$, respectively. They are defined as follows:

$$m_{Z_x}^D = \begin{cases} 95Z_x^D(t) & \text{where } 0.95 = \int_0^{95Z_x^D(t)} p(Z_x(t)|\mathbf{D})dZ_x(t) \\ \bar{Z}_{Z_x}^D(t) & \text{where } \bar{Z}_{Z_x}^D(t) = \int_0^\infty Z_x(t)p(Z_x(t)|\mathbf{D})dZ_x \end{cases} \quad (141)$$

I note that the use of equation (140) leads to a relative calibration by the difference of value and not to an absolute calibration such as those obtained, for example, by the Sun monitoring. In the next section I will describe how the selection of the clutter domain \mathbf{D} can be critical for a meaningful implementation of relative calibration through equation (140).

Ground-clutter analysis by region merging

After the identification of the domain \mathbf{D} (i.e. the set of grid point positions affected by the clutter within the whole radar covered domain) by means of the Bayesian classifier, I can spatially characterize the statistical distributions of Z_{hh} and Z_{dr} affected by ground clutter. However, this is not accomplished in the whole domain \mathbf{D} but, instead, in some subdomains of \mathbf{D} that need to be automatically and objectively identified, in order to find more stable sub-regions in terms of clutter statistical distribution. This step is important to avoid confusing the fluctuations of the intrinsic clutter echoes (for example due to changes in the state of the vegetation covering the clutter source or to changes linked to environmental factors) with variations that are attributable to the radar system deterioration. The selection of the sub-domains of \mathbf{D} , characterized by a stable ground-clutter PDFs and labelled as \mathbf{D}^* , is objectively accomplished using the region merging algorithm [68]. The region merging algorithm takes in input the dynamical clutter map in the domain \mathbf{D} obtained using the Bayes classifier for each time frame within the training dataset and gives as output a subdomain \mathbf{D}^* (consisting of sub-regions not necessarily connected each other, i.e. with no intersections). The subdomain \mathbf{D}^* has the property to show values of reflectivity with a smaller fluctuation than those in the whole domain \mathbf{D} . In a word, the domain \mathbf{D}^* is expected to include grid points which show a more stable clutter PDFs. The basic idea of the region merging algorithm is to identify homogeneous ground clutter areas in terms of probability density distributions of $p(x_1(s, t)|c, k, \sigma, \mu)$ defined in equation (132) where k, σ and μ are the shape, scale and location parameter of a GEV distribution of the radar derived quantity: x_1 . The region-merging algorithm follows several steps:

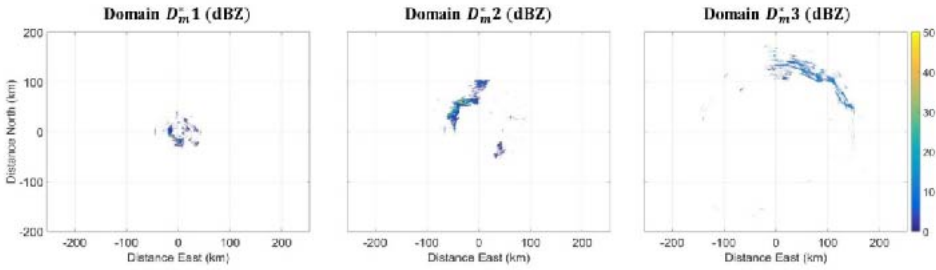


Figure 42: Case of study of the 5 August 2014 at the 17:10 UTC after the application of the Bayesian classification and region merging in which I obtain three clutter maps (in co-polar reflectivity) for three clutter sub-regions selected on spatial base from left to right: " D_m^*1 ", " D_m^*2 ", " D_m^*3 ", respectively.

- Select an initial squared sub-region of ground-clutter such that at least 10×10 samples are available and calculate the GEV distribution parameters (shape k , scale σ , and location parameter μ) of $p(x_l(s, t) | c, k, \sigma, \mu)$ defined in equation (132);
- Moving the squared sub-region neighboring (with at least 5×5 samples) where I compute its GEV distribution parameters and then their Euclidean distance from the GEV distribution parameters obtained for the first sub-region defined at step 1;
- Impose a tolerance threshold on the Euclidean distance defined at step 2 to decide when two sequential sub-regions must be merged or split. In our case, this threshold is set to 0.5. The sub-regions whose distance is below this tolerance threshold are separated by an edge otherwise they are merged;
- Iterate the steps (2) and (3) till the whole clutter map is completely covered that is, the iterations have explored the whole spatial domain D .

After the identification of the sub-regions for each analyzed clutter map in the training dataset by running steps 1-4 above mentioned, I identified the minimum clutter sub- regions (D_m^*), which is common to all the available time sequence of the clutter maps. For my case studies, the region-merging algorithm has identified three different sub-regions or domains: D_m^*1 , D_m^*2 and D_m^*3 . As an example, Figure 42 shows these three domains D_m^*j and $j = 1, 2$ and 3 which are defined considering the data on 3 August 2014 in terms of Z_{hh} , whereas Figure 43 shows the different experimental probability distribution functions for the same regions. The same sub-regions have been tested for the differential reflectivity proving also

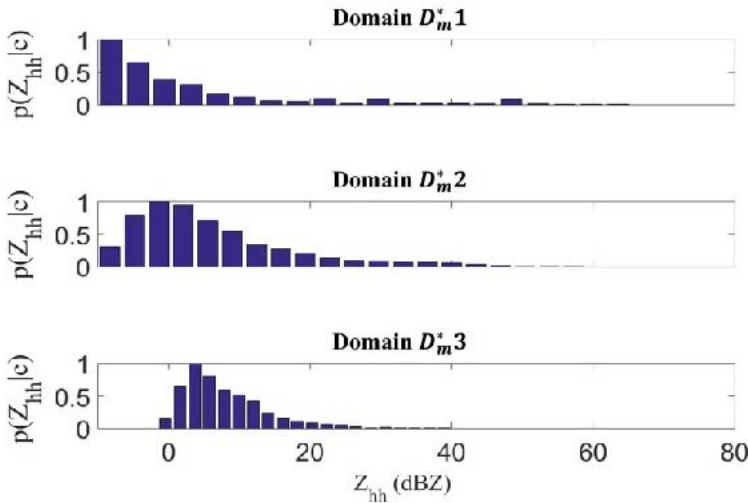
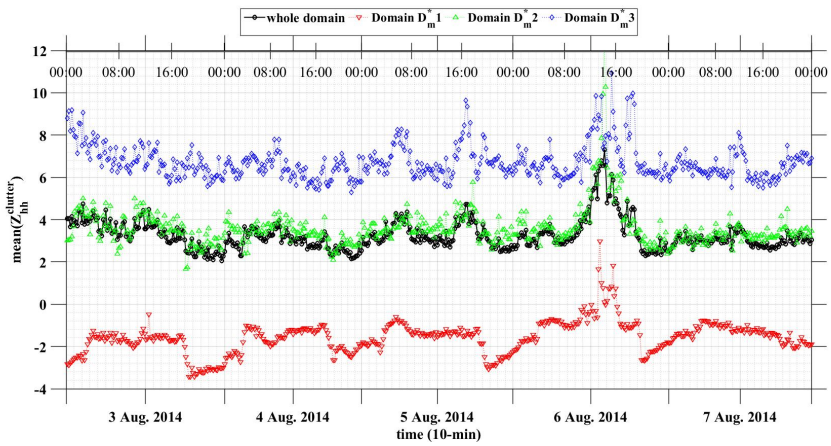
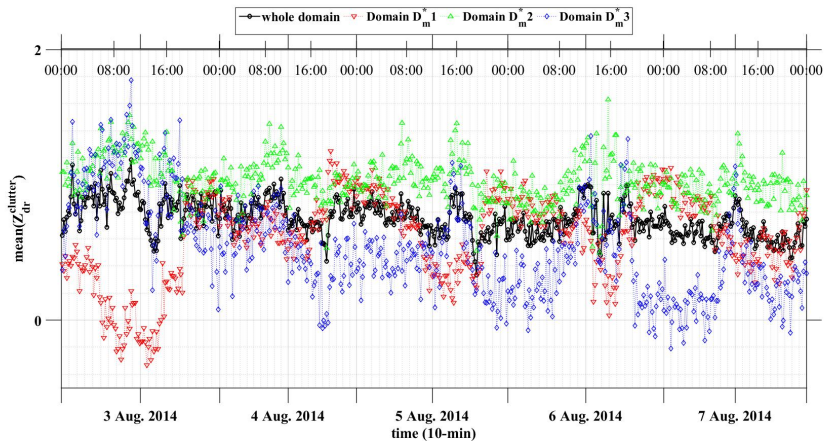


Figure 43: The normalized PDFs of the three clutter sub-regions selected on spatial base. The parameters of this GEV distributions are shape parameter k , scale parameter σ , and the location parameter μ . I describe the first zone with $k = 0.6837$, $\sigma = 5.2009$, $\mu = -5.5193$, the second zone with $k = 0.1773$, $\sigma = 7.0187$, $\mu = 0.2347$ and the last zone with $k = 0.1396$, $\sigma = 3.8257$, $\mu = 4.9951$. The results are presented only for the co-polar reflectivity because the region merging shown three stable regions for the co-polar reflectivity and no stable regions for the differential reflectivity.

in this case a more stable trend. In order to find the domains in D^* which are more stable in terms of clutter statistic of Z_{hh} and Z_{dr} I can analyse the temporal trend of the statistical moments referred to the 95th percentile and the mean values of Z_{hh} and Z_{dr} . They are labelled as $95Z_{hh}^D$ and $95Z_{dr}^D$ and \underline{Z}_{hh}^D and \underline{Z}_{dr}^D , respectively where D_m^*j , in this case, coincides with one of the three domains. The temporal trends of the mean value of the probability distribution for the co-polar reflectivity and differential reflectivity are shown in Figure 44 whereas those of 95th percentile of the cumulative distribution are shown in Figure 45. Both figures show also the temporal trends of the statistical moments when the whole domain D is considered. Reasonably, I can expect the value of each statistical moment in Figures 44 and 44 to be relatively stable on daily basis. Following this consideration, I identify the areas which show the more stable clutter signature by looking at the lowest daily standard deviation in each of the D_m^*j domains. In this respect, Tabs. 6-7 show the standard deviation (s) of

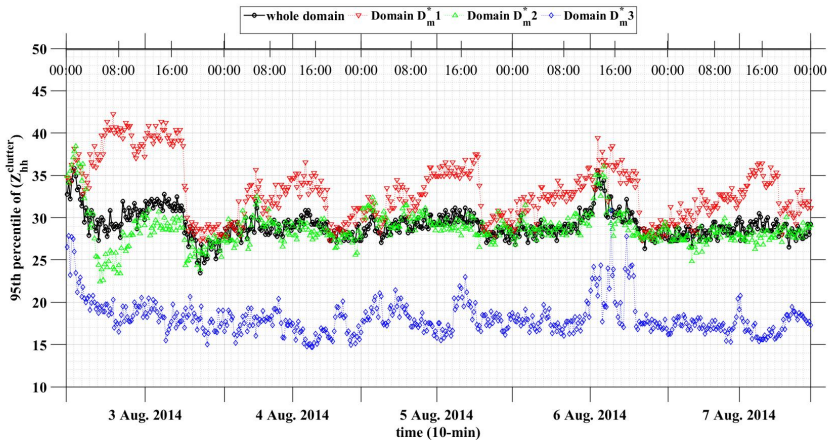


(a)

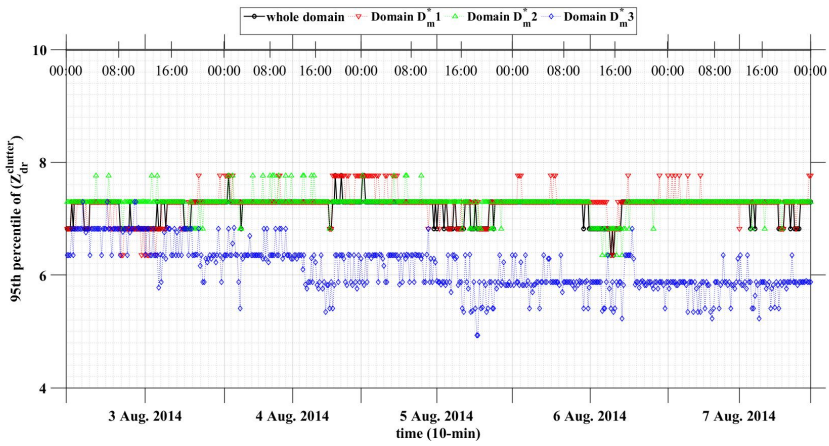


(b)

Figure 44: Temporal trend of acquisition of the mean value of the probability distribution for the co-polar reflectivity (a) and differential reflectivity (b).



(a)



(b)

Figure 45: Temporal trend in time of acquisition of the 95th percentile of the cumulative distribution for the co-polar reflectivity (a) and differential reflectivity (b).

the quantities $Z_{hh}^{D_m^*j}$, $Z_{dr}^{D_m^*j}$ (in Tab. 6) and $95Z_{hh}^{D_m^*j}$, $95Z_{dr}^{D_m^*j}$ in (in Tab. 7) as well as those referred to the whole domain \mathbf{D} .

From these tables, it emerges that the lowest standard deviation is found for domain \mathbf{D} when considering Z_{dr} (look at the lowest standard deviation $s(Z_{dr}^{\mathbf{D}})$ in Tab. 7), whereas in terms of Z_{hh} the lowest standard deviations are found for first sub-region domain, (look at the lowest values of $s(Z_{dr}^{D_m^*1})$ in Tab. 7). This result indicates that areas around the radar system, i.e. those in the domain are more suitable to calibrate the co-polar reflectivity, Z_{hh} , whereas the whole domain \mathbf{D} can be efficiently used to calibrate the differential reflectivity Z_{dr} . The comparison between Tables 6 and 7 highlighted that the standard deviations associated with the mean value statistical parameter (Tab. 6) are lower than those associated to the 95th percentile. Note that, considering that 1 dBZ and 0.1 dB are the typical limits for the estimated precision of the calibration techniques [6], a fluctuation of the same amplitude makes unsuitable the 95th percentile for this purpose.

One of the interesting aspects of this analysis is the possibility to use different domains to analyse the various radar observables, such as in this case. A deeper analysis of the considered dataset also shows that in the whole domain and in the sub-domain the trend of the standard deviation increases during the day and decreases during the night (see Figure 44). This interesting aspect, more visible in the stable first sub-domain, \mathbf{D}_m^*1 (Figure 44a), can be due to ground-clutter induced by anomalous propagation occurring as a result of nocturnal radiative cooling [73]. Further future investigations will be useful to establish this tendency. Concerning the statistical parameter, the mean value of the probability distribution is preferable to the 95th percentile value being it much more variable (based on Tabs 6-7 and also on Figs. 44 and 45). This means that in the overall approach I can use equation (140) applied to the three identified stable sub-domains \mathbf{D}_m^*j .

Relative calibration results

The final result of the overall approach, illustrated in Figure 37, is listed in Table 8 in terms of relative calibration values for Z_{hh} and Z_{dr} and its uncertainty. These results are expressed as a temporal average of the differences on sequential days following equation (141). Tab. 8 also compares my results with the absolute receiver calibration value obtained by means of the Sun-monitoring approach [59]. Note that the latter provides an absolute calibration as opposed to a relative calibration so that they should

Table 6: Standard deviations for the co-polar reflectivity and differential reflectivity of the ground-clutter sub-regions D_m^*1 , D_m^*2 , D_m^*3 and the whole clutter scenario D using the mean value statistical parameter. The clutter domain D is basically the dynamical clutter map for each instant within the training dataset as defined in Section “Ground-clutter analysis by region merging”. The subdomains D_m^*1 , D_m^*2 , D_m^*3 are sub-regions not necessarily connected, output of the region merging algorithm that have more stable clutter PDFs inside it.

	3 Aug 2014		4 Aug 2014		5 Aug 2014		6 Aug 2014		7 Aug 2014	
	$s(\bar{Z}_{hh})$	$s(\bar{Z}_{dr})$								
D	0.6570	0.1324	0.4196	0.1111	0.5372	0.1156	1.1517	0.1207	0.2611	0.0940
D_m^*1	0.5958	0.3881	0.4111	0.1858	0.4981	0.2772	0.7883	0.2388	0.2457	0.2127
D_m^*2	0.7036	0.1710	0.4852	0.1433	0.5140	0.1532	1.6153	0.1849	0.3346	0.1176
D_m^*3	0.7881	0.3215	0.5243	0.2485	0.7650	0.2355	1.1024	0.3281	0.5218	0.2477

Table 7: Standard deviations for the co-polar reflectivity and differential reflectivity of the ground-clutter regions D_m^*1 , D_m^*2 , D_m^*3 and the whole clutter scenario D using the 95th percentile statistical parameter. The definitions of the domain D and sub-domains is in Table 6.

	3 Aug 2014		4 Aug 2014		5 Aug 2014		6 Aug 2014		7 Aug 2014	
	$s(\bar{Z}_{hh})$	$s(\bar{Z}_{dr})$								
D	0.6570	0.1324	0.4196	0.1111	0.5372	0.1156	1.1517	0.1207	0.2611	0.0940
D_m^*1	0.5958	0.3881	0.4111	0.1858	0.4981	0.2772	0.7883	0.2388	0.2457	0.2127
D_m^*2	0.7036	0.1710	0.4852	0.1433	0.5140	0.1532	1.6153	0.1849	0.3346	0.1176
D_m^*3	0.7881	0.3215	0.5243	0.2485	0.7650	0.2355	1.1024	0.3281	0.5218	0.2477

Table 8: Absolute and relative calibrations for the co-polar reflectivity and for the differential reflectivity. All values in the table are in dB.

	3 Aug 2014		4 Aug 2014		5 Aug 2014		6 Aug 2014		7 Aug 2014	
	Z_{hh}	Z_{dr}								
Clutter Daily Difference #= CDD	0	0	0.3511	-0.0568	0.6302	-0.0521	0.0581	0.0044	0.0581	-0.0854
Sun Daily Difference #= SDD	0	0	0.3154	0	0.5213	0.07	0	0	0	0
Sun Absolute Calibration #= SAC	0.0462	0.53	0.3616	0.53	0.8829	0.6080	0.8829	0.6080	0.8829	0.6080

be carefully used by looking at the daily differences (and not as absolute values). For clarity, the absolute calibration gives an estimate of the value of the miscalibration whereas the relative calibration measures the loss of calibration in time as a differences between two temporal measurements. Table 8 shows the Sun absolute calibration (indicated as SAC), the Sun daily differences (indicated as Sun Daily Difference SDD) compared with the Ground-clutter daily differences (indicated as Clutter Daily Difference CDD). The starting value for the relative calibration on the first day (3 August 2014) is zero because 1-2 August 2014 have been used to train the Bayesian classifier (see section "Ground-clutter Bayesian classification"). From Table 8 I show that the relative calibration values for the differential reflectivity have little temporal variations and this feature is confirmed by the absolute Sun monitoring values. The relative calibration values for the co-polar reflectivity have a much bigger variation and agree with the Sun monitoring. The residual error between Sun-interference and clutter-based calibration may be due to the miscalibration of the radar transmitting part, which is taken into account only in the ground-clutter based results. The Sun-interference calibration extracts only the radar receiver miscalibration because the system is considered as a passive monitoring of Sun radiation. On the other hand, the clutter-based calibration considers the whole system evaluating the sum of the transmitter and the receiver miscalibration. The reference works for the clutter-based relative calibration [62, 64, 74] focused their efforts in the evaluation of long temporal trend of calibration values obtained by using the whole clutter domain. The uncertainty on the estimated calibration values was not taken into account in this work. As a matter of fact the standard deviation of these daily temporal trend of the calibration values was guaranteed around 10 dB for the reflectivity. Then an important result of our statistical analysis for the clutter-based relative calibration is also the result in terms of uncertainty, as shown in Table 6. This uncertainty is computed as the standard deviation of daily temporal trend of the calibration values (see Figs. 44 and 45). The estimated uncertainty is not exceeding 1 dBZ and 0.1 dB for Z_{hh} and Z_{dr} respectively [6]. These values are in agreement with upper limit needed for an accurate estimation of precipitation intensity and hydrometeors classification.

4.3 PERMANENT SCATTER ANALYSIS (PSA)

The most limiting aspect of all these statistical approaches is the accuracy of the miscalibration that exceeds in practical cases the value suggested in literature of 1 dBZ and 0.1 dB, respectively for reflectivity and differential

reflectivity [6]. To this aim I want preliminarily investigate the feasibility of using the single permanent scatterers methodology for polarimetric weather radar calibration, as proposed in [60] for individual target return, and to investigate their optimal exploitation and characterization.

To this goal, I have considered in Section 4.3.1 a radar scenario shown in Figure 46 where the single permanent scatterer is a periodic structure of metallic grids, whose features are interesting in terms of stable returns of reflectivity factor and having a differential reflectivity near to zero. Results of the calibration are presented by using one day of measurements for a C-band polarimetric radar in Section 4.3.2. The calibration of the differential reflectivity has validated applying also a well-known literature technique based on observations at vertical incidence [57]. In Section 4.3.3 A full-wave analysis implemented on a commercial code is used for the electromagnetic (EM) characterization of the permanent scatterer and to explain the behavior of the experimental data.

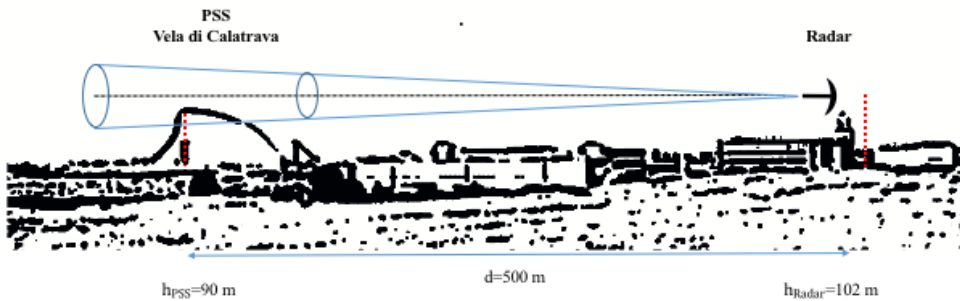


Figure 46: Radar clutter scenario considered: C-band Doppler dual-polarization Polar 55C located South-East of Rome (Italy) and the permanent scatterer used for the study, that is named Vela di Calatrava.

4.3.1 Radar scenario

Radar system

In this analysis I have considered the coherent C-band Doppler dual-polarization Polar 55C located 20 km South-East of Rome (Italy) and installed at a height of 102 m (see Figure 46). The system operates with a polarization agility and single-receiver scheme. For the transmission,

the total power is alternately transported by the horizontal- and vertical-polarized signals by using a pulse-to-pulse basis. The transmitter can operate with three pulse lengths (0.5, 1.5 and 3.0 s) at three corresponding PRFs (1200, 600 and 300 Hz). The alternate reception of the horizontal- and vertical-polarized components guaranteed by a switch.

The powerful of this polarization agility is reflected directly on the high quality of the dual-polarization variables. The corrugated horn antenna illuminates an off-set fed paraboloid with a diameter of 4.57 m and a beam-width respectively of 0.92° and 1.02° in azimuth and elevation. The single off-set geometry together with the avoiding of the radome increases the cross-polarization level and avoids problems related to beam-blocking by antenna struts. The stable expected behavior of the dual-polarization variables makes this radar system a perfect candidate for calibration studies. The reference in [75] illustrates in more details the development of Polar 55C and its many characteristics [76].

Radar scatterer

I define a permanent single scatterer (PSS) as an object that, although with considerable size, partially occupies the pulse volume of the radar within the beam. This definition is clearly different from a typical object, observed by a meteorological radar, that is a weather distributed scatterer (WDS) which likely fills the beam completely.

For this study I take in consideration a PSS, named "Vela di Calatrava" (see Figures 46 and 47), that is a periodic structure of metallic grids devised as a swimming stadium for an ideal City of the Sports in Rome, Tor Vergata, with a design by Santiago Calatrava [77]. The horizontal dimension, occupied by the structure, is of 180 m x 120 m with a height between 90 m and 97 m above the sea level. The PSS is composed by a periodic set of metallic square panels with diagonal intersections, as better highlighted in Figure 47.

The Vela di Calatrava structure is located 500 m from the radar-site, in the near-field region of the radar antenna since the Fraunhofer far-field distance is 779.7 m (derived from $r_f = 2(d_a a^2)/\lambda$, being d_a the diameter of the antenna previously defined in Section 4.3.1). More details about the structure can be found in [77]. Note that, even though the Vela di Calatrava is quite unique in its architecture, its frame characteristic could not be so difficult to be found in other similar buildings around the world. In this respect, the analysis presented later on can be useful to address a more general methodology for radar calibration.



Figure 47: The considered PSS, Vela di Calatrava (Rome, Italy), is shown. Background image from Google Earth.

4.3.2 Calibration: a case study

A challenging case study has been chosen with the aim to test preliminarily the calibration also in presence of heavy precipitation and check for the technical problems related to the antenna. The 14th October 2015 has been selected looking at a day in which a persistent perturbation coming from the South-West with respect to the radar-site and occupying the whole plan position indicator (PPI) at the first elevations [76]. Furthermore, a de-pointing problem was expected on the 75th daily-time index due to some antenna alignment issues caused by strong winds occurred on the analysed day.

In Figure 48 I show the temporal evolution of the reflectivity factor Z_{hh} in dBZ at the range gate that intercepts the Vela di Calatrava for the whole daily-dataset acquired every 5-minutes at lowest elevation scans. As expected, the return signal from the Vela di Calatrava PSS is very stable. Moreover, an optimal check of the de-pointing problem is very simple to verify by considering the sudden variation of the return signal. What I can quantify from Figure 48 is the relative calibration, i.e. the loss of calibration in time as a differences between two temporal measurements [13] and the degree of the antenna de-pointing occurred around the 75th time index.

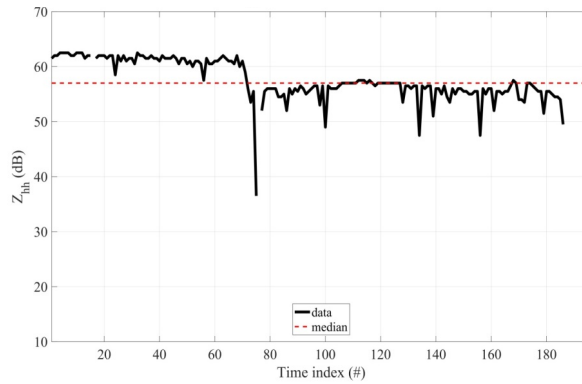


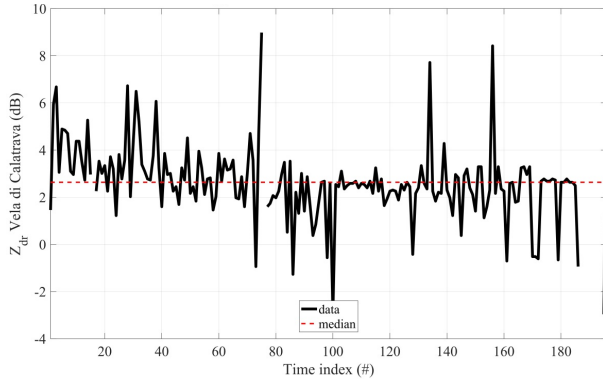
Figure 48: Monitoring of the reflectivity factor (Z_{hh}) looking at the PSS (Vela di Calatrava) on the 14th October 2015. A de-pointing is clearly visible around the 75th daily-time index.

An even more interesting behavior is given by looking at the temporal evolution of the differential reflectivity Z_{dr} in dB, shown in Figure 49a. In fact, comparing Figure 49a with the well-known technique of absolute calibration, obtained considering the vertical measurements in ice or light rain [57], in Figure 49b, I obtain the same median value for the two techniques. The differential reflectivity looking at the PSS shows a median value on daily-bases equal to 2.63 dB with a standard deviation of 1.61 dB. For what concerns the vertical profile, the median value is equal to 2.68 dB with a standard deviation of 0.14 dB.

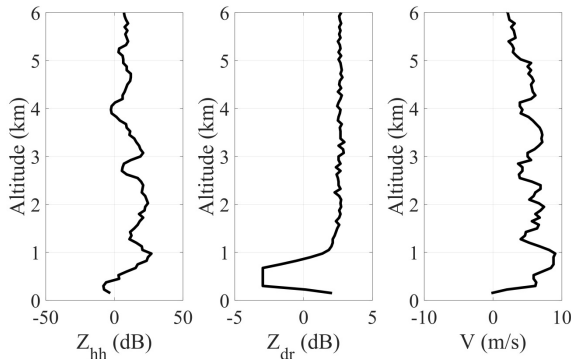
The first experimental observation on the median value shows that a PSS might be a good candidate to make an absolute calibration and estimate the value of the miscalibration for the differential reflectivity [13]. But a further aspect to be investigated is the standard deviation of Z_{dr} and the reason why its value is so high when looking at the PSS. To complete this analysis, a numerical simulation of the PSS behavior is considered by employing a full-wave commercial tool, as discussed in the following section.

4.3.3 Results of Electromagnetic Simulation

Numerical results are presented to complete the dual-polarization EM characterization of grid-framed PSS. The considered PSS is, as said, a periodical structure composed by metallic square grids with diagonal intersections (see Figure 50). I have tested the analysis for a $4\lambda \times 4\lambda$ element of



(a)



(b)

Figure 49: Monitoring of the differential reflectivity Z_{dr} on the 14th October 2015: (a) looking at the PSS (Vela di Calatrava); (b) looking at the vertical profile in ice above the radar (as in [57]) where V is the falling velocity in m/s.

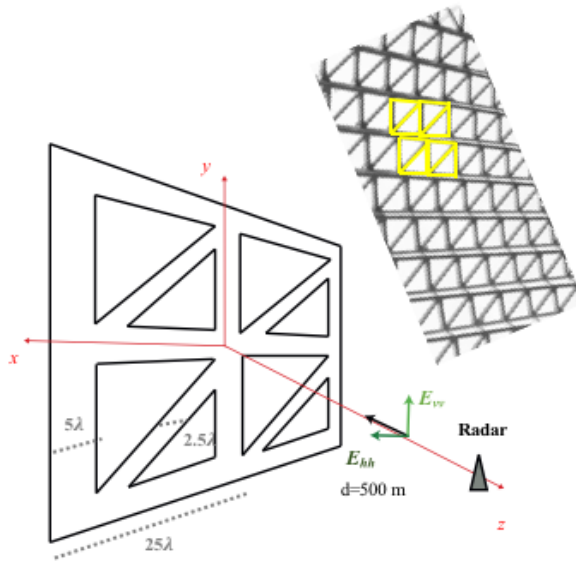


Figure 50: Geometry of the EM scenario represented by the PSS "Vela di Calatrava" element in the full-wave tool.

a structure having scaled dimension of $25\lambda \times 25\lambda$, a square-edge of 5λ and a diagonal-edge of 2.5λ (being the carrier wavelength equals to approximately 0.05 m for a C-band radar). The $4\lambda \times 4\lambda$ element is defined as a PEC material immersed in the free space. The dual-polarized behavior of this element has been analyzed by considering a plane-wave illumination. This assumption can be considered valid because the PSS is in the Fresnel near field where the plane-wave approximation is correct. The polarization agility of the Polar 55C is fully represented by the alternate transmission and reception of a plane-wave polarized along x -axis (E_{hh} , horizontal component of the EM field) and along y -axis (E_{vv} , vertical component of the EM field). The distance is fixed at 500 m between the structure and the receiver point.

In Figure 51a I show the horizontal component on a rectangular received area that has the dimension of the beam-size along azimuth and elevation. Figure 51b shows the differential component of the EM field ($E_{dr} = E_{hh}/E_{vv}$) that as expected has a value in amplitude approximately near to 1 V/m (0 dB). This result confirms the experimental observation and support the use the PSS considered as a good calibrator for the differential reflectivity in absolute terms.

xz-angle (deg)	yz-angle (deg)	E_{hh} (V/m)	E_{vv} (V/m)	E_{dr} (adim)
0	-45	4.9820e-04	6.4662e-04	0.7705
0	45	4.7336e-04	5.9474e-04	0.7959
0	0	0.1399	0.1397	1.0011
-45	0	0.0012	9.3439e-04	1.2977
45	0	0.0013	8.1444e-04	1.6049

Table 9: EM numerical results for the scenario in Figure 50.

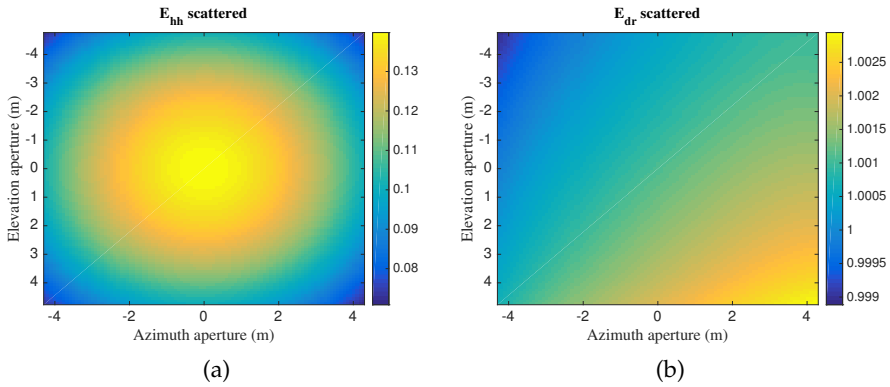


Figure 51: (a) Horizontal component of the EM field (E_{hh}) and (b) differential component of the EM field ($E_{dr} = E_{hh}/E_{vv}$) for the simulated scenario in Figure 50.

Table 9 shows the effect of the rotation of the structure on the differential component of the EM field. The beam-center of the radar is the point in which the E_{dr} is considered. From the table, it emerges that the signal return fluctuation visible in Figure 49a due to the orientation of the PSS. When the illuminated element has a rotation with respect to the xz -plane, the radar sees more components of the structure along the x -axis, whereas the prevailing contribution for the differential component is due to the horizontal field ($E_{dr} > 1$). On the other hand, when the illuminated element has a rotation with respect to the yz -plane the main contribution is due to the vertical field ($E_{dr} < 1$). This means that the PSS structure can be considered as a good radar calibrator for the differential reflectivity in relative terms with an uncertainty due to the rotation angle of its elements with respect to the radar illumination.

4.4 CONCLUSION

In this Chapter I have investigated the WR calibration monitoring. The calibration techniques have been presented, dividing them in: self-consistency, solar calibration and ground clutter techniques. A weather radar relative calibration technique has been introduced to improve the ground-clutter calibration and to use the clutter scenario around the radar for a clutter-based relative calibration. The work is presented as in [13] using data from a C-band polarimetric weather radar located in the complex orography of southern Italy. A PSS technique has been also conducted using for the radar calibration monitoring a peculiar PSS with a periodical metallic structure as in [14]. The PSS has been also tested for the check of antenna de-pointing and validated using full-wave CAD solutions.

SNOW RETRIEVAL FROM MULTIFREQUENCY RADAR

*"Reading snow is like listening to music.
To describe what you've read is like explaining music in writing."*

— Peter Hoeg, *Smilla's Sense of Snow*

The knowledge about the radars at multifrequency applied to the snowfall detection is introduced in Section 5.1. After a radar based snowfall intensity retrieval is investigated at centimeter and millimeter wavelengths using a high-quality database of ground-based precipitation and multifrequency radar observations. Using data from four snowfall events recorded during the Biogenic Aerosols Effects on Clouds and Climate (BAECC) campaign [15], presented in Section 5.2, measurements of liquid-water equivalent snowfall rate S are compared to radar equivalent reflectivity factors Z_e measured by the Atmospheric Radiation Measurement (ARM) cloud radars operating at X , K_a and W frequency bands. Methods to obtain the results are explained in Section 5.3. From the BAECC observations the power-law Z_e - S relations are computed for all the frequencies in Section 5.4.

In the same Section to understand a relation between snowflake microphysical and backscattering properties and how they translate to multifrequency Z_e - S relations, scattering simulations have been performed. The simulations have been carried out by using the soft-spheroid approximation and complex particle models. The soft-spheroid approximation has been computed with the Transition-matrix method (TMM). Instead, for the complex particle models, the scattering properties have been obtained from an existing Discrete Dipole Approximation (DDA) scattering database, from which snowflakes with physical properties that match surface observations were selected. Based on the presented observations it is concluded that the soft-spheroid approximation could be used to derive the observed multi-frequency Z_e - S relations. In some cases, however, in order

to reproduce the observations the soft-spheroid approximation with different aspect ratios is used in computations of the reflectivity factors at different frequencies. An analysis of the backscattering cross sections reveals that in the studied cases, TMM cross sections are higher than the DDA ones for small ice particles and it is lower for the larger particles. These differences explain why the soft-spheroid approximation works rather well, the errors in computed cross sections for larger and smaller particles compensate each other.

5.1 RADAR REMOTE SENSING IN SNOWFALL

The microphysical properties of snow have been given in Section 2.4, instead the main purpose of this part is to show the knowledge about the radars at multifrequency applied to the snowfall detection. The multifrequency approach to estimate hydrometeor size is introduced as in his first version for hail detection by Atlas and Ludlam [78] and after using the same principle for the snow detection. In this case the dual-wavelength and the triple-wavelength approaches are both presented referring to the milestone work by Matrosov in [7] also for the modeling linking these to the Rayleigh-Gans approximation in Sec. 2.2.3 and the TMM in Appendix A. The snowfall retrieval modeling with respect to the equivalent reflectivity factors measured by the radar at multifrequency is presented. At the end the renewed interest for the millimeter-wavelength is shown, as the current success of the highest frequency spaceborne radar mission, and related to the understanding of the snow microphysics that is the main purpose of my work.

5.1.1 *The multifrequency approach*

The multifrequency approach to estimate hydrometeor size was first proposed by Atlas and Ludlam [78] as a means of hail detection. The purpose of this work was to try to explain the features of hailstorm by using three wavelength (S, 10 cm; C, 4.7 cm; X, 3 cm) in Table 1. In 1961 the background about hailstorm were the works of Donaldson [79] showing that:

- when the intensity of radar echoes from hailstorms is remarkably high then the equivalent reflectivity factor Z_e (in equation (100)) reaches $4 \times 10^7 \text{ mm}^6 \text{ m}^{-3} = 76 \text{ dBZ}$;
- the more severe a storm is, and the greater the height of the more intense echo, and the greater the amount by which its intensity

Spectrum	Λ	Median volume diameter	W	R
	cm^{-1}	cm	gm^{-3}	mmh^{-1}
1	2.27	1.62	4.3	278
2	1.80	2.04	10	731
3	1.54	2.38	20	1580
4	1.30	2.83	40	3440

Table 10: Parameters of selected exponential hail size spectra (all have $N_0 = 40 \text{m}^{-3} \text{cm}^{-1}$) in [78].

exceeds that of the echo near the ground (when Z_e is limited to $10^6 \text{mm}^6 \text{m}^{-3}$).

To calculate the intensity of the echo that one might expect from a hailstorm is necessary to know the spectrum size of the particle $N(D)$ and the radar cross-section $\sigma(D)$ and this is what was done in [78]. At that time the size spectrum of the particles within a hailstorm had not yet been measured and so was inferred from observations of the hail and rain that reach the ground. The likely spectrum of particles within a storm cloud (see Figure 52) presented in [80] was used, it has approximately the exponential form, also shown in equations (76) and (96), reported as

$$N(D) = N_0 \exp(-\Lambda D) \quad (142)$$

where $N(D)$ is the concentration of stones with diameters between 0 and $D + \Delta D$, $N_0 = 40 \text{m}^{-3} \text{cm}^{-1}$ and $\Lambda = 2.27 \text{cm}^{-1}$ (previously defined in equation (76)). Similar laws were well-known as approximations to the size spectra of particles in both rain [81] and snow [82]. With the values of N_0 and Λ quoted, and mean spread falling velocity of 8ms^{-1} , median diameter 1.62 cm, the total frozen water content W was 4.3gm^{-3} (in equation (82)) and the precipitation rate was 278mmhr^{-1} . The work, as said, was interested in the radar reflectivity factor of the most intense storms and they had considered a slope to have greater value of R (see Table 10). The value of the backscatter cross-section σ belonged to the sphere of ice based on the work of Atlas [83] for several commonly-used wavelength. For spheres of water the reference work was [84] strictly applied only to a wavelength of 16.23 cm and a water temperature of 20°C , but they are accurate to within 4 per cent for all wavelengths down to 3 cm and temperature down to 0°C for $D/\lambda \geq 0.3$. The Aden [84] data was

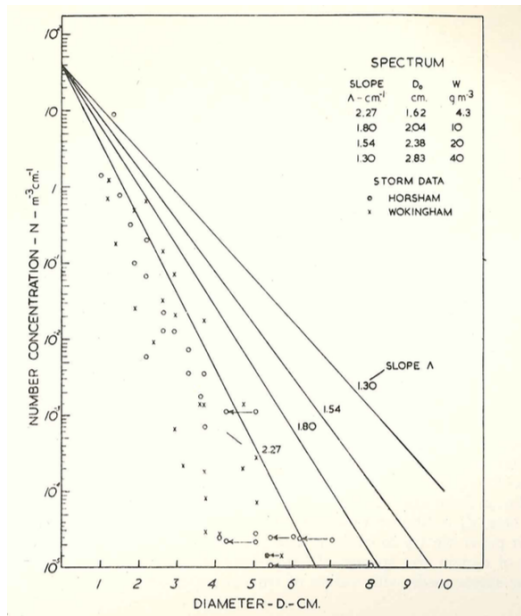


Figure 52: Concentrations in the air of the largest stones which fell at particular places in the Horsham and Workingham (according to [80]), and four exponential hailstone spectra used in the calculations. Figure in [78].

used for $D/\lambda \geq 0.2$ and otherwise Haddock [85] cross-section for 3.0 cm and 18 °C. For $\lambda = 1.8$ cm they had interpolated between Haddock’s data for 0.3 cm and Aden’s data. For large spheres, $D \geq \lambda$, the ice values may exceed the water values by 10 dB or even more, but can be reduced in the melting phase for the effect of a surface-film of liquid water (−5 dB at 3.3 cm, −2 dB at 4.7 cm). When the water coat is sufficiently thick (but no so thick to absorb strongly) the cross-section depends mainly upon D/λ . The necessary thickness is about 10^{-2} cm at 3 cm wavelengths, and greater than 10^{-2} cm at 4.7 cm. The σ of wet spheres is reduced with respect to dry ice spheres for $D > \lambda$ (Figure 53 (a) and (b)). Having the spectrum $N(D)$ and the backscatter cross-section $\sigma(D)$ the radar reflectivity per unit volume cm^2m^{-3} could be calculated (already defined in equation (9))

$$\eta = \int N(D)\sigma(D)dD \tag{143}$$

In the Rayleigh scattering regime is well-known (equation (100)) that

$$\eta = 10^{-6}\pi^5|K|^2Z/\lambda^4 \tag{144}$$

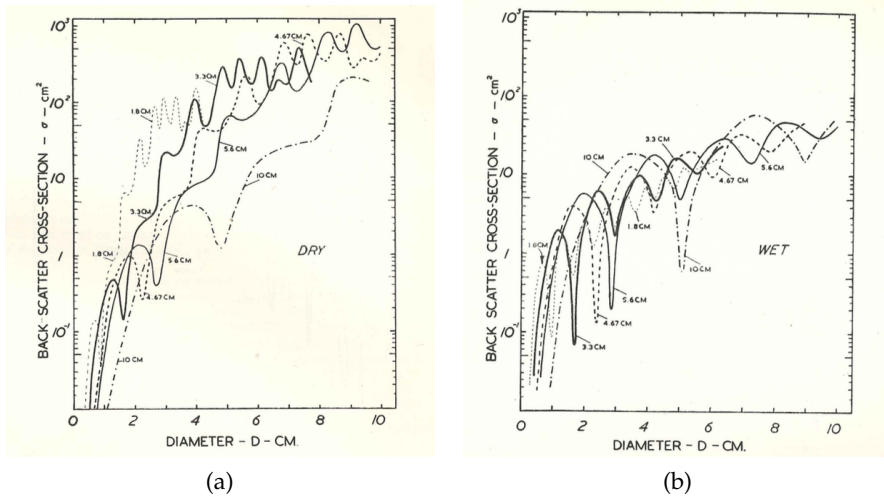


Figure 53: Back-scatter cross-section σ of spheres of ice with dry surfaces (a) and of liquid water (b), at the indicated wavelengths. Figures in [78].

where $K = (m^2 - 1)/(m^2 + 2)$, being m the complex refractive index (for wavelength from 1.8 to 10 cm and for liquid water at temperature from 0 to 20 °C, $|K|^2 = 0.93$), and $Z = \sum ND^6$ (mm^6m^{-3}).

When some of the scattering particles are outside the Rayleigh regime it has become customary to express storm reflectivity as Z_e , the equivalent Z , or the value of Z required to satisfy equation (144) for the observed value of η ; then

$$Z_e = 3.52 \times 10^3 \lambda^4 \eta \quad (145)$$

Using this relation the reflectivity of the hail spectra had expressed in terms of Z_e in Figure 54. They have also calculated the Z_e corresponding of 1 gm^{-3} of hailstones of uniform diameter D at three wavelength (S , C , X) in Figure 55 [87].

Atlas and Ludlam [78, 87] with this milestone work have highlighted for the first time that *"the variation of reflectivity with wavelength is so considerable that the possibility arises of arising measurements of intensity at several wavelengths to make inferences about the sizes and surface condition of the hailstones present"*. They had attempted to make this for the first time using observation of the Workingham storm with three radars taking into account the calibration and the attenuation due to intervening precipitation.

Atlas and Ludlam [78] in the corrigenda of 1962 [87] highlighted also that *"the spheroidal shape of the real stones has significant effects upon their*

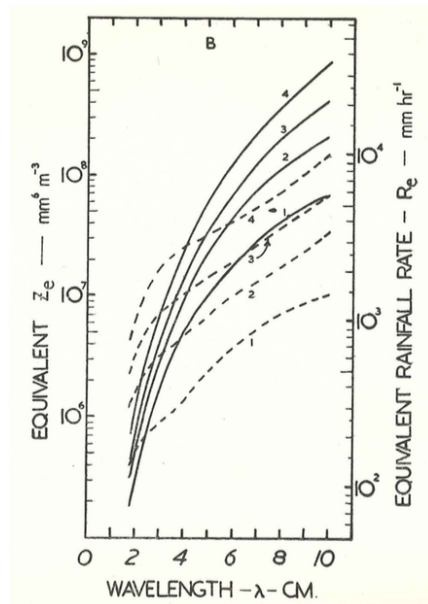


Figure 54: Z_e , the equivalent Z , of the four exponential hail spectra, as a function of wavelength. On the right is a scale of equivalent rainfall rate R_e , derived from the empirical relation: $Z = 486R^{1.37}$ [86]. Figure in [78].

reflectivity”, and it should be taken into account for a correct interpretation of echo intensities measured as I will show you later.

The work of Atlas and Ludlam [78] is not suitable for hail due to the ambiguity caused by the very different scattering properties of wet and dry hail [88]. In particular a multifrequency approach is not convenient for hailstorms detection because of the high polarization signatures can give more information about hail [89, 90].

The multifrequency approach as I will show in the next section is suitable for the dry snow to obtain information about sizes and surface condition in snowfall.

5.1.2 Multifrequency in snowfall detection

A traditional single-frequency radar measures the equivalent radar reflectivity factor Z_e (equation (100)) and it estimates the rain rate R (equation (83)) from a simple Z_e - R relation that is derived in the power-law form [6]. The Z_e - R relation is often significantly less accurate to estimate snowfall than rainfall, due to the microphysical variety of the snowfall characteristics: shapes, densities, and terminal fall velocity (as a func-

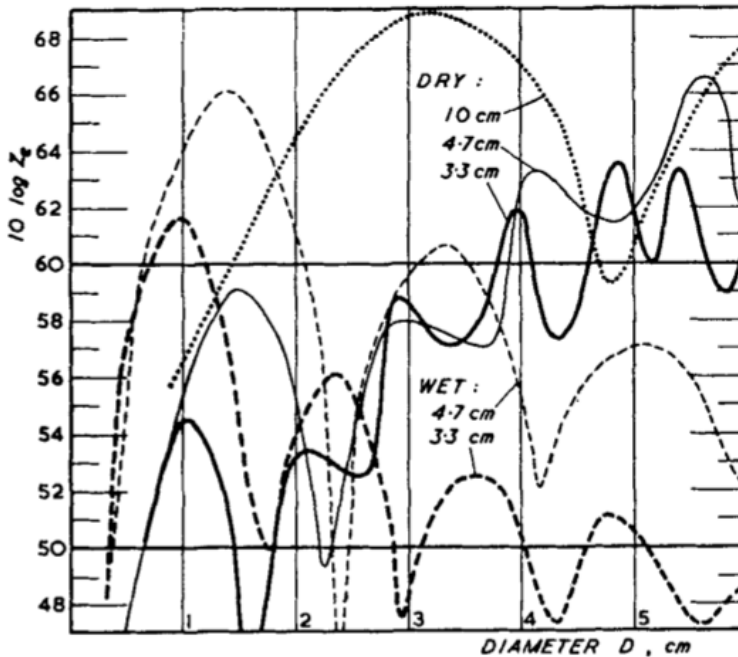


Figure 55: Values of $10\log(Z_e)\text{mm}^6\text{m}^3$ corresponding to 1gm^{-3} of hailstones of uniform diameter D at three wavelength. Figure in [87].

tion of snowflakes size). Moreover, the single-parameter radar retrievals of the liquid-water equivalent snowfall rate S measured in mmhr^{-1} are generally insufficient by reason of low correlation that results in a very high variability in the coefficients of Z_e - S relation. Different polarization approaches, useful to improve rain rate estimation, are non-effective for snowfall measurements because larger, low-density, irregular-shaped aggregate snowflakes usually exhibit weak polarization signatures [91].

The multifrequency approach in snowfall detection adopts the work-line in [78], presented in the previous section, adapting it at a double frequency contest. The aim was to first estimate the effective size of snowflakes D_0 from the logarithmic difference between Z_e at two wavelengths (or dual-wavelength ratio, DWR) and then to use the independent estimate of characteristic size to enhance the snowfall precipitation rate S . After a triple frequency approach has been proposed in [16] to better constrain the slope parameter of exponential size distributions more tightly than conventional single DWR approaches.

Dual frequency approach

By following the work-line of Atlas and Ludlam [78], many authors for first Matrosov [7] have compared Z_e , the equivalent reflectivity factor in equation (100), for different frequencies at the Rayleigh reflectivity Z in equation (98). To compute the radar reflectivity theoretically, it is necessary to define $N(D)$ the size distribution of aggregate snowflakes and σ the backscattering cross section.

Matrosov in [7] and Illingworth et al. [92] have shown that characteristic particle sizes can be inferred from the logarithmic difference between reflectivities measured at two wavelength or DWR:

- one in Rayleigh regime (S and C band)
- one outside of the Rayleigh regime (K_a and W band)

To show this concept that is the hearth of the DWR approach a simple theoretical study of microwave scattering in dry snowfall is shown following the work of Matrosov [7, 91] in which the backscattering cross section was expressed with the Rayleigh-Gans approximation using the spherical model for snowflakes. This approximation can be safely used for theoretical studies of microwave scattering in dry snowfall up to the frequency of K_a band. The backscattering properties of a spherical particle depend on the particle size and its complex refractive m . Infact a snowflake can be considered a mixture of ice, water and air, with P_i , P_w and P_a their relative volume ratios: $P_i + P_w + P_a = 1$. The complex refractive index of snow was calculated in [7] according to the method to calculate the effective dielectric properties of mixtures based on the Wiener's theory [93], using the equation in [94]

$$\frac{(m_s^2 - 1)}{(m_s^2 + \mu_{\rho_s})} = P_w \frac{(m_w^2 - 1)}{(m_w^2 + \mu_{\rho_s})} + P_i \frac{(m_i^2 - 1)}{(m_i^2 + \mu_{\rho_s})} \quad (146)$$

where m_i , m_w and m_s are complex refractive indices of ice, water and snow, respectively, and dimensionless parameter μ_{ρ_s} depends on the snowflake density. Matrosov [7] has neglected a term in equation (146) considering that $m_i^2 = 1$ for the air. Following the empirical consideration in [94], P_w and P_i are related to ρ_s as follows:

$$\begin{cases} P_w = \rho_s^2 \\ P_i = \rho_s(1 - \rho_s)/\rho_i \end{cases} \quad (147)$$

where ρ_i is the density of the ice assumed as: 0.9175 g/cm^3 ($T = -10^\circ\text{C}$) and 0.9189 g/cm^3 ($T = -5^\circ\text{C}$). All the work was based on the dry snow which density was considered between 0.02 and 0.06 g/cm^3 and $\mu = 2$ as in [95, 96]. Different values of ρ_s and μ_{ρ_s} was defined for different kinds of snow, moist and wet. For what concerns the refractive index I mentioned the table shown in [7] replicated in Table 11 where data about m_i and m_w needed for calculations of m_s were taken from [96, 97]. What is relevant in Table 11 is that the real values of refractive indices of dry snow practically do not depend on the frequency: $\text{Re}(m_s) - 1 \gg \text{Im}(m_s)$ instead temperature variations do not cause significant changes in $\text{Re}(m_s)$ but increased $\text{Im}(m_s)$. The inequality expressed between the real part and imaginary part of the refractive index means that the absorption of microwaves by dry snow is small in comparison with scattering, and the backscattering properties of snowflake depend mainly on the snow density and the snowflake size factor $\chi = \pi D_s / \lambda$ where λ is the radar wavelength and D_s is the diameter of a snowflake, expressed as:

$$D_s = D(\rho_s / \rho_w)^{-1/3} \quad (148)$$

where $\rho_w = 0.7407 \text{ g/cm}^3$.

Frequency GHz	T = -10 °C			T = -5 °C		
	$\rho_s = 0.02$ g/cm ³	$\rho_s = 0.04$ g/cm ³	$\rho_s = 0.06$ g/cm ³	$\rho_s = 0.02$ g/cm ³	$\rho_s = 0.04$ g/cm ³	$\rho_s = 0.06$ g/cm ³
34 (K _a)	1.01404 + 0.000085i	1.02869 + 0.000342i	1.04397 + 0.000773i	1.01404 + 0.000075i	1.02872 + 0.000308i	1.04405 + 0.000679i
17 (K _u)	1.01406 + 0.000048i	1.02879 + 0.000192i	1.04420 + 0.000434i	1.01406 + 0.000041i	1.02880 + 0.000163i	1.04422 + 0.000369i
9.3 (X)	1.01407 + 0.000027i	1.02882 + 0.000108i	1.04426 + 0.000244i	1.01407 + 0.000023i	1.02882 + 0.000091i	1.04427 + 0.000206i
5.4 (C)	1.01407+ 0.000016i	1.02883+ 0.000066i	1.04428+ 0.000148i	1.01407+ 0.000014i	1.02883+ 0.000055i	1.04428+ 0.000125i
2.9 (S)	1.01408+ 0.000009i	1.02884+ 0.000034i	1.04429+ 0.000077i	1.01408+ 0.000007i	1.02884+ 0.000029i	1.04429+ 0.000065i

Table 11: Complex refractive indices m_s of dry snow at multifrequency in [7].

For high frequencies the condition of the Rayleigh approximation is well beyond the size of applicability

$$\begin{cases} \chi \ll 1 \\ |m_s| \chi \ll 1 \end{cases} \quad (149)$$

but the consideration of [7] was that snowflakes are apparently within the limits of the validity for Rayleigh-Gans approximation states that [98]

$$\begin{cases} |m_s - 1| \ll 1 \\ |m_s - 1|x \ll 1. \end{cases} \quad (150)$$

The Rayleigh-Gans approximation assumes that the electromagnetic field inside the particle can be approximated by the incident field, and each small volume of the particle produces the Rayleigh types scattering independently from other volumes.

For a spherical snowflake [7] had obtained the backscattering efficiency

$$Q(\pi D_s/\lambda) = |m_s - 1|^2 \left(\frac{\sin(2\pi D_s/\lambda)}{2\pi D_s/\lambda} - \cos(2\pi D_s/\lambda) \right)^2 \quad (151)$$

end then

$$\sigma(D_s) = A Q(\pi D_s/\lambda) = \pi (D_s/2)^2 Q(\pi D_s/\lambda) \quad (152)$$

The Rayleigh-Gans approximation reproduces the oscillating character of backscattering efficiency dependence on the size factor very well respect to the Rayleigh theory ($Q(\pi D_s/\lambda) = |m_s|^2 (\pi D_s/\lambda)^4$, see Chapter 2) as in Figure 56 from [7].

Matrosov in his milestone work [7] has used the exponential size distribution of aggregate snowflakes expressed in terms of the real diameter of snowflakes:

$$N_s(D_s) = N_{0s} \exp(-\Lambda_s D_s) \quad (153)$$

where $N_{0s} = N_0(\rho_s//\rho_w)^{1/3}$ and $\Lambda_{0s} = \Lambda_0(\rho_s//\rho_w)^{1/3}$. The size exponential distribution was chosen following the suggestion of [94] which highlighted this distribution was able to represent dry snowflakes and less wet parts snowflakes. The maximum melted diameter of snowflakes D_{mm} was chosen following [99] as spectrum dependent from the parameter Λ : $D_{mm} = 6.4/\Lambda$. At the end the equivalent reflectivity formula in equation (100) is re-written in terms of the diameter of snowflakes as defined in equation (148) as follows

$$Z_e = \frac{\lambda^4}{|K|^2 \pi^5} \int_0^{D_{ms}} N_s(D_s) \sigma(D_s) dD_s \quad (154)$$

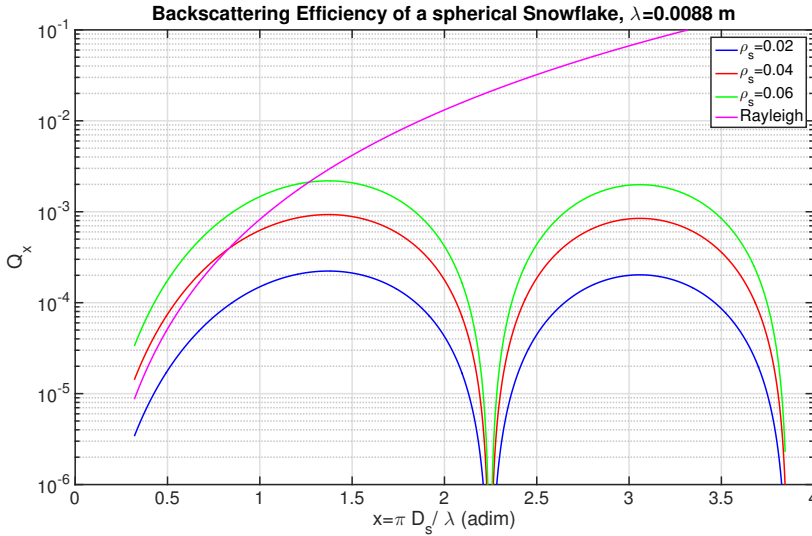


Figure 56: Backscattering efficiency of a snowflake Q as a function of size parameter x for different snow densities in K_a band at $T = -10^\circ\text{C}$: The Rayleigh-Gans approximation (green, red and blue curves), and the Rayleigh approximation (magenta curve). Figure in [7].

where $D_{ms} = D_{mm}(\rho_s/\rho_w)^{-1/3}$ follows equation (148). The reflectivities at different frequencies are shown in Figure 57 as function of the size parameter $\Lambda_s = 3.67/D_{0s}$ (or the snowflake effective size $D_{0s} = D_0(\rho_s/\rho_w)^{1/3}$) and different for different wavelengths. This figure is the hearth of the dual-wavelength approach that shows the dual-wavelength radar measurements between a Rayleigh (S, C and X band) and non-Rayleigh (K_a or highest) of snowfalls can provide information about the snowflake size distribution, Λ and D_0 . In fact discrepancies between reflectivities in Rayleigh regime (Ray) are small but they result larger if compared with the non-Rayleigh regime (NRay). Finally the Dual-Wavelength Ratio DWR can be defined

$$\text{DWR}(\text{Ray}; \text{NRay}) = Z_e(\text{RayBand}) - Z_e(\text{NRayBand}) \quad (155)$$

Figure 58 is the best representation showing the DWR in equation (155) between S and K_a band, and X and K_a band.

In [91] the DWR approach has been consolidated in order to apply the independent information about snowflake characteristic size to improve Z_e -S relationships. The size distributions of snowflakes are modeled by

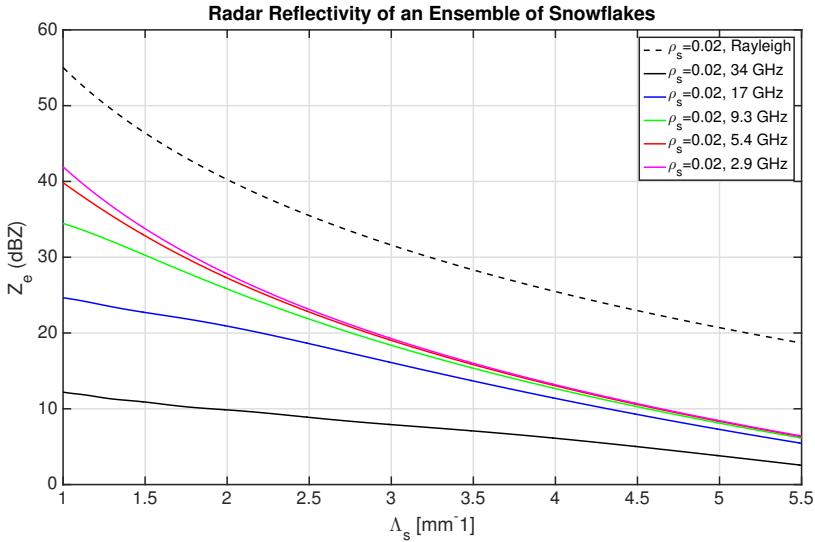


Figure 57: Reflectivities at different frequencies of an ensemble of snowflakes following the Rayleigh-Gans approximation at $T = -10^\circ\text{C}$ for density of 0.02 g/cm^3 : The Rayleigh-Gans approximation increasing the frequency (magenta, red, green and blue curves), and the Rayleigh approximation (dotted curve). Figure in [7].

the gamma function of different orders n in terms of diameter of equal-volume spheres $D_{Ve q}$

$$N(D_{Ve q}) = N_0 D_{Ve q}^n \exp(-\Lambda D_{Ve q}) \quad (156)$$

where the parameter Λ is related to the snowflake characteristic size, with $n = 0$ returns the exponential distribution used in [7].

The main result in the followed work [100] was to point out the fact that especially for high frequencies (K_a and W Band) the effect of non-sphericity should be taken into account for example with the TMM computations.

Triple frequency approach

Several studies have employed triple-wavelength approaches to distinguish different crystal shapes in ice clouds for nonprecipitating particles [101]. The works of Kneifel [16, 102] instead highlighted the potential benefits of triple-frequency radar in distinguishing different snow particle types. The first numerical study in [16] selected the frequency motivated

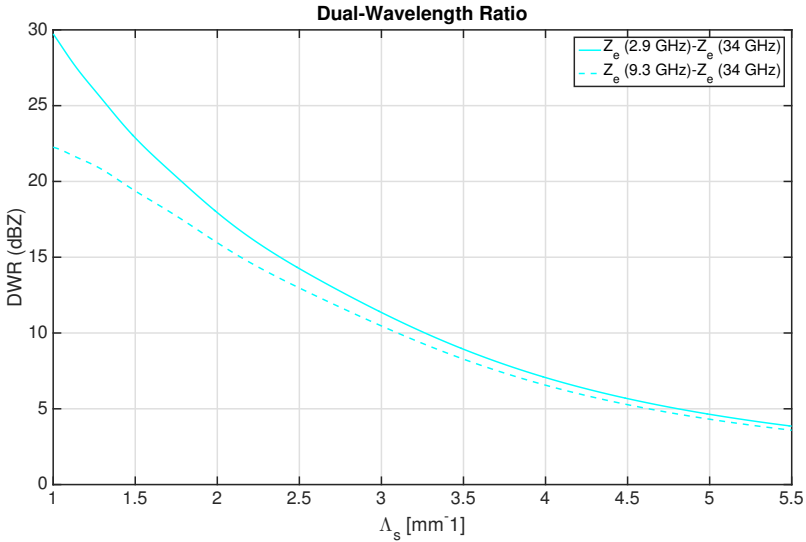


Figure 58: Dual-Wavelength Ratio (DWR) following the Rayleigh-Gans approximation at $T = -10$ °C for density of 0.02 g/cm³: DWR(S; K_a) (cyan curve), and DWR(X; K_a) (cyan dotted curve). Figure in [7].

by its similarity to the frequency set of the upcoming GPM mission [103] corresponds to K_a , K_u and W band (see Table 1). Models studied included soft spheres (MIE), soft spheroids (TMM), randomly oriented pristine (LIU in [104]), nonspherical particles and complex aggregates (AGG in [105]). In Figure 59 is revealed that especially for large DWR_{K_u, K_a} values (related to small Λ values and hence $N(D)$ with a significant fraction of large particles) different particle types can be distinguished.

5.1.3 Z_e - S relations and its importance

The main meteorological measurements in weather radar studies are rainfall and snowfall. Usually, such measurements are based on the approximate relation between the radar equivalent reflectivity factor Z_e and the precipitation rate R :

$$Z_e = AR^b \quad (157)$$

where the equivalent reflectivity is expressed in mm^6m^{-3} and the rain rate is in mmhr^{-1} .

The precipitation type, size, shape distributions and fall velocities of precipitation particles influence the A and b coefficients. A and b show

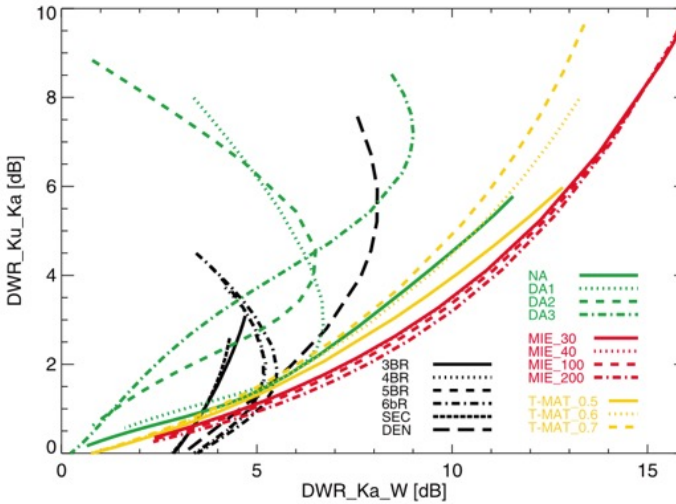


Figure 59: Triple-Frequency space: DWR_{K_u, K_a} against $DWR_{K_a, W}$ in dB. The different particle models are color coded: LIU (black: 3-bullet rosettes (3BR), 4-bullet rosettes (4BR), 5-bullet rosettes (5BR), 6-bullet rosettes (6BR), sector snowflakes (SEC), dendrites (DEN)), AGG (needle aggregates (NA), different aggregates composed of dendrites (DA 1-3)), MIE (red, soft sphere with different snow densities), T-MAT (yellow: ellipsoid with different aspect ratios). Note that all DWR values are independent of the intercept parameter N_0 . Figure in [16].

considerably greater variance for snowfall rate S than for rainfall rate R and are not universal constants, and the approximate relationships is for snowfall:

$$Z_e = AS^b \quad (158)$$

where the equivalent reflectivity is expressed in mm^6m^{-3} and the snow rate is in mmhr^{-1} .

An important problem in radar meteorology is the optimization of the A and b coefficients to find an appropriate Z_e - S relation.

The classical works in literature are developed for the cm wavelength essentially in two ways:

- theoretically [99, 106, 107] from analysis of snowflake size distribution spectra and corresponding calculation of radar reflectivities;
- experimentally [95, 108–113] from the comparison of radar reflectivities and ground data.

The theoretical values obtained in the work of Gunn and Marshall [106] and Sekhon and Srivastava [99], by assuming applicability of the Rayleigh scattering mechanism and equivalence of scattering properties of snowflakes and corresponding melted water drops, have found relatively large values for A (2000 and 1780, respectively) and relatively stable for b (2 and 2.21, respectively). The experimental values found for dry snow have smaller values of A ranging from 230 [109] to 1050 [112] and b more stable ranging from 1.6 to 2.0 ($b = 1.09$ in [95]). The natural variability of snowflake scattering properties is clearly visible in the great variation of coefficient in the Z_e - S relation especially in dry snowflakes.

A first attempt to investigate the snowfall rate S at multifrequency was made by Matrosov [7] that has expressed the snowfall rate S in terms of equivalent water accumulation per unit of time

$$S = (\pi/6)\rho_w \int_0^{D_{\text{mm}}} v(D)D^3N(D)dD \quad (159)$$

where $v(D)$ is the falling velocity of a snowflake and $N(D)$ is the same in equation (153). The general relation for the velocity that Matrosov has used in [7] is from [114] taking into account the densities of snowflakes (ρ_s) and the density of the air (ρ_a)

$$v(D) = 8.8[(\rho_s - \rho_a)D_s]^{0.5}. \quad (160)$$

The relation is shown in Figure 60 and in Table 12 from [7] the variation of the coefficients A and b is evaluated theoretically emphasizing that the coefficients decrease at the highest frequency and there is a dependency on the snow density (small for b and highest for A). The theoretical relations for Z_e - S are also shown in Figure 61.

Snow density ρ_s/cm^3	Coefficients	2.9 GHz	5.4 GHz	9.3 GHz	17 GHz	34 GHz	Rayleigh	Rayleigh
		S Band	C Band	X Band	K_u Band	K_a Band	(dry snow)	(melted snow)
0.02	A	870.	690.	410.	130.	10.	950.	1950.
	b	2.01	1.90	1.60	1.00	0.50	2.03	2.22
0.04	A	570.	510.	340.	160.	20.0	610.	1950.
	b	2.01	1.95	1.75	1.20	0.61	2.03	2.22
0.06	A	460.	420.	240.	170.	28.0	490.	1950.
	b	2.02	1.98	1.95	1.35	0.95	2.03	2.22

Table 12: Theoretical evaluation of the Z_e - S coefficients in [7].

A more recent contribution at the modeling Z_e - S relations in [115] has been realized for the common millimeter-wavelength frequencies of 34.6

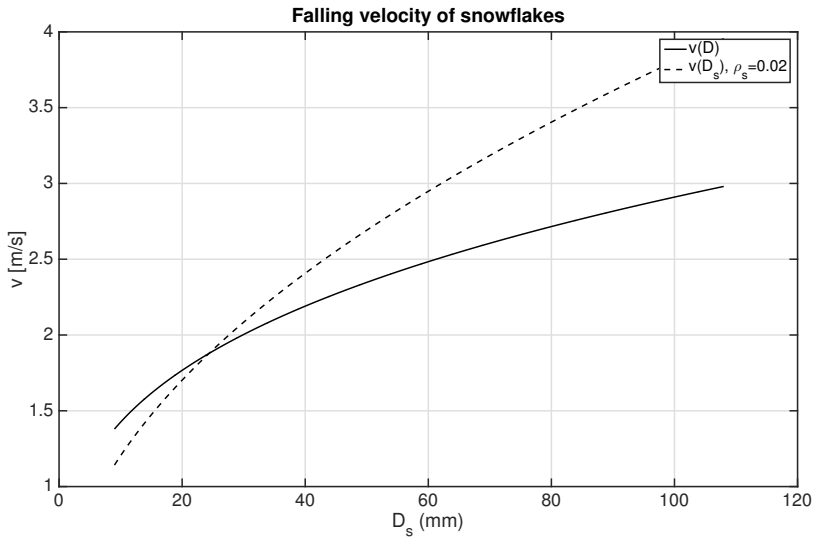


Figure 60: Two theoretical relations for falling velocity of snowfall: $v(D) = 2.07D^{0.31}$ (black curve), and equation (160) with $\rho_s = 0.02 \text{ g/cm}^3$ (black dotted curve).

GHz (K_a Band) and 94 GHz (W Band) and has been based on available information on snowfall size distributions and densities. As before the modeling was concerned for "dry" snow that is snow with negligible amounts of liquid water/riming. Dry snowfalls usually contribute most significantly to snow accumulation at temperature less than about -8°C . For these particles, beyond the bounds of the Rayleigh conditions, the spherical model becomes progressively less suitable. Larger non-spherical ice particles exhibit backscatter dependence on particle orientation and generally greater reflectivities (especially outside the Rayleigh scattering regime) compared to those of spherical particles at the same mass [100]. The simplest geometrical shape that allows describing non-spherical hydrometeors is that of spheroid in Figure 15.

At radar frequencies, the small details in a particle structure usually do not significantly affect the backscatter properties that depend largely on the overall shape [116], which, in the case of spheroid, is determined by the spheroid aspect ratio r . The spheroid model fails for very large dendrites that are not very common but for these the DDA is more detailed.

On the other hand the aspect ratio in the spheroid model in [100] was shown that

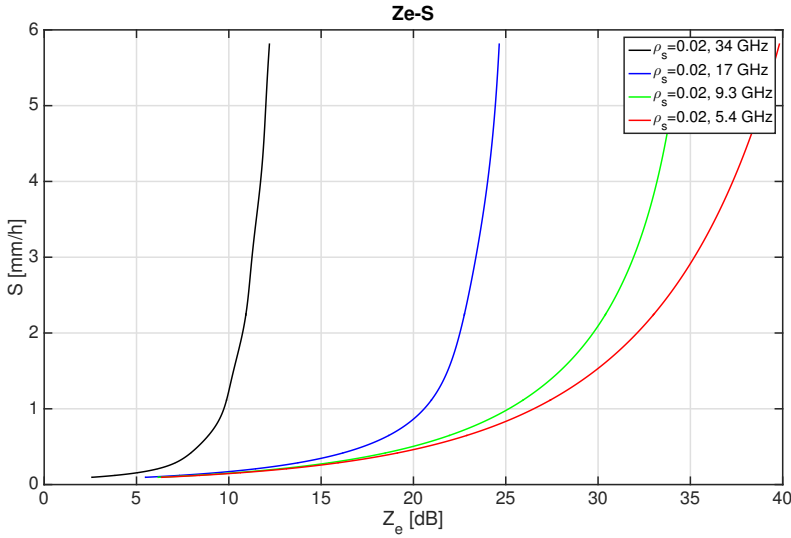


Figure 61: Theoretical relations for Z_e - S in snowfall at multifrequency: K_a Band (black curve), K_u Band (blue curve), X Band (green curve), C Band (red curve).

- $r = 0.1 - 0.3$ are suitable for modeling pristine dendrite snow crystals
- $r = 0.5 - 0.7$ are usually observed for larger aggregate crystals

The TMM applied in [115] had the followed assumption:

- symmetry axes of oblate spheroids that approximate snowflakes are oriented with the 0° mean and standard deviations of about -9° with respect to the vertical. The standard deviation influence the magnitude of Z_e at millimeter-wavelength frequencies;
- the mass is in the power-law form and is used to derive the density and the velocity;
- the complex refractive index of solid ice is adopted from [97].

For what concern the snowfall size distribution the exponential is used as in [7] from equation (153).

The best power-law defined using the TMM and the exponential size distribution inside the equation (154) are presented in Table 13.

The last relevant work that should be mentioned about snowfall retrieval is [117] that illustrated the utility of snowfall estimates using Z_e - S

r	34.6 GHz	94 GHz
	K _a Band	WBand
0.6	$Z_e = 56S^{1.2}$	$Z_e = 10S^{0.8}$
0.8	$Z_e = 34S^{1.1}$	$Z_e = 6S^{0.8}$

Table 13: Theoretical evaluation of the Z_e - S coefficients in [115].

relations for millimeter-wavelength cloud radars. The need of such estimates is important especially where no-surface-based observations are existent and then a polar-orbiting cloud radar could be useful. In Matrosov et al. [117] the Z_e - S relation for W band developed in [115] (and presented in Table 13) was applied to illustrate snowfall retrievals using CloudSat measurements.

Referring to equation (158) in [117], the relative variability of the coefficient A was in terms of model uncertainties about 50% whereas the relative variability of the exponent was generally more modest (10%). These uncertainties can result in snowfall-rate retrieval errors that are as high as a factor of 2 or even greater. The problem of the analysis developed in [117] was related to the uncertainties of the gauge and radar. In spite of this, the work highlighted that radar provides vertically resolved snowfall information and measurements of instantaneous snowfall rate that are typically not available from standard gauges.

The high retrieval uncertainties in the work [117] provides a consistency check for the millimeter-radar estimates of snowfall but not a quantitative comparison. Overall, this study indicates that the use of cloud millimeter-wavelength radars operating at K_a and W bands can be extended to snowfall studies.

5.1.4 Connection to satellite and ground validation

The importance of obtaining an accurate snowfall retrieval for millimeter wavelengths is also related to the increasing number of satellite missions for cloud and precipitation measurements. The NASA has two active satellite missions, the GPM mission with a dual-frequency precipitation radar that uses K_u and K_a bands (13.6 and 35.6 GHz, respectively) and the *CloudSat* mission measuring cloud backscattering with a W band radar. Looking at the future, the European/Japanese (ESA/JAXA/NICT) *EarthCARE* mission, planned for launch in 2018, will carry a Cloud Profiling Radar (CPR), which will be the first W band (94 GHz) Doppler radar aboard a

satellite. The Ground Validation (GV) is a necessary step to obtain validation products for comparison with satellite data and collecting data from ground-based radar at the same frequencies and snow gauges. The GV program for millimeter-wavelength satellites will exploit the network of cloud radars of the U.S. Department of Energy ARM Program presents in several climatologically distinct regions [118].

A realistic application of the ground-based radars for satellite GV and snowfall retrieval is strictly related to the understanding of the snow microphysics in his correlation to the scattering properties that is, as I will show you in the next Section, one of the main purpose of my work.

5.1.5 *Challenges and proposed solution*

For the longer-wavelength radars (S, C or X band), the snowflake sizes typically are seen as much smaller than radar wavelengths and the scattering behavior is near to the Rayleigh regime [115]. Able to control what is going on for centimeter wavelengths, it has provided to define some Z_e -S relations, as said in Section 5.1.3. Diverting from the canonical Rayleigh regime the millimeter wavelengths are less understandable and more critical is to obtain Z_e -S relations only theoretically. From a theoretical point of view, the simple spheroid models of ice particles widely applied at the longer-wavelength radar may result not useful to obtain the scattering signatures linked to the microphysical properties of snowflakes for complex aggregates particles far from the Rayleigh regime [105, 119, 120] as confirmed in [121]. When the particles are not complex aggregates or the related effects due to these aggregates are removed by using temporal averaged, the spheroid particle models can be assumed and used as in [102, 122] for the DWR approach selecting two frequencies (e.g. C and W bands) to obtain a third frequency (for example K_α).

Moving inside the triple-frequency space shaped by the X, K_α and W band, the goal of my work has been to develop the Z_e -S relation for each millimeter-wave frequency using surface-based precipitation measurements in connection with multifrequency radar observations. These high-quality dataset results available thanks to a campaign of measure pursued in the station of Hyytiälä in Finland during the BA ECC campaign. In order to refine the snow retrievals four case studies have been analyzed consisting of a datasets for X, K_α and W band zenith-pointing radars together with in situ microphysical observations. To better understand the Z_e -S relations, I have modeled simulated reflectivities starting from the ground-based measurements of the Particle Imaging Package (PIP) video

disdrometer, to set up the TMM computations along with the Maxwell-Garnett effective medium approximation (EMA) [123]. To improve the simulations, a new mass dimensional relation in power-law form, derived from the hydrodynamic theory applied to PIP measurements, has been considered [124] along with the use of the aspect ratio as a tuning parameter. The numerical results using the TMM have been compared with the DDA to underline the limit of the different scattering computations.

5.2 FIELD CAMPAIGN BAECC

The University of Helsinki Hyytiälä Forestry Field Station hosted the BAECC campaign, an 8-month measurements campaign from February to September 2014 [15]. BAECC was organized by the University of Helsinki, the US Department of Energy ARM program, which has deployed the second ARM mobile facility (AMF₂) to Hyytiälä in Figure 62, and with participation from many other Finnish and international partners. The snowfall intensive observation period (BAECC SNEX IOP) that took place between 1 February and 30 April was carried out in collaboration with the NASA GPM GV program [15]. One of the goals of the IOP [15] was to use observations of microphysical properties of falling snow in combination with multi-frequency radar measurements to establish a link between physical and scattering properties of ice particles. Observations collected during this IOP are used in my study. Surface based snowfall measurements were carried out by PIP [125, 126] and weighing gauge. The multi-frequency radar observations from the X-band scanning ARM cloud radar (XSACR), Ka-band ARM zenith radar (KAZR) and the Marine W band ARM cloud radar (MWACR), all deployed at the measurement site, are used in my study. In addition to these radars, the Finnish Meteorological Institute (FMI) operational C-band dual-polarization Doppler weather radar (IKA), located 64 km west from Hyytiälä in Ikaalinen, is employed as a reference in the cross-calibration procedure of the ARM radars, as discussed below.

5.2.1 *Surface precipitation measurements*

Data from the PIP are used for characterizing frozen precipitation. The 2D-gray scale PIP images of snowflakes are obtained, when they fall between the camera and the lamp (distance between the two is 2 m). The instrument works in the same way as the previous version, the Snow Video Imager (SVI) [126], but the frame rate is increased to 380 frames per second.

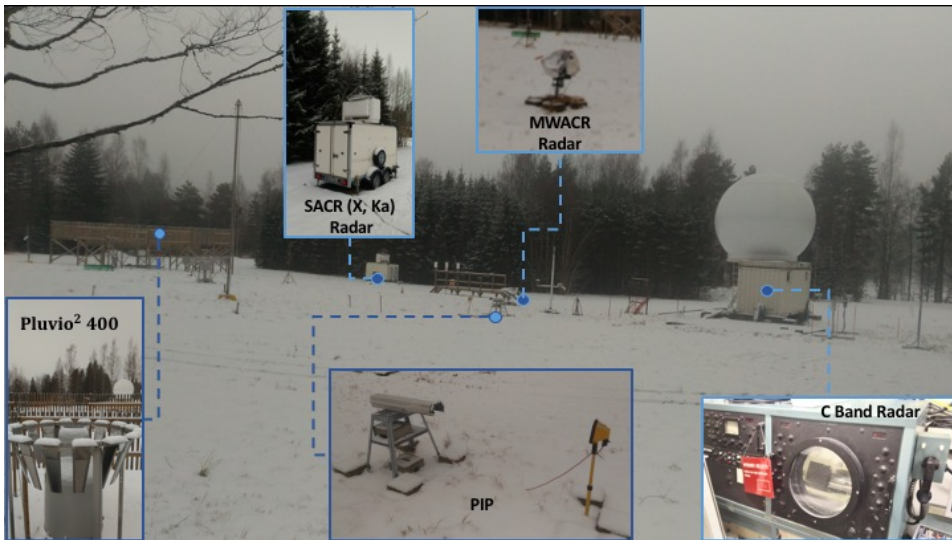


Figure 62: Measurement site shown with in situ and remote sensing instruments during the BAECC campaign 2014 at Hyytiälä, Finland.

Multiple observations of particles are then used to derive particle fall velocities. The focal plane is 1.3 m and the field of view is 64×48 mm with a resolution of 0.1×0.1 mm. The diameter used in PIP measures is the disk-equivalent diameter D_{deq} that is defined as an equivalent diameter of a disk that has the same area as the shadow-contour of the particle. The detection software has a filter that rejects any object with sizes fewer than 14 pixels (approximately 0.2 mm equivalent diameter) or objects that fall partly out of the focus because of the great uncertainty for those measurements. The sizing standard error is estimated approximately at 18% in [126]. Wind, except for heavy conditions, produces minimal errors in the PIP measurements as seen in [127].

The PIP instrument also measures the snow size distribution, that is the number of particles per unit volume per unit size in $m^{-3} mm^{-1}$ computed for each time interval (1 minute) in which D_{deq} is the disc-equivalent diameter subdivided into 105 bins (from 0.125 to 25.875 mm), the last bin being the same for all larger particles in the employed PIP software (release 1308). Fall velocity measurements are also available as a function of D_{deq} . More detailed informations are presented in the next Section about the methods useful to obtain the mass and then the snow rate S from the PIP measurements.

Table 14: Technical properties of the radars: second column for the C-band polarimetric Doppler weather radar monitored by the FMI; the last two columns for the ARM cloud radar systems at X, Ka and W bands.

Acronym	IKA	XSACR	KAZR	MWACR
Location	Ikaalinen	Hyytiälä	Hyytiälä	Hyytiälä
Frequency (GHz)	5.6	9.7	35.3	95.0
Beam width (°)	0.94–0.98	1.27	0.33	0.38
Sensitivity at 1 km (dBZ)	-48	-30 ^a	-50 ^a	-50 ^a
Range gate spacing (m)	-	25	25	30
Temporal sampling	5 min	2s	2 s	2 s

5.2.2 C-band Polarimetric Doppler weather radar

The Polarimetric Doppler weather radar, used for our analysis, belongs to the weather radar network in Finland implemented and monitored by the Finnish Meteorological Institute [128]. The radar is a C-band frequency of 5.6 GHz and is situated in Ikaalinen at circa 64 km from Hyytiälä (labeled with the acronym IKA). The antenna has an half-power beam widths of 1°. The radar observations from IKA are collected in PPI-scans with the possibility to obtain volume scans consisting of 11 elevation angles. The lowest nominal elevation is 0.3° is available every five-minutes and the beam reaches the height of 1 km at the distance of 72 km from the radar. The IKA data are operatively used for quantitative precipitation estimates and then an accurate calibration procedure is operated twice a year [128]. The antenna pointing is obtained in azimuth by using masts at known directions and in elevation with the plumb-line method. Measurements of power loss and using a signal generator as a reference are applied for the calibration of the received power. The online method to monitor the receiver stability and the antenna pointing in azimuth and in elevation is based on the observations of the Sun [129].

The online monitoring of stability for the IKA radar makes it possible to use this system as a reference for the cross-calibration procedure. In order to make this the PPI-scans available for the comparison with the ARM radars, the IKA radar has been mapped on a vertical plane obtaining an equivalent zenith-pointing mode. This radar is kept out from the consistency analysis of the Z_e - S relations to avoid problem related to the radar beam alignment and resolution (see Table 14).

5.2.3 *ARM cloud radar system (X/Ka/W): Sky-noise, cross-calibration and attenuation analysis*

The ARM cloud radar systems (with the acronyms XSACR, KAZR and MWACR) are integral part of the BAECC IOP. The antennas of the XSACR and KAZR are mounted on the same pedestal and then the beam alignment can be assumed optimal. At 17 m in distance from the XSACR and KAZR, the MWACR system has been mounted on a different container. All the ARM radars make zenith-pointing observations and the systems have been carefully aligned to zenith direction during the campaign. Looking at the technical properties of the radar in Table 14 I show you that the range gate spacing and the temporal sampling are comparable but there is a difference in the beam width between the XSACR and the other two systems. All the radar data are averaged over 5 minutes to uniform them in terms of beam width.

The quality of the radar products has been checked to be able to keep out a consistent X, Ka and W band Z_e -S relations with their uncertainty. Two aspects are related to this issue: calibration and attenuation of the radar data. For what concerns the calibration, an absolute calibration procedure has been performed at the beginning of the BAECC IOP using external standard target procedure, but I operate an additional cross-calibration in order to reduce biases between different systems. The selected method is to measure the calibration error at the top of the cloud where the small crystals scatter in the Rayleigh regime [88]. Looking at the particles small in terms of wavelength the particle sized with the DWR procedure is not possible and the DWR is expected to be equals to 0 dB and then any deviation from this value can be considered due to the calibration bias. As said in Section 5.2.2 the reference for this analysis is the IKA C-band radar assumed well-calibrated and compared to the XSACR radar. Then the XSACR is matched with the KAZR radar and the latter with the MWACR radar. In Figure 63 I show you the profile of the 15 February 2014 at 17:13 UTC in which I performed the calibration between 4 and 6 km and in Figure 64 the histograms of the three different calibration errors. The calibration error precision, measured as the standard deviation of the histograms in Figure 64, shows that the best result is for the error between K_a and W band and the worse is for C and X, this is related mostly at the beam width. Looking at Table 14 larger is the beam width greater is the measure dispersion and vice versa.

To solve the attenuation problem a sky-noise analysis has been performed for the millimeter-wavelengths radars, KAZR and MWACR, since they are more sensitive to problem related to the radome attenuation. The

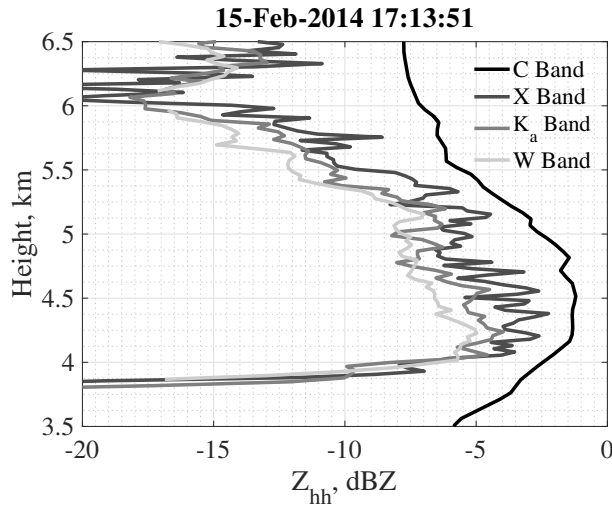


Figure 63: Radar profiles at C, X, Ka and W band for the 15 February 2014 at 17:13 UTC in which I performed the calibration in the most stable interval in height between 4 and 6 km.

flat shape of the radome for the KAZR increases the possibility to have amount of snow during the time. Consequently, when the temperature goes beyond the melting point of ice, the melting snow produces attenuation that should be monitored. On the other hand the conical shape of the MWACR radar limits the amount of snow because of the highest frequency is more sensitive to the freezing snow. The stability analysis made with the sky noise has been shown in figure 66 in terms of histogram of sky-noise power measured along all ten days of BAECC IOP. The standard deviation is around 0.25 and 0.14 dBm respectively for KAZR and MWACR radar; these values validate the selection of one case during the ten days to operate the cross-calibration. For the Ka Band is visible in figure 66 a second Gaussian-like with less occurrence centered around -68.06 dBm and is due to the previously explained radome attenuation problem. Another example is Figure 65 that shows for 12 February 2014 the effect of the jump in the sky noise due to the increased surface temperature responsible for the melting of the snow and then for the radome attenuation.

During the BAECC IOP, as a part of this, a campaign involving radiosondes was performed at Hyytiälä. The physical state of air has been monitored during all the days of the campaign. Then the physical parameters (barometric pressure, dry-bulb temperature and relative humidity) can become the input variables of the Millimeter-wave Propagation Model (MPM) [130] useful to take into account the two-way path attenuation due

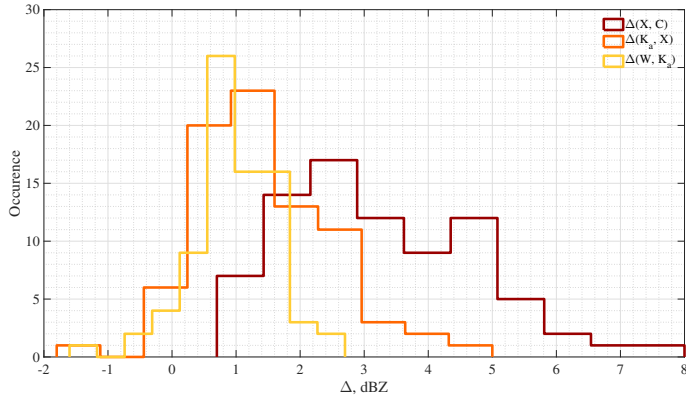


Figure 64: Calibration error histograms relates to the differences (Δ) between: X and C band radars (dark red), Ka and X band radars (orange), and W and Ka radars (yellow).

Table 15: Attenuation for Ka and W band at 6 km for the 15 February 2014 at 17:24 UTC.

	Ka	W
Line-by-Line (dB)	0.1518	0.2228
O ₂ (dB)	0.0299	0.0288
H ₂ O (dB)	0.0351	0.2588
A _{dp, two-way} (dB)	0.4335	1.0206

to line by line spectra and continuum spectra from dry air and water vapor. I made this analysis for all the dataset that confirms also a stable two-ways attenuation trend over Hyytiälä and in Table 15 are reported the values related to the case in which I have performed the cross-calibration. As expected the attenuation for W band is twice as large as for Ka band and most of those was due to the water vapor. Adding at the calibration also the attenuation in Table 15 I obtain the followed correction factors: 2.9 dBZ for the XSACR, 3.9 dBZ for the KAZR and 4 dBZ for the MWACR.

Attenuation analysis

To better define the way in which Table 15 is obtained for the Ka and W band attenuation I can start showing:

$$A = \int_0^H \alpha(h) dh \quad (161)$$

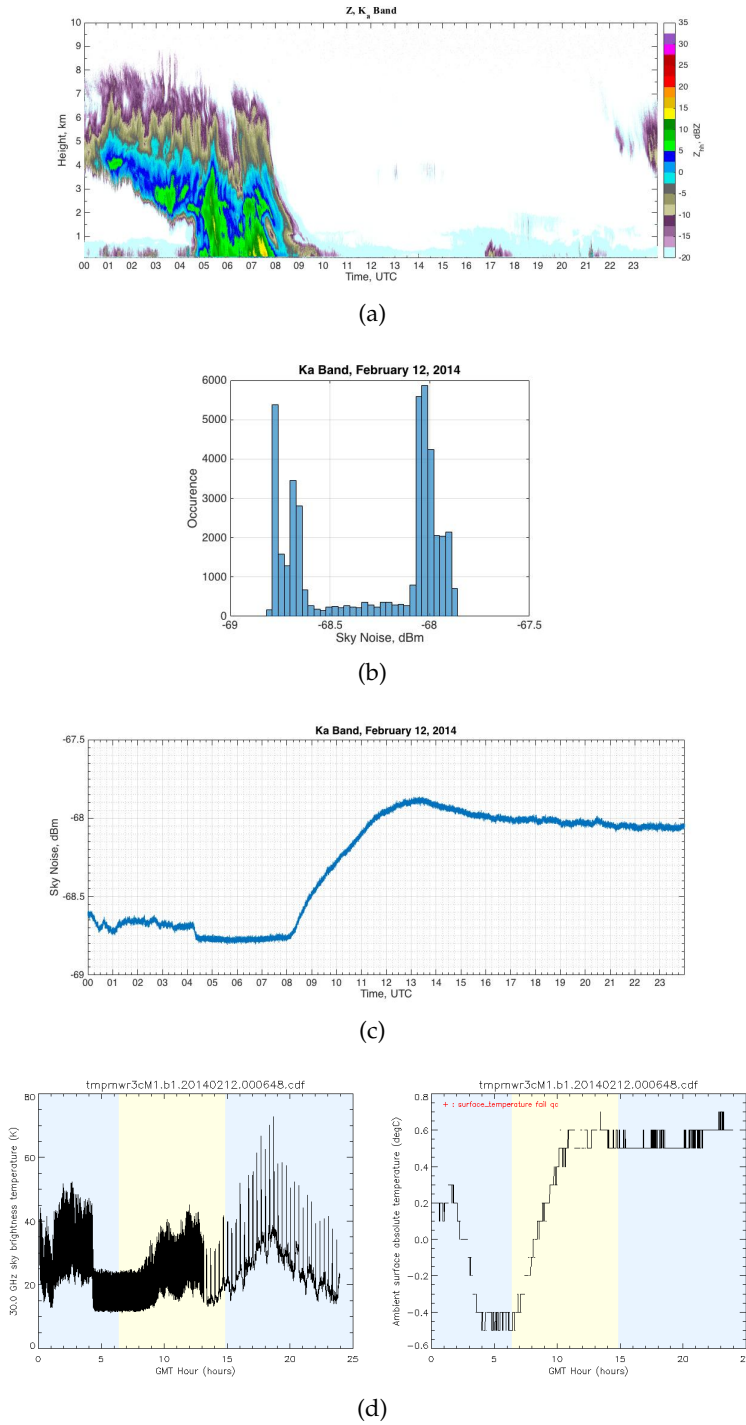


Figure 65: Sky noise for the Ka band for 12 February 2014: (a) A-scope at Ka-band; (b) Sky Noise histogram in dBm; (c) Sky Noise time-series in dBm; (d) Sky brightness temperature on the left, surface temperature on the right.

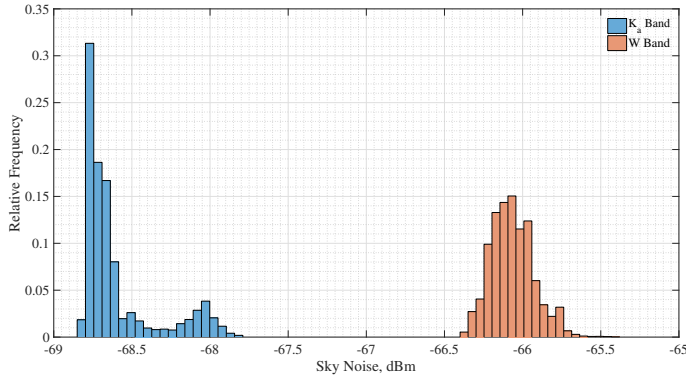


Figure 66: Relative frequency histograms of the sky noise for the Ka and W Band radars for all the ten days of BAECC IOP.

that is the cumulative path attenuation in dB where $\alpha(h)$ is the specific power attenuation measured using the MPM in [130] with respect to the height-path h (km). From equation (161) I am able to define the double-path cumulative attenuation in dB as: $A_{dp} = 2A$. As said Liebe in [130] formulated a practical atmospheric MPM that predicts attenuation, delay, and noise properties of most air frequencies up to 1000 GHz. The heart of the model is a macroscopic measure of interactions between radiation and absorbers expressed as complex refractive index N in units ppm

$$N = N_0 + N'(f) + jN''(f) \quad (162)$$

where N_0 is f -independent, $N'(f)$ is the refractive dispersion spectra and $N''(f)$ is the refractive absorption spectra. The specific power attenuation can be expressed as the imaginary part of equation (162)

$$\alpha = 0.1820fN''(f) \quad (163)$$

where f is the frequency expressed in GHz. The imaginary part $N''(f)$, the absorption spectra, is obtained as the sum of line-by-line spectra plus various continuum spectra N_p (dry air), N_e (water vapor) and N_w (hydrosols)

$$N''(f) = \sum_{i=1}^{n_a} (SF'')_i + \sum_{i=1}^{n_b} (SF'')_i + N''_p + N''_e + N''_w \quad (164)$$

where I take into account the resonance information for $n_a = 48$ oxygen lines and $n_b = 30$ water vapor lines; S is the line strength in kilohertz and F'' is the imaginary part of a line shape function in GHz^{-1} . I can neglect

Table 16: Line parameters defined in [130].

Symbol	O ₂ Lines in Air	H ₂ O Lines in Air
S , KHz	$a_1 p \theta^3 \exp(a_2(1 - \theta))$	$b_1 e \theta^{3.5} \exp[b_2(1 - \theta)]$
γ , GHz	$a_3(p\theta^{(0.8-a_4)} + 1.1e\theta)$	$b_3(p\theta^{0.8} + 4.8e\theta)$
δ	$a_5 p \theta^{a_6}$	0

the N_w or continuum spectra from the hydrosols because the calibration is computed where there is no hydrosols presence ($N_w'' = 0$). I divide the absorption spectra in a line-by-line spectra (1) and a continuum spectra (2)

$$N_1''(f) = \sum_{i=1}^{n_a} (SF'')_i + \sum_{i=1}^{n_b} (SF'')_i \quad (165)$$

and

$$N_2''(f) = N_p'' + N_e'' \quad (166)$$

The line-by-line absorption spectra is composed by the Van-Weisskopf function that was modified to describe, to first order, line overlap effects; this leads to local absorption line profiles in the form:

$$F''(f) = \left(\frac{1}{X} + \frac{1}{Y} \right) \frac{\gamma f}{\nu_0} - \delta \left[\frac{\nu_0 - f}{X} + \frac{\nu_0 + f}{Y} \right] \frac{f}{\nu_0} \quad (167)$$

with the abbreviations $X = (\nu_0 - f)^2 + \gamma^2$, $Y = (\nu_0 + f)^2 + \gamma^2$ and $Z = (\nu_0^2 + \gamma^2)/\nu_0$. The line parameters are calculated according to the Table 16.

Line center frequencies ν_0 and the spectroscopic coefficients a_1 ($\geq 10^{-7}$ Hz/Pa) to a_6 , and b_1 ($\geq 10^{-3}$ Hz/Pa) to b_3 for strength S , width γ and overlap correction δ are listed in [130]. Instead for the continuum absorption spectra is

$$N_2''(f) = N_p'' + N_e'' \quad (168)$$

that increases monotonically with frequency. The dry air continuum

$$N_p''(f) = (2a_0\gamma_0[1 + (f/\gamma_0)^2][1 + (f/60)^2]^{-1} + a_p p \theta^{2.5}) f p \theta^2 \quad (169)$$

where the width parameter for the Debye spectrum of O₂ is $\gamma_0 = 5.6 \times 10^{-3} (p + 1.1e)\theta^{0.8}$ (GHz) [131]. The continuum coefficients are $a_0 = 3.07 \times 10^{-4}$

[132] and $\alpha_p \equiv 1.4(1 - 1.2f^{1.5}10^{-5})10^{-10}$ [133]. The water vapor continuum is derived empirically from fitting experimental data

$$N_e''(f) = [b_f p + b_e e \theta^3] f e \theta^{2.5} \quad (170)$$

where $b_f = 1.4 \times 10^{-6}$ and $b_e = 5.41 \times 10^{-5}$. Gaseous oxygen (O_2), water vapor (H_2O) and suspended water droplets (hydrosols) are considered to be the principal absorbers in moist air. The physical state of air is described by four measurables that are the input variables of the MPM as height distributions (0-30 km)

- Barometric pressure, P (KPa)
- Temperature or dry-bulb temperature, T_{dry} (K)
- Relative Humidity, RH
- Suspended droplet concentration, w

where P - T_{dry} -RH can be measured by a sounding. The input model variables of the MPM can be obtained from the P - T_{dry} -RH variables

- The barometric pressure P (KPa) is the sum of the dry air pressure (p) and partial water vapor pressure (e)

$$P = p + e \quad (171)$$

- The temperature T_{dry} (K) is converted to a relative inverse temperature parameter

$$T_{dry} = 300/\theta \quad (172)$$

- RH can be obtained as

$$RH = (e/e_s)100 \quad (173)$$

- Water vapor is almost always present in the surrounding air. The maximum saturation pressure of the water vapor in moist air varies with the temperature of the air vapor mixture and can be expressed in hPa as

$$e_s = 0.001(\exp(77.3450 + 0.0057T_{dry} - 7235/T_{dry})/T_{dry}^{8.2}) \quad (174)$$

- Suspended droplet concentration $w = w_0 G(RH)$ (g/cm^3).

An example of the MPM is presented in Figure 67 looking at the input of the model for the 15 February 2014 and the specific and cumulative path attenuation for K_a band (Figure 68- 69) and W band (Figure 70- 71).

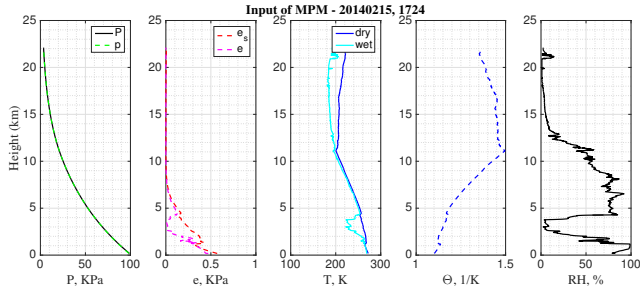


Figure 67: Case study: 15 February 2014 - Input of the MPM.

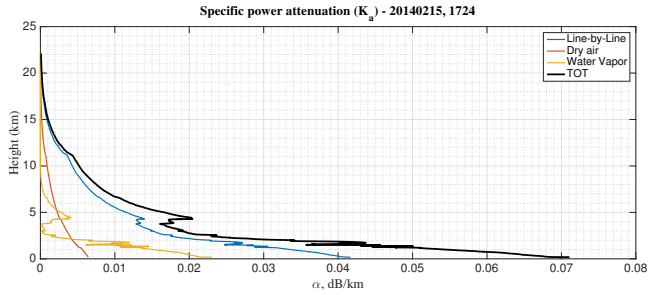


Figure 68: Case study: 15 February 2014 - Specific power attenuation in K_α band.

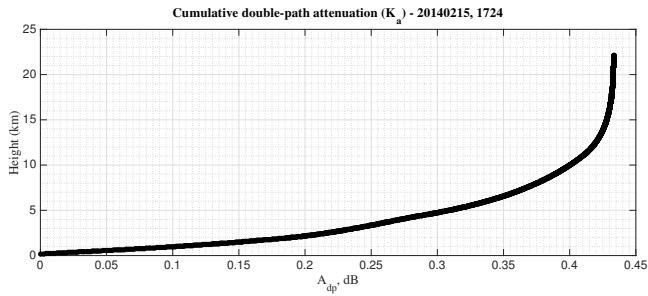


Figure 69: Case study: 15 February 2014 - Cumulative double-power attenuation in K_α band.

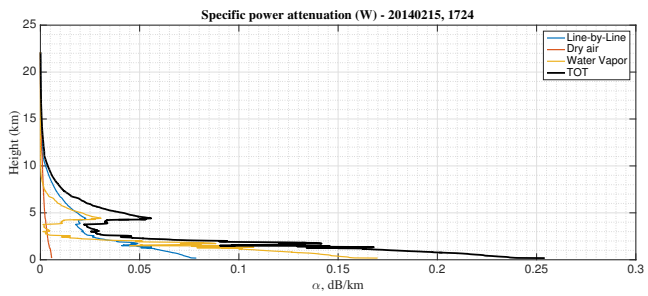


Figure 70: Case study: 15 February 2014 - Specific power attenuation in W band.

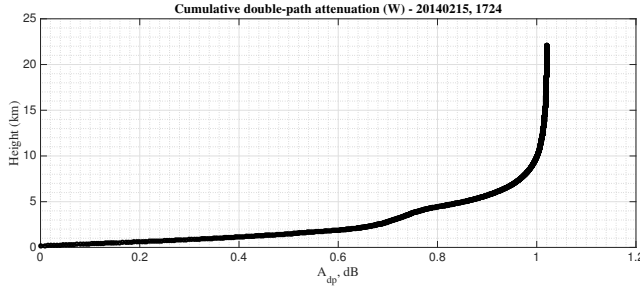


Figure 71: Case study: 15 February 2014 - Cumulative double-power attenuation in W band.

5.3 METHODS

The methods applied to investigate the consistency of the X, Ka and W-band Z_e - S relations are presented in this section. In order to link together the scattering and the microphysical properties two different simulation techniques, TMM and DDA, have been applied.

5.3.1 Z_e - S relations at X/Ka/W-band

The equivalent reflectivity Z_e , measured by the radar systems at different wavelengths, and the liquid-water-equivalent snowfall rate S , evaluated from PIP, are the two correlated variables of the study. The liquid-water-equivalent snow rate S in mm/hr is derived from the well-known formula [124]

$$S = 3.6 \int m_D(D_{deq})v(D_{deq})N(D_{deq})dD_{deq} \quad (175)$$

where all the parameter are derived from PIP: m_D is the mass in g, v is the velocity in cm/s [124] and $N(D)$ is the PSD in $\text{mm}^{-3}\text{m}^{-1}$, all of these expressed in terms of the diameter disk-equivalent D_{deq} .

Radar data are referred to zenith-pointing systems so that the initial reflectivity measurements are in function of the altitude. The first effort has been to set up a coordinated treatment of radar and in-situ PIP measurements in order to match reflectivity and snowfall rate. The nearest path to the ground is the best choice in this respect. I also should take into account a selection of paths spatially consistent for the various radar systems whose 3 dB antenna beamwidth is also different, looking at the Table 14. These differences produce different values for the Fraunhofer

far-field distance that is the distance where the return signal is not affected by near-field effects due to the antenna pattern. The beamwidth difference is related to the antenna diameter that is respectively for XSACR, KAZR and MWACR, 1.82; 1.82; 0.9 m so that the Fraunhofer distance ($2D^2/\lambda$) is approximately 214 m for XSACR, 773 m for KAZR and 514 m for MWACR. Taking into account the near-field influence, all the radar data are selected at 400 m guaranteeing to avoid these effects [134] and to deal with suitable reflectivities.

Another important aspect is related to the different time acquisitions for the different instruments. In Table 14 I note that the temporal sampling of the radars is 2 s instead for the PIP instrument is 1 min. To avoid the introduction of spurious results I decide for a down-scaling of the data averaging on a time-window of 5 min. As said in Section 5.2.3 the averaging is also useful to yield uniform the acquisitions in terms of beam width.

The power-law form is assumed for the Z_e - S relations, $Z_e = AS^b$ as in [110, 117]. I remind that in this general form Z_e is expressed in mm^6m^{-3} and S is in mm/h . From a power-law form I am able to choose at least two different approaches, a non-linear least squares inside the linear space of the measurements or a linear least squares in the log-log space. I have adopted the last approach by applying a linear regression as in [109] thus avoiding non-linearity instabilities. The applied log-log model is given by:

$$\log_{10}\bar{Z}_e = b \log_{10} S + \log_{10} A. \quad (176)$$

where the equation is solved in terms of \bar{Z}_e that is the averaged reflectivity selected in altitude disregarding the near-field effects.

5.3.2 *Direct computations using the T-matrix method*

Single scattering computations are performed using the TMM code by Mishchenko [135] in the version developed by Leinonen [123]. The purpose is to obtain a good approximation for the equivalent reflectivity Z_e in order to investigate the Z_e - S relations in snowfall from the in-situ microphysical parameters. For what concerns the snowflake shape, the TMM allows to model the nonspherical hydrometeors through the spheroids. The radar community usually models raindrops using a spheroidal model and, to some extent the latter is also useful for more complicate particle structures such as snowflakes [115]. This is because the microwave backscatter properties do not depend on the small details, but mostly on the overall structure.

The most important parameter to characterize the whole structure is the spheroid aspect ratio $r = b/a$ where a and b are the horizontal and vertical dimensions of the spheroid ($r = 1$ spherical particle, $r \geq 1$ prolate particle and $r \leq 1$ oblate particle) [116]. The spheroidal model is useful for smaller snowflake size but it loses the applicability for very high frequency, such as W band, in case of larger snowflakes with heavily small aspect ratio (dendrities) as seen in [120]. For a consistency study of the Z_e -S relations in snowfall, the spheroidal model can be considered complete if the average in time weakens the effect of the particle complex structure usually visible only for short time period of observations [123]. Using the spheroid aspect ratio as a tuning parameter, it is possible to identify two different behaviors: $r \approx 0.5 - 0.7$ remains approximately constant changing the frequencies for large particles (such as rimed particles) and r changes value from large to small increasing the frequency for small particles (such as fluffy particles) [114, 115, 123].

The snowflakes in general due to aerodynamic forcing fall with the major axis oriented horizontally [114, 115]. Following a convention presented in [115, 117], the TMM is set with single shaped snowflakes oriented preferably horizontally with the 0° and standard deviation of 10° with respect to the vertical. All the radars (X, Ka and W Band) are as said in Section 5.2.3 vertically pointing system then there is no polarization dependence but the value of standard deviation influences the magnitude of Z_e .

To better define the influence of the snow aspect ratio tuning parameter, I define the density ρ in g/cm^3 as dependent from it

$$\rho = \frac{m}{\pi/6 D_{Veq}^3} \quad (177)$$

in which the mass m_D is defined as in [124] and D_{Veq} is the diameter volume equivalent defined from D_{max} , the maximum diameter obtained by PIP [124], as $D_{Veq} = r^{1/3} D_{max}$. The presence of the aspect ratio inside the density reflects its dependency on the complex refractive index of snow m_S that is defined through the Maxwell Garnett EMA.

The Γ -size distribution in $\text{mm}^{-1} \text{m}^{-3}$ is assumed to model the snowflake number concentration

$$N(D_{Veq}) = N_{w,Veq} f(\mu_{Veq}) \frac{D_{Veq}^{\mu_{Veq}}}{D_{0,Veq}} \exp(-\Lambda_{Veq} D_{Veq}) \quad (178)$$

in which $N_{w,Veq}$ is the intercept parameter in $\text{mm}^{-1} \text{m}^{-3}$, $f(\mu_{Veq})$ and μ_{Veq} parameter are without dimensions, and Λ_{Veq} is the slope of the

distribution in 1/mm. This Γ -PSD can essentially be expressed starting from the moments of the snowflakes distributions measured by PIP, as in [6], taking into account the variable changing from D_{\max} to D_{Veq} as follows

$$N_{w,\text{Veq}} = N_{w,\max} \frac{dD_{\max}}{dD_{\text{Veq}}} = N_{w,\max} \frac{1}{r^{1/3}} \quad (179)$$

$$D_{0,\text{Veq}} = D_{0,\max} r^{1/3} \quad (180)$$

$$\Lambda_{\text{Veq}} = \Lambda_{\max} \frac{dD_{\max}}{dD_{\text{Veq}}} = \Lambda_{\max} \frac{1}{r^{1/3}} \quad (181)$$

$$\mu_{\text{Veq}} = \mu_{\max}. \quad (182)$$

The equivalent reflectivity Z_e of a snowflake ensemble is given by integrating the TMM-derived radar cross section of a single particle with the Γ -PSD in equation (178).

5.3.3 Computations using particle scattering database

Discrete Dipole Approximation (DDA) is used to characterize the single scattering properties of snowflakes using complex and realistic shape models of snow particles. Although the PIP instrument records a 2D image of the falling particles DDA is not used to compute the single scattering properties of individual observed snowflakes, but rather it is used to compile lookup tables (LUT) of scattering properties of generic realistically shaped particles. In fact, even though sophisticated particle imager can provide detailed description of the particle morphology by means of a multi-angle view [136] the internal structure of snowflakes is still not observable; moreover the huge computational cost of DDA would make such approach prohibitive using current available calculators.

LUT can be used to estimate the average scattering properties of observed ice particles by providing some constraints on the microphysical properties of snow. In particular [137] have published an extensive LUT of backscattering properties for realistically shaped snow particle models. The shape model is obtained by accurately simulating the microphysical processes that lead to snowflake growth through their falling path. In particular, the snowflake formation is simulated by aggregation of pristine

dendrites and subsequent or simultaneous riming of those aggregates using multiple values of equivalent liquid water path which in turns drive the riming degree.

The simulation of the riming process allows the scattering database to span through a large range of particle masses and sizes allowing to use those microphysical features to constrain the ice particle scattering properties. The scattering properties of the simulated particles are in fact picked from the LUT by finding the entries that most closely match the particles size and mass as it has been retrieved in [124] as it follows.

For each size range defined by the PSD discretization operated by PIP the LUT is filtered for the particles with a size that falls within the PSD size bin. Than using the retrieved m_D - D relation the LUT entries are sorted with respect to the difference between their mass and the expected particle mass computed using the retrieved mass-dimensional relation. An arbitrary number of 10 entries that most closely match the retrieved m_D - D relation are selected and their scattering properties are averaged in order to define the representative backscattering cross section of that particular size range. Larger number of particles can be picked from the LUT in order to represent a larger variability of particle mass, but the effects of including heavier and lighter particles tends to cancel out in the averaging and does not produce appreciable differences in the final integrated reflectivity.

It is worth noting that [137] scattering properties are computed for randomly oriented particles at fixed orientation, meaning that each particle composing the database does not have any preferential orientation, but its scattering properties are simulated at a fixed orientation. The inclusion of multiple particles within each size range is then required to take into account also for the orientation averaging rather than just the inclusion of some variability in the microphysical properties of realistic snowflakes.

5.4 RESULTS

The results are shown for four case studies taken from the BAECC campaign. The cases are relevant because they show two different microphysical behaviors due to fluffy and rimed snow physical effects that are fully explained using the TMM numerical computations. The selection of only four cases on the ten cases extracted from the BAECC IOP is because they are available for the millimeter wavelengths (Ka and W) along with the PIP instrument data. The numerical modeling is also needed to take into

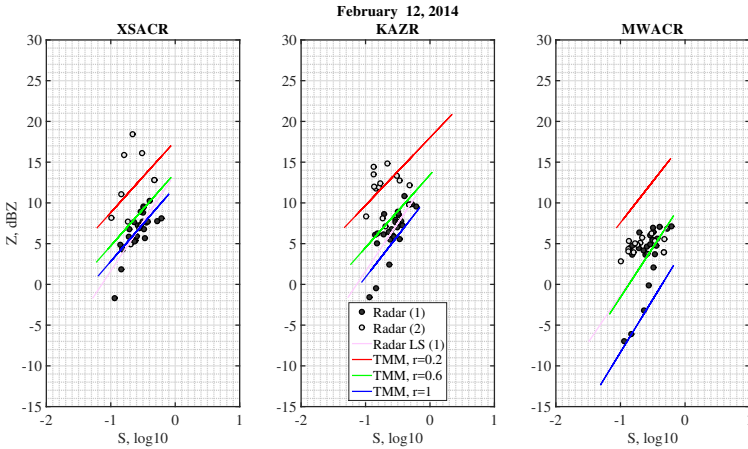


Figure 72: Case study: 12 February 2014 - Scatter plot of the equivalent reflectivities measured by the radar (points) with respect to the snow-rates S measured by PIP are shown. The pink line represents the Z_e - S measured relationship evaluated using a least-square in the log-log space. Z_e - S relations estimated with the TMM are shown for different aspect ratios (0.2, 0.6, 1) in red, green and blue lines.

account the variability of the Z_e - S relations and then the uncertainty of the snowfall retrieval.

5.4.1 Analysis of X, Ka and W band $Z_e - S$ empirical relations

The first purpose of our study is, as mentioned, to compare the radar reflectivity data at different frequencies with the ground based data from PIP expressed as the snowfall rate. Figures 72-75 show the scatterplots of radar reflectivity versus the snowfall rate from PIP in black points for all the available bands. A linear regression, explained in Section 5.2.3, is applied to estimate the Z_e - S line in the logarithmic space represented in pink. The coefficients obtained from the linear regression are summarized in Table 18. The snowfall-rate estimates are also shown in Table 17 for the four different cases observed by the ground-based radars at X, Ka and W bands.

For what concerns the first case study of the 12 February 2014 in Figure 72, I have divided the data time series in two parts by using the median diameter measured by PIP: a part of small diameter particles with D_0 less than 1 mm in black points and a part of larger diameter particles in grey points. This case is well-representative of a fluffy snow case and I

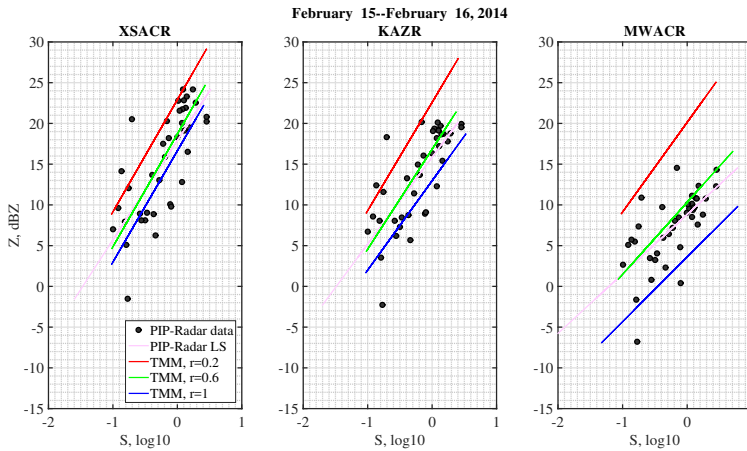


Figure 73: Case study: 15-16 February 2014 - Scatter plot of the equivalent reflectivities measured by the radar (black points) with respect to the snow-rates S measured by PIP are shown. The pink line represents the Z_e - S measured relationship evaluated using a least-square in the log-log space. Z_e - S relations estimated with the TMM are shown for different aspect ratios (0.2, 0.6, 1) in red, green and blue lines.

used only the black point measured by the radar with smaller diameters to characterized the retrieval. A general trend of these results is that, increasing the frequencies, the reflectivity value decreases. The coefficients of the 12 February 2014 shown in Table 18 present similar values for A (22.98 – 21.92) and b (1.19 – 1.18) coefficients for the X and Ka band. For the W band the values are respectively 10.86 and 1.16 for A and b coefficients. This is the only case analyzed not compliant with the values generally presented in literature ([115], [117]) but the fact could be related to the fluffy snow with small diameter particles and then to the low accumulation of snow in the time interval considered. The values in Table 17 highlight that the accumulation estimated by PIP compared to the radar estimation is underestimate for the X band and overestimate for the Ka and W bands.

For the three remaining cases the coefficient values are in line with the literature ([115], [117]). The values of the A and b coefficients decrease progressively increasing the frequencies. The rimed snow cases, 15-16 and 21-22 February, in Figure 77-74 present coefficients very similar with low variation for the A and a little bit higher variation for the b coefficients. For the 15-16 February the radar estimation of the snow accumulation is underestimated for all the three frequencies; instead, for the 21-22 February all the three frequencies present an overestimation with respect to the

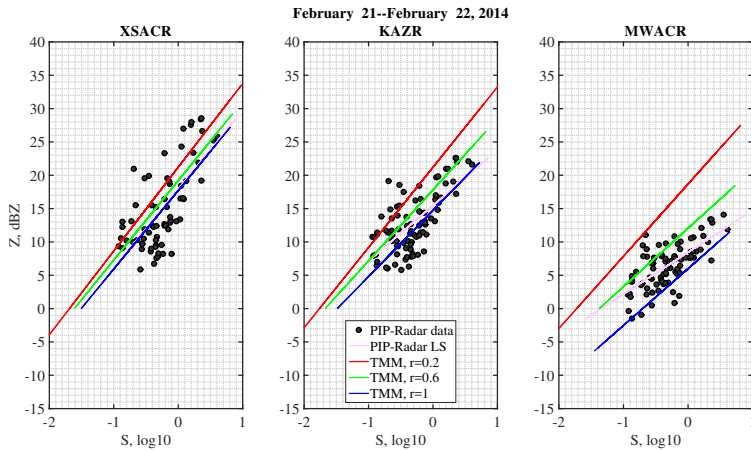


Figure 74: Case study: 21-22 February 2014 - Scatter plot of the equivalent reflectivities measured by the radar (black points) respect to the snow-rates S measured by PIP are shown. The pink line represents the Z_e - S measured relationship evaluated using a least-square in the log-log space. Z_e - S relations estimated with the TMM are shown for different aspect ratios (0.2, 0.6, 1) in red, green and blue lines.

PIP value. The 20 March, in Figure 75 produces an overestimation for the snow accumulation estimated by the radar with respect to PIP but in this case the coefficients are bigger with respect to the previous two for the A coefficient.

5.4.2 Explaining Z_e - S relations with computations

T-Matrix Method (TMM)

The TMM is the selected scattering numerical method, taking in input the PIP data, to represent the real behavior of the radar observable Z_e . The overall shape is the factor that mainly influenced the backscatter properties on larger temporal scale data (minutes), whereas the particle structure is more significant on shorter temporal scale data (seconds). For our purpose in which the data are averaged on five minutes scale, the overall shape has been taken into account using the spheroid aspect ratio r . In the TMM computations, the snowflakes are assumed spheroidal and I have used the scattering modeling in Section 5.4.1 to evaluate the uncertainty of the data in terms of the independent term r .

For each case study I am able to compare the radar equivalent reflectivity with the numerical one that referring to Figs. 76, 77, 78 and 79, this

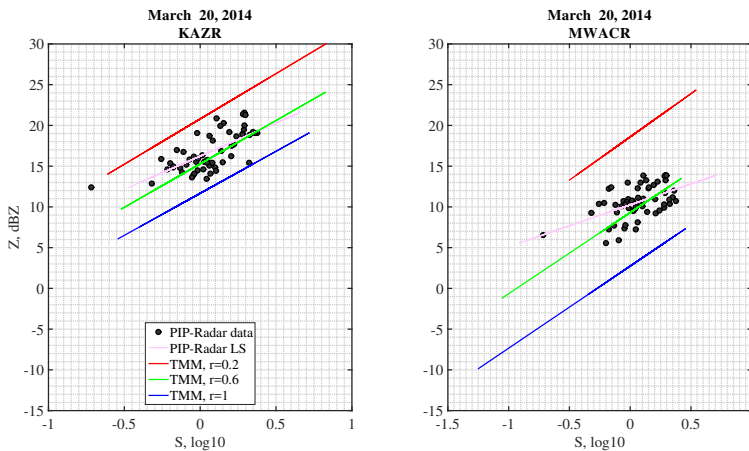


Figure 75: Case study: 20 March 2014 - Scatter plot of the equivalent reflectivities measured by the radar (black points) respect to the snow-rates S measured by PIP are shown. The pink line represents the Z_e - S measured relationship evaluated using a least-square in the log-log space. Z_e - S relations estimated with the TMM are shown for different aspect ratios (0.2, 0.6, 1) in red, green and blue lines.

can be visualized as a uncertainty bounds of possible Z_{TMM} functions depending on the aspect ratio r . The highest values of these uncertainty bounds are defined by TMM with an aspect ratio of 0.2 (red), useful to model complex particles with extremely oblate behaviors. The low values of the uncertainty bounds are related to the aspect ratio of 1 that is the scattering signature for a spherical particles (blue). Inside the uncertainty bounds, the black points are the radar observable values for the equivalent reflectivity.

All the results are expressed in Figs. 76, 77, 78 and 79 as a function of time and I note that the measured data are included inside the uncertainty curves. The dotted line is the $r = 0.6$ curve assumed as a reference because there are many past studies showing that non-spherical particle modeling agree better with aspect ratio of about $r = 0.6 - 0.7$ than using a spherical model with $r = 1$, especially for larger aggregate crystals [115]. Using the spherical model to obtain the equivalent reflectivity computed from the PIP measurements, it may result in an underestimation bias that changes with frequency. The bias is approximately on average 1.7 dBZ for the X band, 2.5 dBZ for the Ka band and 6 dBZ for the W band. This effect is due to the fact that by increasing the frequency (from X to W band) the reflectivity is more sensible to the shape of the non-spherical particles. The Figs. 76-79 show also that is possible to have low aspect-

Table 17: Z_e -S at X, Ka and W band measured by the radars and PIP instrument evaluated using the least-square in the log-log space.

Date	Band	A	b
12 Feb. 2014	X	22.98	1.19
	Ka	21.92	1.18
	W	10.86	1.16
15-16 Feb. 2014	X	61.45	1.22
	Ka	38.39	1.06
	W	7.65	0.73
21-22 Feb. 2014	X	61.73	1.19
	Ka	35.23	0.83
	W	7.0	0.63
20 Mar. 2014	X	-	-
	Ka	41.98	0.81
	W	10.60	0.51

ratio values $r = 0.2 - 0.3$ for modeling dendrites that are larger than the millimeters. In these cases the underestimation can progressively increase having (for $r = 0.2$) approximately double values with respect to the previous ones 5.5 dBZ for the X band, 7 dBZ for the Ka band and 12 dBZ for the W band.

The Figs. 76-79 have a different behavior, in terms of standard deviations, with respect to the frequency. Looking at the uncertainty bounds described by the edge line ($r = 0.2$) and the spherical line ($r = 1$), I note that the thickness of the uncertainty bounds are approximately constant for the X band and vary progressively increasing the frequency. In Figure 76 I note that with respect to the starting time 04:50 UTC, the period of most strong precipitation between 06:50-07:30 UTC presents a great variation of the thickness in the highest frequencies (Ka and W band). This is also visible in Figure 77 in the period between 00:00-01:00 UTC and in Figure 78 between 23:00-00:00 UTC.

Note that X band is a centimeter band and all the particles are basically small with respect to this wavelength; this means that in this case the backscatter is less sensitive to the particle sizes. The difference between the spherical ($r = 1$) and the extremely non-spherical particle ($r = 0.2$) with re-

Table 18: Variability of the Z_e - S (Z_e in mm^6m^{-3} , S in mmh^{-1}) relations due to main assumption about the aspect ratio that influenced the refractive index and the scattering properties.

Date	Band	Z_e - S ($r=0.2$)	Z_e - S ($r=0.4$)	Z_e - S ($r=0.6$)	Z_e - S ($r=0.8$)	Z_e - S ($r=1$)
12 Feb. 2014	X	$63.24S^{0.79}$	$34.08S^{0.78}$	$25.11S^{0.78}$	$20.05S^{0.79}$	$16.61S^{0.80}$
	Ka	$63.34S^{0.83}$	$32.08S^{0.84}$	$22.12S^{0.89}$	$16.48S^{0.95}$	$12.71S^{1.02}$
	W	$58.72S^{1.01}$	$22.90S^{1.12}$	$11.44S^{1.22}$	$5.77S^{1.27}$	$2.91S^{1.30}$
15-16 Feb. 2014	X	$195.25S^{1.38}$	$105.17S^{1.39}$	$74.13S^{1.38}$	$57.17S^{1.37}$	$46.09S^{1.36}$
	Ka	$181.23S^{1.33}$	$82.49S^{1.29}$	$48.18S^{1.23}$	$30.29S^{1.16}$	$19.78S^{1.10}$
	W	$103.23S^{1.10}$	$28.44S^{0.97}$	$10.76S^{0.88}$	$4.71S^{0.83}$	$2.29S^{0.79}$
21-22 Feb. 2014	X	$132.02S^{1.26}$	$108.05S^{1.19}$	$83.08S^{1.19}$	$68.86S^{1.18}$	$58.91S^{1.18}$
	Ka	$131.92S^{1.20}$	$93.20S^{1.10}$	$60.49S^{1.06}$	$41.85S^{1.03}$	$29.72S^{0.99}$
	W	$73.82S^{1.08}$	$36.22S^{0.92}$	$16.05S^{0.88}$	$7.74S^{0.86}$	$3.97S^{0.85}$
20 Mar. 2014	X	-	-	-	-	-
	Ka	$120.18S^{1.11}$	$55.92S^{1.09}$	$33.72S^{1.06}$	$21.84S^{1.049}$	$14.68S^{1.03}$
	W	$72.35S^{1.06}$	$21.42S^{1.03}$	$8.52S^{0.99}$	$3.83S^{0.99}$	$1.88S^{1.01}$

spect to the particle sizes varies around 1.7 dBZ constant value. Increasing the frequencies to the millimeter band (Ka and W band), the particles on average are comparable or larger with respect to the wavelength and the backscatter is progressively more sensitive to the particle sizes. In fact for the Ka and W band the difference between the spherical and the extremely non-spherical particle increases linearly with the particle size.

Furthermore I note that I have different accords during the time between the TMM and the measured value. For example, starting with the first case study of the 12 February 2014 that is a fluffy snow case, I have a trend before the heavy precipitation period (07:00-08:00 UTC) that shows as the aspect ratio tuning parameter decreases increasing the frequency: the X band data are in accord with the spherical particle simulated by the TMM ($r = 1$) and the Ka and W band are in agreement with the aspect ratio of 0.6. After the 07:00 UTC in the heavy precipitation period I have not available data for the X band but I note that the aspect ratio change at $r = 0.8$ for the millimeter radar. For the 15-16 February 2014 that is a rimed snow case I have two periods: before the heavy precipitation (until 22:10 UTC), as for the previous case, the aspect ratio decreases increasing the frequency, during the heavy period (from 22:50 to the end) the aspect ratio is constant with the frequency at 0.6. The case study of 21-22 February 2014 is also a rimed snow case before the 22:00 UTC the relation is 1, 0.8 and 0.8 and during the heavy precipitation period is constant at $r = 0.6$ independently from the frequency. The consideration is also valid for the last case study of 20 March 2014 in which is clearly visible that the constant $r = 0.6$ is able to represent all the time series for the millimeter wavelengths (Ka and W bands). For this case the X band data are not available and then are not shown.

The power-law formula defined in Section 5.3 as $Z_e = AS^b$ together with the log-log formula for the least square algorithm in equation (176) provides different Z_e -S relations as a function of the aspect ratio, as shown in Table 18. Figs. 72, 73, 74 and 75 show the Z_e -S relations obtained from the TMM numerical computations using the method explains in Section 5.3 plotted over the radar data. Figure 72 referred to the case study of the 12 February 2014 easily shows the behavior of the micro-physical properties (represented by the TMM with aspect ratio of 0.2, 0.6 and 1) with respect to the scattering properties: when the frequency increases progressively the aspect ratio decreases. This general trend is visible also for the remained two case studies; note that the aspect ratio of 0.6 for the 15-16 February and 20 March 2014 and the aspect ratio of 0.8 for 21-22 February 2014 could be taken as a benchmark for all the bands. These two effects are

related to the presence of fluffy snow for the whole 12 February 2014 and in the first part of the remained days and of rimed snow for the last part of the 15-16 and 21-22 February 2014 and the whole 20 March 2014.

In order to obtain one Z_e - S relation for each case study a weighted least squares approach is applied on the time interval i

$$Q = \sum_i w(i)(Z_e(i) - Z_{TMM}(i, r_s))^2 \quad (183)$$

where as in the least square the unknown values of the aspect ratio r in the regression function are estimated by finding the numerical values for the parameter estimates that minimize the sum of the squared deviations between the radar measurements Z_e and the TMM scattering model Z_{TMM} . Each term in the weighted least squares criterion includes an additional weight, $w(i)$, that is in our case the snow rate S estimated from PIP that determines much influence from the period of heavy precipitation on the final parameter estimates.

Using the weighted least square in equation (183) I obtain a generalized aspect ratio for each case study that is useful to obtain Z_e - S relations for all the bands (highlighted in Table 18 with the bold text). Directly from these highlighted relations applied to the radar data, I obtain the liquid snowfall accumulation estimated respectively from PIP and the different radars in Table 17.

In general, the consistency of the TMM has been demonstrated for rimed snow case studies out of the heavy period of precipitation as in [138]. Within these time periods by selecting one aspect ratio for each case study is possible to obtain a good approximation of the radar measurements. On the other hand inside the heavy period of precipitation or for fluffy snow case studies, when the snow particle sizes are larger, the TMM is not able to represent the radar measurements using a single aspect ratio.

Comparison between TMM and DDA

The single particle model obtained with the TMM is compared also with the Amsterdam DDA code (ADDA) by [139].

In Figure 80 I see the co-polar backscatter cross section σ_{hh} of oblate particles for the four case studies computed at the W band. I show the highest band because is more critical, where the particles are approximately similar or larger with respect to the wavelength (millimeter) and then the scattering migrates from the Rayleigh region. The TMM in red, green and blue line is referred to different aspect ratios ($r = 0.2, 0.6, 1$, respectively) and is compared to the DDA method (triangle marker). The black

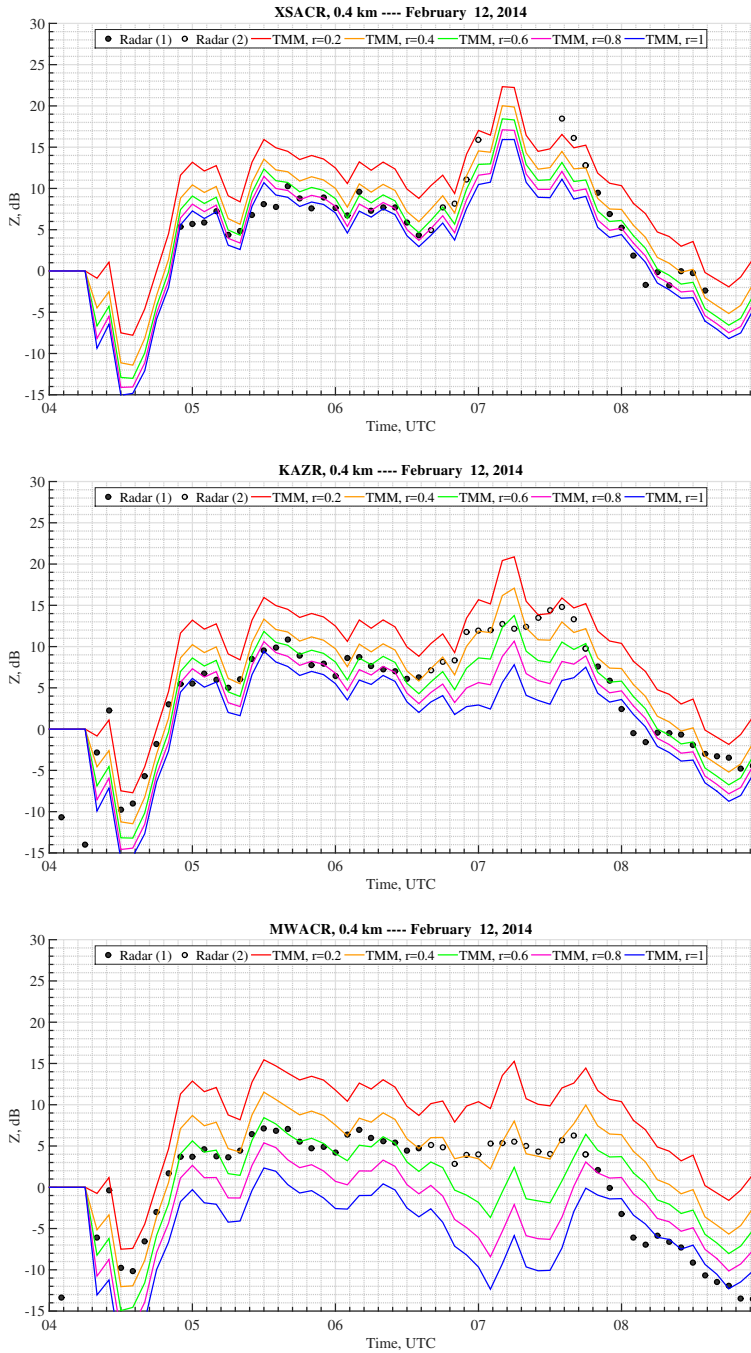


Figure 76: Case study: 12 February 2014 - Equivalent reflectivity measured by the radar (black points) compared with the TMM results for aspect ratios from 0.2-1.

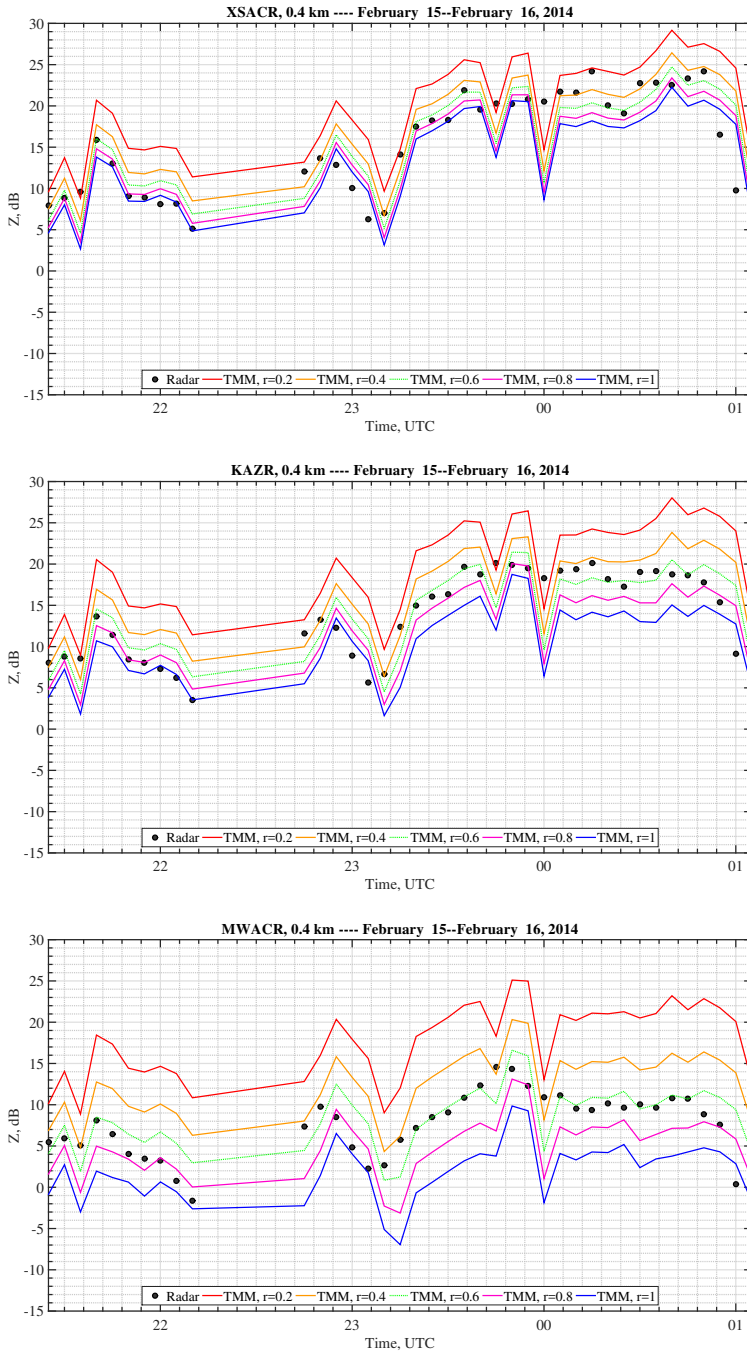


Figure 77: Case study: 15-16 February 2014 - Equivalent reflectivity measured by the radar (black points) compared with the TMM results for aspect ratios from 0.2-1.

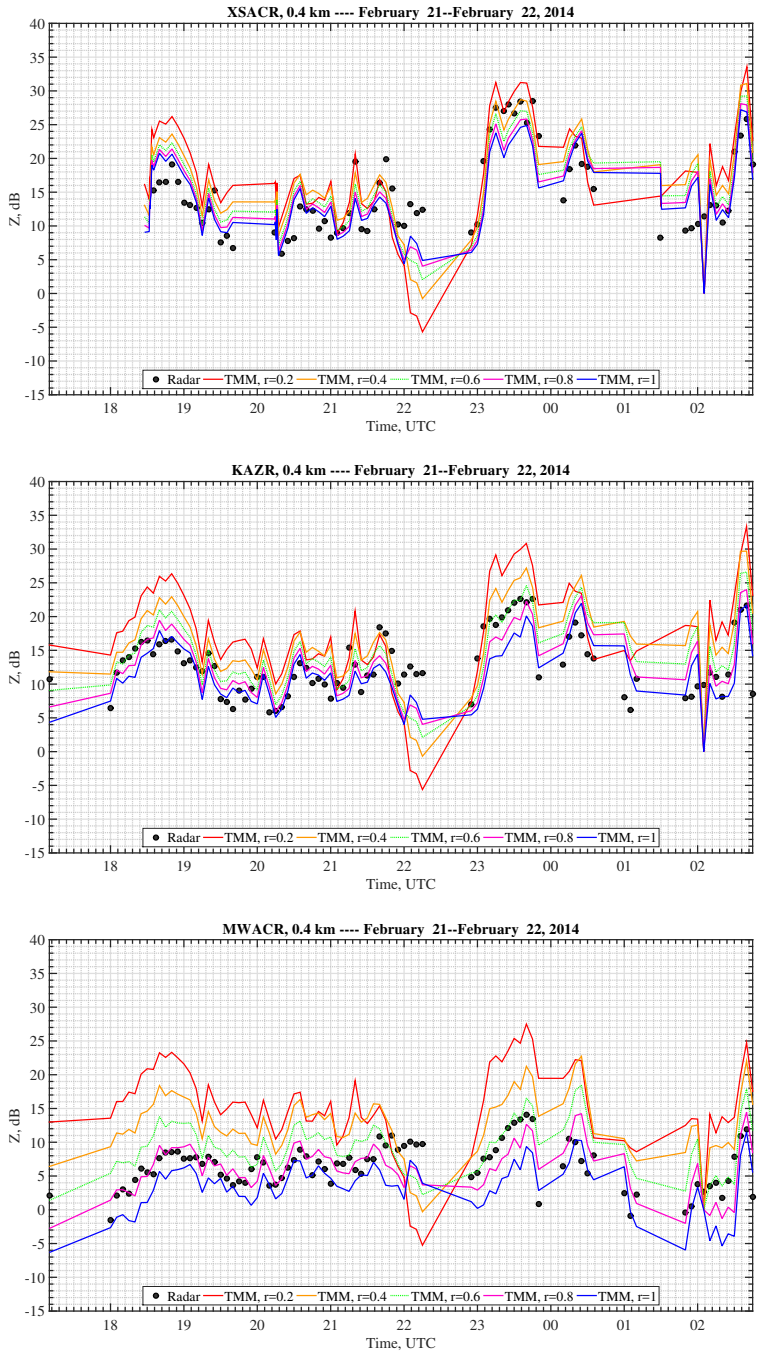


Figure 78: Case study: 21-22 February 2014 - Equivalent reflectivity measured by the radar (black points) compared with the TMM results for aspect ratios from 0.2-1.

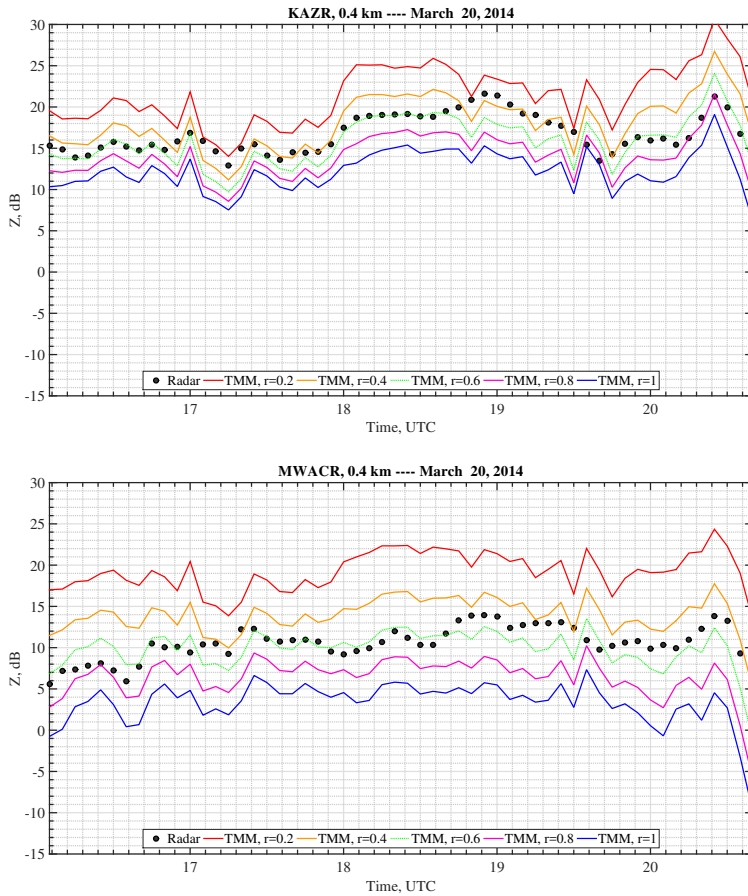


Figure 79: Case study: 20 March 2014 - Equivalent reflectivity measured by the radar (black points) compared with the TMM results for aspect ratios from 0.2-1.

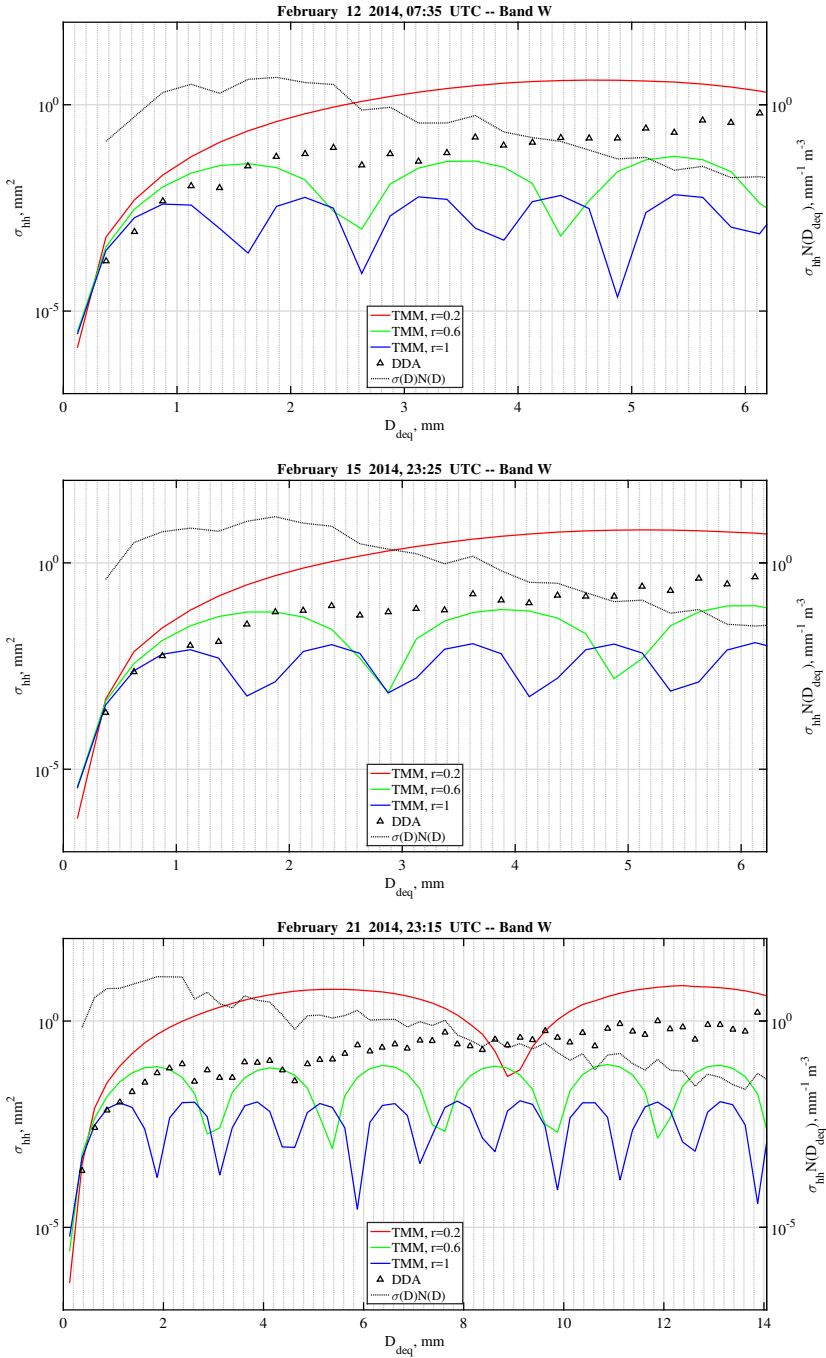


Figure 80: The horizontal cross section in the W band by comparing DDA computations (triangles) and TMM computations (dotted line). The product between the horizontal cross section and snowflake size distribution (red line) shows the main contribute of the particles with respect to the diameter disk-equivalent.

line shows the product between the snowflakes PSD and the backscatter cross section, useful to understand which part contributes to the reflectivity. In terms of time of selected data, in all the four cases one instantaneous sample has been taken within the period of heavy precipitation.

The first and more important consideration from Figure 80 is that the DDA results are within the uncertainty bounds defined by the TMM as a function of the aspect ratio r and then it is possible to obtain the same result of the DDA tuning the TMM using a single parameter. This result is related to the averaged time of five minutes, under sampling the time period leads to avoid effects due to complex aggregates with extremely shape and large sizes that are visible in short scale time [102]. For our purposes TMM is a good compromise between flexibility and accuracy and is able to give us general Z_e - S relations in function of the aspect ratio (see Table 18).

Looking at the single case study of 12 February 2014, I see that as expected in the Rayleigh region (until $D_{deq} \ll \lambda$, and then considering Table 14, for value of D_{deq} smaller than 0.32 mm) the DDA and the TMM (for all the aspect ratio) have the same behavior. Moving away from the Rayleigh region to the Mie region, up to the particle sizes are approximately as the wavelength, DDA and TMM are in agreement for extreme values of the aspect ratio $r = 0.2$. When the particle size becomes larger than the wavelength, DDA and the TMM are reasonably similar for values of the aspect ratio $r = 0.4 - 0.6$. The product of the PSD and σ_{hh} highlights in this case that the most influent part of the particle are less bigger than 4 mm. Same consideration can be made for the case study of 15-16 February 2014 with the only difference that the DDA behavior when the particle becomes bigger than the wavelength are strictly nearest to $r = 0.6$. Instead the case study of 21-22 February 2014 presents when the dimension of the particles are equal or bigger than the wavelength (until 4 mm) a DDA more in accord with a TMM for aspect ratio of $r = 0.6 - 0.8$. The previous discussion is in agreement with the results obtained by applying the weighted least square in equation (183) at the radar equivalent reflectivities and shown in Table 18 where for the W Band in the four cases I have an aspect ratio of: 0.6 for 12 February, 15-16 February and 20 March and 0.8 for 21-22 February 2014.

5.5 CONCLUSION

In this Chapter I have discussed the snowfall intensity retrieval Z_e - S at multifrequency using a high quality dataset of radar and in situ measure-

ments. The theoretical background on radars at multifrequency applied to the snowfall detection has been introduced. Z_e -S results have been obtained using data from four snowfall events recorded during the BAecc campaign, and the dataset has been extensively presented. Numerical results, such as TMM soft-ice spheroid approximation and DDA complex particle models, have been carried out for validation and comparison.

CONCLUSIONS

"Occorre la prospettiva d'una terra promessa, per avere forze bastanti da proseguire nel moto."

— Lev Nikolaevič Tolstoj, *Guerra e pace*, 1867

My PhD thesis has investigated three major topics of interest for the modern RADAR community. These topics are basically related to the Forward Scatter Radar (FSR) and Weather Radar (WR).

My FSR study has addressed the electromagnetic modeling of the target signature characterizing the transition from far-field to near-field regions. Results of this analysis, aimed to extend the model approach suggested by Gashinova et al. [9], named near-field simplified model [51, 52], show some valuable differences of the FS signature in this far-field-to-near-field transition. The influence of the target shape has been also investigated in terms of diffraction looking at two canonical shapes: rectangular and circular targets. The ripples from the sharp diffracting edges have been shown in comparison to the less visible one from the smooth circular profile. A more complete model has been presented after, named near-field receiver model [11, 53–55], derived directly from the Huygen's principle expressed in terms of extinction. Different representations of the transition from far-field to near-field have been shown in terms of a FSR scenario in which the Rx-target distances are progressively changed. Square and rectangular metallic plates are considered by changing also the dimensions to investigate the effect of the target size on the signature. Effects of the trajectory have been also investigated to take into account the target moving not necessarily perpendicular to the baseline (BL). All the results from this model have been validated by means of the full-wave CAD solution showing an excellent agreement. For completeness, results of the Arago spot appearance and the shadow contour theorem have been also shown. An attractive extension of this study would be related to develop a more

complete electromagnetic modeling of a realistic transmitter with respect to a plane-wave source, as suggested in Equation (127). Another interesting development would be to investigate the shadow radiation of 3D radar targets in the near-field as preliminarily shown in [50] and in general the transition from 2D to 3D shapes.

The WR studies which I have considered in my thesis are related to two different topics: radar calibration monitoring and radar based snowfall intensity retrieval at multifrequency. The first part of this investigation on radar calibration monitoring has been devoted to the improvement of ground-clutter classification and clutter-based relative calibration monitoring, using a C-band polarimetric weather radar located in the complex orography of southern Italy [13]. In the available literature there are several works presenting results on different weather-radar calibration techniques, but only few of them use ground-clutter echoes as calibration targets monitoring [62, 64, 74]. The main goal of this work has been to propose an overall self-consistent approach for clutter-based relative calibration including both a Bayesian radar-signal classifier and region-merging algorithm to objectively identify those radar grid-points affected by ground clutter with a more stable behaviour in terms of its temporal and spatial statistical features. Both classification and segmentation algorithmic steps have been discussed, showing potentials and limitations of the proposed methodology. The results, based on a relatively limited dataset, have shown that a relative radar calibration can usefully exploit the identification of stable clutter sub-domains and the analysis of the daily mean value of co-polar and differential reflectivity. It is worth noting that the standard deviation, both for co-polar and differential reflectivity shows a diurnal cycle, a feature which might be exploited to better characterize clutter scenarios. A future development of this work would be focused on the enlargement of the available radar dataset and possibly extend the analysis to other C-band polarimetric radar systems. Moreover, the same overall approach could be further developed in order to include other polarimetric observables such as the co-polar correlation coefficient. In this way, we could obtain several estimates of calibration errors, derived from each polarimetric variables and then merge them all together (e.g. using a fuzzy logic approach) into a single diagnostic quality index of radar calibration. The latter would represent an easier approach to check the calibration status of the whole radar system.

The second part of the work on radar calibration monitoring has been conducted on a PSS technique that provides a continuous monitoring of the system calibration [14]. A complete analysis for a peculiar PSS with

a periodical metallic structure has been carried out. Preliminary results from the actual data have been considered for the monitoring of both reflectivity and differential reflectivity, highlighting that the signal returns from the PSS are very stable for Z_{hh} in time even in presence of heavy precipitation. In terms of Z_{dr} , the stability of the echoes is actually higher than needed for an accurate calibration whereas PSS-derived median values are in agreement with other calibration techniques. The PSS has been also tested for the check of antenna de-pointing. The experimental observations, carried out using radar data, are confirmed by the EM numerical results obtained with a full-wave commercial tool. In summary, the presented study supports the use of PSS in near-field region for radar calibration purposes. A future extension of this work could be focused on the development of an automatic method to select and classify various PSSs with characteristics similar to those here considered. A theoretical analysis of the near-field PSS should be also addressed in order to identify a searching criterion to fully exploit PSS features. A verification of the technique using other dual-polarization radar systems can be also planned in order to generalize the PSS calibration approach and support its exploitation within an operational context.

The snowfall intensity retrieval Z_e -S at multifrequency has been finally investigated using a high quality dataset of radar and in situ measurements. The coefficients, extracted for the snowfall radar and in-situ measurements within a power-law regressive model, are in line with the available literature and confirm also the appealing application of millimeter wavelength radars for the snowfall estimation. For validation and comparison, numerical results have been carried out by using the TMM soft-ice spheroid approximation and DDA complex particle models. TMM has been also implemented, setting microphysical parameters from the in-situ instrument and imposing a new mass-dimensional relation and introducing the aspect-ratio as a tuning parameter. Numerical results have emphasized the presence of two different microphysical behaviors related to the fluffy and rimed snow. An analysis of the backscattering cross sections reveals that in the studied cases, TMM cross sections are higher than the DDA ones for small ice particles and it is lower for the larger particles. These differences explain why the soft-spheroid approximation works rather well, since the errors in computed cross sections for larger and smaller particles compensate each other. This work can represent an important step for the design of the snowfall retrieval coefficients derived from measurements and for the definition of effective approximations for scattering simulations at centimeter and millimeter wavelengths. Future developments can

be related to the improvement of the retrieval investigating also the difference between linear and non-linear regression techniques. Another interesting aspect of research might be the difference between a Z_e -S retrieval and S- Z_e one.

COMPUTING SCATTERING: T-MATRIX

T-matrix method (TMM) is a formulation of the scattering problem originated by P.C. Waterman (1969) using the extinction theorem in equation (32) [22]. The idea is to use the extinction theorem as the extended boundary condition, to obtain an integral equation for the surface field that take into account the interior volume of the object for analytic continuity. This concept is used to derive the transition matrix (T-matrix) which relates the scattered wave to the incident wave.

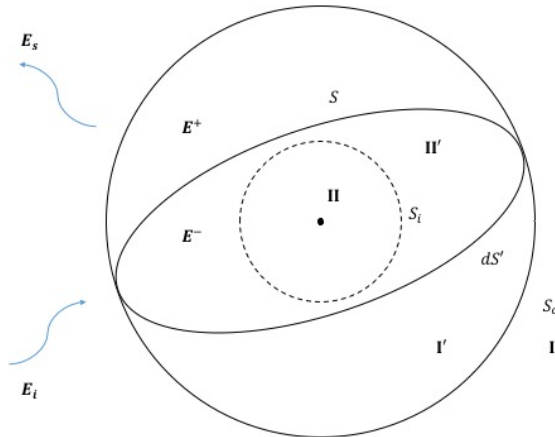


Figure 81: T-matrix method geometry.

I consider an incident wave E_i impinging on an object with surface S where Dirichlet's boundary condition is valid [22]. The incident field is expressed as a series of cylindrical harmonics

$$E_i(\mathbf{r}) = \sum_{n=-\infty}^{+\infty} a_n J_n(kr) e^{jn\Phi} \quad (184)$$

where a_n is the known coefficient. In the region I outside the circumscribed cylinder S_C (see Figure 81) in the same cylindrical harmonics I define the scattered field $E_S(\mathbf{r})$

$$E_S(\mathbf{r}) = \sum_{-\infty}^{+\infty} b_n H_n^{(2)}(kr) e^{jn\Phi} \quad (185)$$

where I used the second kind Hankel function to satisfy the radiation condition [22].

The transition matrix or T-matrix [T] is the square matrix defined by

$$[b] = [T][a] \quad (186)$$

where $[b] = [b_n]$ and $[a] = [a_n]$ are the column matrices [22]. To obtain the T-matrix I apply the extinction theorem in equation (32) to region II and II', starting with the region II inside the inscribed cylinder S_i . Because of $r < r'$ I can write the Green's function

$$G(\mathbf{r}, \mathbf{r}') = -\frac{j}{4} \sum_{-\infty}^{+\infty} J_n(kr) H_n^{(2)}(kr') e^{jn(\Phi - \Phi')} \quad (187)$$

Now I substitute equations (184) and (187) in equation (32)

$$\begin{aligned} & \sum_{-\infty}^{+\infty} a_n J_n(kr) e^{jn\Phi} = \\ & = -\frac{j}{4} \int_S \left[E(\mathbf{r}') \frac{\partial}{\partial n'} \sum_{-\infty}^{+\infty} J_n(kr) H_n^{(2)}(kr') e^{jn(\Phi - \Phi')} - \right. \\ & \left. \frac{\partial}{\partial n'} E(\mathbf{r}') \sum_{-\infty}^{+\infty} J_n(kr) H_n^{(2)}(kr') e^{jn(\Phi - \Phi')} \right] dS'. \end{aligned} \quad (188)$$

Since $J_n(kr)$ is orthogonal, I can equate each coefficient of $J_n \exp(jn\Phi)$ to zero and obtain

$$\begin{aligned} a_n = \frac{j}{4} \int_S & \left[E(\mathbf{r}') \frac{\partial}{\partial n'} H_n^{(2)}(kr') e^{jn\Phi'} + \right. \\ & \left. - \frac{\partial}{\partial n'} E(\mathbf{r}') H_n^{(2)}(kr') e^{jn\Phi'} \right] dS'. \end{aligned} \quad (189)$$

Then I obtain the scattered field E_S in region I using the Helmholtz-Kirchoff formula in equation (35) with the Green's function for $r > r'$

$$G(\mathbf{r}, \mathbf{r}') = -\frac{j}{4} \sum_{-\infty}^{+\infty} J_n(kr') H_n^{(2)}(kr) e^{jn(\Phi - \Phi')} \quad (190)$$

and from equation (185) using the orthogonality of $H_n^2(kr)e^{jn\Phi}$, I obtain

$$b_n = -\frac{j}{4} \int_S \left[E(\mathbf{r}') \frac{\partial}{\partial n'} J_n(kr') e^{-jn\Phi'} - \frac{\partial}{\partial n'} E(\mathbf{r}') J_n(kr') e^{-jn\Phi'} \right] dS'. \quad (191)$$

At this point I remember that the extended boundary condition was the extinction theorem and then $E = 0$ on S and finally [22] I have

$$\begin{aligned} a_n &= -\frac{j}{4} \int_S \frac{\partial}{\partial n'} E(\mathbf{r}') H_n^{(2)}(kr') e^{jn\Phi'} dS', \\ b_n &= \frac{j}{4} \int_S \frac{\partial}{\partial n'} E(\mathbf{r}') J_n(kr') e^{-jn\Phi'} dS'. \end{aligned} \quad (192)$$

I expand the unknown surface function $\partial E/\partial n'$ in a series of a complete set of functions

$$\frac{\partial}{\partial n'} E(\mathbf{r}') = \sum_{n=-\infty}^{+\infty} \alpha_n \frac{\partial}{\partial n'} [J_n(kr') e^{jn\Phi'}] \quad (193)$$

where α_n is the unknown coefficient [22].

Substituting equation (193) in equation (192), I get

$$\begin{aligned} [a] &= [Q^-][\alpha], \\ [b] &= -[Q^+][\alpha], \end{aligned} \quad (194)$$

where $[a]$, $[b]$, and $[\alpha]$ are column matrices and

$$\begin{aligned} Q_{mn}^- &= -\frac{j}{4} \int_S E_m \phi_n' dS', \\ Q_{mn}^+ &= -\frac{j}{4} \int_S E_{rm} \phi_n' dS', \\ E_m &= H_m^{(2)}(kr') e^{-jm\Phi'}, \\ E_{rm} &= J_m(kr') e^{-jm\Phi'}, \\ E_n' &= \frac{\partial}{\partial n'} [J_n(kr') e^{jn\Phi'}]. \end{aligned} \quad (195)$$

Finally, I eliminate the surface field $[\alpha]$ and get the T matrix

$$\begin{aligned} [b] &= [T][a] \\ [T] &= -[Q^+][Q^-]^{-1}. \end{aligned} \quad (196)$$

I consider Neumann's problem for which the boundary condition on S that is $(\partial/\partial n')E(\mathbf{r}') = 0$. From equations (189) and 191 I get a_n and b_n in terms of $E(\mathbf{r}')$ on the surface. I expand $E(\mathbf{r}')$ in a complete set of functions

$$E(\mathbf{r}') = \sum_{n=-\infty}^{+\infty} \alpha_n J_n(kr') e^{jn\Phi} \quad (197)$$

where α_n are the unknown coefficients [22]. Substituting this into equations (189) and (191) I get

$$\begin{aligned} [\mathbf{a}] &= [\mathbf{Q}^-][\boldsymbol{\alpha}], \\ [\mathbf{b}] &= -[\mathbf{Q}^+][\boldsymbol{\alpha}] = [\mathbf{T}][\mathbf{a}] \\ [\mathbf{T}] &= -[\mathbf{Q}^+][\mathbf{Q}^-]^{-1}, \end{aligned} \quad (198)$$

where

$$\begin{aligned} Q_{mn}^- &= \frac{j}{4} \int_S E'_m \phi_n dS', \\ Q_{mn}^+ &= \frac{j}{4} \int_S E'_{rm} \phi_n dS', \\ E'_m &= \frac{\partial}{\partial n'} [H_m^{(2)}(kr') e^{-jm\phi'}] = \frac{\partial}{\partial n'} E_m, \\ E'_{rm} &= \frac{\partial}{\partial n'} [J_m(kr') e^{-jm\phi'}] = \frac{\partial}{\partial n'} E_{rm}, \\ \phi_n &= J_n(kr') e^{jn\phi'}. \end{aligned} \quad (199)$$

The T-matrix method describes a two-media problem, where the wave numbers and the densities outside the surface S are k_0 and ρ_0 and those inside S are k_1 and ρ_1 , I let E^+ and E^- denote surface field just outside and inside the surface S [22]. Then I expand in cylindrical harmonics the field inside S with the wave number k_1 and is regular and I get

$$E(\mathbf{r}) = \sum_{n=-\infty}^{+\infty} \beta_n J_n(k_1 r) e^{jn\phi}, \quad (200)$$

where β_n is the unknown coefficient. Using this expression I can write

$$\begin{aligned} E^-(\mathbf{r}') &= \sum_{n=-\infty}^{+\infty} \beta_n J_n(k_1 r') e^{jn\phi'} \\ \frac{\partial E^-(\mathbf{r}')}{\partial n'} &= \sum_{n=-\infty}^{+\infty} \beta_n \frac{\partial}{\partial n'} [J_n(k_1 r') e^{jn\phi'}] \end{aligned} \quad (201)$$

and the boundary conditions are

$$\begin{aligned} E^+(\mathbf{r}') &= \frac{\rho_1}{\rho_0} E^-(\mathbf{r}') \\ \frac{\partial E^+(\mathbf{r}')}{\partial n'} &= \frac{\partial E^-(\mathbf{r}')}{\partial n'} \end{aligned}$$

The field outside the surface S is contained in equations (189), (191) for a_n and b_n and it is related to the field inside given by β_n

$$\begin{aligned} [\mathbf{a}] &= [\mathbf{Q}^-][\boldsymbol{\beta}], \\ [\mathbf{b}] &= -[\mathbf{Q}^+][\boldsymbol{\beta}] = [\mathbf{T}][\mathbf{a}] \\ [\mathbf{T}] &= -[\mathbf{Q}^+][\mathbf{Q}^-]^{-1}, \end{aligned} \quad (202)$$

where

$$\begin{aligned}
 Q_{mn}^- &= \frac{j}{4} \int_S \left(\frac{\rho_1}{\rho_0} E'_m \phi_n - E_m \phi'_n \right) dS', \\
 Q_{mn}^+ &= \frac{j}{4} \int_S \left(\frac{\rho_1}{\rho_0} E'_{rm} \phi_n - E_{rm} \phi'_n \right) dS', \\
 E_m &= H_m^{(2)}(k_0 r') e^{-jm\phi'}, \\
 E'_m &= \frac{\partial}{\partial n'} E_m, \\
 E_{rm} &= J_m(k_0 r') e^{-jm\phi'}, \\
 E'_{rm} &= \frac{\partial}{\partial n'} E_{rm}, \\
 \phi_n &= J_n(k_1 r') e^{jn\phi'}, \\
 \phi'_n &= \frac{\partial}{\partial n'} \phi_n.
 \end{aligned} \tag{203}$$

The scattering from body of complex shape such as particles with irregular shapes can be modeled with the T-matrix method [22]. For two-dimensional problem I use the TMM with cylindrical harmonics and for three-dimensional problem with spherical harmonics.

B

ANALYTICAL FORMULAS FOR FSR EM MODELS

In this Appendix I show you the mathematical steps that lead to the analytical expression of the EM model at 1-O approximation in equation (120) and at 2-O approximation in equation (123).

B.1 NEAR-FIELD RECEIVER 1-O

I focus here on the mathematical steps that lead to the analytical expression of the EM model in eq. (120). Recalling the generalized expression in eq. (118)

$$E_T(\tilde{\mathbf{r}}) = E_0 \left(e^{-j\tilde{k}\tilde{z}_{Rx}} - \frac{1}{2\pi} \int_{\tilde{\Lambda}} \left(j\tilde{k} + \frac{1}{\tilde{R}} \right) \frac{\tilde{z}_{Rx}}{\tilde{R}^2} e^{-j\tilde{k}\tilde{R}} d\tilde{\Lambda}' \right) \quad (204)$$

I follow the approximations done in Section 3.3 by replacing the distance \tilde{R} with eq. (119). And then I consider the integral solution

$$\begin{aligned} & \int_{\tilde{\Lambda}} e^{-j\tilde{k} \frac{(\tilde{x}_t - \tilde{x}')^2 + (\tilde{y}_t - \tilde{y}')^2}{2\tilde{z}_{Rx}}} d\tilde{x}' d\tilde{y}' = \\ & = \left[- \int_0^{-\tilde{a}/2} e^{-j\tilde{k} \frac{(\tilde{x}_t - \tilde{x}')^2}{2\tilde{z}_{Rx}}} d\tilde{x}' + \int_0^{\tilde{a}/2} e^{-j\tilde{k} \frac{(\tilde{x}_t - \tilde{x}')^2}{2\tilde{z}_{Rx}}} d\tilde{x}' \right] \\ & \left[- \int_0^{-\tilde{b}/2} e^{-j\tilde{k} \frac{(\tilde{y}_t - \tilde{y}')^2}{2\tilde{z}_{Rx}}} d\tilde{y}' + \int_0^{\tilde{b}/2} e^{-j\tilde{k} \frac{(\tilde{y}_t - \tilde{y}')^2}{2\tilde{z}_{Rx}}} d\tilde{y}' \right] = \\ & = \frac{\tilde{z}_{Rx}}{2} [-C_F(p^-) + jS_F(p^-) + C_F(p^+) - jS_F(p^+)] \\ & [-C_F(q^-) + jS_F(q^-) + C_F(q^+) - jS_F(q^+)] \end{aligned} \quad (205)$$

being $\tilde{R}_0 = \sqrt{\tilde{x}_t^2 + \tilde{y}_t^2 + \tilde{z}_{Rx}^2}$, C_F and S_F the cosine and sine Fresnel integrals [10], and

$$p^\pm = \left(\tilde{x}_t \pm \frac{\tilde{a}}{2} \right) \sqrt{\frac{2}{\tilde{z}_{Rx}}} \quad (206)$$

$$q^\pm = \left(\tilde{y}_t \pm \frac{\tilde{b}}{2} \right) \sqrt{\frac{2}{\tilde{z}_{Rx}}}. \quad (207)$$

The last expression is related to the Fresnel integrals $\int_0^z \exp(-j(\pi/2)t^2) dt = C_F(z) - jS_F(z)$ [10] and leads directly to the EM formulation in eq. (120). Similar mathematical steps have been applied to the expression valid only in far-field (Fraunhofer) condition of eq. (125).

B.2 NEAR-FIELD RECEIVER2-O

I focus here on the mathematical steps that lead to the analytical expression of the EM model in equation (123), looking the equation (118) and by replacing the distance \tilde{R} with equation (124).

First of all, I re-write the distance \tilde{R} in equation (124) in a more easy way to solve the integral, such as

$$\begin{aligned} \tilde{R} &= \tilde{R}_0 \left[1 + \frac{\tilde{x}'^2 - 2\tilde{x}_t\tilde{x}' + \tilde{y}'^2 - 2\tilde{y}_t\tilde{y}'}{2\tilde{R}_0^2} - \frac{4\tilde{x}_t^2\tilde{x}'^2}{8\tilde{R}_0^4} \right] = \\ &= \tilde{R}_0 - \frac{\tilde{x}_t^2}{2\tilde{R}_0 \left(1 - \frac{\tilde{x}_t^2}{\tilde{R}_0^2}\right)} + \frac{1}{2\tilde{R}_0} \left(1 - \frac{\tilde{x}_t^2}{\tilde{R}_0^2}\right) \left[\tilde{x}' - \frac{\tilde{x}_t}{\left(1 - \frac{\tilde{x}_t^2}{\tilde{R}_0^2}\right)} \right]^2 + \\ &\quad - \frac{\tilde{y}_t^2}{2\tilde{R}_0} + \frac{1}{2\tilde{R}_0} (\tilde{y}' - \tilde{y}_t)^2 \end{aligned} \quad (208)$$

As already done in the previous Appendix B.1 I solve the integral expression in which the previous distance \tilde{R} is replaced in equation (118) and then

$$\begin{aligned} \int_{\tilde{A}} e^{-jk\tilde{R}} d\tilde{x}' d\tilde{y}' &= e^{-jk\tilde{R}_0} e^{+jk \left[\frac{\tilde{x}_t^2}{2\tilde{R}_0 \left(1 - \frac{\tilde{x}_t^2}{\tilde{R}_0^2}\right)} + \frac{\tilde{y}_t^2}{2\tilde{R}_0} \right]} \\ &\int_{-\tilde{a}/2}^{+\tilde{a}/2} e^{-jk \frac{1}{2\tilde{R}_0} \left(1 - \frac{\tilde{x}_t^2}{\tilde{R}_0^2}\right) \left[\tilde{x}' - \frac{\tilde{x}_t}{\left(1 - \frac{\tilde{x}_t^2}{\tilde{R}_0^2}\right)} \right]^2} d\tilde{x}' \\ &\int_{-\tilde{b}/2}^{+\tilde{b}/2} e^{-jk \frac{1}{2\tilde{R}_0} (\tilde{y}' - \tilde{y}_t)^2} d\tilde{y}' \end{aligned} \quad (209)$$

Now to figure out this difficult integral I apply the change of variables formula with \tilde{x} ($\tilde{x} = \sqrt{(2/\tilde{R}_0)}(1 - \tilde{x}_t^2/\tilde{R}_0^2)\tilde{x}'$) and \tilde{y} ($\tilde{y} = \sqrt{2/\tilde{R}_0}\tilde{y}'$), I obtain

$$\begin{aligned}
& \int_{\tilde{\mathcal{A}}} e^{-jk\tilde{R}} d\tilde{x}' d\tilde{y}' = e^{-jk\tilde{R}_0} e^{+jk \left[\frac{\tilde{x}_t^2}{2\tilde{R}_0 \left(1 - \frac{\tilde{x}_t^2}{\tilde{R}_0^2}\right)} + \frac{\tilde{y}_t^2}{2\tilde{R}_0} \right]} \\
& \left[\int_{-\tilde{a}/2\sqrt{(2/\tilde{R}_0)(1-\tilde{x}_t^2/\tilde{R}_0^2)}}^{+\tilde{a}/2\sqrt{(2/\tilde{R}_0)(1-\tilde{x}_t^2/\tilde{R}_0^2)}} e^{-j\pi/2 \left[\tilde{x}_t \sqrt{\frac{2}{\tilde{R}_0} (1-\tilde{x}_t^2/\tilde{R}_0^2)} - \tilde{x} \right]^2} \sqrt{\frac{\tilde{R}_0}{2(1-\tilde{x}_t^2/\tilde{R}_0^2)}} d\tilde{x} \right] \\
& \left[\int_{-\tilde{b}/2\sqrt{2/\tilde{R}_0}}^{+\tilde{b}/2\sqrt{2/\tilde{R}_0}} e^{-j\pi/2 \left(\tilde{y}_t \sqrt{2/\tilde{R}_0} - \tilde{y} \right)^2} \sqrt{\frac{\tilde{R}_0}{2}} d\tilde{y} \right] = \\
& = e^{-jk\tilde{R}_0} e^{+jk \left[\frac{\tilde{x}_t^2}{2\tilde{R}_0 \left(1 - \frac{\tilde{x}_t^2}{\tilde{R}_0^2}\right)} + \frac{\tilde{y}_t^2}{2\tilde{R}_0} \right]} \frac{\tilde{R}_0}{2\sqrt{1 - \frac{\tilde{x}_t^2}{\tilde{R}_0^2}}} \\
& [-C_F(p^-) + jS_F(p^-) + C_F(p^+) - jS_F(p^+)] \\
& [-C_F(q^-) + jS_F(q^-) + C_F(q^+) - jS_F(q^+)] \tag{210}
\end{aligned}$$

being $p^\pm = \left(-\frac{\tilde{x}_t}{1-\tilde{x}_t^2/\tilde{R}_0^2} \pm \tilde{a}/2 \right) \sqrt{2(1-\tilde{x}_t^2/\tilde{R}_0^2)/(\tilde{R}_0)}$ and $q^\pm = \left(-\tilde{y}_t \pm \tilde{b}/2 \right) \sqrt{2/(\tilde{R}_0)}$.

The last expression is the same of equation (123).

BIBLIOGRAPHY

- [1] F. F. Sabins. *Remote Sensing: Principles and Applications*. Waveland Press, 2007.
- [2] T. Lillesand, R. W. Kiefer and J. Chipman. *Remote sensing and image interpretation*. John Wiley & Sons, 2014.
- [3] M. I. Skolnik. *Introduction to radar systems*. McGraw Hill, 2001.
- [4] R. J. Doviak and D. S. Zrnic. *Doppler radar and weather observations*. Academic Press, 1993.
- [5] M. Cherniakov. *Bistatic radars: emerging technology*. Vol. 1. John Wiley & Sons, 2008.
- [6] V. N. Bringi and V. Chandrasekar. *Polarimetric Doppler weather radar: principles and applications*. Cambridge university press, 2001.
- [7] S. Matrosov. 'Radar reflectivity in snowfall.' In: *IEEE Transactions on Geoscience and Remote Sensing* 30 (1992), pp. 454–461.
- [8] P. Y. Ufimtsev. *Fundamentals of the Physical Theory of Diffraction*. Wiley and Sons, 2007.
- [9] M. Gashinova, L. Daniel, V. Sizov, E. Hoare and M. Cherniakov. 'Phenomenology of Doppler forward scatter radar for surface targets observation'. In: *IET Radar, Sonar & Navigation* 7 (2013), pp. 422–432.
- [10] A. Ishimaru. *Electromagnetic Wave Propagation, Radiation, and Scattering*. Prentice-Hall, 1991.
- [11] M. T. Falconi, D. Comite, A. Galli, D. Pastina, P. Lombardo and F. S. Marzano. 'Forward Scatter Radar for Air Surveillance: Characterizing the Target-Receiver Transition from Far-Field to Near-Field Regions.' In: *Remote Sensing* 9.1 (2017), p. 50.
- [12] R. L. Ice, A. K. Heck, J. G. Cunningham and W. D. Zittel. 'Challenges of polarimetric weather radar calibration.' In: *Proc. ERAD*. 2014.
- [13] M. T. Falconi, M. Montopoli and F. S. Marzano. 'Bayesian statistical analysis of ground-clutter for the relative calibration of dual polarization weather radars.' In: *European Journal of Remote Sensing* 49.1 (2016), pp. 933–953.

- [14] M. T. Falconi, M. Montopoli, F. S. Marzano and L. Baldini. 'Weather Radar Performance Monitoring using a Metallic-Grid Ground-Scatterer.' In: *SPIE Remote Sensing*. 2017.
- [15] T. Petaja et al. 'BAECC: A Field Campaign to Elucidate the Impact of Biogenic Aerosols on Clouds and Climate.' In: *Bulletin of the American Meteorological Society* 97.10 (2016), pp. 1909–1928.
- [16] S. Kneifel, M. S. Kulie and R. Bennartz. 'A triple-frequency approach to retrieve microphysical snowfall parameters.' In: *Journal of Geophysical Research* 116 (2011), pp. 1–15.
- [17] G.L. Stephens et al. 'The Cloudsat Mission and the A-train.' In: *Bull. Amer. Meteor. Soc.* 83.12 (2002), 1771–1790.
- [18] G. Skofronick-Jackson et al. 'Global Precipitation Measurement (GPM) Mission for Science and Society.' In: *Bull. Amer. Meteor. Soc.* 98 (2017), 1679–1695.
- [19] A.J. Illingworth et al. 'The EarthCARE Satellite: The Next Step Forward in Global Measurements of Clouds, Aerosols, Precipitation, and Radiation.' In: *Bull. Amer. Meteor. Soc.* 96 (2015), 1311–1332.
- [20] W. L. Melvin and J. A. Scheer. *Principles of Modern Radar*. SciTech Publishing, 2013.
- [21] F. T. Ulaby, R. K. Moore and A. K. Fung. *Microwave remote sensing: Active and passive - From theory to applications*. Vol. 3. Artech House, 1986.
- [22] C. A. Balanis. *Antenna Theory: Analysis and Design (3rd ed.)* New Jersey: Wiley and Sons, 2005.
- [23] K. Balman and E. Jordan. *Electromagnetic waves and radiating systems*. Prentice-Hall, 1968.
- [24] N. J. Willis. *Bistatic Radar*. SciTech Publishing, 2005.
- [25] N. J. Willis and H. D. Griffiths. *Advances in Bistatic Radar*. SciTech Publishing, 2007.
- [26] D. V. Nezlin, V. I. Kostylev, A. B. Blyakhman, A. G. Ryndyk and A. V. Myakinkov. *Bistatic radar: principles and practice*. John Wiley & Sons, 2007.
- [27] C. Hu, V. Sizov, M. Antoniou, M. Gashinova and M. Cherniakov. 'Optimal signal processing in ground-based forward scatter micro radars'. In: *IEEE Transactions on Aerospace and Electronic Systems* 48 (2012), pp. 3006–3026.

- [28] N. E. A. Rashid, M. Gashinova, V. Sizov, M. Cherniakov and N. N. Ismail. 'The influence of different baseline lengths to ground target signature in a FS micro-radar network,' in: *IEEE 9th International Colloquium on Signal Processing and its Applications*. 2013, pp. 21–26.
- [29] S. Hristov, L. Daniel and M. Gashinova. 'Software defined radio for profile reconstruction in Forward Scatter Radar,' in: *11th European Radar Conference*. 2014, pp. 573–576.
- [30] G. Brussaard and P. A. Watson. *Atmospheric modelling and millimetre wave propagation*. Springer Science & Business Media, 1994.
- [31] P. S. Ray. 'Broadband complex refractive indices of ice and water'. In: *Applied optics* 11 (1972), pp. 1836–1844.
- [32] C. Magono. 'On the shape of water drops falling in stagnant air'. In: *Journal of Meteorology* 11 (1954), pp. 77–79.
- [33] H. R. Pruppacher and R. L. Pitter. 'A semi-empirical determination of the shape of cloud and raindrops'. In: *Journal of Atmospheric Sciences* 28 (1971), pp. 86–94.
- [34] H. R. Pruppacher and K. V. Beard. 'A windtunnel investigation of the internal circulation and shape of water drops falling at terminal velocity'. In: *Quarterly Journal of Royal Meteorological Society* 96 (1970), pp. 247–256.
- [35] G. E. R. T. Brussaard. 'A meteorological model for rain-induced cross polarization'. In: *IEEE Transactions on Antennas and Propagation* 24 (1976), pp. 5–11.
- [36] D. Atlas and C. W. Ulbrich. 'Path-and area-integrated rainfall measurement by microwave attenuation in the 1–3 cm band'. In: *Journal of Applied Meteorology* 16 (1977), pp. 1322–1331.
- [37] A. R. Jameson and A. B. Kostinski. 'What is a raindrop size distribution?' In: *Bulletin of the American Meteorological Society* 82 (2001), pp. 1169–1177.
- [38] J. S. Marshall and W. McK. Palmer. 'The distribution of raindrops with size'. In: *Journal of Meteorology* 5 (1948), pp. 165–166.
- [39] C. W. Ulbrich. 'Natural variations in the analytical form of the raindrop size distribution'. In: *Journal of Climate and Applied Meteorology* 22 (1983), pp. 1764–1775.
- [40] R. S. Sekhon and R. C. Srivastava. 'Doppler radar observations of drop-size distributions in a thunderstorm'. In: *Journal of the Atmospheric Sciences* 28 (1971), pp. 983–994.

- [41] C. D. Ahrens and R. Henson. *Meteorology Today*. Cengage Learning, 2015.
- [42] S. G. Warren. 'Optical constants of ice from the ultraviolet to the microwave'. In: *Applied optics* 23 (1984), pp. 1206–1225.
- [43] G. Hufford. 'A model for the complex permittivity of ice at frequencies below 1 THz'. In: *Int. Journal of Infrared and Millimeter Waves* 12 (1991), pp. 677–682.
- [44] T. S. Glickman. *Glossary of Meteorology*. American Meteorological Society., 2000.
- [45] J. M. Straka, D. S. Zrnić and A. V. Ryzhkov. 'Bulk hydrometeor classification and quantification using polarimetric radar data: synthesis of relations'. In: *Journal of Applied Meteorology* 39 (2000), pp. 1341–1372.
- [46] I. Steinhorn and D. S. Zrnić. 'Potential uses of the differential propagation phase constant to estimate raindrop and hailstone size distributions'. In: *IEEE Transactions on Geoscience and Remote Sensing* 26 (1988), pp. 639–648.
- [47] J. C. Maxwell-Garnett. 'Colors in metal glasses and in metallic films'. In: *Philosophical Transactions of the Royal Society of London* 203 (1904), pp. 385–420.
- [48] R. S. Sekhon and R. C. Srivastava. 'Snow size spectra and radar reflectivity'. In: *Journal of Atmospheric Sciences* 27 (1970), pp. 299–307.
- [49] H. E. Hernandez-Figueroa, M. Zamboni-Rached and E. Recami. *Non-diffracting Waves*. New Jersey: Wiley and Sons, 2013.
- [50] D. Comite, M. T. Falconi, P. Lombardo, F. S. Marzano and A. Galli. 'Investigating Shadow Radiation of 3-Dimensional Radar Targets in the Near Field.' In: *Proc. 2017 Radar Conference (EuRAD)*. 2017.
- [51] M. T. Falconi, D. Comite, A. Galli, P. Lombardo and F. S. Marzano. 'Forward scatter radar modeling: Effects of near field for canonical targets.' In: *IEEE International Symposium on Antennas and Propagation & USNC/URSI National Radio Science Meeting*. 2015.
- [52] M. T. Falconi, D. Comite, F. S. Marzano, A. Galli and P. Lombardo. 'Analysis of canonical targets in near field for Forward Scatter Radar applications.' In: *European Radar Conference (EuRAD)*. 2015.

- [53] M. T. Falconi, D. Comite, D. Pastina, A. Galli, F. S. Marzano and P. Lombardo. 'Analysis of canonical targets in near field for Forward Scatter Radar applications.' In: *European Radar Conference (EuRAD)*. 2016.
- [54] M. T. Falconi and D. Comite. 'Electromagnetic Modeling of Forward Scatter Radar.' In: *Rinem*. 2016.
- [55] M. T. Falconi, D. Comite, A. Galli, F. S. Marzano, D. Pastina and P. Lombardo. 'Monitoring by forward scatter radar techniques: an improved second-order analytical model.' In: *SPIE Remote Sensing*. 2017.
- [56] V. Chandrasekar, L. Baldini, N. Bharadwaj and P. Smith. 'Calibration procedures for global precipitation measurements ground-validation radars.' In: *URSI Radio Science Bulletin* 88.1 (2015), 45–73.
- [57] E. Gorgucci, G. Scarchilli and V. Chandrasekar. 'A procedure to calibrate multiparameter weather radar using properties of the rain medium.' In: *IEEE Transaction on Geoscience and Remote Sensing* 37.1 (1999), pp. 269–276.
- [58] V.R. Ryzhkov, S.E. Giangrande, V.M. Melnikov and T.J. Schuur. 'Calibration issues of dual-polarization radar measurements.' In: *Journal of Atmospheric and Oceanic Technology* 22.1 (2005), pp. 1138–1155.
- [59] I. Holleman, A. Huuskonen, M. Kurri and H. Beekhuis. 'Operational monitoring of weather radar receiving chain using the Sun.' In: *Journal of Atmospheric and Oceanic Technology* 27.1 (2010), pp. 159–166.
- [60] R. E. Rinehart. 'On the Use of Ground Return Targets for Radar Reflectivity Factor Calibration Checks.' In: *Journal of Applied Meteorology* 17.1 (1978), pp. 1342–1350.
- [61] S. Serrar, G. Delrieu, J. D. Creutin and R. Uijlenhoet. 'Mountain reference technique: Use of mountain returns to calibrate weather radars operating at attenuating wavelengths.' In: *Journal of Geophysical Research: Atmospheres* 105.1 (2000), pp. 2281–2290.
- [62] D. S. Silberstein, D. B. Wolff, D. A. Marks, D. Atlas and J. L. Pippitt. 'Ground clutter as a monitor of radar stability at kwajalein, RMI'. In: *Journal of Atmospheric and Oceanic Technology* 25 (2008), pp. 2037–2045.

- [63] D.A. Marks, D.B. Wolff, D.S. Silberstein, A. Tokay, J. L. Pippitt and J. Wang. 'Availability of high-quality TRMM ground validation data from kwajalein, RMI: A practical application of the relative calibration adjustment technique'. In: *Journal of Atmospheric and Oceanic Technology* 26 (2009), pp. 413–429.
- [64] D.B. Wolff, D. A. Marks and W. A. Petersen. 'General application of the relative calibration adjustment (RCA) technique for monitoring and correcting radar reflectivity calibration'. In: *Journal of Atmospheric and Oceanic Technology* 32 (2009), pp. 413–429.
- [65] S. Bertoldo, L. Bracco, R. Notarpietro, C. Lucianaz, O. Rorato, M. Allegretti and G. Perona. 'A standalone application to monitor the stability of a low cost maintenance free X-band mini weather radar, using ground clutter echoes'. In: *Proc. 2012 International Conference on Electromagnetics in Advanced Applications*. 2012, pp. 1040–1043.
- [66] L. Borowska and D. Zrnica. 'Use of ground clutter to monitor polarimetric radar calibration'. In: *Journal of Atmospheric and Oceanic Technology* 29 (2012), pp. 159–176.
- [67] M.A. Rico-Ramirez and I.D. Cluckie. 'Classification of Ground-clutter and Anomalous Propagation Using Dual-Polarization Weather Radar.' In: *IEEE Transaction on Geoscience and Remote Sensing* 46.7 (2008), pp. 1892–1904.
- [68] Nock R. and Nielsen F. 'Statistical region merging.' In: *IEEE Transactions on Pattern Analysis and Machine Intelligence* 26.11 (2004), pp. 1452–1458.
- [69] P.P. Alberoni, L. Ferraris, F. S. Marzano, S. Nanni, R. Pelosini and F. Siccardi. 'The Italian radar network: current status and future developments.' In: *Proceedings of ERAD 2002* (2002), pp. 339–344.
- [70] G. Vulpiani, M. Montopoli, L.D. Passeri, A.G. Gioia, P. Giordano and F.S. Marzano. 'On the use of dual-polarized C-band radar for operational rainfall retrieval in mountainous areas.' In: *Journal of Applied Meteorology and Climatology* 51.2 (2012), pp. 405–425.
- [71] S. Kotz and S. Nadarajah. *Extreme value distributions: theory and applications*. World Scientific, 2000.
- [72] J.T. Schaefer. 'The critical success index as an indicator of warning skill.' In: *Weather and Forecasting* 5.4 (1990), pp. 570–575.

- [73] S. Moszkowicz, G. J. Ciach and W.F. Krajewski. 'Statistical Detection of Anomalous Propagation in Radar Reflectivity Patterns.' In: *Journal of Atmospheric and Oceanic Technology* 11 (1994), pp. 1026–1034.
- [74] M.-H. Golbon-Haghighi, G. Zhang, Y. Li and R.J. Doviak. 'Detection of Ground Clutter from Weather Radar Using a Dual-Polarization and Dual-Scan Method.' In: *Atmosphere* 7.6 (2016), p. 83.
- [75] E. Gorgucci, L. Baldini and G. Scarchilli. 'Dual-polarization developments at CNR: Past and present research'. In: *Proc. 2006 IEEE International Symposium on Geoscience and Remote Sensing*. 2006, pp. 1666–1669.
- [76] M. Montopoli, N. Roberto, E. Adirosi, E. Gorgucci and L. Baldini. 'Investigation of Weather Radar Quantitative Precipitation Estimation Methodologies in Complex Orography'. In: *Atmosphere* 8 (2017).
- [77] A.V. Bergami and F. Sylos Labini. 'Forme e applicazioni tecniche del calcestruzzo armato: La Città dello Sport di Tor Vergata in Roma (un progetto dell'Arch. Ing. Santiago Calatrava'. In: *Proc. AICAP*. 2011.
- [78] David Atlas and Frank H. Ludlam. 'Multiwavelength radar reflectivity of hailstorms.' In: *Quarterly Journal of the Royal Meteorological Society* 87 (1961), pp. 523–534.
- [79] Ralph J. Donaldson. 'Radar Reflectivity Profiles in Thunderstorms.' In: *Journal of Meteorology* 18 (1961), pp. 292–305.
- [80] Frank H. Ludlam and W. C. Macklin. 'Some aspects of a severe storm in S.E. England.' In: *Nubila* 2 (1959), pp. 38–50.
- [81] J. S. Marshall and W. C. Palmer. 'The distribution of raindrops with size.' In: *Journal of Meteorology* 5 (1955), pp. 165–166.
- [82] K. L. S. Gunn and J. S. Marshall. 'The effect of wind shear on falling precipitation.' In: *Journal of Meteorology* 12 (1955), pp. 339–349.
- [83] D. Atlas, W. G. Harper, F. H. Ludlam and W. C. Macklin. 'Radar scatter by large hail.' In: *Quarterly Journal of the Royal Meteorological Society* 86 (1960), p. 468.
- [84] A. L. Aden. 'Electromagnetic scattering from metal and water spheres.' In: *Journal of Applied Physics* 22 (1951), p. 601.
- [85] F. T. Haddock. 'Scattering and attenuation of microwave radiation through rain.' In: *Naval Research Laboratory (unpublished manuscript)* (1948).

- [86] D. M. A. Jones. 'Rainfall drop-size distribution and radar reflectivity.' In: *Met. Lab. Res. Rep.* 6 (1956).
- [87] David Atlas and Frank H. Ludlam. 'Corrigenda Multiwavelength radar reflectivity of hailstorms.' In: *Quarterly Journal of the Royal Meteorological Society* 88 (1962), pp. 207–208.
- [88] R. J. Hogan, A. J. Illingworth and H. Sauvageot. 'Measuring crystal size in cirrus using 35- and 94 GHz radars.' In: *Journal of Atmospheric and Oceanic Technology* 17 (2000), pp. 27–37.
- [89] T. A. Seliga and V. N. Bringi. 'Potential use of radar differential reflectivity measurements at orthogonal polarizations for measuring precipitation.' In: *Journal of applied meteorology* 15 (1976), pp. 69–76.
- [90] K. Aydin, T. A. Seliga and V. Balaji. 'Remote sensing of hail with a dual linear polarization radar.' In: *Journal of climate and applied meteorology* 25 (1986), pp. 1475–1484.
- [91] S. Matrosov. 'A Dual-Wavelength Radar Method to Measure Snowfall Rate.' In: *Journal of climate and applied meteorology* 37 (1998), pp. 1510–1521.
- [92] A. J. Illingworth, J. W. G. Thomason, J. W. F. Goddard, H. Sauvageot and P. Simpson. 'Sizing of ice aggregates and snowflakes using coincident 3 and 35 GHz reflectivity observations.' In: *Pre-prints, 27th Conf. on Radar Meteorology, Vail, CO, American Meteor. Soc.* (1995), pp. 50–52.
- [93] T. Oguchi. 'Electromagnetic wave propagation and scattering in rain and other hydrometeors.' In: *Proc. IEEE* 71 (1983), pp. 1029–1078.
- [94] T. Ihara, Y. Furuhashi and K. Tohma. 'Measurement of depolarization due to snowfall at 34.5 GHz.' In: *Trans. IECE Japan* 65 (1982), p. 1622.
- [95] Y. Fujiyoshi, T. Endoh, T. Yamada, K. Tsuboki, Y. Tachibana and G. Wakahama. 'Determination of a Z-R relationship for snowfall using a radar and high sensitivity snow gauges.' In: *Journal of Applied Meteorology* 29 (1990), pp. 147–152.
- [96] V. I. Rozenberg. *Scattering and Extinction of Electromagnetic Waves by Atmospheric Particles*. Leningrad: Gidrometeoizdat, 1972.
- [97] S. G. Warren. 'Optical constants of ice from the ultraviolet to the microwave.' In: *Applied Optics* 23 (1984), pp. 1206–1225.

- [98] C. F. Bohren and D. R. Huffman. *Absorption and Scattering of Light by Small Particles*. New York: Wiley, 1972.
- [99] R. S. Sekhon and R. C. Srivastava. 'Snow size spectra and radar reflectivity.' In: *Journal of Atmospheric Sciences* 27 (1970), pp. 299–307.
- [100] S. Y. Matrosov, A. J. Heymsfield and Z. Wang. 'Dual-frequency radar ratio of nonspherical atmospheric hydrometeors.' In: *Geophysical research letters* 32 (2005).
- [101] Y. Yoshida, Shoji A. and Koyuru I. 'Retrieval of microphysical properties of water, ice, and mixed-phase clouds using a triple-wavelength radar and microwave radiometer.' In: *Journal of the Meteorological Society of Japan. Ser. II* 84.6 (2006), pp. 1005–1031.
- [102] S. Kneifel, A. von Lerber, J. Tiira, D. Moisseev, P. Kollias and J. Leinonen. 'Observed relations between snowfall microphysics and triple-frequency radar measurements.' In: *Journal of Geophysical Research: Atmospheres* 120.12 (2015), pp. 6034–6055.
- [103] T. Iguchi, R. Oki, E. Smith and Y. Furuhashi. 'Global Precipitation Measurement program and the development of dual-frequency precipitation radar.' In: *Journal Communications Research Laboratory* 49 (2002), pp. 37–46.
- [104] G. Liu. 'A database of microwave single-scattering properties for nonspherical ice particles.' In: *Bulletin of the American Meteorological Society* 89.10 (2008), pp. 1563–1570.
- [105] G. W. Petty and W. Huang. 'Microwave backscatter and extinction by soft ice spheres and complex snow aggregates.' In: *Journal of the Atmospheric Sciences* 67.3 (2010), pp. 769–787.
- [106] K. L. S. Gunn and J. S. Marshall. 'The distribution with size of aggregate snowflakes.' In: *Journal of Meteorology* 15 (1958), pp. 452–461.
- [107] R. E. Passarelli. 'A theoretical explanation for 2-R relationships in snow.' In: *Preprints, 18th Conf Radar Meteor. (Atlanta, CA)*. Boston: Amer. Meteorol. Soc. (1978), pp. 332–335.
- [108] R. J. Boucher. 'Snowfall rate obtained from radar reflectivity within a 50 km range.' In: *Preprints, 20th Conf Radar Meteor. (Boston, MA)*. Boston: American Meteorological Society (1981), pp. 271–275.

- [109] R. J. Boucher and J. G. Wieler. 'Radar determination of snowfall rate and accumulation.' In: *Journal of Climate and Applied Meteorology* 24 (1985), pp. 68–73.
- [110] P. E. Carlson and J. S. Marshall. 'Measurement of snowfall by radar.' In: *Journal of Applied Meteorology* 11 (1972), pp. 494–499.
- [111] I. Imai. 'Raindrop size distribution and Z-R relationships.' In: *Preprints, 8th Conf. Radar Meteor. (San Francisco, CA)*. Boston: American Meteorological Society (1960), pp. 211–215.
- [112] T. Puhakka. 'On the dependence of the Z-R relationship on the temperature in snowfall.' In: *Preprints, 16th Conf Radar Meteor. (Houston, TX)*. Boston: American Meteorological Society (1975), pp. 504–507.
- [113] J. W. Wilson. 'Measurement of snowfall by radar during the IFYGL.' In: *Preprints, 16th Conf: Radar Meteor., (Houston, TX)*. Boston: American Meteorological Society (1975), pp. 508–513.
- [114] C. Magono and T. Nakamura. 'Aerodynamic study of falling snowflakes.' In: *J. Meteor. Soc. Japan* 43 (1965), pp. 139–147.
- [115] S. Y. Matrosov. 'Modeling backscatter properties of snowfall at millimeter wavelengths.' In: *Journal of the atmospheric sciences* 64 (2007), pp. 1727–1736.
- [116] C.E. Dungey and C. F. Bohren. 'Backscattering by Nonspherical Hydrometeors as Calculated by the Coupled-Dipole Method: An Application in Radar Meteorology.' In: *J. Atmos. Oceanic Technol.* 10 (1993), pp. 526–532.
- [117] S. Y. Matrosov, M. D. Shupe and I. V. Djalalova. 'Snowfall Retrievals Using Mm-Wavelength Cloud Radars.' In: *J. Appl. Meteor. Climatol.* 47 (2008), 769–777.
- [118] P. Kollias, M. A. Miller, E. P. Luke, K. L. Johnson, E. E. Clothiaux, K. P. Moran, K. B. Widener and B. A. Albrecht. 'The ARM Program Cloud Profiling Radars: Second-Generation Sampling Strategies, Processing, and Cloud Data Products.' In: *Journal of Atmospheric and Oceanic Technology* 24.7 (2007), pp. 1199–1214.
- [119] G. Botta, K. Aydin and J. Verlinde. 'Modeling of Microwave Scattering From Cloud Ice Crystal Aggregates and Melting Aggregates: A New Approach.' In: *IEEE Geoscience and Remote Sensing Letters* 7.3 (2010), pp. 572–576.

- [120] J. Tyynelä, J. Leinonen, D. Moisseev and T. Nousiainen. 'Radar Backscattering from Snowflakes: Comparison of Fractal, Aggregate, and Soft Spheroid Models.' In: *Journal of Atmospheric and Oceanic Technology* 28.11 (2011), pp. 1365–1372.
- [121] D. Ori, T. Maestri, R. Rizzi, D. Cimini, M. Montopoli and F. S. Marzano. 'Scattering properties of modeled complex snowflakes and mixed-phase particles at microwave and millimeter frequencies.' In: *Journal of Geophysical Research: Atmospheres* 119.16 (2014), pp. 9931–9947.
- [122] J. Leinonen, D. Moisseev, V. Chandrasekar and J. Koskinen. 'Mapping Radar Reflectivity Values of Snowfall Between Frequency Bands.' In: *IEEE Transactions on Geoscience and Remote Sensing* 49.8 (2011), pp. 3047–3058.
- [123] J. Leinonen. 'Numerical approximation and analysis; Atmospheric scattering; Radar; Scattering, particles.' In: *Opt. Express* 22.2 (2014), pp. 1655–1660.
- [124] A. Von Lerber, Moisseev D., L. F. Bliven, W. Petersen, A.-M. Harri and V. Chandrasekar. 'Microphysical properties of snow and their link to Ze–S relation during BAECC 2014.' In: *Journal of Applied Meteorology and Climatology* (2017).
- [125] J. Tiira, D. N. Moisseev, A. von Lerber, D. Ori, A. Tokay, L. F. Bliven and W. Petersen. 'Ensemble mean density and its connection to other microphysical properties of falling snow as observed in Southern Finland.' In: *Atmospheric Measurement Techniques* 9.9 (2016), pp. 4825–4841.
- [126] A. J. Newman, P. A. Kucera and L. F. Bliven. 'Presenting the Snowflake Video Imager (SVI).' In: *Journal of Atmospheric and Oceanic Technology* 26.2 (2009), pp. 167–179.
- [127] V. Nešpor, W. F. Krajewski and Kruger A. 'Wind-Induced Error of Raindrop Size Distribution Measurement Using a Two-Dimensional Video Disdrometer.' In: *Journal of Atmospheric and Oceanic Technology* 17.11 (2000), pp. 1483–1492.
- [128] E. Saltikoff, A. Huuskonen, H. Hohti, J. Koistinen and H. Jarvinen. 'Quality assurance in the FMI Doppler weather radar network.' In: *Boreal environment research* 15.6 (2010), pp. 579–594.

- [129] A. Huuskonen and I. Holleman. 'Determining Weather Radar Antenna Pointing Using Signals Detected from the Sun at Low Antenna Elevations.' In: *Journal of Atmospheric and Oceanic Technology* 24.3 (2010), pp. 476–483.
- [130] H. J. Liebe. 'An updated model for millimeter wave propagation in moist air.' In: *Radio Science* 20.5 (1985), pp. 1069–1089.
- [131] P. Rosenkranz. 'Comment on Absorption and dispersion in the O₂ microwave spectrum at atmospheric pressures.' In: *The Journal of Chemical Physics* 77.4 (1982), pp. 2216–2217.
- [132] P. Rosenkranz. 'Shape of the 5 mm oxygen band in the atmosphere.' In: *IEEE Transactions on Antennas and Propagation* 23.4 (1975), pp. 498–506.
- [133] N. W. B. Stone, L. A. A. Read, A. Anderson, I. R. Dagg and W. Smith. 'Temperature dependent collision-induced absorption in nitrogen.' In: *Canadian journal of physics* 62.4 (1984), pp. 338–347.
- [134] S. M. Sekelsky. 'Near-Field Reflectivity and Antenna Boresight Gain Corrections for Millimeter-Wave Atmospheric Radars.' In: *Journal of Atmospheric and Oceanic Technology* 19.4 (2002), pp. 468–477.
- [135] M. I. Mishchenko. 'Calculation of the amplitude matrix for a non-spherical particle in a fixed orientation.' In: *Applied Optics* 39.6 (2000), pp. 1026–1031.
- [136] T. Garrett and S. Yuter. 'Observed influence of riming, temperature, and turbulence on the fallspeed of solid precipitation.' In: *Geophys. Res. Lett.* 41.18 (2014), pp. 6515–6522.
- [137] J. Leinonen and W. Szyrmer. 'Radar signatures of snowflake riming: A modeling study.' In: *Earth and Space Science* 2.8 (2015), pp. 2333–5084.
- [138] M. T. Falconi, A. von Lerber, D. Ori, F. S. Marzano and D. Moisseev. 'Snowfall retrieval at X, Ka and W band: consistency of backscattering and microphysical properties using BAECC ground-based measurements.' In: *Atmos. Meas. Tech. Discuss.* ().
- [139] M.A. Yurkin, V.P. Maltsev and A.G. Hoekstra. 'The discrete dipole approximation for simulation of light scattering by particles much larger than the wavelength.' In: *Journal of Quantitative Spectroscopy and Radiative Transfer* 106 (2007), pp. 546–557.

Rome, Italy, February 2018

Marta Tecla Falconi

Final Version as of 16th February 2018 (classicthesis).